

Dilute-Nitride Low-Dimensional Nanostructures Formed on Non-Planar Substrates

THÈSE N° 5814 (2013)

PRÉSENTÉE LE 22 JUILLET 2013

À LA FACULTÉ DES SCIENCES DE BASE
LABORATOIRE DE PHYSIQUE DES NANOSTRUCTURES
PROGRAMME DOCTORAL EN PHYSIQUE

ÉCOLE POLYTECHNIQUE FÉDÉRALE DE LAUSANNE

POUR L'OBTENTION DU GRADE DE DOCTEUR ÈS SCIENCES

PAR

Romain CARRON

acceptée sur proposition du jury:

Prof. N. Grandjean, président du jury
Prof. E. Kapon, directeur de thèse
Prof. A. Fontcuberta i Morral, rapporteur
Prof. M. Hopkinson, rapporteur
Prof. A. Rastelli, rapporteur



ÉCOLE POLYTECHNIQUE
FÉDÉRALE DE LAUSANNE

Suisse
2013

A Bénédicte

Abstract

The properties of semiconductor heterostructures of nanoscopic dimensions change from that of bulk material according to the rules of quantum mechanics. The planar quantum wells (QWs) are widely used in various diode and laser devices thanks to the relative ease of fabrication and to their improved electronic and optical performance compared to bulk materials. Quantum effects become more apparent when the charge carriers are confined in more than 1 spatial dimension. Much scientific interest was initially dedicated to the quantum wire (QWR) structures, which confine carriers into a quasi-1D space. But their sensitivity to disorder and the development of efficient fabrication methods of quantum dots (QD) shifted the attention to this latter system. The carrier confinement in the three directions of space confers to these structures a discrete spectrum of energy states, with the state occupancy ruled by the Pauli exclusion principle. The prospective applications are numerous in domains such as ultra-low threshold lasers, quantum cryptography, true random numbers generation, quantum electrodynamics experiments, etc.

One of the prominent semiconductor growth techniques is the metalorganic vapour phase epitaxy (MOVPE). We used this method to produce ordered QWRs and QDs at the bottom of V-shaped and tetrahedral recesses, respectively. These nanostructures form by the complementary actions of nano-capillarity and growth rate anisotropy in these recesses etched in GaAs substrates. This fabrication process offers some key advantages over other methods. The emission energy is very well controlled, with a narrow inhomogeneous broadening and a high uniformity across the wafer. Combined with the highly precise control on the formation site, this offers the possibility of high-yield integration of one or even several nanostructures, e.g., into photonic crystal devices. Other advantages of this approach are the impressive tunability of the electronic potential within the nanostructures and the possible use of well-defined intraband transitions. However, the emission energy of V-groove QWRs and pyramidal QDs studied so far is quite limited due to the formation mechanism imposing a low degree of strain.

Incorporation of nitrogen has dramatic effects on the band structure of GaAs-based materials. Dilute concentrations ($< 5\%$) lead to a huge shrinkage of the bandgap, as well as to large changes in various other electronic properties. Addition of nitrogen into QWRs and QDs nanostructures may thus allow emission wavelengths above $1\text{ }\mu\text{m}$, possibly up to the $1.3\text{ }\mu\text{m}$ telecommunication window of silica optical fiber.

In view of these opportunities, the first part of this work is dedicated to the study of N incorporation into QWs grown on vicinal-(100) GaAs substrates. The substrate miscut angle is often neglected in growth studies, and is of great importance in the cases of V-grooves and pyramidal recesses because of the large misorientations of the recesses facets. In our studied dilute-nitride QWs grown by MOVPE, large emission redshifts are achieved (> 250 meV). The substrate miscut and the surface corrugations are shown to play an important role in the N incorporation efficiency: QWs grown on large substrate misorientations emit at longer wavelength than those grown on usual (100)-"exact" substrates, while exhibiting a comparable luminescence efficiency. The importance of a uniform N distribution within the QW is stressed, which appears difficult to achieve when the effect of surface corrugation is combined with that of In segregation.

The second part of the work focuses on the N incorporation into V-groove QWRs. Important emission redshifts are achieved, in the ~ 250 meV range. We first detail the emission spectrum and assert the 1D-character of the carrier wavefunctions. The influence of various growth and structural parameters is explored, leading to the fabrication of QWRs emitting at $1.3\mu\text{m}$ at room temperature. The evolution of the polarization properties with temperature is also characterized.

The third main topic and primary goal of this thesis is the nitrogen incorporation into QDs formed in inverted pyramids etched on (111)B GaAs substrates. A study is first conducted to understand the effects of several growth and structural parameters on the emission properties of InGaAs QDs. Nitrogen incorporation into QDs is then successfully demonstrated. The monitoring of the lateral QWR emission energy suggests a peculiar N incorporation pattern, or a significant perturbation of the formation of these lateral nanostructures. By contrast to what achieved with QWs and QWR structures, only limited emission redshifts were achieved (~ 75 meV). The QD linewidths, degree of linear polarization and fine structure splitting are significantly deteriorated when compared to the InGaAs counterparts. These results cast serious doubts on the perspective of high-quality GaAs-based QDs in pyramids emitting at long wavelength.

Our results demonstrate that nitrogen does not have the potential to shift the emission wavelength of InGaAs pyramidal QDs up to $1.3\mu\text{m}$, while simultaneously satisfying strict quality requirements. But other material systems may offer such opportunities. We briefly explore the possibilities of growing InGaAs/InAlAs nanostructures on patterned InP wafers. This ongoing project may open new possibilities for exploiting the pyramidal QD system.

A kinetic Monte-Carlo numerical algorithm was implemented, reproducing by deposition and diffusion processes the evolution of the pyramidal template during growth. The numerical experiments were compared with post-growth AFM measurements of real samples. The recesses are observed to strongly affect the monatomic step flow on the neighboring (111)B surfaces. The simulations especially evidence the strong attraction of the pyramid apex on the atoms of the surrounding area, tending to elevate the QD formation site from the nominal C_{3v} symmetry toward a hexagonal one.

Keywords: semiconductor, heterostructure, nanostructure, epitaxy, MOVPE, nanoscale, quantum well, quantum wire, quantum dot, nitrogen, dilute nitride, GaAs, GaAsN, InGaAsN, V-groove, pyramid, vicinal substrate, photoluminescence, InP, Monte-Carlo, symmetry elevation, 1.3 μm .

Résumé

La mécanique quantique modifie les propriétés des hétérostructures semiconductrices de dimensions nanoscopiques par rapport à celles des matériaux massifs. Les puits quantiques (quantum wells - QW), des structures planaires, sont aujourd'hui largement exploités dans de nombreux équipements comportant diodes et lasers, du fait de leur facilité de fabrication ainsi que de leurs performances dépassant celles des matériaux massifs. Les effets quantiques deviennent plus aisément observables lorsque les porteurs de charge sont confinés dans plus d'une dimension spatiale. Les structures de fils quantiques (quantum wires - QWR) dont les charges sont confinées dans un espace quasi-1-dimensionnel suscitèrent initialement un large intérêt scientifique. Cependant leur sensibilité au désordre, ainsi que le développement de méthodes efficaces de fabrication des boîtes quantiques (quantum dots - QD) détournèrent l'attention vers ces dernières. Le confinement des porteurs de charge dans les 3 directions de l'espace confère à ces structures un spectre discret d'énergies d'états, dont l'occupation est conforme au principe d'exclusion de Pauli. Les perspectives d'applications sont nombreuses dans des domaines tels que les lasers à seuil ultra-bas, la cryptographie quantique, les générateurs de nombres vraiment aléatoires, les expériences d'électrodynamiques quantiques, etc.

Une des techniques phare de croissance des semiconducteurs est l'épitaxie en phase vapeur aux organométalliques (metalorganic vapour phase epitaxy - MOVPE). Nous avons utilisé cette méthode afin de produire des réseaux ordonnés de fils et de boîtes quantiques, logés respectivement dans des sillons en forme de V et au sein de cavités tétraédriques, gravés dans des substrats de GaAs. Ces nanostructures se forment par les actions complémentaires de nanocapillarité et d'anisotropie du taux de croissance. Ce processus de fabrication offre des avantages certains par rapport à d'autres méthodes. L'énergie d'émission se révèle extrêmement bien maîtrisée, avec un très faible élargissement inhomogène et une grande uniformité sur la surface du substrat. Combiné à la haute précision du contrôle du site de formation, cela permet l'intégration à haut rendement d'une voire plusieurs nanostructures, par exemple dans des dispositifs à cristaux photoniques. Parmi les autres avantages de cette approche, on distingue l'impressionnante adaptabilité du potentiel électronique dans les nanostructures ainsi que la possible utilisation des transitions intrabandes bien définies. Cependant, l'énergie d'émission des QWR dans les sillons en V et des QD pyramidaux étudiés jusqu'à présent s'avère assez limitée, en raison du mécanisme de formation nécessitant un degré de contrainte réduit.

L'incorporation d'azote a des effets drastiques sur la structure de bande des matériaux à base de GaAs. Des concentrations diluées (inférieures à 5 %) provoquent une diminution marquée de la bande interdite, et fait varier diverses autres propriétés électroniques de manière significative. L'addition d'azote dans les fils et les boîtes quantiques offre donc la possibilité d'émettre à des longueurs d'onde supérieures à $1\text{ }\mu\text{m}$, et potentiellement à la fenêtre de $1.3\text{ }\mu\text{m}$ des télécommunications par fibre optique en silice.

Compte tenu de ces perspectives, la première partie de ce travail est consacrée à l'étude de l'incorporation d'azote dans des QWs déposés sur des substrats GaAs (100) désorientés. L'angle de désorientation est un paramètre fréquemment négligé lors des études de croissance, et revêt une grande importance dans le cas des sillons en V et des pyramides en raison des grandes désorientations des facettes concernées. Nous avons obtenu d'importants décalages d'émissions ($> 250\text{ meV}$). L'angle de désorientation et la rugosité de surface jouent un rôle capital dans l'efficacité d'incorporation : les QWs déposés sur des substrats de grande désorientation émettent à plus grande longueur d'onde que ceux déposés sur les substrats (100) habituels, tout en maintenant une intensité de luminescence comparable. Nous soulignons l'importance d'une distribution d'azote uniforme dans la structure, laquelle est difficile à obtenir lorsque l'effet de la rugosité de surface se combine à la ségrégation d'In.

La seconde partie de ce travail se concentre sur l'incorporation d'azote dans des QWR formés dans des sillons en V. De considérables décalages de l'émission vers le rouge sont atteints, de l'ordre de $\sim 250\text{ meV}$. Tout d'abord, nous détaillons le spectre d'émission et nous assurons du caractère 1-dimensionnel des fonctions d'onde des porteurs de charge. L'influence de plusieurs paramètres structuraux et de croissance est ensuite explorée, aboutissant à la fabrication de QWR émettant à $1.3\text{ }\mu\text{m}$ à température ambiante. L'évolution en température des propriétés de polarisation est finalement détaillée.

Le troisième thème et but principal de ce travail de thèse est l'incorporation d'azote dans des QD formés dans des pyramides inversées gravées sur des substrats de GaAs (111)B. Une étude est menée pour comprendre les effets de plusieurs paramètres structuraux et de croissance sur les propriétés d'émission de QD composés d'InGaAs. Ensuite, nous démontrons l'incorporation réussie d'azote dans de telles boîtes. L'évolution de l'énergie d'émission des QWR latéraux suggère soit que l'azote s'incorpore de manière non uniforme, soit que le processus de formation de ces nanostructures est perturbé. Contrairement à ce que nous avons réussi avec les puits et les fils quantiques, seul un décalage vers le rouge limité a été atteint ($\sim 75\text{ meV}$). Plusieurs indicateurs de qualité des QDs régressent suite à l'incorporation d'azote, parmi lesquels la largeur d'émission, le degré de polarisation linéaire (degree of linear polarization - DOP) ainsi que la séparation de structure fine (fine structure splitting - FSS). Ces résultats rendent peu plausible la perspective de QD pyramidaux sur substrats GaAs de haute qualité émettant à grande longueur d'onde.

Nos résultats démontrent que les nitrures n'ont pas la capacité de décaler jusqu'à $1.3\text{ }\mu\text{m}$ la longueur d'onde d'émission des QD pyramidaux, tout en satisfaisant à des critères de qualité stricts. Cependant, d'autres matériaux peuvent proposer des opportunités intéressantes. Nous

explorons brièvement les possibilités de croissance de nanostructures InGaAs/InAlAs formées sur des substrats InP. Ce projet en cours pourrait permettre d'ouvrir de nouveaux horizons au système de QD pyramidaux.

Un algorithme de simulation numérique Monte-Carlo cinétique a été implémenté, qui reproduit l'évolution du canevas pyramidal au cours de la croissance au moyen des processus de diffusion et de déposition. Les expériences numériques ont été confrontées à des mesures AFM d'échantillons après croissance. Les pyramides affectent fortement les marches mono-atomiques environnantes situées sur la surface (111)B. Les simulations mettent spécialement en évidence la forte attraction de l'apex de la pyramide sur les atomes du voisinage, tendant à élever la symétrie du site de formation du QD de la symétrie initiale C_{3v} vers une forme hexagonale.

Mots clés : semiconducteur, hétérostructure, nanostructure, épitaxie, MOVPE, échelle nanométrique, puit quantique, fil quantique, boîte quantique, azote, nitrure dilué, GaAs, GaAsN, InGaAsN, V-groove, pyramide, substrat désorienté, photoluminescence, InP, Monte-Carlo, élévation de symétrie, 1.3 μ m.

Contents

Abstract	v
Résumé	ix
1 Introduction	1
1.1 Nanotechnologies	1
1.2 Semiconductors	2
1.2.1 Crystallographic structure	2
1.2.2 Band structure	3
1.2.3 Semiconductors alloys	5
1.3 Optical fibers communications	6
1.4 Nanostructures	7
1.5 Dilute nitride GaAs	9
1.5.1 Discovery and historical background	9
1.5.2 Applications of dilute nitrides alloys	9
1.6 Thesis goal and outline	10
2 Quantum nanostructures and the dilute-nitride compound system	13
2.1 V-groove QWRs and pyramidal QDs	13
2.1.1 Fabrication methods of low-dimensional nanostructures	13
2.1.2 V-groove QWRs and QDs in inverted pyramids	16
2.2 Toward long wavelength emission: the use of dilute nitrides	22
2.2.1 Theoretical description of GaAsN and InGaAsN alloys	22
2.2.2 Fabrication and optimization of (In)GaAsN alloys	28
2.2.3 Experimental determination of the N content	39
2.2.4 Sb incorporation for material improvement of long-wavelength material	40
2.2.5 Hydrogenation	40
2.2.6 The so-called 2-step growth	42
2.3 Chapter summary	43
3 Fabrication and characterization of nanostructures on patterned substrates	45
3.1 Substrate patterning	45
3.2 MOVPE growth procedure	47
3.3 Photoluminescence measurements	50

3.3.1	Microphotoluminescence setup	50
3.3.2	Characteristics of the new setup	51
3.3.3	Equivalent power density	53
3.3.4	Polarization-resolved measurements	54
3.4	Scanning electron microscopy	54
3.5	Transmission electron microscopy	55
3.6	Atomic Force Microscopy	55
3.7	Secondary Ion Mass Spectroscopy	56
3.8	Chapter summary	56
4	2D-nanostructures: dilute nitrides quantum wells	57
4.1	Dilute nitrides QW on misoriented substrates: growth procedure	58
4.2	Photoluminescence spectroscopy	59
4.2.1	Reference InGaAs quantum well	60
4.2.2	N-containing quantum wells	63
4.3	AFM interface characterization	66
4.4	SIMS characterization of N repartition	67
4.4.1	SIMS samples and measurement conditions	68
4.4.2	PL spectra and expected samples characteristics	68
4.4.3	In distribution uniformity and In content	69
4.4.4	N concentration	71
4.4.5	N distribution in the QW	73
4.4.6	Photoluminescence of hydrogenated N-QWs	75
4.4.7	Summary of N incorporation effects	76
4.5	Thermal annealing and S-shape behavior with temperature	76
4.6	Chapter summary	78
5	1D dilute-nitride nanostructures: V-grooves QWRs	81
5.1	Incorporation of nitrogen into V-groove QWRs	82
5.1.1	Photoluminescence spectra	83
5.1.2	TEM cross sections	86
5.1.3	Chemical composition	88
5.1.4	QWR segmentation experiments	90
5.2	Quantum confinement in V-groove dilute-nitride QWRs	92
5.2.1	Diamagnetic shift of PL spectra	92
5.3	Influence of growth and structural parameters on nitrogen incorporation	94
5.3.1	Choice of a proper reference sample	95
5.3.2	QWR pitch and groove-groove interaction	97
5.3.3	Effect of substrate misorientation	98
5.3.4	QWR thickness	102
5.3.5	GaAs cap layer on QWR	105
5.3.6	Growth temperature	107
5.3.7	DMHy flux	109

5.3.8	Growth rate	110
5.3.9	Summary	112
5.4	QWR disorder characterization	113
5.4.1	Defects incorporation determined by PL temperature dependence . . .	113
5.4.2	Sample annealing	116
5.4.3	QWR segments measurements	119
5.4.4	QWR emission polarization	121
5.5	Chapter summary	123
6	0D-nanostructures: dilute nitrides quantum dots	125
6.1	Growth of InGaAs pyramidal QD	126
6.1.1	Influence of growth parameters	129
6.2	Nitrogen incorporation in InGaAs/GaAs pyramidal QDs	134
6.3	Single pyramidal QD emission spectra	136
6.4	Polarization properties of InGaAsN pyramidal QDs	142
6.4.1	Methodology	143
6.4.2	Polarization properties of QD ensembles	143
6.4.3	Polarization properties of isolated QD	148
6.5	Chapter summary	151
7	Conclusions and outlook	155
	Appendices	159
A	QD grown in inverted pyramids on InP substrates	159
A.1	Brief review of the InP-based system	159
A.2	Substrate patterning	160
A.3	Determination of the best material for barrier composition	160
A.4	Detailed morphology of InAlAs growth in pyramids	162
A.5	Growth study of InAlAs on InP (111)A substrates	162
A.6	Outlook	163
B	Kinetic Monte Carlo simulations of growth in pyramidal recesses	165
B.1	Kinetic Monte Carlo algorithm	165
B.2	Step flow interaction with the recesses	170
B.3	Evolution of the pyramidal recesses	173
B.4	Appendix summary	177
C	List of Tables	181
C.1	Substrate patterning	181
C.2	QW samples	181
C.3	QWR samples	182
C.4	QD samples	184

Contents

Bibliography	187
Acknowledgments	217
Publications and conferences	219
Curriculum Vitae	221

1 Introduction

Some concepts at the basis of the present experimental research work are introduced in this chapter. At first are defined the nanotechnologies and some examples and applications are given. The semiconductors, a peculiar class of materials acting as a bridge between electricity and light, are introduced in the second section. Then an important application domain of semiconductors is presented: the optical fiber telecommunications. The subject of the next section is the shaping of semiconductors at the nanoscale level, and the resulting quantum effects. The last topic tackled is the dilute nitride materials, which are semiconductor alloys with peculiar properties that find applications in optical fibers telecommunications and solar cells. The aim of this work is the fabrication of nanostructures using dilute nitride materials, in order to tune their emission properties to the characteristic wavelengths employed in optical fibers.

1.1 Nanotechnologies

As this name suggests, the nanotechnology is the ensemble of techniques used to shape materials or the material properties, with a spatial characteristic length close to or below $0.1\ \mu\text{m}$. An object of such size cannot be characterized by optical techniques except only under peculiar conditions, due to the scale of the wavelength of visible light ($0.4 - 0.75\ \mu\text{m}$). The materials, fabrication techniques and applications are very diverse: one may cite surface patterning for self-cleanable materials, silver nano-droplets as antibacterial agent, titanium dioxide additives in suncreams or cosmetics, new materials for future (opto)electronic applications (QDs, graphene, etc.), etc.

Indeed nature did not wait the appearance of mankind to develop some sort of nanotechnology. The shiny colors of butterfly wings are produced by a nanometric patterning of the surfaces, and not by pigments. The lotus leaves strongly repel water due to the surface geometry, a phenomenon called super-hydrophobicity now used in industrial processes. The processing of the genetic information by living cells is a wonderful ensemble of nanotechnology: molecular machines read, copy, repair, and interpret the DNA information.

The nanotechnology fabrication processes can be divided into two categories, according to the strategy of realization. The “top-down” approaches target the shaping of physical properties by using external, larger devices. Lithography (e.g., by electron beams) or nanopatterning techniques follow this strategy. The desired device may be more efficiently achieved when relying on the self-assembling of elemental building block. This strategy is named “bottom-up”, and examples are the self-assembled and colloidal QDs, or the DNA manipulation techniques.

1.2 Semiconductors

The “semiconductors ” are materials with an electrical conductivity intermediate between that of a conductor such as copper or steel, and that of an insulator such as glass or plastic. This class of materials exhibits peculiar electronic properties and is at the basis of all modern electronics (radio, computers, phones, but also signal amplification, energy conversion, etc.). Semiconductors also interact easily with light, and are used advantageously in light emitters such as light-emitting diodes (illumination, signalization, etc.) or lasers (CD/DVD players, printers, laser surgery, telecommunications, research, etc.), and in light detectors (cameras, photodiodes) and energy converters (solar cells). The next subsections introduce some basic concepts related to semiconductors, such as their crystallographic arrangement of atoms, their electronic band structure and the properties of semiconductor alloys.

1.2.1 Crystallographic structure

The most common semiconductor is Silicon, a cheap material widely used in electronics and in solar panels. With 4 valence electrons, Si is a member of the group-IV family, together with C (diamond) and Ge. When pure, these materials crystallize in the diamond structure shown on Figure 1.1. This rather complex atomic arrangement can be seen as two interpenetrating face-centered cubic (FCC or cubic close-packed) lattices, shifted by $(\frac{1}{4}, \frac{1}{4}, \frac{1}{4})$ lattice vectors. Each atom shares its four valence electrons with the nearest neighbors.

GaAs, InP or GaN are members of the III-V semiconductor family. These alloys are composed in equal proportions of elements of the third column of the Mendeleev table (Ga, In, Al are the most widespread) and of elements of the fifth column (N, P, As). When crystallized in the zinc blende structure, group-III and group-V elements each occupy the sites of a given FCC sublattice, as shown on Figure 1.1. The valence electrons are shared and the overall properties are similar to that of the group-IV semiconductor family. Some semiconductors such as GaN tend to crystallize in the wurtzite structure, which can be derived from hexagonal close-packed the same way zinc blende is from the cubic close-packed or FCC.

Other semiconductor materials can be obtained by combining elements of the second and sixth column (II-VI family), such as CdSe, CdTe, ZnO, ZnSe, etc.

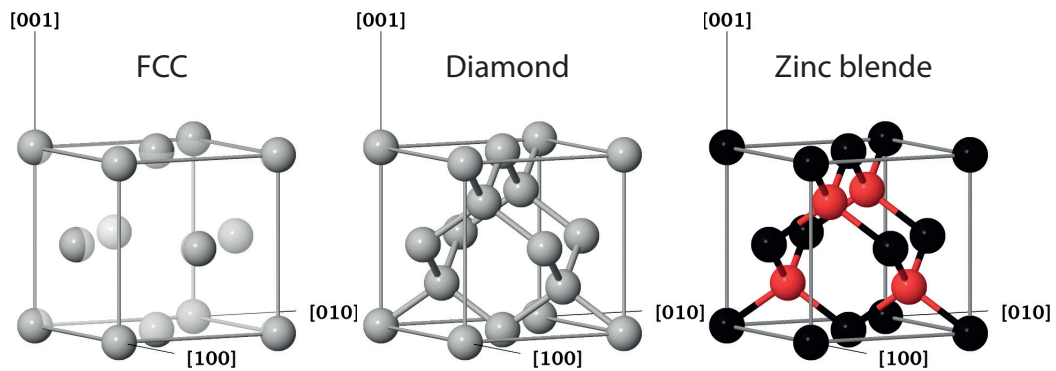


Figure 1.1: Arrangement of the atoms in a crystal unit cell. The diamond structure (group-IV semiconductors: diamond, Si, Ge) can be seen as two interlocked FCC lattices. GaAs crystallizes in the zinc blende structure, where Ga, respectively As atoms occupy the sites of the two underlying FCC lattices.

1.2.2 Band structure

When atoms are bound together in a molecule, the energy levels of the valence orbitals split due to the Pauli exclusion principle. States with different energy are formed, in a number proportional to that of valence electrons. A crystallized solid contains such a large number of atoms that individual energy levels cannot be distinguished anymore: the electronic structure is better described in terms of bands, formed by a quasi-continuum of states. Electrons tend to fill the states with lowest energy: the bands below a certain energy called Fermi level are populated, while the bands at higher energy remain empty. The low-energy bands correspond to states tightly bound to the atom nuclei and are named the valence bands. The high-energy bands are delocalized in the crystal and contribute to the electrical conductivity, and are named conduction bands. When the temperature is non-zero, the transition between occupied and empty states becomes smooth (following the Fermi-Dirac statistics), progressively populating states with higher energy than the Fermi level.

In conductors, there are bands continuously covering the vicinity of the Fermi level, as shown on Figure 1.2(a). There are always electrons populating the conduction band, explaining why these material conduct electricity. In insulators, a large energy gap separates the conduction from the valence band: in usual conditions no electrons populate the conduction band, hence these materials do not conduct electricity. Semiconductors are the intermediate case, where the small energy gap between the valence and conduction bands may permit a residual thermal population of the conduction band, hence the name “semiconductor”. Under standard conditions (no doping, no bias, etc.) the Fermi level is located at mid-distance from the valence and conduction bands.

Calculation of the electronic band structure can be performed in the framework of several different approximations, for example the pseudopotential, linear muffin-tin-orbital, linear combination of atomic orbitals, tight-binding or $\mathbf{k} \cdot \mathbf{p}$ methods. The later was used to compute

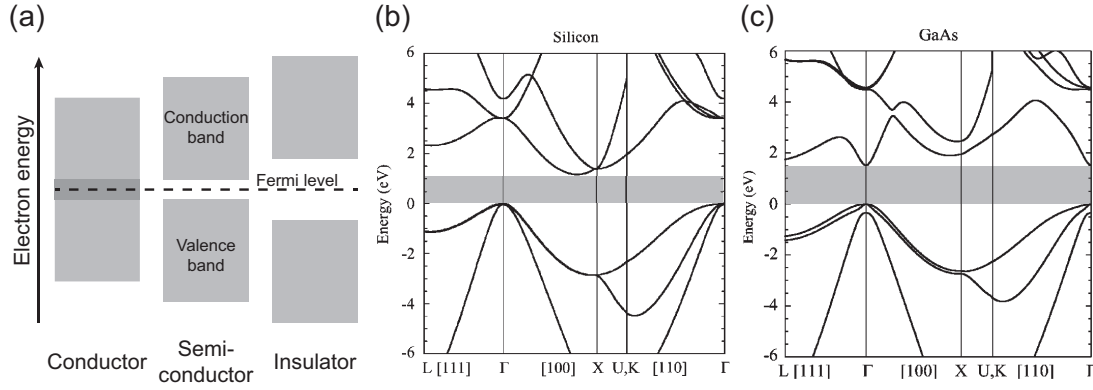


Figure 1.2: (a) Schematics of the conduction and valence band in the cases of a conductor, a semiconductor and an insulator. (b), (c) Band diagrams of silicon (indirect bandgap) and of GaAs (direct bandgap at the Gamma point). The bandgaps are evidenced with a shade of grey. Graphs from [1].

the band structure of silicon and GaAs shown on Figure 1.2. The energy of an electronic state depends on its wavevector (closely related to the momentum carried by the electron), and therefore is better represented in the reciprocal space. Due to the crystal symmetry, the reciprocal space can be “folded” into the so-called first Brillouin zone, effectively representing all the possible wavevectors. The Γ point corresponds to the wavevector of norm 0, at the centre of the Brillouin zone. L, X, U and K are wavevectors pointing to high symmetry locations on the edge of the first Brillouin zone. To represent the band structure as function of the wavevector, Figure 1.2(b)-(c) shows the energy of bands along selected, high-symmetry directions in the reciprocal space.

On the diagrams are evidenced the bandgap openings in a shade of grey. GaAs is a “direct” bandgap semiconductor: both the top of the valence band and the bottom of the conduction band are located at the same point (Γ). Oppositely, Si is an “indirect” bandgap, as the conduction band minimum is not at the same point as the valence band maximum.

Direct bandgap semiconductors are especially interesting for optical applications. When a valence band electron absorbs a photon (see Figure 1.3(a)), it gains the photon energy and moves to an upper band (by energy conservation). The momentum must also be conserved, but as the momentum carried by a photon is negligible when compared to that of an electron, the transition is quasi-vertical in a $E(k)$ diagram. The electron leaves an empty state in the valence band, which behaves as an actual particle and is called a “hole”. The electron and hole then quickly release energy by emitting optical and acoustic phonons as in Figure 1.3(b) (the upwards motion of the hole can be understood as the relaxation of the other valence band electrons). After some characteristic time, the electron and hole recombine near the bandgap energy, emitting a low-energy photon. An important point is that holes can also move and transport electricity. In direct bandgap semiconductors, vertical transitions can occur close to the bandgap energy without assistance of phonons. These materials, such as GaAs, InP or

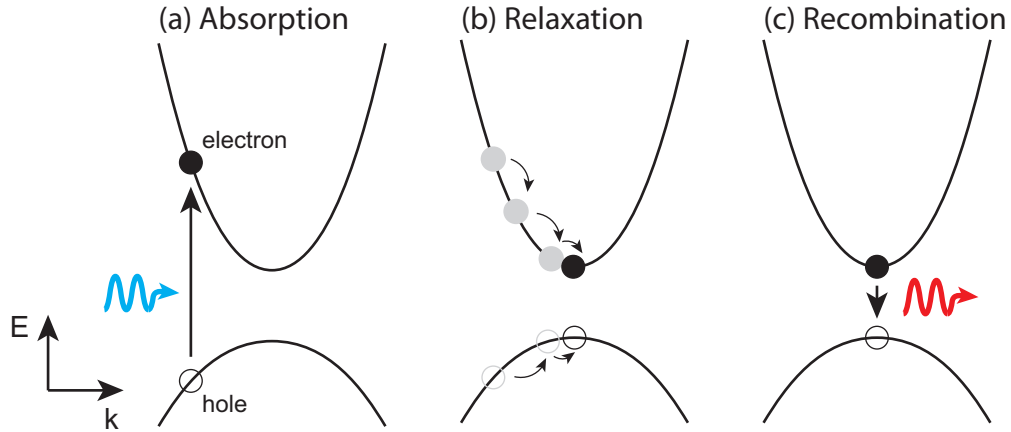


Figure 1.3: Schematics of (a) photon absorption, (b) electron and holes relaxation, and (c) carriers recombination in a direct bandgap semiconductor.

GaN, are therefore preferred for optical applications.

The band structure formalism can be applied to the propagation of light in materials structured with a periodic modulation of the refractive index. Thus “photonic crystals” (PhC) can be designed and fabricated, that forbid photons with given frequencies to propagate in the material. The distributed Bragg reflector (DBR) is an example of 1-dimensional photonic crystal. Another common design is a triangular pattern of holes etched in a thin (~ 150 nm) 2-dimensional slab. Photonic crystal waveguides can be fabricated by introducing linear defects in such PhC, and photonic crystal cavities by creating point-defects [2] in the periodic arrangement. These cavities can be used as laser resonators using as light emitters QWs [3], QWRs [4] or QDs [5, 6, 7]. These light emitters are described in the next section. A complex and rich physics can be initiated by inserting quantum light emitters (QDs) in such cavities [8, 9, 10, 11, 12].

1.2.3 Semiconductors alloys

Pure IV or III-V semiconductors exist only in a limited number, with a restricted choice of bandgaps. Most devices are actually made of heterostructures fabricated by combining materials with different properties: bandgap energy, doping level (hence Fermi level), refractive index, lattice parameter (introducing strain), etc. Alloys are obtained by substituting a fraction of atoms of a given group by an equivalent number of atoms of the same group (i.e. Al or In instead of Ga). Substituting 30 % of Ga atoms by Al in a GaAs crystal leads to the alloy noted $\text{Al}_{0.3}\text{Ga}_{0.7}\text{As}$. The lattice parameter evolves almost linearly with the chemical composition, according to the Vegard’s law. Layers of different compositions can be epitaxially grown by means of molecular beam epitaxy (MBE) or metalorganic vapor phase epitaxy (MOVPE) techniques. Alloys with slightly different lattice parameters are accommodated in the same crystalline structure by strain: the unit cell is horizontally stretched to match the lattice of the

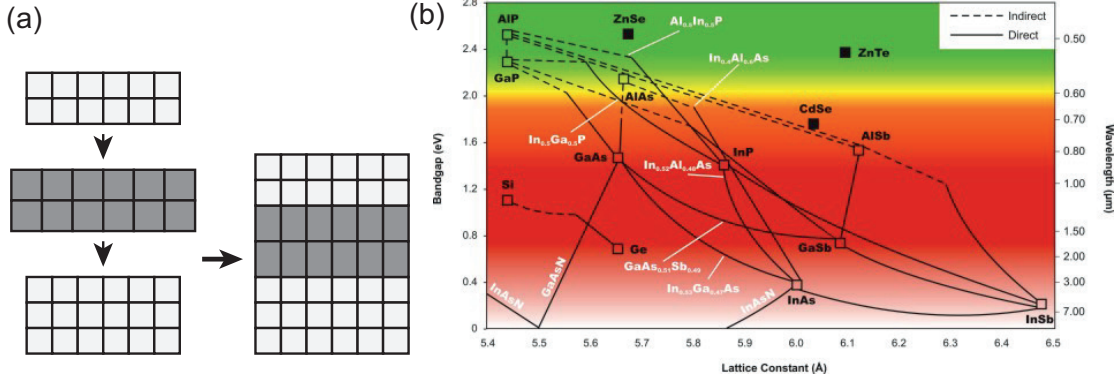


Figure 1.4: (a) Layers with different lattice parameters are accommodated by elastic deformation. (b) Bandgap as a function of lattice parameter for a selection of semiconductor alloys. Direct bandgaps are displayed with continuous lines while dashed lines stand for indirect transitions. Graph from [13].

substrate, and vertically relax according to the Poisson's ratio. This deformation is represented on Figure 1.4. The AlGaAs alloy is almost strain-free when grown epitaxially on GaAs due to the similarity of the GaAs and AlAs lattice parameters. The layers can only accommodate for a moderate strain level before initiating a more complex, 3D growth mode. The InGaAs and InGaAsN strained nanostructures fabricated in this work were all fabricated with a moderate amount of strain that did not exceed the threshold of a 2D-3D growth mode transition.

The bandgap energy can also be described by an empirical law similar to Vegard's, with the addition of a quadratic corrective term with rather small intensity b named bowing parameter:

$$E_{g,AB} = xE_{g,A} + (1-x)E_{g,B} - bx(1-x).$$

It is remarkable that such a simple formula remains valid in spite of the loss of translational symmetry in the crystal. Actually, the formula only holds true if the chemical properties of the substituted elements are similar: it works well for InGaAs or AlGaAs, but fails to describe GaAsN alloys (see Section 2.2). The electronic band structures can be calculated. The $\text{Al}_x\text{Ga}_{1-x}\text{As}$ bandgap is direct up to $x \sim 43\%$, and the InGaAs bandgap is direct over the whole composition range. On Figure 1.4(b) is shown a diagram of the bandgap energy as function of the lattice parameter of various semiconductor alloys.

1.3 Optical fibers communications

One of the most efficient, robust and cost-effective telecommunication channels is the silica (glass) optical fiber. These fibers are a long, thin (core diameter $\sim 10\mu\text{m}$ for monomode fibers, often $65\mu\text{m}$ for multimode fibers), flexible waveguides where light is confined by total internal reflection by a profiled of a step-like grading of the refractive index. The radial tuning of the refractive index is achieved by heating a short, large-diameter "preform" and pulling it into its

long, thin final shape. Among the main applications are telecommunications, light guides and decoration, endoscopes or optical amplifiers.

The most common material used in optical fibers is the inexpensive glass, especially transparent in the infrared. This material exhibits two peculiar telecommunications windows, at 1.3 and 1.55 μm . The 1.3 μm window corresponds to the zero dispersion wavelength of single mode glass fibers. Due to the energy-time uncertainty, a pulsed signal is not purely monochromatic. The different frequency components travel at slightly different speeds in a dispersive medium, a phenomenon called group-velocity dispersion (GVD). The resulting distortion of the signal limits the transmission distance and/or modulation speed. Glass induces zero dispersion at a wavelength close to 1.3 μm : optical signals emitted close to 1.3 μm wavelength are only weakly deformed, allowing a more efficient data transmission in single-mode fibers (a proper treatment of this problem should also include the waveguide dispersion, caused by a geometrical effect). The 1.55 μm wavelength corresponds to the absorption minimum in glass optical fibers, and is desirable for long-distance communication. The signal distortion can be neutralized using specific dispersion compensation fibers.

Efficient and reliable light emitters and sensors operating in this wavelength range are requested. The choice of the active material is presented in more details in Section 1.5.

1.4 Nanostructures

Bulk materials are not best suited for the realization of light-emitting devices, and new physics can be unveiled by confining the charge carriers in dedicated regions of space. Quantum effects appear when the size of the confining region is reduced to $< 100 \text{ nm}$: the physics of such system matches that of the “particle in a well” or “particle in a box” problems of quantum mechanics, that lead to the appearance of quantized electronic states and/or bands with specific energies.

These bands modify the density of states (DOS), which quantifies the number of electronic states as function of the energy. The DOS of the bulk material increases as the square root of the energy (see Figure 1.5). A quantum well (QW) is a structure confining charge carriers in one spatial direction, as sketched on Figure 1.5. Electronic bands appear (the carriers are free to move in the plane), resulting in a step-like DOS. The transition energies are affected by the QW composition and thickness. Strong and sharp luminescence signals are emitted by these structures. The fabrication process is quite simple: common fabrication methods typically grow layer-by-layer structures, so that QW structures can be obtained by a simple tuning of the fluxes of the precursors/sources. QW-based devices are now widespread thanks to the easy fabrication process and their unique electronic and optical properties. The carriers can be further confined in 1D nanostructures called QWRs. The sharper DOS evolves as the inverse of the energy, leading to a nominally infinite DOS at energy of the $k=0$ transition. In practice, 1D structures are extremely sensitive to disorder, and it is difficult to fabricate real structures with a true 1D behavior. With time the fabrication of quantum dots (QDs)

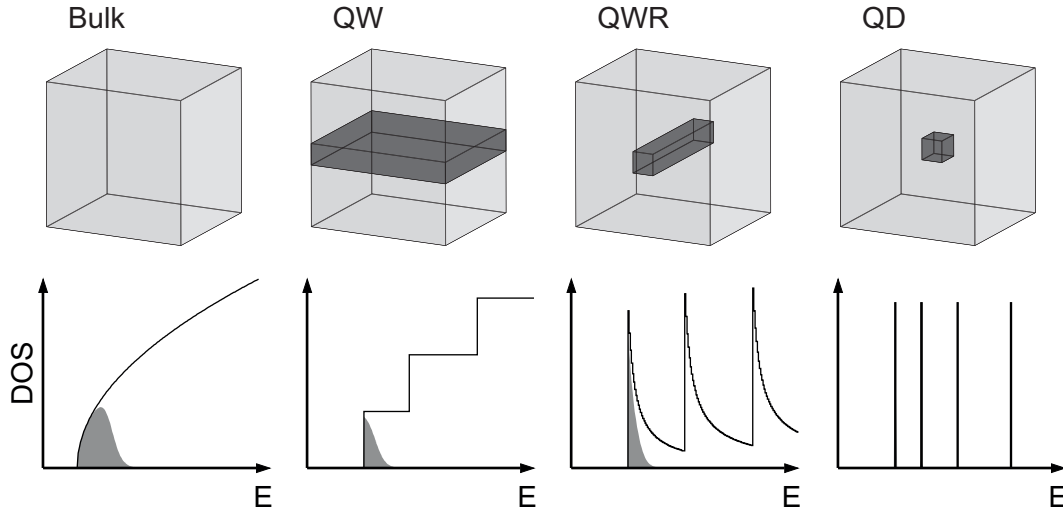


Figure 1.5: Schematic representation of bulk material and nanostructures of different dimensionalities, together with the corresponding density of states. The shaded areas represent occupied states for comparable chemical potentials and temperatures.

proved easier than that of QWRs, and these structures are the host of many more interesting phenomena. The complete carrier confinement only allows the existence of a discrete number of states with well-defined energy: the DOS looks like a comb. The QD energy spectrum actually resembles that of an atom, hence their appellation as artificial atoms. QDs are indeed more controllable than individual atoms, and as such are better candidates for quantum electrodynamics experiments.

The sharper density of states of quantum confined structures leads to a reduced sensitivity to temperature of devices. The QD can be efficiently used as photon sources with non-classical statistics: on-demand single photon [14, 15, 16], or entangled photon pairs [17] for keys distribution in quantum cryptographic schemes [18, 19]. QD integration into photonic crystals can lead to ultra-low threshold lasers, but also to new optoelectronic devices, such as spin memories [20] or optical circuit logic [21, 22]. In such prospective schemes, QWRs may be used for local charge transport thanks to the fast diffusion of carriers trapped within and to their increased life time when compared to high-dimensionality heterostructures.

The characteristics of various solid-state QWR and QD fabrication schemes are reviewed in Subsection 2.1.1 : nanotubes, self-assembled, T-shape or V-groove QWRs, and self-assembled or pyramidal QDs. The colloidal QDs synthesized in liquid phase are also worth mentioning, having especially important applications in medical imaging.

1.5 Dilute nitride GaAs

The III-V semiconductor family contains materials with a wide range of bandgaps, ranging from the far infrared (InAs), infrared (GaAs), visible (GaP) to the ultraviolet domain (AlN, GaN). In the middle of the XX century, the GaAsN was foreseen as a light source for optical devices covering the visible range, as a combination of GaN ($E_g = 390$ nm at room temperature in zinc blende phase) with GaAs ($E_g = 870$ nm). But the actual effect of N on GaAs proved quite different from that expected.

1.5.1 Discovery and historical background

The growth of high-quality GaAsN with significant N incorporation is by itself a demanding task. The N solubility in GaAs is pretty low, and high concentrations lead to phase separation [23, 24], thus requiring growth conditions far from thermodynamic equilibrium. In the eighties, GaAs samples with impurity levels of N revealed many defect lines analogous to those observed within the bandgap of GaP(N), attributed to N, N pairs and N complexes [25, 26]. Shortly afterwards, incorporation of N at percent-level was observed to dramatically shrink the bandgap [27], in total opposition to the naively expected behavior. The PL emission was consistently attributed to the band edge, excluding isolated N-N pairs transitions. Approximating the bandgap evolution with a Vegard law (see Subsection 1.2.3) leads to giant values of the bowing parameter ($b = 18$ eV) [28]. Such values suggest a complete closing of the bandgap above 10 % N concentration. Dilute nitride materials were therefore seen as potential active material for long-wavelength devices. The potential applications were even extended when InGaAsN was proposed for long-wavelength devices [29], with the prospects of a further redshift, and of lattice matching on GaAs. Theoretical efforts were soon dedicated [30], confirming the dramatic effects of N on GaAs.

1.5.2 Applications of dilute nitrides alloys

A first major target for the InGaAsN semiconductor alloy is light emission in the 1.3 and 1.55 μm wavelength range, linked to the glass optical fibers, a relatively inexpensive transmission medium composing most of the current optical communication network as described in Section 1.3. Efficient and reliable light emitters and photodiodes are required to operate in these infrared wavelength. A suitable material is the InGaAs lattice-matched on InP, that has a 0.7 eV room-temperature bandgap associated with a high optical efficiency. However this material suffers from limitations. Integrated distributed Bragg reflectors (DBRs) lattice-matched on InP are not as efficient as those grown on GaAs. Moreover, this material offers rather poor thermal conductivity, which hinders the cooling of the active layer. Kondow *et al.* [29] proposed InGaAsN grown on GaAs as an alternative for low-cost telecom-wavelength lasers with simple fabrication process. Shortly afterwards, InGaAsN-based laser devices were realized, using both monolithic VCSEL [31, 32, 33] or ridge waveguide designs [34], with calculated gain spectra comparable to or exceeding these of InP-based lasers [35, 36]. However,

material quality issues were raised, and InGaAs/InP devices are nowadays common.

Another major interest in the InGaAsN alloys is the fabrication of multijunction photovoltaic solar cells. The active structure of the widespread Si cells consists in a single absorbing layer, with a uniform bandgap. As a result, incoming photons with energy below the bandgap are not absorbed, and only the bandgap energy can be recovered from photons with higher energy because of the relaxation of the carriers. With efficiencies in the order of 25 %, single junction Si cells approach the theoretical 33.7 % Shockley-Queisser limit [37] for unconcentrated sunlight. Efficiency improvements can be achieved by concentrating the sunlight using inexpensive mirrors or Fresnel lenses. Further improvements are achieved by stacking absorbing layers with different bandgaps, each one absorbing photons close to its own the bandgap, thus limiting the energy losses by carrier relaxation. For durability reasons strained layers must be avoided, in favor of lattice-matched materials, or the more challenging wafer bonding. Good combinations are obtained by combining InGaP as large, GaAs as medium, and Ge or InGaAsN [38] as low bandgap materials. In this context, the bandgap tunability of InGaAsN lattice-matched to GaAs is a clear advantage. The solar cell state-of-the-art efficiency under concentrated sun is 43.5 % [39], later increased at 44 %, using a triple junction design with InGaAsN as ~ 1 eV absorber.

Among other possible applications of the dilute nitride (In)GaAsN material is the fabrication of saturable absorbers for ultrafast applications [40]. Other uses may outcome from the realization of high power lasers in the 1.1 - 1.3 μm range [41], eventually frequency-doubled up to yellow wavelengths, in view of astronomy [42], medical [43], laser projection or display application.

1.6 Thesis goal and outline

In this work, we are especially interested in incorporating nitrogen into nanostructures grown on patterned substrates. As described earlier, V-groove QWRs and QDs in inverted pyramids with InGaAs as active material are limited to ~ 1 μm emission wavelength due to the growth constraints. Therefore, nitrogen incorporation may provide the required shrinkage of the bandgap allowing QWRs and especially QDs to emit in the 1.3 μm telecommunication window.

The work was accomplished in several successive steps, which are reported in the successive thesis chapters.

Chapter 2 introduces various notions required for understanding the experimental results. Sections are dedicated to the QWR and QW nanostructures in general and especially to the V-groove and pyramid designs, as well as to the properties of dilute nitride alloys. The Chapter 3 presents the experimental techniques used during our work. The fabrication of the samples is described in sections dedicated to the substrate patterning performed in a clean-room environment, as well as to the MOVPE growth technique and processes. The samples characterization was primarily performed by means of low-temperature microphotoluminescence (μPL). We designed and realized a new low-temperature μPL setup dedicated to

long wavelength, as our samples could not be properly characterized in the existing setups in our Laboratory equipped with Si-CCD. Valuable information was also retrieved from various techniques presented in later sections: secondary electron microscopy (SEM), transmission electron microscopy (TEM), atomic force microscopy (AFM) and secondary ion mass spectroscopy (SIMS).

In Chapter 4 are presented our results on the fabrication of dilute nitride QW using the 2-step MOVPE growth method. This study confirmed the proper N incorporation into our nanostructures. The focus was set on the effect of substrate misorientation, as the effect of this parameter is not well known and becomes important in the growth of nanostructures on patterned substrates.

Chapter 5 focuses on the growth of dilute nitride V-groove QWRs. The nitrogen incorporation is asserted and the 1D-character of the carrier wavefunctions is confirmed. The influence of various growth and structural parameters is studied, enabling the growth of QWRs emitting at $1.3\text{ }\mu\text{m}$ at room temperature.

Chapter 6 presents the effect of nitrogen incorporation into QDs grown in pyramids. The influence of several growth parameters is explored, in view of finding the best window for N incorporation. We present in some details the emission properties of QD ensembles and of isolated QDs, and in particular the effect of nitrogen on the QD linewidth, on the emission anisotropy and on the fine structure splitting.

Our results presented in Chapter 6 suggest that the fabrication of high-quality InGaAsN QD emitting at $1.3\text{ }\mu\text{m}$ cannot be achieved. We propose, and briefly explore in Appendix A, the possibility of growing QDs into pyramidal recesses etched in InP substrates.

A second appendix (Appendix B) presents a kinetic Monte-Carlo approach that we implemented to reproduce the evolution of the pyramidal recesses during growth. This study was performed in close collaboration with Dr. A. Surrente, and this appendix is to be seen as a detailed complement to the Chapter 3 of his thesis document [44].

2 Quantum nanostructures and the dilute-nitride compound system

This chapter presents some notions introduced in Chapter 1, that deserve a more extensive treatment in view of understanding the results of our work. This chapter is articulated on two main themes. The first section is dedicated to the QWR and QD nanostructures. Common fabrications methods are reviewed, before presenting the specific systems of V-groove QWRs and pyramidal QDs. The second section presents the peculiar dilute nitride (In)GaAsN alloys. First, we describe some elements of the unusual physics ruling these materials. Secondly, we present the fabrication and optimization issues that must be addressed when fabricating these alloys.

2.1 V-groove QWRs and pyramidal QDs

This section focuses on the QWR and QD systems. The first subsection reviews various methods used to fabricate these kinds of nanostructures. Then we present the systems of V-groove QWR and pyramidal QD as fabricated in LPN. The fabrication aspects are detailed, and the advantages, limitations and perspectives of these techniques are discussed.

2.1.1 Fabrication methods of low-dimensional nanostructures

The realization of the lateral carrier confinement characterizing 1D and 0D nanostructures is a challenging task. Many fabrication methods were developed through the years with different objectives and degrees of success. The first fabrication attempts of QWRs and QDs were performed by the etching and regrowth of QWs, but this straightforward method leads to poor crystal quality and optical properties. In-situ formation mechanisms are required to achieve the desired high structural quality. The following subsection describes existing nanostructure fabrication methods, focusing on solid-state techniques.

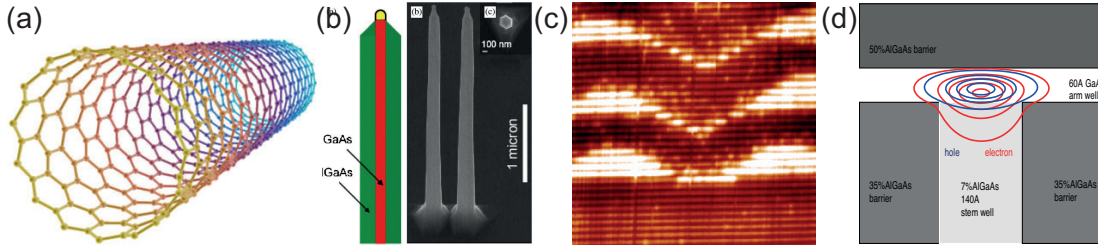


Figure 2.1: Various QWR designs as described in the text. (a) Carbon nanotube. (b) Nanowiskers [45]. (c) Cross-section STM view of in-plane self-assembled QWR, with atomic resolution [46]. (d) Schematics of a T-shape QWR [47].

2.1.1.1 QWR fabrication techniques

The carbon nanotubes (CNTs) are long structures made of pure carbon, where the C atoms are arranged into a monolayer-thick hexagonal array rolled on itself as shown on Figure 2.1(a). These cylindrical molecules have extraordinary mechanical (strength, hardness, sliding, etc.) and electrical properties, and may especially be metallic or semiconductor according to the folding configuration. Applications exist or are foreseen in various domains, including material strengthening, solar cells, hydrogen storage, etc. Boron nitride nanotubes can also be fabricated, presenting somewhat different properties. A limitation to the use of CNTs is their high degree of toxicity when inhaled.

The growth of out-of-plane nanowiskers or nanowires is possible with a wide range of material combination, of bandgap ranging from infrared to ultraviolet. In this technique, catalyst droplets enable the growth of microns long, defect-free nanowires as shown on Figure 2.1(b). The flexibility of this system allows the fabrication of sharp heterointerfaces, the control of the doping level and the formation of radial core-shell nanostructures. These properties are very attractive for electronic, optoelectronic and solar cells applications [48]. The prefix nano- is used because the carriers are not laterally quantum confined (even though a lateral spatial confinement is possible [49, 45, 50]). The wafer coverage with inert SiO₂ or SiN masks may open the way to significant developments, for example the growth of high-quality Ge or GaAs on Si [51, 52]. Vertical nanowires also demonstrated promising results in the field of solar cells applications [53].

Self-assembled InAs/InP in-plane QWRs can be grown on (100) InP surfaces following a 2D-3D transition of the growth mode (see Figure 2.1(c)). The elongated (more than 1 μm long) shape is obtained thanks to a large strain anisotropy buildup upon growth [54, 55, 56, 46]. These QWRs can emit in the 1.55 μm wavelength range. However, like for other strain-driven formation mechanism, the nanostructure nucleation critically depends on local concentration fluctuations that lead to inhomogeneities.

The T-shaped QWR design consists in the intersection of two perpendicular QWs grown by cleaved edge overgrowth [57, 58], generally using MBE technique (see Figure 2.1(d)). These QWRs are suitable for laser emission [59, 60] and offer the best QWR uniformities achieved so

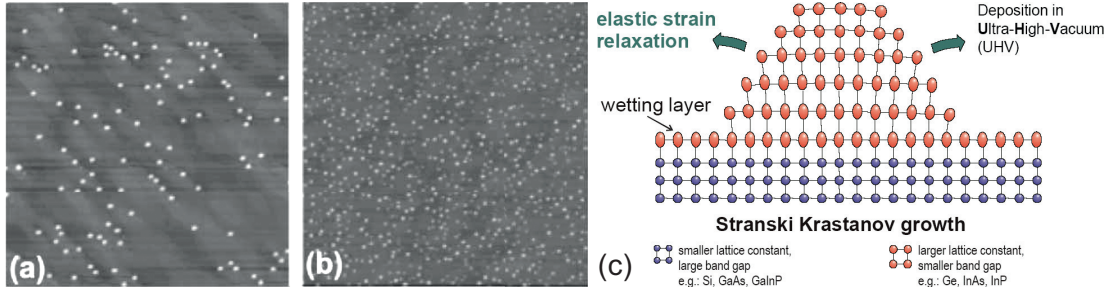


Figure 2.2: (a)-(b): $2\mu\text{m} \times 2\mu\text{m}$ AFM image of SK-QDs, deposited with growth rates of 0.01 and 0.025 ML/s. Images from [69]. (c) Schematics of the SK-QD formation process. The ultra-high vacuum is not a requirement. Graph from [70].

far [61]. However, the presence by design of the lateral QW leads to a relatively weak lateral carrier confinement in the QWR. The growth of N-containing (In)GaAsN/GaAs T-shape QWRs was reported, based on photoreflectance and optical studies [62, 63, 64].

More details about QWR fabrication methods and experimental results can be found for example in Ref. [65] and references therein.

2.1.1.2 QD fabrication techniques

The realization of 0D nanostructures (QD) requires the confinement of the charge carriers in the three spatial directions. The interest of these structures comes from the quantum nature of the electronic states responsible for the non-classical statistics of the emitted photons (on-demand single photons [17], indistinguishable photons or entangled photons pairs for cryptographic applications [17, 18, 66, 67, 68]), and from the perspective of various spintronics devices like spin memories [20] or all-optical circuit logic [21, 22].

Self-assembled QD are the most common solid-state QDs. Their fabrication process relies on the deposition of a highly strained layer, where strain instabilities prompt the nucleation of islands, a growth mode first described by Stranski and Krastanow [71], hence the abbreviation SK-QD. Narrow emission linewidths only limited by the exciton lifetime are reported for such single QDs [72], and densities large enough for lasing are routinely achieved [73, 74, 75, 76]. The stochastic nature of the formation process limits the control of the emission energies: the QD emission energy distribution is typically larger than 10 meV. The nucleation site can be controlled to some extent by various methods: shallow substrate patterning [77, 78, 79, 80], selective area growth [81, 82, 83, 84] or vertical structure stacking [85, 86, 87, 88]. However, the control in the nucleation site tends to deteriorate the emission quality [89]. The C_{2v} symmetry of these dots generally causes a non-vanishing fine structure splitting: the emission of entangled photons requires forcing the energy levels into degeneracy by applying an external, dot-specific control via electric [90], magnetic [67] or strain [91] fields. In spite of the difficult control of the QD location and energy, a deterministic integration of SK-QD into photonic devices has been repeatedly demonstrated [92, 10, 93]. A far-from-resonance

coupling with the cavity was evidenced [10, 94, 95, 93, 96, 97], that departs from the ideal picture of a 2-level system interacting with a cavity mode. The (high-yield) fabrication of multiple dot-in-cavity systems remains a technological challenge.

2.1.2 V-groove QWRs and QDs in inverted pyramids

The V-groove QWR and QDs grown in inverted pyramids are two alternative systems, with interesting advantages compared to the previously mentioned fabrication methods. These nanostructures are grown by MOVPE in recesses wet-etched in GaAs substrates. The lateral shaping of these 2 types of nanostructures originates from a competition between two opposing mechanisms: capillarity and growth rate anisotropy [98, 99]. The surface profile is therefore self-limited, which ensures a high uniformity of the nanostructure properties across the wafer.

2.1.2.1 Interest of the V-groove QWR and pyramidal QD designs

The suitability of the V-groove QWRs as active medium for lasing was demonstrated more than 20 years ago [100, 101]. Nanolasers were also fabricated by introducing QWRs into photonic crystal cavities [4]. In such devices the reduced volume of the active medium allows an extremely small lasing threshold. These QWRs can be vertically stacked in the same V-groove, thus increasing the achievable optical gain. The integration of these QWRs into vertical DBR cavities for simultaneous carrier and photon confinement was also demonstrated [102, 103].

The 1D behavior of V-groove QWRs was the subject of numerous studies. Charge transport evidenced quantized conductance along the QWR [104, 105]. The spatial uniformity remains however inferior than the one of the T-shape QWR, where electronic states can extend over microns [47]. By contrast, the low-temperature, low-excitation potential landscape of the V-groove QWR resembles more to a chain of QDs elongated by a few hundred of nanometers [106], one micron at best [107]. The temperature onset of carriers diffusion has been observed close to 50K by time-of-flight experiments in GaAs/AlGaAs QWRs, while confirming that the diffusion is limited by the interfaces roughness [108]. Decreasing the confinement can reduce the amplitude of disorder and permit a delocalization of the wavefunctions.

The InGaAs/GaAs pyramidal QD emission lines are commonly resolution-limited in our spectrometer setup (linewidth $< 100 \mu\text{eV}$). The uniformity of pyramidal QD arrays is better than any other technique [109, 110] thanks to the self-limited nanostructure profiles. Additionally, the QD properties can be tailored on the same wafer by controlled modifications of the recess size, pitch and surroundings [109].

A decisive advantage of the V-groove QWR and pyramidal QD is the extremely precise control ($\sim 20 \text{ nm}$ positioning accuracy when alignment using electron beam lithography is used) of the location of the nanostructure formation site. This accuracy comes at no cost in terms of quality or design flexibility, contrary to other QD systems. This precision paves the way to a

deterministic high-yield integration of QWRs and QDs into photonic crystal and other types of optical cavity devices [111, 112, 113].

The fabrication process provides QD in pyramids with a C_{3v} symmetry, which confers a natural vanishing fine structure splitting (FSS) [114, 115]. This quantity characterizes the degeneracy lifting of states with opposite spins. Pyramidal QD are therefore promising candidates for emission of entangled photon pairs [17].

Ternary alloys like AlGaAs tend to phase separate in non-planar growth, forming a vertical 1D QWR structure at the center of the pyramid. The shape of the potential along the QWR is impressively flexible, as its chemical composition is controlled by the precursor fluxes. Transitions from QD to QWR [116, 117], quantum dots molecules [118, 119] or QWRs with arbitrary potential shapes [120] have been demonstrated. In pyramids, the vertical QWR can also provide a direct electrical connection to the QD [121, 122], as do the vertical QWs in the V-groove system [104, 105].

2.1.2.2 Nanostructures formation mechanism

The QWRs and QD are formed in V-grooves and in inverted tetrahedral recesses, respectively. To fabricate QWRs, trenches are etched on (100) GaAs substrates along the [110] crystallographic direction by wet chemical etching (see Section 3.1). Some elements of crystallography may help understanding the peculiar formation of our recesses. The common (001)-oriented wafers expose a (001) facet, evidenced on Figure 2.3(a) on top of a crystal unit cell. Figure 2.3(b) evidences two orthogonal {110} cleavage planes. A selective chemical wet etching can reveal the (111)A facets on (001)-oriented wafers, forming a V-profile groove in which a QWR can be grown (see Subsection 2.1.2.2 and Chapter 3). The two {111}A facets of the groove are shown on Figure 2.3(c). These planes are Ga-terminated and expose dangling bonds perpendicular to the surfaces. On Figure 2.3(d) is evidenced a {111}B plane, terminated by As atoms. A similar etching process on a (111)B-oriented wafer can reveal the {111}A facets. On Figure 2.3(e) are reported a {111}B plane, parts of the {111}A planes of Figure 2.3(c) as well as another one by symmetry, forming a tetragonal recess in which a QD can be grown.

The nanostructure formation results from a competition between growth rate anisotropy and capillarity. On the one hand, the higher growth rate on the (111)A recess sidewalls tend to sharpen the profile at the bottom of the recess, increasing the local surface curvature as depicted on Figure 2.4(a). On the other hand, the growing material behaves like a fluid on the surface, and is drawn by capillarity to the bottom of the recess by the strong local curvature. This is the same phenomenon that drives water up in glass pipes and paper towels, and leaves dark circles on the table when the careless consumer removes the coffee cup. The liquid moves as to minimize the total surface energy and results in the filling (expulsion depending on the materials) by liquid of cavities such as pipes, air gaps between cellulose fibers, concave gaps between cups and tables, or V-grooves and pyramidal recesses. This additional material flattens the bottom of the recess, until a stable self-limited profile is reached as shown on

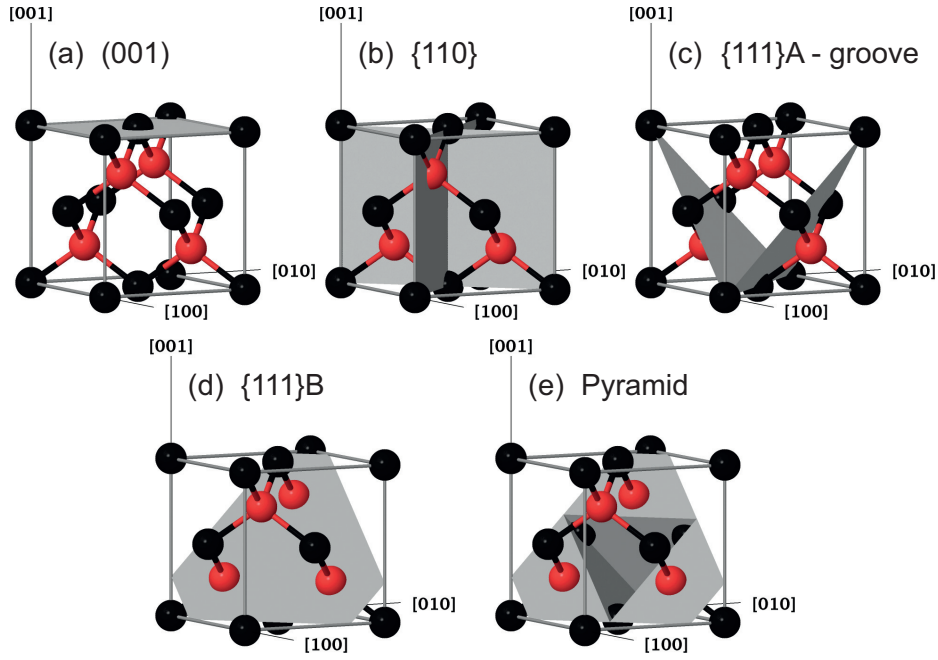


Figure 2.3: Zincblende cubic unit cells, showing Ga (black) and As (red) atoms. Crystallographic orientations are evidenced on the panels. (a) (001) plane. (b) Two {110} cleavage planes. (c) Two {111}A dense planes terminated by Ga atoms, forming a V-groove. (d) A {111}B plane, exposing As atoms. (e) Tetragonal recess can be etched on a {111}B surface.

Figure 2.4(b) (see also Refs. [98, 99]). The self-limited formation mechanism grants a high degree of control in the emission energy, as well as excellent uniformity and reproducibility of the resulting QWR.

The effect of capillarity is strongly enhanced when a second material, that has a longer adatom diffusion length, is deposited. The capillarity is more effective, attracting more material to the concave center of the recess: the profile broadens, tending to a new, larger equilibrium. This second material is found thicker at the recess bottom than at any other location. The profile resulting from the deposition of a thin InGaAs layer in-between two GaAs is shown on Figure 2.4(c). It happens that on GaAs substrates, In has a longer diffusion length than Ga, which in turn is more mobile than Al. The diffusion length thus increases when decreasing the effective bandgap, which permits the formation of various confining nanostructures using the three alloys InGaAs, GaAs and AlGaAs.

QDs are grown in arrays of tetragonal recesses (pyramids), that are wet-etched through circular or triangular apertures in a mask thanks to the orientation of crystallographic planes on (111)B substrates, as detailed in Section 3.1. The physics of the QD formation is essentially similar to that of the V-groove QWRs, except that no precursor decomposition occurs on the planar (111)B ridge. The adatoms are instead massively released in the recesses themselves, resulting in a dramatically enhanced growth rate. The growth rate acceleration is ca. 3-fold in micron-sized pyramids, but can be substantially larger than 10 in small pyramids. Large growth rates

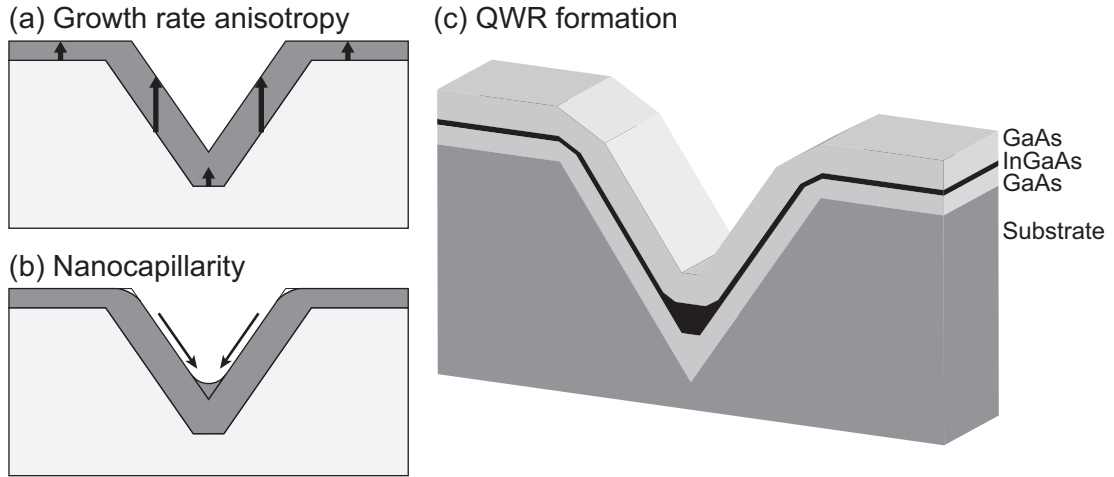


Figure 2.4: (a) The growth rate anisotropy sharpens the V-groove profile. (b) The capillarity simultaneously drives material to the bottom (and possibly depletes the upper regions). Its action is more efficient in sharp recesses, resulting in a self-limited profile. (c) Sketch of a V-groove section, with a InGaAs (black) is deposited between two GaAs layers. The capillarity affects more strongly the In atoms with longer diffusion length, thus enlarging the width of the bottom facets. A succession of various facets approximates the ideal profile.

also tend to “close” the pyramids, as the upper regions may grow faster than the inner ones, resulting in steeper facets. To compensate for these effects, the nominal growth rates must be reduced to extremely low values: our 0.013 nm s^{-1} rate was adapted from existing, slower MOVPE growth processes, and significantly lower growth rates are adopted on other sample designs, as detailed in Section 3.1.

Additional structures form when growing ternary alloys due to the difference in sensitivity of the different adatoms to capillarity. The In composition is increased at the center of InGaAs/GaAs QWR, as confirmed by EELS measurements [123]. Ga-rich vertical structures also form in V-groove QWRs made of AlGaAs alloys: there is a set of three vertical QWs at the center of V-grooves [99], and different vertical structures form in pyramids (vertical QWR along the pyramid axis, and three vertical QWs connected radially to the central vertical QWR) [124, 119]. The dominant formation mechanism of these structures is the capillarity effect, but the entropy of mixing must be taken into account in order to quantitatively calculate the alloy concentration [98, 99], as well as strain in InGaAs alloys.

Requirements for nanostructure formation

Several conditions must be satisfied in order to form capillarity-induced nanostructures of the type discussed above.

First, atomically smooth layers must be obtained when depositing the different alloys on each different facet involved in the growth (especially (100) and (111)A). The interfaces would otherwise be irregular and uncontrolled, leading to the formation of parasitic nanostructures. Second, the growth rate must be higher on the sidewalls than on the bottom facet. In our case,

the effective growth rate is larger on (111)A GaAs facets than on (100) and (111)B.

Third, the adatoms of the low-bandgap active material must have a longer diffusion length than those that compose the barrier. In the GaAs system, this condition is satisfied by Al, Ga and In adatoms ($L_{In} > L_{Ga} > L_{Al}$). Therefore nanostructures can be grown with various material compositions, like InGaAs/GaAs or GaAs/AlGaAs.

Fourth, a sizeable quantum confinement is obtained with widths below 30 nm. Such lateral sizes can be achieved with adatoms diffusion length in the 5 - 200 nm range. The growth rate and the reactor temperature can be tuned to adjust the surface diffusion. This, and purity considerations, explain why the In-containing material are generally grown at 590 °C, and the Al-containing alloys above 750 °C. Alternative techniques like flow-rate modulation epitaxy [125, 126] may also promote the adatoms diffusion.

A high growth rate of the intermediate planes between (100), (111)A and (111)B is a plus, as it better preserves the original template and prevents the formation of nanostructures at undesired locations in the recess. A quite slow growth rate of the top-(311) facet is sketched on Figure 2.4(c), leading to the development of this facet upon growth. The parasitic nanostructures formed in the upper regions of GaAs/AlGaAs pyramids can be removed by post-growth surface etching.

Suitable precursors

MOVPE group-III precursors are generally chosen among the trimethyl family for the growth of V-groove QWR and pyramidal QD structures: trimethylgallium (TMGa), trimethylindium (TMIn) and trimethylaluminium (TMAl). Arsine is used as group-V precursor. However, the use of TMGa needs to be further commented on.

As detailed in Subsection 2.2.2, the use of TMGa is a delicate matter at the low growth temperature required for efficient nitrogen incorporation. The transition between mass flow to kinetic limited growth lies around 500 - 550 °C, depending on the TMGa partial pressure [127, 128]. At slightly higher temperatures there exists a regime where the surface reconstruction differs from the usual $c(4 \times 4)$ one. A large increase in the GaAs residual doping level is also observed below 600 °C with this precursor [129]. By comparison, triethylgallium (TEGa) is very suitable for the growth of InGaAsN at low temperature [130]. Thanks to its lower cracking point, TEGa can be used with reactor temperatures lower by ~ 100 °C than with TMGa [127]. However, QWR grown using this precursor revealed a degraded morphology [131]. It was also observed unsuitable for the formation of QDs in pyramids by our group. Nevertheless, one could imagine the following workaround: TEGa may be used for the growth of the active layer and/or of the upper barrier, probably without affecting the crucial lower interface.

2.1.2.3 Fabrication issues and limitations

Ideal and real profile development

The evolution of an ideal recess can be reproduced with analytical models [98, 99]. However, the evolution of the real recesses differs on some points from that representation. For example,

the size of the recess shrinks as more material is deposited. Some intermediate facets also develop or shrink, according to the growth rate anisotropies. At high temperatures, the V-groove template remains self-similar during growth, but close to or below 600 °C the top {311} facets develop significantly. These facets progressively dominate the upper part of the V-groove and ultimately consume the initial {111}A sidewalls. In small grooves the recess shape may significantly differ from that expected due to faceting, affecting the nanostructure formation.

Density issue and lasing

If QWR cavity coupling or lasing was demonstrated using several types of optical cavities [100, 102, 103, 4], achieving stimulated emission using QDs as active medium proved not as straightforward. The areal QD density is difficult to increase above $5 \times 10^9 \text{ cm}^{-2}$ [132], whereas the density of SK-QD in lasers is typically in the $10^{10} - 10^{11} \text{ cm}^{-2}$ range [76]. Pyramidal QD lasing is still to be demonstrated.

Limited wavelength range of emission

The V-groove system was originally developed using the strain-free GaAs/AlGaAs alloys. The emission wavelength can be pushed to the red by using InGaAs as active medium. However, the In composition and the thicknesses must remain moderate, in order to stay in a capillarity-driven nanostructure formation regime, and to avoid the 2D-3D growth mode transition. The interband transitions are therefore limited to the $\sim 0.7 - 1 \mu\text{m}$ wavelength range. The usual alloys cannot reach the optical telecommunication windows.

A possible solution to extend the operating wavelength toward the optical fiber windows is the incorporation of nitrogen into InGaAs alloys. As presented in Section 2.2, the introduction of this group-V element at percent levels causes a huge shrinkage of the bandgap [133, 134]. The incorporation of N into the QWR and QD will be studied in Chapters 5 and 6, respectively.

The fabrication of nanostructures by capillarity may also be achieved in principle using different materials. A breakthrough would be the realization of InP-based nanostructures, which would open the telecommunication windows near 1.3 and 1.5 μm wavelength to nanostructures formed by capillarity. The growth of InGaAs/InP V-groove QWR was already reported using MOVPE [135, 136, 137, 138] and gas-source MBE [139]. However, the InP growth was reported unable to preserve the sharp V-groove tip, required for a strong lateral confinement of the carriers. In an appendix to this work (Appendix A), we present a brief study of fabrication of InP-based QDs that opens perspectives with the InGaAs/AlInAs alloys combination.

2.2 Toward long wavelength emission: the use of dilute nitrides

V/III alloys generally undergo almost linear evolution of material parameters when the chemical composition is modified. This is illustrated on Figure 2.5, which displays the bandgap energy of several semiconductors as a function of the lattice parameter. Physical quantities like the bandgap of alloys usually fit quadratic functions of the composition, with the so-called bowing parameters (here b) characterizing the deviation from linear behavior:

$$E_g(A_{1-x}B_x) = (1-x)E_g(A) + xE_g(B) - x(1-x)b,$$

where A and B are the 2 pure binaries. As an example, the InGaAs bowing parameter characterizing the bandgap variation is $b = \sim 0.477$ eV [140].

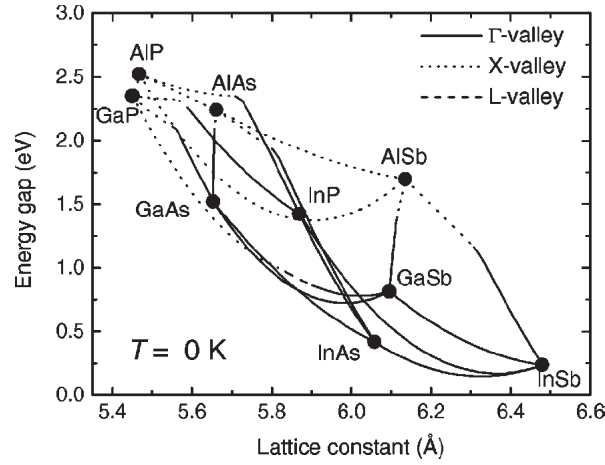


Figure 2.5: Bandgap energy as a function of the lattice parameter for a set of low-bandgap III-V semiconductors and alloys. Direct bandgaps are displayed with continuous lines while dashed lines stand for indirect transitions. Most of the alloys only slightly differ from linear behavior. Graph from [140].

The situation of dilute nitrides alloys strongly differs from this picture. The bandgap of GaN in the zinc blende structure (~ 3.299 eV at 0 K) lies well above that of GaAs (1.519 eV), therefore incorporation of N into GaAs is expected to enlarge the bandgap energy. However, the N atoms strongly differ in size and electronegativity from more common group-V atoms (As, P), introducing a large modification of the bandgap. Extremely large and composition dependent optical bowing parameters in the range of ~ 20 eV were measured [29, 141, 142], resulting in an effective strong shrinking of the bandgap [27, 28].

2.2.1 Theoretical description of GaAsN and InGaAsN alloys

Theoretical effort was soon deployed to explain the large effect of N on the bandgap evolution [143, 144, 145, 30, 146], assigned to strain effects. The idea was emerging that strongly localized

nitrogen levels play a role in the theoretical description; however results were not satisfying for a while.

2.2.1.1 The analogy with GaP

Another dilute nitride III-V material, GaPN, shows some similarities with GaAsN. This indirect bandgap material exhibits localized, optically active states, slightly below the conduction band minimum: N-related states can be observed at very low N concentration [147]. Some intense optical transitions were assigned to individual N atoms, as well as to N-N pairs with different interspacing [148]. These defects consist in P atoms replaced by N or other group-V elements, and are called isoelectronic traps. This name comes from the similar electronic structures of exchanged atoms (group-V) associated with significant differences in size and electronegativity. These differences explain the difficulty of alloying significant amounts of N, as well as the large effects of modest incorporations. Notably, in spite of being neutral defects, isoelectronic traps can exhibit acceptor-like or donor-like behavior [149]. In a simplified picture, an electron (hole) can be attracted to the vicinity of the defect by the electronegativity difference of the impurity relative to the host's. Later, a hole (electron) can be also trapped by the Coulomb attraction, eventually forming a localized exciton placed on the impurity. The relative N electronegativity compared to As or P explains its acceptor-like behavior, similarly to O atoms in the ZnTe system. The opposite behavior is observed for Bi impurities.

When increasing the N doping in GaP crystal, the observable spectral lines evolve from single N transition at low concentration levels, to N-N pairs observable at concentrations up to $x = 0.4\%$. Then N clusters progressively take over most of the emission intensity. No well-defined structure can be observed in the spectrum for concentrations higher than $x = 1.3\%$, and the emission is progressively redshifted with increased N concentration [150].

2.2.1.2 The band anticrossing model

The similarity of As and P allows assuming similar N effects on GaAs as on GaP, in spite of the apparent different behavior [151]. A major difference is that almost all N-complexes levels do not lie in the bandgap of GaAs but above, in the conduction band [152]. A direct observation of the individual N and the different N pair states can be achieved by applying hydrostatic pressure, that shifts upwards the GaAs bandgap much faster than the N-related lines [26]. In a key article, Shan *et al.* [153] assumed and treated as a perturbation problem the interaction of the GaAs E_g state at the conduction band minimum, with a single localized E_N level, leading to the following eigenvalue equation:

$$\begin{vmatrix} E - E_M & V_{MN} \\ V_{MN} & E - E_N \end{vmatrix} = 0,$$

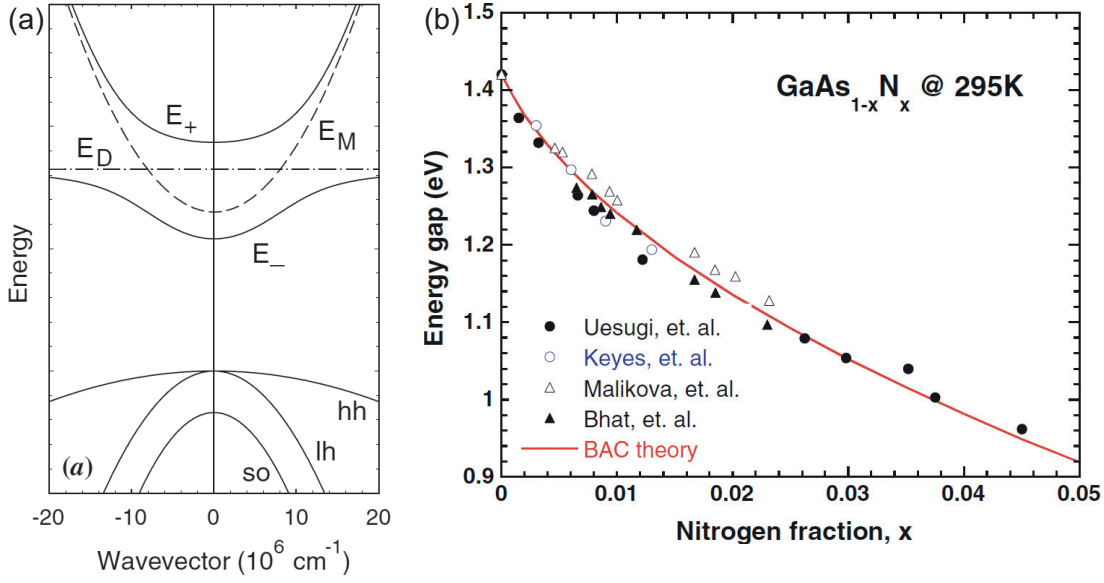


Figure 2.6: (a) Illustration of the effects of band anticrossing on the conduction band structure in the vicinity of the Γ point. The N localized states E_D interact with the GaAs E_M band (dashed lines), forming 2 new hybrid E_- and E_+ states (continuous). Graph from [155]. (b) Comparison of experimental data of the bandgap of $\text{GaAs}_{1-x}\text{N}_x$ alloys with predictions of the BAC model ($C_{MN} = 2.7 \text{ eV}$). Graph from [156].

with V_{MN} the matrix element describing the interaction between the two types of states. Such a formalism leads to states mixing and anticrossing, with 2 solutions E_+ and E_- that can be written as:

$$E_{\pm} = \frac{E_N + E_M}{2} \pm \frac{1}{2} \sqrt{(E_N - E_M)^2 + 4V_{MN}^2}.$$

This formalism can be extended close to the vicinity of the Γ point, leading to the band structure shown on Figure 2.6(a). The optically active E_- band lies at lower energy than the original bandgap and has a mostly extended character (still exhibiting a partly localized character) [152, 154]. The predicted E_+ solution was observed by photoreflectance spectroscopy, and has a dominant localized character (and optically less active) at usual pressure conditions.

In this description, few parameters are left as unknowns. The N-free GaAs bandgap E_M can be measured independently, while the E_N localized N states were determined by a fitting procedure $E_N = 1.65 \text{ eV}$ above the valence band maximum at room temperature. The coupling strength V_{MN} varies with the nitrogen concentration x , from $V_{MN} = 0.12 \text{ eV}$ at $x = 0.009$ to 0.4 eV at $x = 0.023$. V_{MN} can be better parametrized as $V_{MN} = C_{MN} * x^{1/2}$ [157], with the $C_{MN} = 2.7 \text{ eV}$ in the case of GaAs(N) alloys. The BAC model well reproduces the evolution of the bandgap energy, as shown on Figure 2.6(b).

Remarkably, the BAC model quite accurately describes the bandgap of InGaAsN alloys, with a smaller value of the C_{MN} parameter [158]. The energy of the N levels is obtained independent

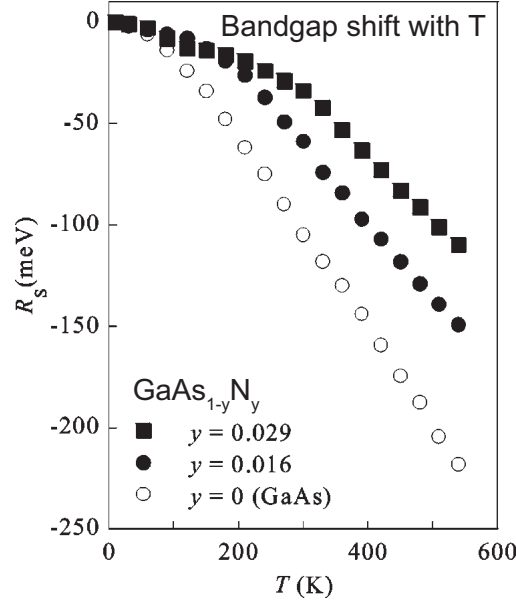


Figure 2.7: Redshift R_S of the PL emission relative to its $T = 10$ K value for different nitrogen concentrations y . Graph from [165].

from the In concentration [159].

This simple BAC model assumes only the interaction between a nitrogen state and the conduction band close to the Γ point. Experimental results conclusively excluded significant interaction with the χ and L conduction band minima [160]. Also, the effect of N on the valence band and on the spin-orbit splitting Δ_0 [153] was determined to be almost negligible ($< 10\%$ of that on the conduction band), and independent from the In concentration [159]. The insensitivity of the valence band on nitrogen was confirmed by surface photovoltage measurements [161]. Nevertheless, N-related strains effects must be taken into account for an accurate description of the valence band. As a result, the confinement of holes is fairly weak as compared to that of electrons. This favors thermionic escape of holes from InGaAsN heterostructures, hindering the devices performances at high temperatures [162, 163, 164].

A first consequence of the BAC model is the reduced temperature dependence of the bandgap. The bandgap energy of semiconductors tends to decrease when increasing the temperature, mostly due to the enlarged interatomic spacing (dilatation) and to the variation of the electron interactions with the phonon bath, dominant at high temperature. The evolution of semiconductor bandgap can be described empirically using the Varshni formula:

$$E_g(T) = E_g(0) - \frac{\alpha T^2}{T + \beta},$$

with E_0 the bandgap at 0 K, and α and β materials constants.

When compared to GaAs, dilute-nitride materials typically exhibit a reduced dependence of

the bandgap energy on the temperature [166, 167]. This can be understood in the framework of the BAC model, if the E_N nitrogen level is assumed nearly insensitive to temperature. A large anticrossing occurs at low temperature when the E_M and E_N states are close to each other. At high temperatures, the E_M N-free band is shifted to lower energies, thus increasing the energy difference between E_M and E_N . The intensity of the anticrossing repulsion is lower: the E_- state shifts less than the E_M state with temperature. If impurity-related effects perturb the measurement at low temperatures, experiments confirm the reduced bandgap dependence on temperature [165, 168, 167] as shown on Figure 2.7, and obtained smaller Varshni coefficients.

The BAC model can be extended to compute the band structure $E(k)$ near the Γ point [159, 155]. Due to the state mixing, the low-energy state E_- becomes non-parabolic [157] and exhibits a lower curvature, as shown on Figure 2.6(a). This also corresponds to an increase in the electron effective mass m_e^* , as evidenced using magneto-tunneling spectroscopy [169] and optical detection cyclotron resonance [170], the latter work mentioning $m_e^* = 0.12m_0$ and $0.19m_0$ at 1.2 % and 2.0 % N respectively. The non-parabolicity was also confirmed experimentally [171, 172]. The BAC model was also shown to quantitatively account for the drastic decrease of the electron mobility [155], due to the partial localized character of the electron wavefunctions [173]. This low charge mobility hampers, but does not forbid, some of the possible applications of dilute nitride materials, such as solar cells fabrication [174].

2.2.1.3 Beyond the simple BAC model

A major issue with the simple BAC model is the existence of multiple, non-degenerate N complexes states lying in the conduction band [152]. These states are simply ignored by the 2-state interaction presented above. However, detailed theoretical studies [175, 176, 171] revealed that the BAC model actually provides an excellent description of the conduction band edge, despite treating the N perturbation as originated from a single E_N state and not from a multiplicity of N complexes.

On the other hand, the conduction band actually undergoes breakups due to successive anticrossings with different N complexes states [177]. As a result, the BAC model does not describe satisfactorily the evolution of more complex physical quantities. The onset of strong N-N interactions can be estimated to be at 0.1 - 0.2 % N and is marked by a large evolution of various parameters [178, 179, 177, 180], like the electron effective mass m_e^* , or the electron gyromagnetic moment g_e^* . Moreover, the BAC model predicts the bandgap to depend solely on the N concentration. The local atomic configuration actually starts playing an important role for concentrations above 1 % [181]. Post-growth treatments such as annealing can shift the bandgap without affecting the nitrogen concentration (see Subsection 2.2.2.5). A further blow to the simple BAC model is that the E_+ transition evidenced by photoreflectance, initially thought to be related to the N levels close to the Γ point, seems to originate from L -valley states [134]. The band structure of dilute nitride alloys is actually perturbed well beyond the only band edge.

Measurements of the electron effective mass m_e^* in GaAsN alloys revealed a considerable

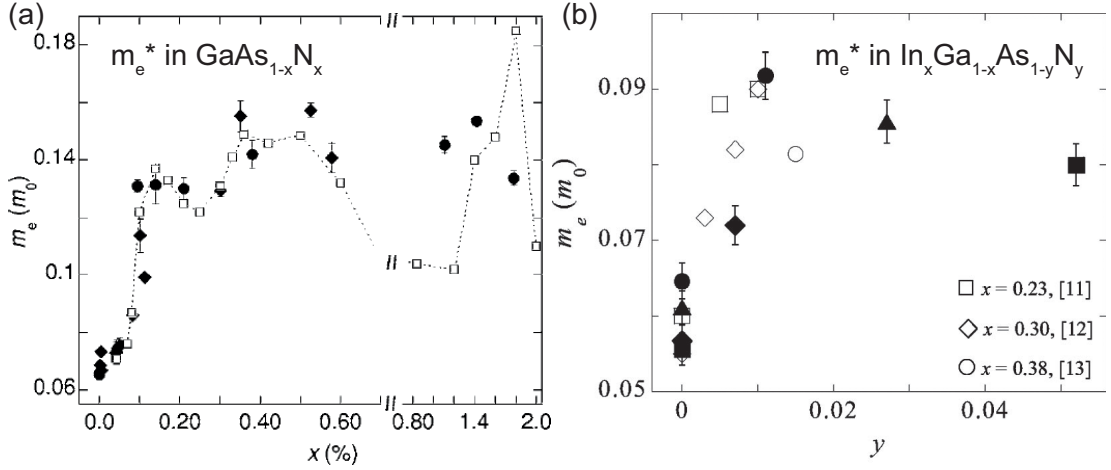


Figure 2.8: (a) Experimental (full symbols) and calculated (open squares) values of the electron effective mass m_e^* in GaAsN alloy, as function of the N concentration x . The strongly non-monotoneous evolution is originated from the interaction of N-cluster states with the GaAs conduction band edge, and is not reproduced by the BAC model. Graph from [182]. (b) Experimental values of m_e^* as function of N concentration y in InGaAsN samples. The increase in the effective mass is reduced when compared to GaAsN. The BAC model reproduces quite well the results. Graph from [180].

increase compared to the N-free counterpart (m_e^* almost $0.2m_0$ at N content $y = 2\%$ [170]). More detailed magnetopholuminescence [182] and Seebeck and Hall [183] studies revealed a complex, non-monotoneous evolution with increased N content, as depicted on Figure 2.8(a). A sudden change occurs at N concentration of 0.1 %, due to the crossing of the conduction band minimum with N-cluster states. The evolution was reproduced by a modified $k \cdot p$ model taking into account hybridization effects between N clusters states and the conduction band edge (LCINS model - linear combination of randomly distributed isolated nitrogen states [154]). The N clusters states close to the GaAs band edge interact with it, leading to the complex evolution of m_e^* with nitrogen concentration. On the contrary, the BAC model only predicts a regular increase of m_e^* saturating at $0.1m_0$.

An increase of m_e^* is also observed in the case of InGaAsN alloys [180] (see Figure 2.8(b)), although less dramatic than that of GaAsN alloys. The In shifts the conduction band edge away from the N clusters states, and the BAC model framework explains satisfactorily the observations.

A similar issue affects the electron gyromagnetic factor g_e^* in GaAsN alloys [184]. Small concentrations are sufficient to reverse the g_e^* sign. A theoretical treatment of N-clusters states qualitatively similar to that used for the calculation of m_e^* is able to explain this behavior.

The incorporation of N in dilute concentrations in other III/V compounds also leads to a large reduction of the bandgap. The BAC model consistently describes the behavior of InAsN [185, 186]. The InPN alloy is also likely to be accurately described by this model [187]. Although similar in some aspects, the situation is a bit more complex in the case of the larger, indirect

bandgap GaPN where the bandgap seems to evolve purely from the N discrete levels [151]. More details on the theoretical treatment of the dilute nitrides properties can be found in Ref. [188]. A detailed description of the models of band structure calculations as well as various materials parameters can be found in Refs. [140, 158].

2.2.2 Fabrication and optimization of (In)GaAsN alloys

Incorporation of nitrogen into GaAs at concentrations in the percent range is not a trivial task. This is mainly due to the low thermodynamic solubility, evaluated by valence-force field (VFF) calculations in the 10^{14} cm^{-3} range [189], depending on temperature. This is merely a doping level, orders of magnitude below the desired percent values. Higher concentrations are thermodynamically unstable, prone to phase separation, N clustering and spinodal decomposition. Yet thermodynamic equilibrium considerations are of limited use in the description of epitaxial growth. In far-from-equilibrium growth conditions, the predicted limit concentrations can be overcome by orders of magnitude thanks to surface reconstructions [190] and kinetic effects [191].

The growth temperatures are lower in MBE systems than in MOVPE, and so MBE lies further away from thermodynamic equilibrium. It is therefore not so surprising if higher nitrogen content can be achieved using MBE. $1.5 \mu\text{m}$ lasing was reported as soon as 2000 [192], QW photoluminescence was observed up to $1.7 \mu\text{m}$ [193], and a $1.9 \mu\text{m}$ emission at the ground state was even evidenced using contactless electroreflectance [194]. Band engineering can further extend the possibilities while keeping good radiative properties [195].

On the other hand, MOVPE growth of $1.5 \mu\text{m}$ quantum wells [196, 197] and lasers [198] was also demonstrated, although most of the effort was directed to the $1.3 \mu\text{m}$ window. In addition to the lower level of N incorporation, the performance of MOVPE-grown devices is also hindered by the quite large p-type C (and H) residual doping [142, 199].

We are mostly interested here in the MOVPE method as only this technique is able to grow V-groove QWRs and QDs in inverted pyramids. In the following, the characteristics of the MOVPE growth of GaAsN and InGaAsN alloys are reviewed. However, the comparison of different reports is uneasy due to the extremely wide space of growth parameters and to their strong inter-dependencies. We tried to present the MOVPE growth of dilute nitride (In)GaAsN alloys while keeping the discussion as synthetic as possible.

In order to help placing this review in the perspective of our work, we mention that our MOVPE growth were performed in an horizontal reactor using 20 mbar N_2 as carrier gas, and arsine, DMHy, TMGa and TMIIn as precursors.

2.2.2.1 N precursors in the MOVPE technique

Several liquid or gaseous precursors can be used as a nitrogen source in the MOVPE technique. The simplest molecules like molecular nitrogen or ammonia (NH_3) are very stable. Plasma cracking was initially employed [27] with such gases but this approach is only effective at very low growth pressure: it is better suited to MBE environments. More apt precursors can be found in the hydrazine family. The most common are the unsymmetrical dimethylhydrazine (DMHy) and the tributylhydrazine (TBHy). Other sources like hydrazine (Hy) or nitrogen trifluoride (NF_3) are available, but present important drawbacks summarized below.

The most widespread N source for MOVPE is unsymmetrical dimethylhydrazine (DMHy). The growth of high-quality GaAs is usually performed close to 600 °C, but significant N incorporations require to be further away from thermodynamic equilibrium, i.e. at lower temperatures. The best temperature range for InGaAsN was evaluated as 500-530 °C [200]. At these temperatures, DMHy is not fully decomposed (50 % decomposition at 550 °C [201]), leading to a very poor incorporation efficiency. At temperatures suitable for MOVPE growth of dilute nitrides, tertiarybutyl hydrazine (TBHy) has a higher incorporation efficiency than DMHy due to its lower decomposition temperature (50 % decomposition at 300 °C versus 550 °C) [202, 203]. The hydrazine (Hy) source presents higher efficiency incorporation than TBHy and DMHy, but requires a high As/III ratio for the surface morphology to remain acceptable ($\text{As/III} \sim 70$). Formation of liquid In, Ga, N droplets in the injection pipes was also reported, requiring an extensive cleaning of the facility with no certainty of avoiding memory effects [204]. This precursor is generally avoided in favor of the TBHy or DMHy. Nitrogen trifluoride (NF_3) has reportedly a high N incorporation efficiency when compared to DMHy, with minimal influence of In on N incorporation ($(1-x)^2$ dependency) [204]. However, interactions with Ga species lead to a difficult control of the effective growth rate, and the residual doping issue is not solved [191].

A major issue of the MOVPE crystal growth is the incorporation of carbon, providing a large p-type background doping. The different N precursors were characterized regarding this issue, but no significant doping reduction was observed [142].

Hydrazine-based precursors experiment a complex decomposition process, and the large number of different radicals in the gas phase leads to numerous and complex reactions that might explain some apparent contradictions in the literature, together with the various reactor growth conditions [128]. We will nevertheless try to summarize the main trends.

2.2.2.2 Growth of GaAsN alloys

The growth processes of GaAsN and InGaAsN alloys share numerous similarities. However the addition of In cannot be merely considered as a perturbation of the GaAsN growth. In order to maintain some clarity, in the following the growth the ternary GaAsN will be first described, before switching to the more technologically relevant InGaAsN alloy.

Many growth parameters can influence the incorporation of atoms into a crystal. As mentioned previously, the nature of the N precursor affects its incorporation. The precursor flux is an evident parameter to adjust, but is not the only knob to tune. The growth temperature acts as a key parameter, affecting all the growth kinetics and especially determining the rates of decomposition, reaction and surface desorption. The growth rate and reactor pressure affect the N incorporation. Interactions with Ga precursors were also mentioned. The influence of different parameters can be reviewed separately, but these are generally not independent from each other. It is therefore of prime importance to carefully monitor and calibrate the growth conditions, layers thicknesses and concentrations.

Temperature

Temperature is certainly the most important growth parameter concerning N incorporation into GaAs-based crystals. While GaAs is commonly grown at 600 °C, early results evidenced a drop in the incorporation efficiency when raising the temperature by even moderate values [205]. Commonly no significant N incorporation is observed at or close to ~ 700 °C [191, 203]. A more efficient incorporation is observed below 540 °C. This behavior is common to different MOVPE precursors (NH₃, NF₃, DMHy, hydrazine), but is not observed using MBE with atomic N precursors [206]. This suggests a surface desorption process of the N precursors that is thermally activated [34].

Other precursors

Such low growth temperatures cause the incomplete decomposition of several widely used precursors, thus switching the growth regime from mass transport limited to kinetic limited. In this situation, temperature variations of a few degrees can cause important changes in the incorporation efficiencies, hindering the control of the chemical balance. Our usual GaAs precursors, arsine and TMGa, are actually not fully decomposed at 520 °C. The incomplete arsine decomposition leads the effective As/III and DMHy/As ratios to change with temperature, affecting the N incorporation. A similar situation is also observed with TBAs, which is fully decomposed even at low temperatures [207]. This latter precursor might be used instead of arsine for the better control of the As/III ratio.

The TMGa also experiences an incomplete decomposition in the low-500 °C range [191, 128]. The effective growth rate is reduced and may become difficult to control. At low temperatures, TMGa also leads to a quite large incorporation of carbon [129]. TEGa can be used instead of TMGa, as it fully decomposes at low temperature and lowers the C contamination level [208]. The GaA surface reconstruction was also reported to change from the usual $c(4 \times 4)$ form at the temperature of interest when using TMGa, possibly affecting the growth rate and the N incorporation; this was not observed when using TEGa [127]. The use of TBAs is reported to promote the decomposition of TMGa [209]. Gas-phase interaction of TEGa with DMHy was also reported, leading to undesired changes in the growth rate and N concentration [201, 210]. In this work, arsine and TMGa were used as As and Ga precursors. TEGa was discarded as the surface diffusion is strongly enhanced when compared to TMGa, and produces extremely large V-groove QWRs with no lateral quantum confinement [131].

Reactor pressure

The reactor pressure affects the decomposition rates of the precursors. Whenever a partial decomposition takes place, changing the reactor pressure can significantly alter the growth rate (group-III precursors) and/or the N incorporation (group-V). Gas-phase parasitic reactions might also alter the decomposition rate and the quantity of atoms available for crystal growth, thus affecting the width and composition of N-containing QWs [34, 201]. At 525 °C the N incorporation evolves with the reactor pressure in a non-monotoneous way, signature of the pressure-assisted DMHy decomposition [203]. That study reported a maximal efficiency was observed close to 200 mbar (though this value certainly depends on the details of the reactor geometry and on the fluxes).

Surface effects and chemistry

Other factors than the gas-phase precursor decomposition affect the N incorporation, surface effects also play a very important role. AlGaAsN samples grown with a low Al concentration (5 %) revealed a strong increase in the N incorporation [203]. Al facilitates the N incorporation thanks to the favorable Al-N bond. This supports the hypothesis that only a small fraction of the N atoms arriving on the surface is actually incorporated, the large part being desorbed [203, 34].

Growth rate

Assuming that a large fraction of the N atoms arriving on the surface actually desorbs before incorporation, increasing the growth rate should increase the N incorporation by letting less time for atoms to desorb. Experimental reports are somewhat contradictory on that point. If increases were reported [191, 34], sometimes no trend was observed [203] and even decreases were reported [211]. The latter study performed kinetically limited growths, and suggests that the growth of the previous reports were actually limited by the mass transport. Higher growth rates lead to increased carbon doping levels and to decreased carrier lifetime [208]. Low growth rates also allow more H desorption, and may increase the diffusion length of N atoms before incorporation, thus helping forming less defects in the crystal. While most of the studies used growth rates close to $1 \mu\text{m h}^{-1}$, values as low as $0.15 \mu\text{m h}^{-1}$ were recommended [34]. The growth rate used during our QW and QWR depositions was $1 \mu\text{m h}^{-1}$ (the nominal growth rate of the QD depositions cannot be compared).

DMHy/V ratio

The growth of GaAs-related materials is performed in a group-V-rich environment to avoid formation of Ga droplets on the surface of the sample. The growth rate is therefore controlled by the flux of group-III precursors. As and N atoms are in competition to occupy the V-sites of the lattice: huge N precursors fluxes are required for a decent incorporation due to the low N incorporation efficiency. This competition suggests that the N incorporation efficiency is proportional to the gas-phase ratio of As and N precursor, which is confirmed by experimental evidences [203, 204].

V/III ratio

Lowering the flow rate of group-V precursors while keeping constant their internal DMHy/As ratio favors nitrogen incorporation, and tends to decrease the effective growth rate [211]. However, other reports showed no dependence of the N incorporation on the total V/III ratio [207]. If a low flux of N-precursor is desirable to avoid some of the multiple parasitic reactions between precursors, care must be taken to maintain good layer morphology and crystalline quality.

DMHy influence on growth rate

With the numerous interactions between precursors occurring when using DMHy, it is not surprising that changes in the growth rate have been observed when increasing the flux of this precursor. Moderate DMHy fluxes increases were reported to decrease the growth rate at usual temperatures (530-600 °C) [207]. Beaudry *et al.* observed the growth rate alternatively accelerated and lowered according to the growth temperature [211]. Therefore a special care must be dedicated to a consistent calibration of the effective growth rate when growing N-containing layers.

Strain

The strain developing in the grown layer has a detrimental influence on the N incorporation in GaAs. Epitaxial GaAsN layers on GaAs have a tensile strain, and increasing the N content linearly increases this strain. GaP has a smaller lattice parameter than GaAs and can be used as a substrate for the growth of compressively strained GaAsN. In this case, increasing the N content releases the strain of the layer. Experiments revealed that under similar growth conditions, the N incorporation in GaAs is favored ~ 5 -fold when growing GaAs on GaP substrates rather than on GaAs, confirming the importance of strain-driven incorporation mechanisms [203].

2.2.2.3 InGaAsN alloys growth

Reaching the technologically relevant 1.3-1.55 μm spectral windows with GaAsN alloys requires extreme concentrations of nitrogen, impossible to achieve by MOVPE without incorporating defects hindering the performances of devices. In this context, the idea seems natural to add N into a lower bandgap material such as InGaAs. However, it was quickly noticed that the N incorporation is superlinearly hindered in the presence of In [212]. A drastic decrease in the N incorporation efficiency is generally observed [203], although a more complex situation was observed in atmospheric pressure reactors using TBAs as As precursor, with an In concentration of 23 % reported optimal for N incorporation [197].

In composition

A first explanation of the marked decrease of N incorporation efficiency in the presence of In is related to the kinetics of surface incorporation. VFF calculations demonstrated that on the surface, individual Ga-N bonds are strongly preferred to In-N ones [213], even though the opposite situation prevails in the bulk. This effect explains partly, although not totally, the drastic fall of N uptake with increasing In concentration. The well-known In surface segrega-

tion in InGaAs layers [214] was proposed as an explanation. A significant part of incoming In adatoms is not directly incorporated but stays at the surface, forming an In-rich layer on the sample. Therefore, N atoms diffusing on the surface “see” an effective In content much higher than the bulk concentration, thus explaining the marked decrease in their incorporation.

Thanks to a quantitative study of the In segregation based on TEM results, Volz *et al.* were able to explain a $(1 - 2.5x)^2$ dependency of the N incorporation efficiency on the In concentration x : this formula explains most, but not all the observed incorporation quenching [203] (for In contents below 0.1, a dependency of ca. $(1 - 6x)^2$ is observed, with a less drastic evolution at higher In contents).

The mathematical expressions above are derived from a naive model sketching the N incorporation on a group-V lattice site, which is only successful if the two underlying group-III lattice sites are occupied by Ga atoms. Whenever one of these two sites is occupied by In, the N atom desorbs and is lost. This simple model predicts the N incorporation efficiency to evolve with the In concentration x as $(1 - x)^2$. The In segregation leads to an increased effective In concentration at the surface, and is accounted for by a prefactor to x .

The same study proposed several other mechanisms to explain the discrepancy: a TMIn- or methyl-induced stabilization of the N-radicals, encounters of N with In atoms favored by diffusion, or an altered surface reconstruction less favorable to N incorporation than the one of usual GaAs.

Temperature

First reports indicated no N incorporation in $\text{In}_{0.08}\text{Ga}_{0.92}\text{As}$ alloys grown at 600 °C [212]. More generally, for a fixed In concentration, the N incorporation strongly depends on temperature, with the characteristic dependency of the thermally activated processes. This evolution is much clearer and steeper than in the case of GaAsN alloys [203].

A degradation of the structural quality of the layers was also observed by XRD measurements above 530 °C [200]. For this reason, growths are generally performed in the 510 - 530 °C window.

Growth rate

The N incorporation efficiency increases when the growth rate is increased [200], a clearer trend than for GaAsN alloys. The relationship is actually close to linear proportionality [203]. This asserts that the N incorporation is governed by an In-induced, temperature-dependent reduction of the sticking coefficient of the reactive N species.

2.2.2.4 Presence of defects and the so-called S-shape bandgap evolution

A non-monotonous evolution of the bandgap energy with sample temperature is generally observed below 150 K. When decreasing the temperature below ~ 100 K, the emission is found to redshift and broaden, before possibly blueshifting with a reduced linewidth when the temperature is further reduced. This behavior is illustrated on Figure 2.9(a). The bandgap energy curve as function of temperature has an S-shape. It is usually characterized by the localization energy, defined as the maximum energy difference between the PL emission energy and the

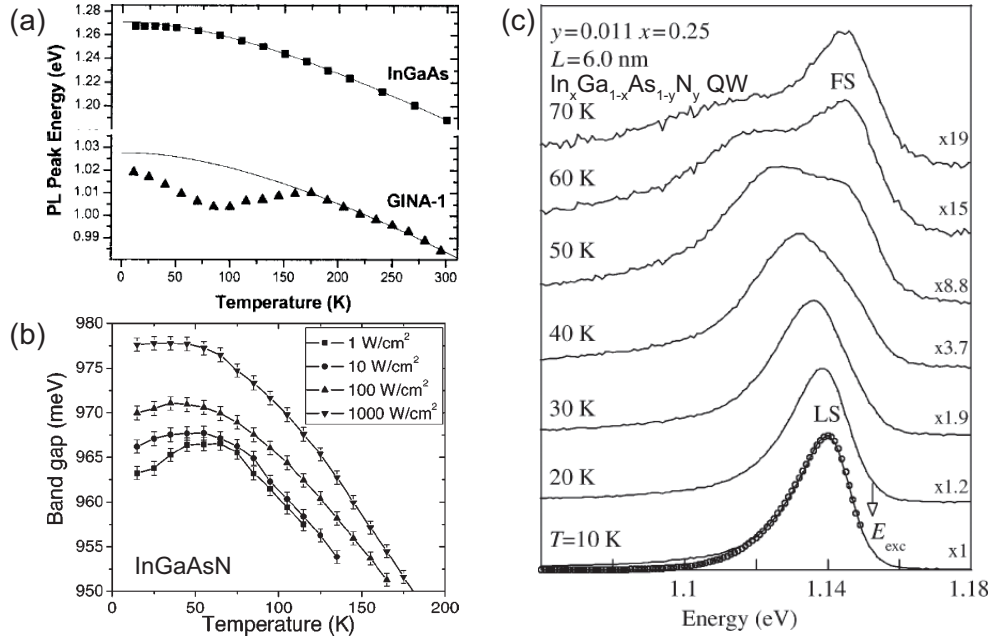


Figure 2.9: (a) PL energy of InGaAs and InGaAsN (GINA) samples. The continuous lines are Varshni fits, evidencing the S-shape evolution of InGaAsN. Graph adapted from [217]. (b) Bandgap energy as function of the excitation power. The S-shape is more pronounced at low power levels. Graph from [218]. (c) Temperature dependent PL spectra of MBE-grown InGaAsN QW, showing the transition from localized states emission (LS) at low temperature, to delocalized (free) states (FS) at higher temperature. E_{exc} indicates the 10 K free exciton energy. Graph from [134].

Varshni curve fitted to the high temperature data.

This behavior is associated with a transition from free excitons at high temperature, to localized carriers at low temperature [215], an interpretation confirmed by near-field optical microscopy (SNOM) measurements [216]. Optical spectroscopy on high-quality samples can reveal the change in the PL origin, as shown on Figure 2.9(c). As the S-shape is related to carrier localization on defects, it is increasingly apparent when the excitation power density is lowered, as evidenced on Figure 2.9(b).

The PL emission generally undergoes a blueshift when increasing the excitation power, as visible on Figure 2.9(b). At low excitation power, the low-temperature emission is dominated by the defects contribution. Increasing the power causes the defect emission to saturate, increasing the contribution of the free excitons, resulting in a blueshift of the emission.

The μ PL spectrum can be consistently linked to the macro-PL emission. The low-power, low-temperature μ PL spectrum of InGaAsN QW consists in a forest of peaks (signature of localized states) at the energy of the localized states tail of the macro-PL spectrum. When the power is increased, these lines progressively merge into a broad feature progressively shifting toward the bandgap located at a slightly higher energy. The activation energies of the individual PL lines was observed to be constant and independent on their energy, which indicates that these

features are due to excitons bound on deep donor or acceptor-like states [219]. These defects become progressively optically inactive at temperatures above 50 - 100 K [220].

The magnitude of the S-shape is observed to increase with increasing N content, indicating a degradation of the material quality directly related to the N incorporation [167]. The S-shape is observed to be more pronounced in InGaAsN alloys than in the ternary GaAsN material. As a general rule, the magnitude of the S-shape and of the transition temperature are observed to depend on material quality, and are correlated with the PL efficiency [217]. A healing of defects is sometimes possible by using sample annealing, as is briefly reviewed below.

2.2.2.5 Annealing

Short-duration postgrowth annealing, also called rapid thermal annealing (RTA), is long known to improve the PL efficiency of various type of samples grown under non-optimized conditions, as well as to significantly decrease the lasing threshold [221]. In that specific case, the improvement of the InGaAs layers performances was attributed to the cure of defects, which were acting as carrier traps.

Similar performance improvements were quickly reported on N-containing structures, when performing annealing in the 650 - 750 °C range. The PL intensity of GaAsN [207] and InGaAsN [222] is strongly enhanced upon annealing, as well as the performances of solar cells [38]. Drastic improvements are also observed for MBE-grown layers [206]. The PL emission linewidth [223] is found reduced upon annealing, as well as other indicators of crystal quality such as the electron mobility [224]. The onset of the S-shape bandgap evolution and the magnitude of the associated blueshift are also reduced upon annealing [225], signature of an improved material quality. However, the quality improvement is associated with a strong emission blueshift (up to 100 meV), which is obviously not desired. Moderate (< 100 meV) blueshifts are actually not associated with N diffusion out of the sample, but instead originate from a local rearrangement of atoms.

GaAsN alloys

The annealing of GaAsN materials usually leads to increased PL intensity, resulting from the healing of non-radiative defects. Almost no associated blueshift is observed [226].

During the growth, the N atoms tend to aggregate and form chains along the [001] direction due to the strain energy. First-principle [152] and VFF [227] calculations suggested that such N clusters form localized states in the bandgap, tending to shift the emission to the red if the cluster concentration is increased. However, these clusters are thermodynamically stable in an In-free environment, and are not dissociated upon annealing in GaAsN alloys [228, 227]. No long-range N diffusion occurs at the typical annealing temperature and duration [229], thus preventing the diffusion of N out of the sample. However, some local, possibly strain-assisted, diffusion can occur. Volz *et al.* [230] conducted a TEM-based study of GaAsN QWs prior to and after annealing. The annealed samples revealed a pronounced tendency for N

pileup, resulting in narrower, N-enriched GaAsN QW. The total amount of N was determined to be unchanged. Nevertheless, even though the total amount of N was not modified, the PL emission energy can be slightly affected upon annealing by a redistribution of N within the layer, or by modifications in the concentration and size of the N clusters.

Several other types of crystalline defects can generate non-radiative or below-bandgap transitions and can be affected by annealing. During epitaxy, the N atoms tend to bind to Ga vacancies, and the creation of such defects is promoted in the presence of H [231]. The mobility onset of the resulting defects lies close to 700 °C, allowing diffusion of vacancies out of the samples as observed experimentally [232]. The optical transitions of these N atoms bound to Ga vacancies were presumably observed in samples grown by MOVPE using hydrogen as carrier gas [178]. The spectrum consists in a broad (~ 150 meV) feature emission lying 250 meV below the bandgap, with intensity decreasing with decreased reactor pressure or increased temperature, and almost vanishing after a 700 °C annealing. Transitions associated with donors traps have been observed by deep-level transient spectroscopy and Laplace-transform deep-level spectroscopy. If most of the transitions could be related to known GaAs contaminants defects, two new levels were spotted, certainly associated with N-containing defects [233].

While the annealing has a non-negligible effect on GaAsN structures, more drastic effects are observed on InGaAsN layers.

InGaAsN alloys

Annealing is usually performed for these alloys using a temperature in the 650 - 750 °C range. Such temperatures restrict the N diffusion to a nanometer scale, preventing large changes in the chemical composition [230]. A threshold is the 750 °C onset of In-Ga interdiffusion, above which the QW width and In concentration becomes significantly affected by the thermal treatment [234]. Some individual N atoms may however diffuse to the GaAs barrier at lower temperatures, yielding longer wavelength emission [197].

VFF calculations demonstrated that on the growing surface, individual Ga-N bonds are strongly preferred to In-N [213]. This results in an anticorrelation of N and In atoms in the matrix: the initial local atomic environment of N atoms can thus be described as $\text{Ga}_4\text{In}_0\text{N}$. This was experimentally confirmed by TEM [235]; and 10 - 20 nm vertical strain fields are observed in as-grown InGaAsN layers, similar to those in GaAsN.

If on the surface mostly Ga-N bonds are formed, In-N bonds are thermodynamically favored in the bulk due to the strain energy [227]. For this reason, the N atoms migrate upon annealing close to In, initiating an In-N short-range ordering (SRO). The atomic environment of the N atoms changes, increasing the number of nearest-neighbor In atoms [236]. The N chains are also observed to disappear after annealing [237, 238, 228]. Experimental confirmation of this scenario was provided afterwards by means of TEM-based and X-ray absorption results [235, 223, 239].

The change of local configuration from Ga- to In-rich environment impacts the bandgap. A 20 to 100 meV blueshift is commonly observed depending on annealing conditions [240, 241], corresponding to a progressive change of the average number of In atoms in nearest-neighbor positions. Theoretical studies confirmed this dependency, with a step-like evolution of the bandgap as a function of the number of In atoms as nearest neighbors [242, 240]. Every additional In atom increases the bandgap by 20 - 25 meV. Theoretical results suggest the $\text{Ga}_1\text{In}_3\text{N}$ configuration to be the most stable.

A strong correlation is found between the PL intensity and the local environment of N atoms deduced from the annealing blueshift. The maximum PL signal is observed when the configuration roughly matches the $\text{Ga}_2\text{In}_2\text{N}$ configuration, i.e. before the full blueshift is achieved [234]. This means that the PL efficiency is not only dependent on the atomic arrangement but also on the concentration and activity of point defects, that are increased in number in Ga-rich environments [233]. The concentration of various defects can be modified during annealing: N clusters, N-related defects as interstitials, As or Ga vacancies as well as various contaminants like C [243, 244, 227]. Some PL optimization is possible by a careful tuning of the annealing conditions, by selectively acting on these defects.

Annealing conditions

The most important parameters of the annealing process are the temperature, the duration and the ambient atmosphere. The ideal conditions depend of the sample chemical composition. In low In content layers, the few In-rich sites are located far away from each another. The diffusing N atoms thus need more time before finding an appropriate site. As a consequence, In-poor layers lattice-matched to GaAs (typical for solar cell applications) require annealing of tens of minutes in the 700 °C range, and the PL intensity improvement can reach several orders of magnitude [241]. By contrast, In-rich layers may only need 10 min at 650 °C, and the associated PL intensity improvement is smaller [222].

The annealing atmosphere is an important parameter for material optimization. An annealing performed under a sizeable partial pressure of As precursors is said “stabilized”. The PL intensity enhancement is larger when using no stabilization, and the blueshift occurs at lower temperature. This is evidenced on Figure 2.10(a)-(c). This suggests that the additional As atoms provided by the atmosphere can block the reorganization processes to a certain extent. In particular, the vertical columnar strain fields evidenced by TEM do not dissolve after a stabilized annealing. However, a lengthened annealing in As-poor conditions leads to a degraded optical quality. Best results were achieved by a combination of successive stabilized and unstabilized annealings [223, 241].

Spectral linewidth limitations

In addition to concentration fluctuations, a major source of PL line broadening is the wide distribution of the energy of states, which depends on the number of In atoms bound to N. As a result of the impossibility to perfectly control the local environments [179], as well as of the influence of the N clusters remaining after annealing, the emission linewidth of dilute nitride

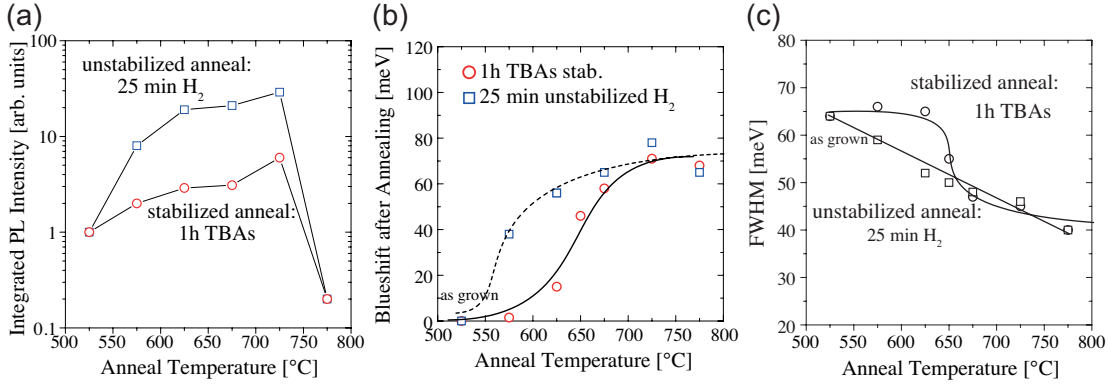


Figure 2.10: (a) PL emission intensity of an InGaAsN layer of composition suited for solar cells applications, as a function of annealing temperature, for 1 hour TBAs stabilized or 25 minutes unstabilized annealing. (b) Blueshift of the PL emission, for the series previously described. (c) Decrease of the corresponding emission FWHM with annealing time. Graphs adapted from [223].

QWs are considerably broadened when compared to other N-free alloys. The achievable linewidth depends on the N concentration, but layers with a high-N content usually show a PL emission FWHM larger than 20 meV.

2.2.2.6 Carbon incorporation

The growth of dilute nitride layers by MOVPE results in a quite large residual doping. Hence, the fabrication of devices requires a good control on the electrical properties of the epitaxial layers, hindered by the unintentional doping. For example, a residual p-type doping prevents the fabrication of highly n-type doped layers. Moreover, the residual doping can affect the optical characteristics by introducing undesired recombination channels. This can result in a large increase in the lasing threshold when additional C is incorporated [227]. The origin of the carbon doping in MOVPE epitaxy of dilute nitride is rather unclear, but numerous efforts make it appear as unavoidable. No significant differences were identified by SIMS experiments when using DMHy or TBHy. If a careful optimization of the MOVPE process is possible [227], the MBE technique is less prone to the residual C doping and is therefore preferred in devices fabrication.

2.2.2.7 Carrier diffusion limitation

The fabrication of solar cells based on dilute nitride shifted from MOVPE to MBE techniques because of the combined intrinsic material limitations and the MOVPE specific fabrication issues. In dilute nitrides, the carrier scattering cross-section of substitutional N in GaAs intrinsically limits the charge mobility to values in the range of $1000 \text{ cm}^2 \text{ V}^{-1} \text{ s}^{-1}$ [245, 246, 247]. This is especially a concern for solar cells applications where rather thick absorbing layers are

needed. A workaround is to widen the depletion region, thus increasing the carrier diffusion length so as to exceed the layer thickness [174]. This imposes to reduce the background doping level well below $1 \times 10^{15} \text{ cm}^{-3}$. Such values are very hard to achieve by MOVPE due to C incorporation, but possible by MBE [248]. State-of-the-art multijunction solar cells are now achieved with embedding MBE-grown InGaAsN layers [249, 39].

2.2.2.8 Devices applications

As demonstrated in the previous paragraphs, even limited N concentrations invariably lead to the formation of various types of defects affecting the proper device operation. Lasers and light-emitting diodes usually rely on thin QW layers, which tolerate some internal strain. Best performances are achieved by layers with low N content, high In concentration. A limit arises from the 2D-3D growth mode transition. Dilute-nitride experimental lasers emitting up to $1.55 \mu\text{m}$ were successfully fabricated, but to the best of our knowledge, commercial devices were only demonstrated up to $1.3 \mu\text{m}$ wavelength.

Solar cells applications employ micron-scale layers. Internal strain fields must be avoided as these eventually lead to plastic relaxation that dramatically affects the transport properties. Strain-free layers are therefore required. The chemical composition of InGaAsN layers for solar cells applications is thus limited to a specific relation between In and N concentrations, close to $(x_{\text{In}} = 3x_{\text{N}})$.

A more complete overview of the applications of dilute nitride alloys can be found in Subsection 1.5.2.

2.2.3 Experimental determination of the N content

The N content of thick layers can be characterized by several methods. Direct measurement by SIMS is one of the most reliable ones [23], which however requires a good calibration. The most common method is the analysis of the X-ray diffraction rocking curves, able to discriminate changes in the lattice parameter. The crystal distortion can be related to the N content assuming a Vegard law between the lattice parameters of the zinc blende phases of GaAs and GaN. Moreover, this technique is able to reveal the existence of phases or precipitates [23]. If the X-ray diffraction can also be used to characterize QW superlattices, individual QWs are difficult to characterize with these 2 methods due to the small layer thickness.

The PL spectroscopy can also be used to determine the N content. However, if the BAC model is well established for bandgap calculations, the values of the crucial coupling strength C_{MN} tend to vary in publications. Also, changes in local atomic configuration can generate changes of 100 meV in the emission energy with the same N concentration, as evidenced by the annealing process. Moreover, for thin QWs and QWRs, the growth process is likely to alter the calibrated growth rate and the In concentration determined under N-free conditions. For these reasons, in this work we generally display the N-induced redshift instead of estimates of

the N concentration.

2.2.4 Sb incorporation for material improvement of long-wavelength material

If 1.3 μm emitting InGaAsN laser were quickly realized using both MBE [250, 33, 251] and MOVPE [252] techniques, the realization of 1.5 μm InGaAsN lasers proved much more difficult. In this field essentially dominated by MBE, defects come together with the increased N content: ion damage [253, 254], non-radiative traps [199, 38] and phase separation [237, 238]. If these difficulties do not entirely prevent 1.5 μm GaInAsN lasing [192, 255, 256, 198], it became apparent that other trails should be explored.

Material improvements and a further bandgap redshift of InGaAsN alloys can be achieved by the addition of Antimony, a group-V compound with reactive surfactant properties. Sb was reported to improve the optical quality and lower the lasing threshold [257, 258]. The improvement is achieved by the limitation of the surface group-III surface diffusion length, thus improving the composition uniformity by limiting the phase segregation and roughening [259, 260]. The bandgap energy is also further lowered, essentially by changes in the valence band. Quaternary and quinary alloys are practically difficult to handle because of the high sensitivity to composition miscalibrations. Achieving controllable and reproducible material optical properties is an issue by itself. Nevertheless, the InGaAsSb material is reported to behave satisfactorily when compared to other long-wavelength semiconductors [261, 262].

2.2.5 Hydrogenation

The post-growth atomic hydrogen irradiation is long known to passivate both shallow and deep defects incorporated during the growth of III/V materials [263, 264, 265]. This technique dramatically affects dilute nitrides alloys. The bandgap experiments a blueshift with increased hydrogen dose, to finally saturate at the value of a corresponding reference sample grown without nitrogen [266]. This effect was observed in GaAsN [267, 268], InGaAsN [266, 269] and GaPN [270]. The electron effective mass is also modified upon hydrogenation, tending toward the corresponding N-free value [271, 182]. Comparable observations were also made on the gyromagnetic factor [184]. As a matter of fact, hydrogenated samples are sometimes presented in the literature as samples with lower effective N content [271, 184]. Due to its remarkable effects, the introduction of hydrogen in a sample is called passivation, and the full sample passivation is achieved when the PL energy corresponds to the N-free counterpart.

The hydrogen passivation technique is also reversible: a quite low temperature annealing (close to 300 °C) is sufficient to allow hydrogen diffusion out of the sample, thus restoring the initial properties of the sample.

The precise determination of hydrogen concentration by SIMS or other methods is strongly hindered by external contamination. The chemical sensitivity can be greatly enhanced by using another isotope, namely deuterium (D) instead of H (see Section 4.4). With an additional

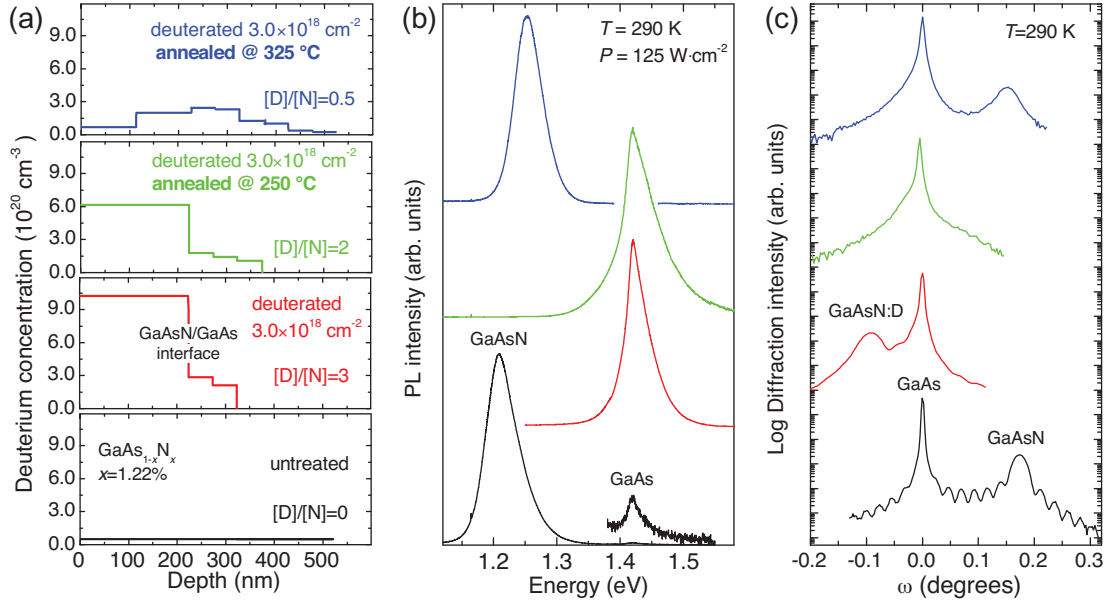


Figure 2.11: (a) Deuterium depth profile of GaAsN sample before (black), and after hydrogenation process that generates (N-2H)-H complexes (red). Successive annealings remove the third H (250°C , green), then the majority of H atoms (325°C , blue). (b) PL spectra of corresponding samples. (c) (004) X-ray diffraction rocking curves of the same samples, revealing changes in the lattice parameter. Graphs from [274].

neutron in the nucleus, the chemical properties of this element are essentially similar to H. A deuterated sample behaves identically to a hydrogenated one.

Hydrogenation compensates for the tensile strain induced by N, and even causes an additional compressive strain when the passivation is complete. This compressive strain is observed independently of the growth method (MBE, MOVPE), only depending on the initial nitrogen concentration [268, 272]. A more detailed study [273] later revealed that in usual hydrogenation conditions, 3 H atoms bind to every N, forming (N-2H)-H complexes (see Figure 2.12) causing the neutralization of N effects, the bandgap recovery and the compressive strain. The central N-2H complex is quite stable, and is responsible for the change in the electronic properties and for the strain cancellation. The third H is only lightly bounded and causes the additional compressive strain. A light 250°C annealing can remove this atom, leaving a passivated material almost with the same strain level as the N-free counterpart, that contains only N-2H complexes [274]. This scenario is illustrated on Figure 2.11(a)-(c). A GaAsN was deuterated and then subjected to a first annealing at 250°C , and later to a final annealing at 325°C . Between each processing step the sample was characterized. Figure 2.11 shows (a) the hydrogen concentration determined according to Ref. [273], (b) the PL emission and (c) the X-ray rocking curve, of the sample after each processing step.

The local conformation of the N-2H complex remained unclear for some time while contradictory information was gathered [271, 275, 276, 277]. According to latest results [278], the

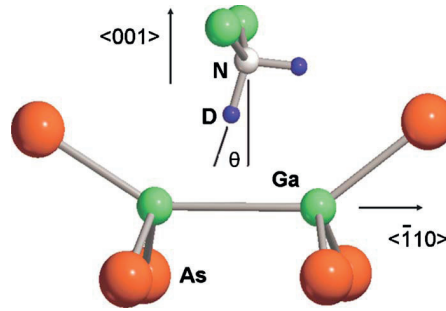


Figure 2.12: Illustration of the conformation of the relaxed N-2H complex responsible for N passivation. Graph from [278].

complex is canted with a C_{1h} symmetry, as represented in Figure 2.12.

A potentially useful aspect of hydrogen passivation is the evolution of the H forefront during the irradiation process. The material close to the surface becomes quickly saturated with hydrogen as every N atom is surrounded by 3 H. Then H freely diffuses through the passivated material, pushing the hydrogenation front deeper in the layers [279]. The transition between H and H-free regions is abrupt: the D concentration falls by a factor 10 within 10 nm [274]. This opens the way to a post-growth lateral engineering of the bandgap. H-blocking metallic masks, or a direct H atoms removal by electron-beam “writing” allows tailoring the in-plane electronic confinement [280], with the advantages of site control, and of a very high degree of freedom in the design. As an example, the tuning of the strain-induced emission polarization was demonstrated, by isolating low-bandgap QW stripes [281]. More impressive, the hydrogenation interface is actually steep enough to allow lateral quantum confinement: the post-growth fabrication of site-controlled quantum dots has been reported [282]. The sample hydrogenation can also be selectively cancelled by means of laser-induced dissociation of the N-H complexes, allowing for direct writing of arbitrary patterns with sub-micron resolution [283]. A detailed review on the effect and potential applications of GaAsN hydrogenation can be found in Ref. [274].

2.2.6 The so-called 2-step growth

As detailed in Subsection 2.2.2.5, a local In-N anticorrelation is generated during the growth, and is frozen in the matrix if annealing is not performed. However, the incorporation of In also affects the N incorporation on a larger scale, with a marked reduction of N incorporation efficiency when increasing the In content (see Subsection 2.2.2.3). The primary cause of this dramatic decrease is In segregation, which generates a In-rich layer on top of the growing surface [203]. Several other explanations were additionally proposed to explain the larger-than-expected incorporation lowering. TEM-based measurements revealed a large-scale In-N anticorrelation in MBE-grown QWs [284, 235, 213] : while the In profile looks like a rounded square, the N concentration is observed to be maximal close to the two interfaces. This anticorrelation is similar for the first and second interfaces. Similar measurements performed

on MOVPE grown layers were less conclusive, although the hypotheses of the model may hinder the accuracy of the reconstructed profiles [230].

Albo *et al.* reported the PL characterization of QWs grown with various thicknesses : counter-intuitively, the thinnest QW emitted at the lowest energy [285]. The N is mostly incorporated at the first (lower) interface, and the N concentration is considerably reduced in the upper region of the QWs, as SIMS measurements confirmed. This suggests that the N incorporation is governed by surface kinetics effects and strongly dependent on the local In gradient. Especially, N is strongly incorporated at the first interface, when the In-rich segregation layer is still not fully established. Later on, when the segregation regime is stable, N atoms are more likely to desorb before incorporation, and the resulting N concentration is lowered down. To counterbalance this mechanism and achieve a uniform N concentration throughout the QW thickness, the authors proposed a 2-step growth, where the N precursor flux is initially kept reduced for the first stage of the QW growth, when the In segregation layer is not fully established (a few monolayers). A DMHy flux corresponding to one eighth of its later value was proposed by the authors. This procedure led to the fabrication of QWs with enhanced quality [285].

2.3 Chapter summary

This chapter presents in some details the two themes central to this thesis work. First, the formation mechanism of the V-groove QWRs and QDs in pyramids is reviewed. The potential applications of these systems are limited by their emission wavelengths, constrained with usual materials in the range ca. 0.7 - 1 μm . The second part presents peculiar alloys, the dilute nitride GaAsN and InGaAsN, which enable to shift the operating wavelength of GaAs-based devices up to the technologically relevant 1.3 μm and 1.55 μm telecommunication windows of silica optical fibers. The central topic of this work is the fabrication of nanostructures grown on non-planar substrates with that latter alloy, aiming at reaching 1.3 μm -emission wavelength. After presenting in the next Chapter the experimental techniques involved in our work, the incorporation of nitrogen into our nanostructures is presented. The focus is initially set on the planar QWs in Chapter 4, and then shifts on the 1-D QWRs system in Chapter 5, to end up on the more complex 0-D QD nanostructures in Chapter 6.

3 Fabrication and characterization of nanostructures on patterned substrates

In the present Chapter we detail the fabrication process and the characterization methods that were used during our study. As most of the epitaxial growths were performed on patterned substrates, we first present sample pre-growth processing methods, and then detail the metalorganic vapor phase epitaxy (MOVPE) growth process, as well as some technical details relative to the incorporation of nitrogen in our nanostructures. Later on, we present the methods of sample characterization. The focus will first be set on the micro-photoluminescence (μ PL) setup that we assembled to characterize the optical properties of our long-wavelength emitting structures. We also briefly describe the several other experimental techniques used in this work: scanning electron microscopy (SEM), transmission electron microscopy (TEM), atomic force microscopy (AFM) and secondary ion mass spectroscopy (SIMS).

3.1 Substrate patterning

The fabrication of QWR in V-grooves and that of QDs in inverted pyramidal recesses requires patterning the GaAs substrates before growth. This is performed by selective chemical wet etching revealing $\{111\}$ A crystallographic facets through the apertures of a mask. V-grooves naturally form under etching through apertures on (100)-oriented substrates (see Figure 3.1), and tetragonal pyramids on apertures made on (111)B-oriented substrates (see Figure 3.2). The fabrication of V-groove QWR samples is the simplest, requiring a single cycle of e-beam writing and etching. The QD samples were prepared following a more elaborated recipe involving three processing cycles: “big” pyramids, alignment marks and “small” pyramids were successively etched, as shown on Figure 3.2. In the following, we first describe the individual steps of a processing cycle, and then detail the different cycles of a QD sample patterning.

The patterning procedure of a V-groove template is as follow. First, a rigid SiO_2 layer and a spun electron beam resist (polymethylmethacrylate, PMMA) are deposited on the (100) GaAs wafer. The resist is written by Dr. B. Dwir using a Vistec EBPG5000 electron beam, with proximity effect correction in order to improve the uniformity. After development, the mask is

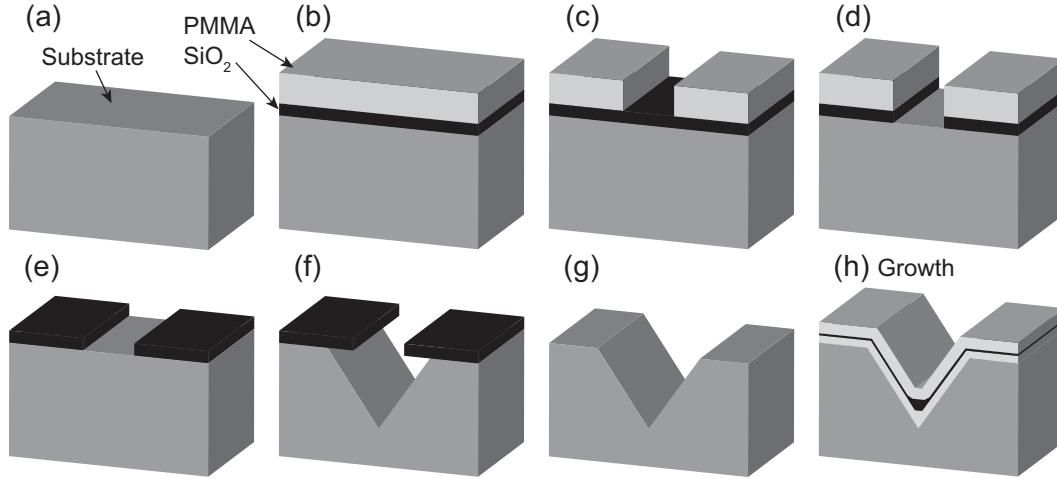


Figure 3.1: Cartoons of the typical processing steps leading to the fabrication of a V-groove QWR. (a) Initial wafer. (b) Deposition of SiO₂ and PMMA. (c) Electron beam patterning and resist development. (d) RIE mask transfer. (e) PMMA removal. (f) Recess wet etching. (g) Sample cleaning. (h) MOVPE growth.

transferred to the SiO₂ layer using a dry CHF₃/Ar reactive ion etching (RIE), and the resist is removed by acetone ultrasound bath and oxygen plasma. The etching of the recess is preceded by a short Ar plasma RIE attack. The grooves are wet-etched using a HBr:Br:methanol solution, that reveals the {111}A dense planes. The presence of HBr in the solution leads to a slow attack of the {111}A facets, producing recesses larger and smoother than the apertures in the oxide mask, in order to improve the QWR uniformity. The etching time must be carefully calibrated, since heavily depending on the substrate miscut angle, actual temperature, and recess size and pitch. A 2-step HF etching is finally used to remove the remaining SiO₂ and the native oxide prior to growth. This processing cycle is summarized on Figure 3.1, and some technical details can be found in Table C.1 in Appendix C.

The substrate patterning of pyramidal recesses for QD growth is similar. The wafers used are (111)B GaAs wafers in order to benefit from the crystallography in the etching and growth steps. The etching solution for the pyramid fabrication is Br:Methanol, which provides an extremely slow etching rate of the {111}A planes. The recess size and uniformity is thus determined by the quality of the mask apertures. An overshoot in attack time results in a small, but uncontrolled etching under the mask. This limits the uniformity of pyramid on samples with different pyramid sizes.

The growth rate is dramatically enhanced in the pyramids as compared to a reference (100) surface, because the growth is concentrated in the pyramids, excluding the neighboring (111)B surfaces (see next Section). A large growth rate limits the uniformity of QD arrays, hinders the control of the QD electronic properties and causes the so-called “closing” of the pyramid, i.e. a non-conformal deposition concentrated in the periphery of the recess. In order to slow down the growth rate, the QD fields were surrounded by regions patterned with large pyramids

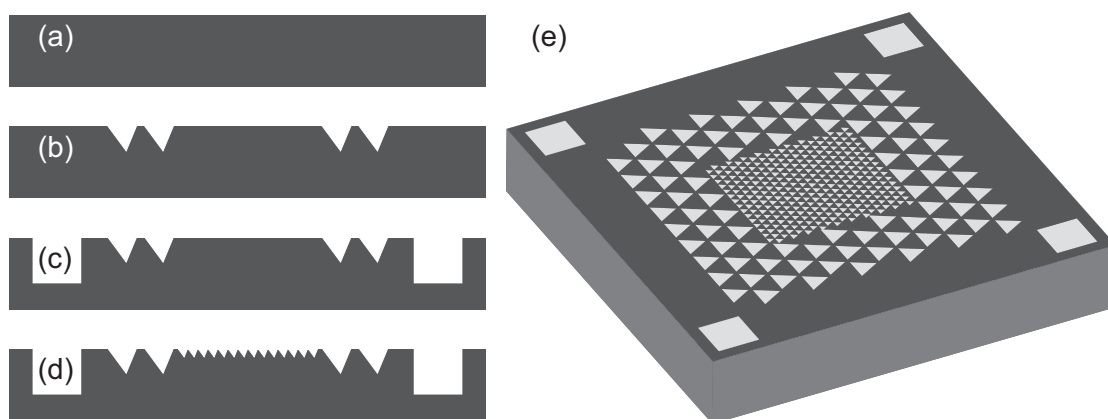


Figure 3.2: Cross-section representation of the successive processing cycles, prior to growth. (a) Initial wafer. (b) Big pyramid etching. (c) Alignment marks. (d) Small pyramids etching. (e) Perspective view of the (simplified) overall design.

($\sim 10\mu\text{m}$), as shown on Figure 3.2(e). The large pyramids introduce exposed $\{111\}\text{A}$ surfaces on which material grows and thus removes precursors from the small pyramids. These big pyramids were processed prior to the ones of interest, using the same procedure (except for a more concentrated Br:Methanol etching solution).

When post-growth processing was required (e.g., QD isolation), alignments marks were also engraved in the wafer. The writing of the alignment marks is best performed after the big pyramids etching, in order to prevent the degradation of the marks during the big pyramid etching. The processing is quite similar, with the following modifications. Thicker SiO_2 and PMMA layers were used, and the mask transfer etching time was adapted accordingly. The marks were dry-etched by means of a BCl_3/N_2 inductively coupled plasma (ICP) etching. The marks consist in several patterns of square recesses (which are simplified on Figure 3.2 to a single square) flat-bottom recesses.

The presence of alignment marks on the samples allows efficient positioning of various types of post-growth structures (for example mesas), with accuracy down to 20 nm. The mesas processing was performed after growth, using a procedure identical to that employed for the alignment marks.

3.2 MOVPE growth procedure

The MOVPE technique is one of the most popular epitaxy methods for fabricating semiconductor heterostructures. In this epitaxial growth method, the sample is maintained at high temperature in a reactor, in which a flux of gas is flowing. Most of the gas is inert, nitrogen in our case, and carries a variable flux of precursor gases. Due to the high temperature, the precursor gas molecules are cracked when arriving close to the substrate surface. The cracking proceeds in successive steps, initially in gaseous phase and finally physical adsorption on the substrate surface. The chemical nature of the surface affects the decomposition rate of

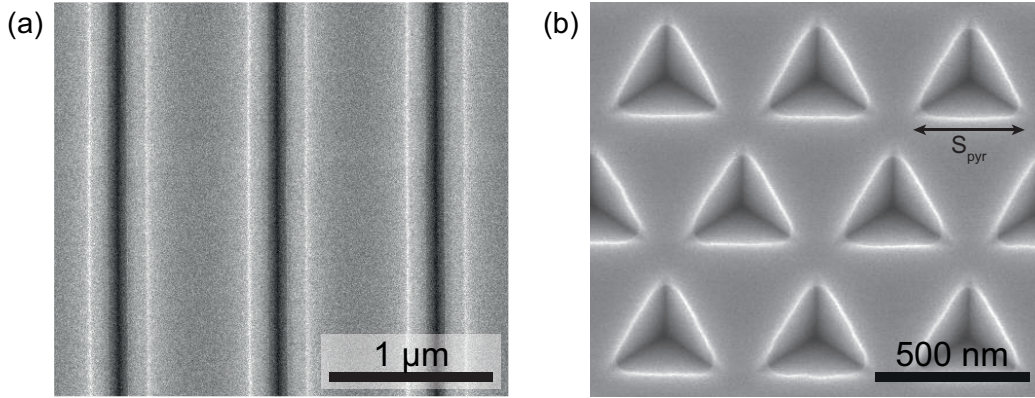


Figure 3.3: (a) Top-view SEM image of 1 μm pitch V-grooves before the removal of the oxide mask. The grooves are significantly wider (350 nm) than the oxide aperture (~ 120 nm). (b) Top-view SEM image of an array of tetragonal pyramids before oxide removal. Almost no etching is visible under the mask, except at the corners.

the precursors: for example almost no precursors decomposition occurs on the inert (111)B GaAs surfaces. The Ga, In, As and N atoms released and adsorbed diffuse on the surface over some distance before being incorporated, a distance called the adatom diffusion length. For material quality reasons, the growth rate is controlled by the flux of group-III precursors, and a large excess of group-V As atoms is maintained in the reactor. In this work, we quantify the arsine excess by the As/III ratio of the precursors partial pressures in the reactor. The partial pressure of the gas source arsine is deduced from the dilution of the initial gas flux. Liquid precursors (e.g. TMGa, TMIIn, DMHy) are stored in a bubbler in which a carrier gas is flowing. The partial pressure is calculated from the vapor pressure at the liquid temperature, the flux of carrier gas in the bubbler and its dilution. The usual V/III notation is avoided in order to avoid confusion with nitrogen, another group-V specie. The incorporation of N requires specific MOVPE conditions, reviewed in Subsection Subsection 2.2.2.

The depositions were performed in a horizontal Aixtron reactor, using low pressure (20 mbar) N_2 as carrier gas. We used arsine and unsymmetrical dimethylhydrazine (DMHy) as group-V precursor, and trimethylindium (TMIIn) and trimethylgallium (TMGa) as group-III precursors. The growth procedure of our N-containing nanostructures was based on existing recipes, with some changes intended to ensure the proper incorporation of nitrogen in the matrix. The MOVPE reactor was operated by Prof. D. Fekete, Dr. A. Rudra and Dr. P. Gallo.

The growth process is described here, as well as at the start of Chapters 4, 5 and 6. The first step is the sample deoxidation, performed at 570°C , with little material deposition. The growth of the GaAs buffer (or inferior cladding) takes place at 590°C , a temperature suitable for the growth of both GaAs and InGaAs alloys. The As/III ratio is kept high, as this gives the best quality samples (for QWRs: 100, for QDs: 2600). However, the optimal temperature window for the InGaAsN growth is widely recognized to be close to the 520°C range. Before the deposition of the active layer, the reactor is cooled down and the growth is interrupted for ~ 7 min to

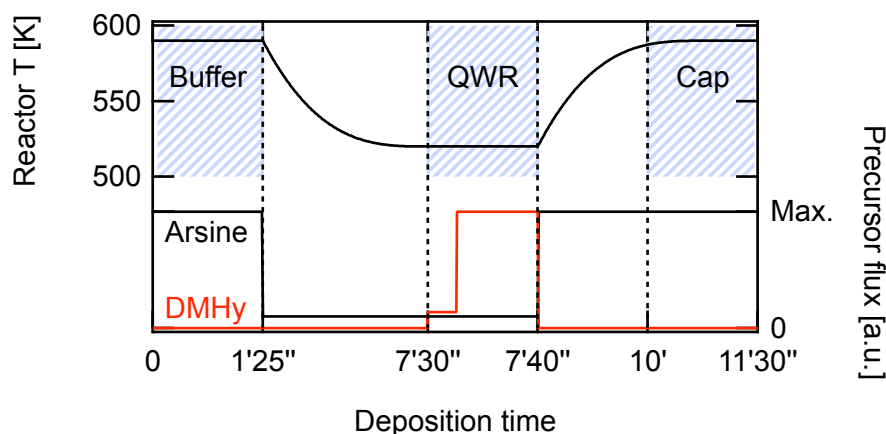


Figure 3.4: Schematics of the growth procedure used for the N-containing V-groove QWRs. The temperature (left) and the arsine and DMHy fluxes (right) are shown as functions of time. The growth periods are indicated in dashed blue lines. The time scale is not uniform.

ensure the proper stabilization of the reactor temperature. This interruption tends to flatten the recess profile and the shape of the resulting nanostructure [98, 99]. TEM images revealed that the radius of curvature of our QWR remains acceptable, maybe thanks to the temperature decrease (see Section 5.1).

The active InGaAsN layer is then deposited, using the 2-step growth procedure proposed by Albo *et al.* [285]. The DMHy flux is kept low during the first few monolayers (ML) when the In segregation layer is not fully established, in order to avoid a large N incorporation at the first interface. The optimal thickness of this layer was evaluated by Prof. D. Fekete to be close to 1.5 nm, corresponding to ~ 5 ML. The QW was grown in two layers of 1.5 and 4.1 nm. On non-planar substrates, the effective thickness significantly exceeds the nominal value. If not specified otherwise, the thicknesses given in this work will be the nominal values calibrated on (100) GaAs reference substrate. The effective thicknesses will be given where known and appropriate. The QWR nominal thickness was typically $0.8 + 2.2 = 3$ nm, and the effective thickness was determined by TEM to be close to 10.5 nm, corresponding to a growth rate acceleration of ~ 3.5 . The nominal QD thickness was $0.1 + 0.4 = 0.5$ nm. One can guess that the effective QD thickness is close to ~ 5 nm, based on the pyramid size and pitch. The growth rate of the active layer was set higher than usual for similar InGaAs structures, in order to favor the N incorporation: 0.278 nm s^{-1} for the QWR, and 0.013 nm s^{-1} for the QD.

After the InGaAsN deposition, the growth is again interrupted for ~ 3 min to let the temperature rise and stabilize to 590°C . This may cause mass transport and a flattening of the QWR/QD. The N may also diffuse to the surface and be replaced by As atoms. In spite of these possibilities, the arsine flux was kept as high as for the GaAs growth during the second growth interruption. These effects remain less important than that of sample annealing, a common practice for dilute nitride alloys.

The two growth interruptions were slightly adapted in the QD deposition processes. The interruption durations were limited to 3, respectively 1 min in order to limit the surface

degradation and hinder the mass transport. Moreover, during the first interruption, the arsine flux was kept high during the first 2 minutes in order to protect and stabilize the surface. Only during the last minute the arsine flux was lowered down to the level of the subsequent InGaAsN deposition, in order to stabilize the concentration of the free As atoms on the surface ($\text{As/III}=50\text{-}250$).

All the temperatures given in this work are the thermocouple values. The actual temperatures are estimated to be $\sim 30^\circ\text{C}$ lower at 600°C , and $\sim 20^\circ\text{C}$ lower at 520°C . Therefore the actual growth temperature can be estimated as $\sim 560^\circ\text{C}$ for the GaAs, and $\sim 500^\circ\text{C}$ for the GaInAsN layers. This is lower than the optimal temperature window reported in the literature [200], but was found suitable after an optimization process performed by Prof. D. Fekete on N-containing QWs.

3.3 Photoluminescence measurements

Photoluminescence is a technique widely used to probe the electronic characteristics of semiconductor samples. In this technique, light is shone on the sample (usually a focused laser beam), with photon energy higher than the semiconductor bandgap. The photon absorption excites an electron from the valence band to a high-energy state of the band structure, generating an electron-hole pair. Quickly the electron and hole lose energy by phonons emission, and stabilize in some low-energy states (for example close to the band edges, or in the QW states). After some time characterized by the recombination lifetime, an electron-hole pair recombines by emitting a photon characteristic of the band structure of the sample considered. When the sample is cooled down with liquid helium, the carrier emission quite closely matches the low-energy electronic states. The emitted light is collected, wavelength-dispersed and analyzed to provide valuable insights into the electronic band structure of the sample.

3.3.1 Microphotoluminescence setup

In our case, microphotoluminescence (μPL) was used as a standard approach of optical characterization. In this variant, a laser beam is tightly focused on the sample surface by an objective lens, resulting in a μm -size excitation spot (the diffraction limits the spot size to $\sim 800\text{ nm}$, depending on the wavelength and numerical aperture of the objective lens). This size is comparable to the diffusion length of charge carriers; so individual radiative centers can be evidenced thanks to this technique. Individual QDs, or micron-sized QWR segments can be characterized in this way.

Several experimental setups were used in this work according to specific requirements, but all share a conception similar to that detailed on Figure 3.5. (a) First, a high-power laser beam is generated, possibly passing through spatial and/or spectral filters. (b) Neutral density filters attenuate the light down to the desired level before entering the microscope column. (c) The beam is focused on the sample surface by a 50x objective lens. The sample is usually placed

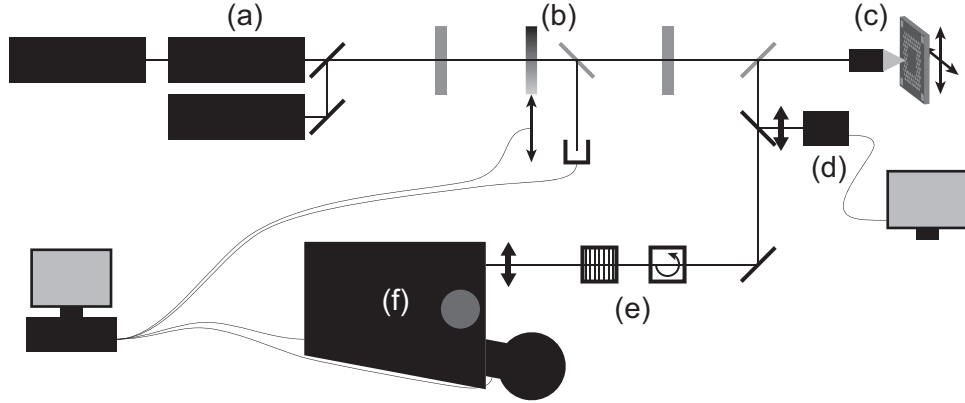


Figure 3.5: Schematic of the μ PL experiment used in this work. (a) Various laser sources could be inserted in the optical excitation path. (b) The excitation power is monitored and controlled by computer. (c) An objective lens focuses the laser beam on a sample mounted in a cryostat placed on a micrometric stage. The lens also collects the signal. (d) The sample surface is imaged thanks to a camera and a screen. (e) Various optical elements (here a polarization rotator and a polarizer) can be inserted in the detection path. (f) The signal is dispersed by a 550mm-long spectrometer equipped with 3 gratings, and equipped with a nitrogen-cooled InGaAs array.

in a helium-flux cryostat mounted on translation stages. The same objective lens is used to collect the PL signal. A beamsplitter separates the outgoing signal from the incoming laser beam, and directs it to the detector. (d) The sample surface can be imaged thanks to a second beamsplitter, a light source and a camera. (e) According to the needs, filters or polarization optics could be placed on the detection optical path. (f) The signal is dispersed by a monochromator, and measured by a liquid-nitrogen cooled detector (Si charge-coupled device or InGaAs photodiode array).

3.3.2 Characteristics of the new setup

Samples emitting up to $1\ \mu\text{m}$ were mostly characterized in laboratories equipped with high performance Horiba silicon CCD detectors. In those cases, the laser sources were 532 nm YAG or tunable Ti:sapphire lasers operating in continuous wave (CW) mode. However, most of our dilute nitrides samples emit above the $\sim 1\ \mu\text{m}$ cut-off of Si detectors. Therefore we designed and assembled a new μ PL setup on an independent optical table, optimized for long-wavelength (1 - $1.6\ \mu\text{m}$) detection.

This new setup was designed to operate effectively over a large spectral range (sample emission ranging from 820 nm to $\sim 1.5\ \mu\text{m}$), with optimized signal collection. The detector is a liquid nitrogen cooled Horiba InGaAs linear array of 1024 pixels, sensitive up to $1.6\ \mu\text{m}$. The quantum efficiency is excellent down to 870 nm. The detector is mounted on a JobinYvon iHR 550 monochromator (550 mm focal length). To maximize the setup versatility, the spectrometer is equipped with three different gratings (300, 900 and 1200 l/mm).

Chapter 3. Fabrication and characterization of nanostructures on patterned substrates

Several laser sources were used according to the needs and issues. Most of the spectra were acquired using a CW Ti:sapphire laser set at 735 nm, or with a 650 nm laser diode. A solid-state 532 nm YVO and a 543 nm HeNe laser were also available. We systematically performed the optical pumping in the barriers.

A remote control of the excitation power was installed, by connecting to the computer an actuator moving a graded neutral density filter (4 orders of magnitude), as well as a photodiode for the feedback loop.

We choose the objective lens (long working distance Mitutoyo 50X) and the lens focusing the signal on the spectrometer slits as to optimize the 1 - 1.5 μm performance.

The cryostat is a He-flow Konti model, initially dedicated to low-temperature transmission measurements. New internal pieces were designed and fabricated to improve the configuration in top-view geometry. In spite of our efforts, large samples ($> 1\text{ cm}$) exhibited an effective temperature significantly higher than the nominal 10 K (between 20 K and 30 K, deduced from the high-energy tail of GaAs peak).

A special care was dedicated to the choice of the beamsplitter separating the signal from the excitation beam. It is difficult to design a beamsplitter that is polarization insensitive in the full spectral range of interest, together with a constant, and possibly high, transmission (or reflection) ratio. We found a satisfying workaround by using as a beamsplitter an optical-quality, slightly metalized glass plate with high transmission. The laser reflection on the back does not enter the objective lens. Placing a similar plate in cross-configuration in the detection path effectively compensates for the induced polarization anisotropy. The transmittance of the two successive plates remains fairly high. To assess this setup, we consistently characterized the emission polarization of samples placed with various orientations, and the variations observed were within the sample homogeneity.

The sample surface can be illuminated by injecting in the excitation path the light of a diode emitting at $\sim 850\text{ nm}$. The image is formed on a camera, after reflection of the detection path by a mirror (see Figure 3.5(d)). This mirror is flipped out of the path during measurements. Polarization-resolved measurements were performed using a linear polarizer and a polarization rotator. High performance, broadband polarizers are available on the market. A Fresnel rhombs Newport PR-950 was chosen to rotate the light polarization because of its superior broadband operating range. This type of device uses four successive total internal reflections with carefully adjusted angles to provide the polarization rotation, without modifying the output beam path. The specifications of the chosen model indicate a retardation angle ranging from 180.47° at 830 nm, to 179.07° at 1300 nm. To facilitate the measurements, the rotator was mounted on a customized computer-controlled rotation stage.

In order to facilitate the optical alignment of the setup, we aimed at placing the cryostat in and out of the μPL setup, without having to move any optical element. This was realized by mounting the cryostat on a metallic plate, which can be fixed at will on the translation stage casing. The cryostat is removed by simply releasing and sliding the plate. Also, the focus of the laser spot is achieved by adjusting the vertical position of the objective lens alone. This configuration minimizes the misalignment of the setup when manipulated.

An existing Labview software was adapted to control the μ PL setup by Dr. B. Dwir and the author of this work. This involved the coding of drivers dedicated to the control of the excitation power and polarization rotation, in addition to the interfacing of the existing software with the new hardware. The author later performed an important rewriting of the software. The communication protocols between the main software, the drivers and the hardware were standardized, and based on this the hardware handling by the main software was made generic and easily extendable. This will greatly facilitate future hardware implementations (automatic translation stage, laser wavelength control, etc.), by considerably minimizing the modifications required in the main program. In addition, if the software was transposed to the other optical laboratories, it would be possible to borrow and use hardware installed in other labs: 30 minutes would be largely sufficient link the main program with the copied driver.

Another software improvement, we proceeded with preprocessing of the InGaAs array output. A detector output should be ideally proportional to the incoming signal. However, some noise and artifacts always perturb the data precision. In the case of InGaAs arrays, two main contributions can be identified in addition to the signal. First, an offset (~ 1000 counts) is present independently of the measurement conditions. Second, random thermal charges are generated, forming the so-called dark current. Negligible in the case of Si CDD devices, it is close to 70 e^- per second in our InGaAs array, significantly different in each pixel. The dark current was observed to be linear with time for acquisitions up to 30 s: longer acquisitions were sliced in order to satisfy this condition. The signal preprocessing removed the two artifact contributions, by subtracting from the pixel value of each pixel the contributions of the offset and of dark current measured individually. However, the dark current tends to slightly vary on a timescale of hours, probably due to slight temperature changes: a final manual subtraction of the background was required (this could probably be automated). After these operations, the noise level of the InGaAs array becomes quite comparable to Si-CCD for short acquisition times (≤ 30 s).

Some data were acquired using an optical spectrum analyzer (OSA HP 86140), sensitive from 600 to 1700 nm and equipped with an optical fiber input. This device is actually intended for the characterization of laser diodes, and is not well suited for high-sensitivity μ PL experiments. The signal-to-noise is limiting factor: a notice will be displayed on spectra acquired with this detector.

3.3.3 Equivalent power density

The equivalent power density of a PL setup is obtained by dividing the incoming optical power by the spot area. The resolving power of the objective lens we used is $0.7\text{ }\mu\text{m}$. However, the imaging system and the laser beam quality were such that the spot is probably not diffraction-limited. The spot diameter is asserted smaller than $2.2\text{ }\mu\text{m}$ (upper bound given by a direct measurement of the spot image). But a major uncertainty to the effective spot diameter is the carrier diffusion prior to recombination, which is about a micron by comparing the

luminescence spot to that of the laser. Overall, the equivalent power density using 1(100) μW excitation power can be estimated to $\sim 100(10^4)\text{W cm}^{-2}$, if assuming an effective spot size of $2\mu\text{m}$.

3.3.4 Polarization-resolved measurements

Polarization-resolved measurements were conducted by rotating the signal polarization with a linear polarization rotator, before selecting the polarization of interest thanks to a fixed linear polarizer placed in front of the monochromator. In this configuration, the transmitted signal is always polarized in the same direction, and the measurement is not affected by the anisotropic response of the monochromator. The polarization anisotropy is characterized by a scalar number named degree of linear polarization (DOP), defined as follow:

$$DOP = \frac{I_{max} - I_{min}}{I_{max} + I_{min}},$$

with I_{min} and I_{max} the minimum and maximum of the signal intensity. This expression can be used as-it-is in the case of QWRs, where the polarization is constrained by the geometry. This analytical form is less adapted in the case of QD, where the preferential orientation depends on local random imperfections, and may change depending on the feature of interest. When characterizing such structures, the full dependence on the angle $I(E, \theta)$ was first measured. The DOP, the average amplitude A and the preferential orientation angle θ_0 were fitted for each pixel with the expression:

$$I(\theta) = \frac{1}{2} I_0 [1 + DOP \cos(2(\theta - \theta_0))]$$

For more details on the analysis of the polarization properties, see Section 6.4.

3.4 Scanning electron microscopy

The spatial resolution of a characterization technique is limited by the probe size. Optical microscopes are limited due to diffraction by the wavelength of visible photons, in the 400 - 700 nm range. Finer probes are to be used in order to observe nanometer-scale details. The scanning electron microscope (SEM) is a convenient and versatile tool, which benefits from the picometric de Broglie wavelength of electrons. We used a Jeol JSM 6710F, equipped with a 1 - 30 keV electron beam generated by field effect. Electron optics move the focused beam on the sample surface in a raster fashion: at each point a signal is collected, and assembled to produce an image. The electrons of the beam interact with the sample, experiencing multiple scattering and absorption processes. Various signals can be collected to form images: primary backscattered electrons, secondary electrons generated by inelastic processes, or high-energy electromagnetic waves (X-ray). We preferred the low-energy secondary electrons,

which provide the highest spatial resolution since generated within a few nanometers from the surface. The contrast primarily originates from the ease of electrons to escape from the sample, thus essentially depends from the topography (edges and slopes are especially enhanced). The signal also weakly depends on the chemical composition: Al- (easily) and In- (more difficult) containing layers can be differentiated from GaAs or InP. We routinely achieved a lateral resolution better than 5nm.

3.5 Transmission electron microscopy

The transmission electron microscope (TEM) represents a very powerful ensemble of techniques, which exploits electrons transmitted through a thin sample slice. Valuable information is obtained on the composition, crystallography, defects, strain etc. The penetration depth of an electron beam increases with its energy. In a typical TEM setup, a ~ 300 keV electron beam crosses a sub-micrometric sample slice, initiating rich physics involving absorption, elastic and inelastic scatterings, diffraction, secondary electron and X-rays emissions, etc. Various signals can be monitored to retrieve the information of interest.

To obtain the atomic resolution images presented in this work, the direct transmitted beam was selected (bright field mode) and was imaged. The contrast essentially originates from the chemical-dependent interactions of the beam with the sample.

If equipped with a detector of secondary electron, the setup can act as a SEM when the electron beam is focused and scanned on the sample surface. But the high beam energy is better exploited in this raster mode by using an X-ray dispersion detector. Electrons of the atom's deep shells are excited, and relax by emitting X-rays characteristic of the atom. This method delivers quantitative data on the spatial distribution of different chemical species. It is well suited for heavy atoms like Ga or In, whereas lighter atoms like N only provide a weak contrast.

3.6 Atomic Force Microscopy

The SEM technique is not able to discriminate individual atomic steps, and deep recesses may only be depicted as dark regions. A technique better suited for these targets is the atomic force microscopy (AFM). Here, a small solid-state tip mounted on an oscillating cantilever is scanned over the sample surface. The tip follows the relief thanks to an altitude feedback loop based on the deflection of the cantilever induced by Van der Waals forces (in the so-called non-contact mode). A topography map is obtained, with a lateral resolution of a few nm and vertical sensitivity in the picometer range, allowing observation of atomic steps on a crystal surface. Other signals can also be monitored: the information delivered by the amplitude and phase of the cantilever oscillation may be especially relevant when characterizing faceted, non-planar surfaces. The model of the AFM used in this work was PSIA XE-100.

3.7 Secondary Ion Mass Spectroscopy

The secondary ion mass spectroscopy (SIMS) is a technique delivering quantitative information on the chemical composition of materials. A focused primary ion beam bombards the sample, regularly eroding the surface. This process ejects secondary ions, initially incorporated into the material. A mass spectrometer monitors the fluxes of selected ejected ions, establishing the concentration profiles of several atomic species as functions of the erosion depth. This capability allowed us to track and/or quantify the amounts of In and N in our planar QWs.

Part of the SIMS measurements was performed on a TOFSIMS5 from Ion-TOF GmbH, at the Technion Institute of Technology (Israel). A 500 eV Cs^+ sputter beam was used, sequentially with an analysis ion beam offering a better yield of secondary ions. The mass spectrometer can monitor either positively or negatively charged ions, with a resolution depth of ~ 1 nm close to the surface. The analysis beam was 25 keV Bi_1^+ when in negative mode, and 25 keV Bi_3^+ when in positive mode. More details on the SIMS technique can be found in the literature, for example in Ref. [286].

3.8 Chapter summary

This chapter summarizes the different fabrication and characterization methods used throughout this study. The two aspects of the sample fabrication are detailed: the substrate patterning performed in clean-room environment, and the epitaxial growth by the MOVPE technique presented with some details on the deposition processes. The capabilities and operation mode of various characterization techniques was also presented, namely: photoluminescence, secondary and transmission electron microscopy, atomic force microscopy and secondary ion mass spectroscopy. Special attention was dedicated to the presentation of the μPL setup that we designed and realized, and was the primary characterization tool of this study. The experimental results obtained thanks to these different techniques are presented in the next chapters.

4 2D-nanostructures: dilute nitrides quantum wells

The quantum well (QW) heterostructure is one of the simplest semiconductor nanostructures, yet at the basis of numerous applications and devices. In these nanostructures the electricity-light conversion is especially facilitated thanks to the increased oscillator strength in confined structures. A major market for light sources is telecommunication infrastructures for which the most relevant wavelengths lie in the 1.3 and 1.55 μm optical fiber windows [287, 133]. If III-V materials like InP present good performances in that spectral region, GaAs-based materials offer some comparative advantages like the better features of the distributed Bragg reflectors (DBRs) for vertical cavity surface emitting laser (VCSEL) applications [288, 31], or the higher electron confinement that may improve the high temperature device performances. In this context, in the nineties [27, 28] was discovered the huge bandgap shrinkage of GaAsN alloys incorporating nitrogen at percentage-levels. Dilute nitrides were then seen as a very promising new material for telecommunication and other long wavelength devices. This class of materials also presents an extremely strong electron confinement, opening possibilities in the use of intersubbands transitions [289, 290, 291]. In the next two decades an intense research activity was conducted to determine the best growth methods and conditions of this system. The optimization proved itself not straightforward, as summarized in Section 2.2. The MBE technique is generally preferred as it allows for a larger N incorporation, an improved material quality and a lower residual background doping level. However, MOVPE-based layers are also technologically relevant up to 1.3 μm and can be used in devices like lasers or photodetectors [287, 292].

Another major interest in the MOVPE technology is its capability of fabrication of high quality quantum dots (QD) and quantum wire (QWR) ordered nanostructures, which offer scalability together with an impressive simultaneous control in energy, uniformity and formation site [109, 4, 113]. However the emission energy range of these non-relaxed GaAs-based nanostructures is limited, and an extension toward long wavelength would open many perspectives to this technology. The growth of these nanostructures proceeds essentially like regular QWs, although affected by a combination of growth rate anisotropy and nano-capillarity. Therefore, the study of nitrogen incorporation in QW is a first step toward the main goal of this thesis,

being the fabrication of QWRs and QDs nanostructures emitting at long wavelengths. Some detailed reviews are available on the MOVPE growth of dilute nitrides on planar substrates [293, 200, 191, 208, 203]. Here a special focus will be set on the influence of the substrate misorientation, often neglected in growth studies but of crucial importance for the growth on non-planar substrates. A study lead by Prof. D. Fekete [294] for which the author of this work contributed to the data analysis and redaction of the manuscript, already details some aspects of this thematic. The present chapter intends to deliver an original contribution to the study of N incorporation in InGaAs QW grown on vicinal (100) surfaces. The MOVPE growth were performed by Prof. D. Fekete and Dr. A. Rudra. The data analysis is entirely the contribution of the author, as are the measurements unless specified otherwise. The samples are characterized by means of PL, AFM and SIMS techniques, and the combination of the resulting information reveals precious insights into the internal QW structures and elemental distributions.

4.1 Dilute nitrides QW on misoriented substrates: growth procedure

In the perspective of producing non-planar nanostructures emitting at long wavelengths, we choose to specifically study the influence of the substrate misorientation on the N incorporation. Samples were characterized by means of PL, AFM and SIMS techniques, which results were combined to analyze in detail the influence of substrate misorientation on the nitrogen incorporation in InGaAsN QWs. Different wafers miscut angles relatively to (100) were systematically explored, yielding the two natural crystallographic directions corresponding to two types of atomic steps: samples series displaying miscuts toward [110] (A direction) and $[1\bar{1}0]$ axis (B direction). By convention, in the following a sample named as $+2^\circ\text{A}$ is a (001) sample misoriented by 2° in the [110] direction, and $+5^\circ\text{B}$ refers to a (001) sample misoriented by 5° in the $[1\bar{1}0]$ direction. Growth runs involved 4 wafer quarters placed side by side in the reactor. The growth runs were shortly separated in time. A quarter misoriented by $+2^\circ\text{A}$ was systematically placed in the reactor as a reference to ensure reproducibility. All growth runs were conducted on semi-insulating substrates.

The sample design consists in a double QW structure with a N-free reference QW together with the N-containing layer. This combination allows the simultaneous spectral characterization of the 2 QWs as the emission energies are well separated. The N-containing QW is deposited last, to avoid the incorporation of defects that could propagate upon growth to subsequent QWs. The 2-step growth procedure of the N-containing QW was first introduced by Albo *et al.* [285] and is described more in-depth in Section 3.2. First, a thick (~ 235 nm) GaAs buffer is grown at 590°C . After a growth interruption to decrease the temperature down to 520°C , the 5.6 nm-thick $\text{In}_{0.25}\text{Ga}_{0.75}\text{As}$ reference QW is deposited and the temperature is brought back to 590°C . During this process the arsine flux is kept high ($\text{As}/\text{III} = 100$ when relevant) to ensure a high crystal quality and limit the adsorption of defects. A ~ 60 nm GaAs layer is then deposited before interrupting again the growth to lower the reactor temperature. The

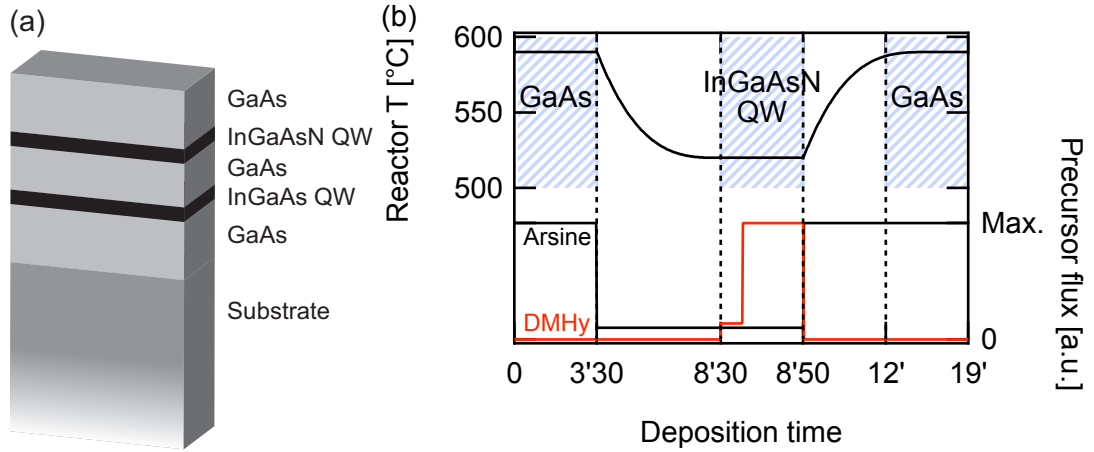


Figure 4.1: (a) Cartoon of the double QW design. (b) Schematics of the 2-step growth procedure used for the upper InGaAsN QW deposition. Are depicted the reactor temperature (left scale) and DMHy and arsine precursor flux (right scale). The horizontal time axis is not uniform.

$\text{In}_{0.25}\text{Ga}_{0.75}\text{AsN}$ QW is deposited using the 2-step growth method intended to prevent the N accumulation at the first growth interface. The InGaAsN is deposited in 2 successive layers: 1.5 nm with moderate DMHy flux (26 ccm) followed by 4.1 nm with higher flux (190 ccm). The As/III=8 ratio is kept low during the N-containing QW deposition, and a similar arsine flux is used during the last minutes of the preceding growth interruption. The temperature is finally increased to 590 °C to deposit a ~ 120 nm GaAs cap. This epitaxial sequence is summarized in Table C.2 in Appendix C, and the different growth runs are listed on Table C.3.

The deposition rate and In composition of the layers grown at the 520 °C reactor temperature were independently calibrated to take into account the changes in the incorporation efficiency. The reactor temperatures mentioned in this work are nominal, known from previous experiments to be overestimated by ~ 30 °C at 600 °C. The real InGaAsN growth temperature is therefore closer to 500 °C than the nominal 520 °C. Such value lies in the lower range of the optimal temperature window published in the literature [200].

4.2 Photoluminescence spectroscopy

While most of the MOVPE growth parameters are discussed at length in several publications [200, 293, 191, 208, 203], the characteristics of growth on substrates with miscut angle is barely discussed. This parameter is crucial as it determines the QW growth template roughness. For example, it has been shown that the emission linewidth of GaAs/AlGaAs QWs is dramatically improved when the substrate misorientation angle lies in the 0.2-0.3° window, as the most regular step flow order is obtained with such substrate misorientations [295, 296].

The samples were primarily characterized by micro-photoluminescence spectroscopy (μPL), at liquid nitrogen temperature ($T=77\text{ K}$) in order to partly get free of the influence of defects

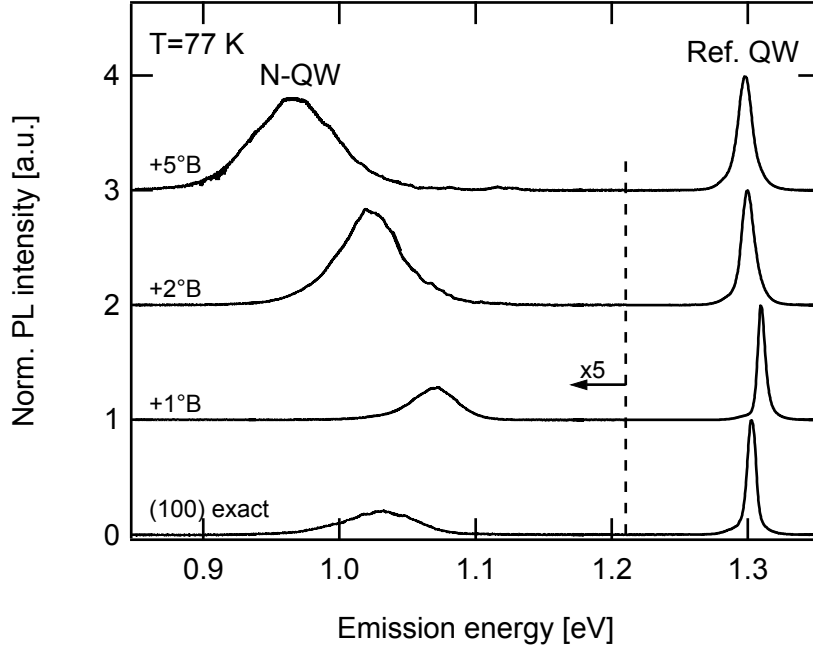


Figure 4.2: Typical μ PL spectra of the double QW structure studied in this work, for identical growths performed on substrates with 4 different miscut angles ($P_{\text{exc}}=30\mu\text{W}$). The spectra were normalized to the reference InGaAs QW intensity, and for clarity the intensity of the N-containing QW was increased 5-fold. The N incorporation is significantly affected by the substrate misorientation.

on the luminescence spectrum. The excitation was performed at a photon energy above the barriers, using a 532 nm wavelength laser. If most spectra were obtained on a μ PL setup using an InGaAs detector array mounted on an iHR550 spectrometer, many earlier data were acquired using a less sensitive HP 86140 spectrum analyzer, or on a macro-PL setup equipped with a Ge photodiode. Typical μ PL spectra of samples with various substrate misorientations are shown on Figure 4.2. It can be seen that the N incorporation is strongly affected by the substrate misorientation. At small miscut angles, the N-induced redshift is lowered (+1°B sample), but the trend is then reversed at higher angles (+2°B and +5°B). The reference InGaAs QW is only marginally affected by the substrate misorientation, with a small redshift of the emission coupled with a progressive broadening of the linewidth. These modifications are discussed in the following sections.

4.2.1 Reference InGaAs quantum well

The emission energy of the reference N-free QW is shown on Figure 4.3 as a function of the substrate misorientation. Substrates probed had miscuts toward both A (red circles) and B (black crosses) directions. The samples were grown in groups of 4, growth runs shortly separated in time, with an additional +2°A oriented sample always present as a reference. Error bars displayed correspond to the emission energy spread of samples of different growth

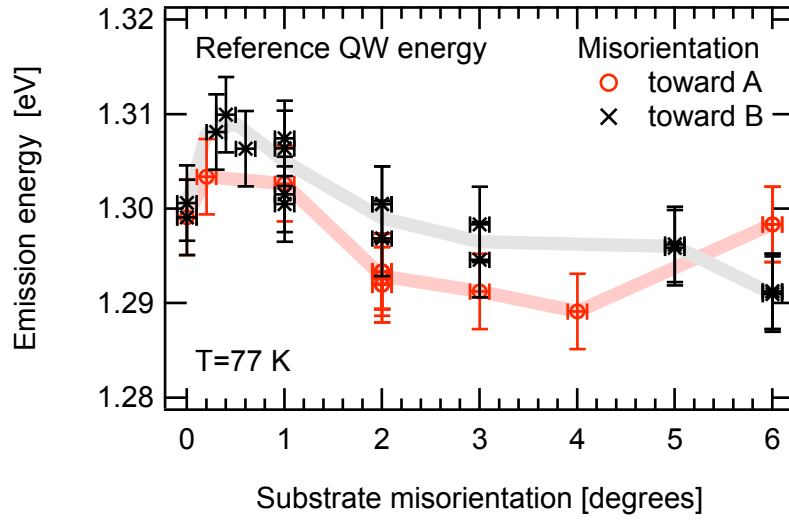


Figure 4.3: μ PL emission energy of the reference InGaAs QW as function of the substrate misorientation, for substrate miscut toward A (red circles) and B (black crosses) directions ($P_{\text{exc}}=100\mu\text{W}$). The QW energy is only marginally shifted in spite of the large substrate miscut angles involved.

runs. The highest emission energy is observed close to a half-degree substrate misorientation. Increasing the sample miscut angle progressively lowers the emission energy. The energy differences observed can be translated into QW thickness variations of only ± 1 -2 monolayers. The trends are approximately similar on A and B type misorientations, although the A-type samples generally exhibit lower emission energies than the B counterparts.

Figure 4.4(a) reports the reference QW emission FWHM as a function of the substrate misorientation in the B direction. The narrowest emissions are observed in the 0.3 - 0.4° B window, with FWHM below 5 meV. This is comparable to state-of-the-art QWs of similar thicknesses. With our growth conditions, we observe a significant emission narrowing of InGaAs QWs when using slightly misoriented substrates, similarly to what was observed in the AlGaAs/GaAs system [296]. At higher miscut angles, the emission is broadened above 12 meV, signature of a degraded QW structural quality. The emission linewidth of samples misoriented toward the A direction was to be observed significantly broader (up to 10 meV larger than the B counterpart).

The emission broadening and the evolution of the emission energy can be explained by the evolution of the QW interfaces roughness, characterized by AFM, as shown in Section 4.3. The smoother interfaces are found on slightly misoriented substrates, where the step flow regulates the large-scale surface corrugations. The (100) exact surface presents monoatomic steps but exhibits some long-range disorder, leading to a slight broadening of the emission. The stacking of multiple atomic steps on strongly misoriented surfaces generates large local variations (step bunches) of the QW thickness: the resulting emission is broadened and redshifted as carriers tend to recombine in the QW thickest regions. A direct confirmation of this mechanism could

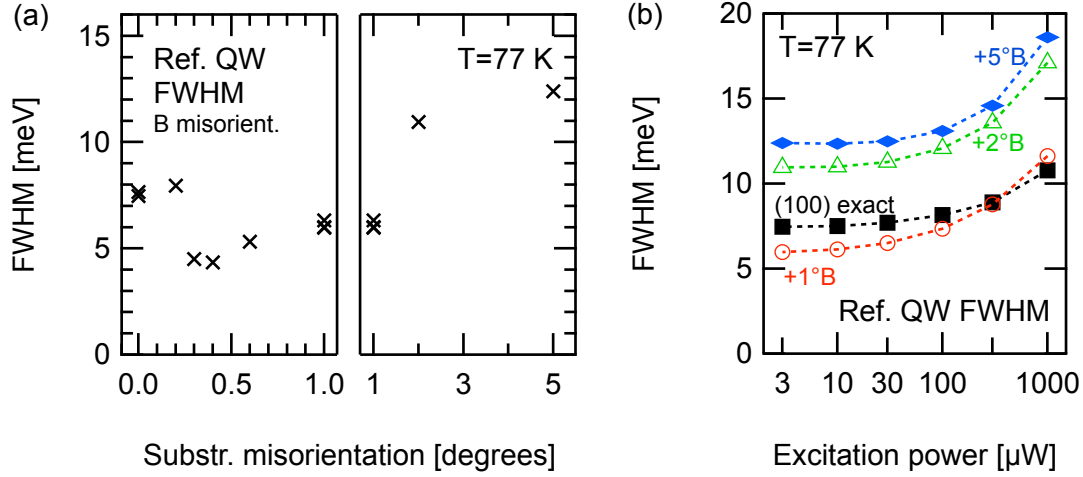


Figure 4.4: (a) μ PL emission FWHM of reference InGaAs QWs as function of the substrate miscut angle ($P_{\text{exc}}=3 \mu\text{W}$), separated in two panels in order to clearly depict small and large miscut angles. The lowest linewidths are observed close to $+0.4^\circ\text{B}$ substrate miscut. (b) μ PL emission FWHM of InGaAs QWs as a function of excitation power, for samples grown on exact-(100), and on $+1^\circ\text{B}$, $+2^\circ\text{B}$ and $+5^\circ\text{B}$ misoriented substrates. The FWHM of the N-free QWs evolves like for the regular QWs.

be brought by the measurement of the Stokes shift by combining PL and PLE data.

The emission FWHM of a few selected samples is detailed on Figure 4.4(b) as function of the excitation power. As expected, the FWHM only start to enlarge above a certain power level, signature of the saturation of the states of lower energy and subsequent filling of higher energy states. By opposition, the N-containing QWs will not behave according to this simple description, as will be shown on Figure 4.6. As mentioned in the previous chapter (3.3), the equivalent power density to $3 \mu\text{W}$ can be estimated to $\sim 100 \text{ W cm}^{-2}$ if assuming a spot size of $2 \mu\text{m}$ (taking into account the significant carrier diffusion),

An effective In content was extracted from the reference QW emission energy assuming a 5.6 nm QW thickness, using a model of parameters taken from the literature [140, 158]. This model calculates the first solution of the finite square potential well problem for electrons, heavy and light holes, with well depths determined by the alloy composition and affected by the uniaxial strain field in the case of holes states. N-containing alloys are reproduced in the model by introducing several modifications. The well depth for electrons is increased according to a band anti-crossing calculation (see Ref. [158] or Subsection 2.2.1), the electron (and holes) effective mass is modified according to the In and N fractions, and the holes states are slightly affected via the change in the strain field, following the procedure suggested in the references cited above ([140, 158]). At least the parameterization of the electron effective mass is debatable ($\sim 0.11 m_0$ in $\text{GaAs}_{0.98}\text{N}_{0.02}$), and could be chosen more appropriately according to more recent results [180, 182]. The effective In content deduced from the model is slightly higher than the nominal value ($\sim 27\%$ versus 25%), reflecting either a slight miscalibration of

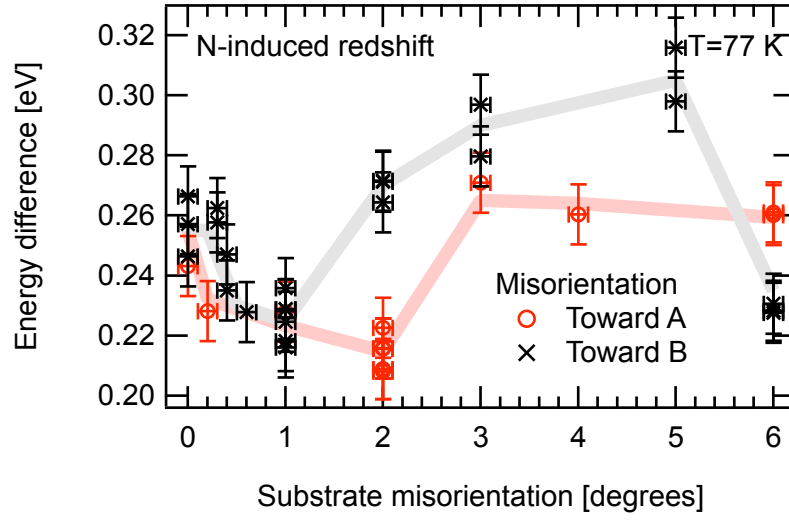


Figure 4.5: Emission energy difference between the reference InGaAs and the N-containing QWs ($P_{\text{exc}}=100\text{ }\mu\text{W}$). The N-induced redshift is strongly influenced by the misorientation, similarly but not identically in A and B misorientations. Several regimes can be identified, where the redshift is successively reduced (up to 1-2° miscuts), then increased (1-5°) and finally decreased again (>5°).

the MOVPE growth settings, or a deviation of the QW potential shape from the ideal, square profile.

4.2.2 N-containing quantum wells

The substrate misorientation affects the N-containing QW to a much larger extent than the N-free reference QW. The Figure 4.5 displays the difference in the emission energies of the InGaAs reference and the N-containing QWs (hereafter labeled N-induced redshift) of the samples described in the previous subsection. These samples were grown under identical nominal reactor conditions and therefore should have the same N content. The redshift is large (> 200 meV), hinting at above-percent N concentration. Thanks to SIMS analysis (see Section 4.4), the In content of the N-QW is found to be similar to that of the InGaAs reference QW, implying that the redshift is caused by N incorporated in the QW or in its immediate vicinity in the barriers.

The emission energy is strongly influenced by the substrate miscut angle, with $\sim 75\text{ meV}$ energy difference between the N-QWs grown on +1°B and +5°B misoriented substrates. 2 successive trends can be unambiguously identified. First the N-induced redshift is slightly reduced at low substrate miscut (up to 1-2°). Above a certain threshold (1-2°) the redshift is strongly enhanced. The N-induced redshift then slowly increases or stays similar up to +5°. Finally, extremely misoriented substrates like +6°B present a reduction of the redshift.

The μPL spectra of a few selected N-containing QWs are shown on Figure 4.6(a), measured

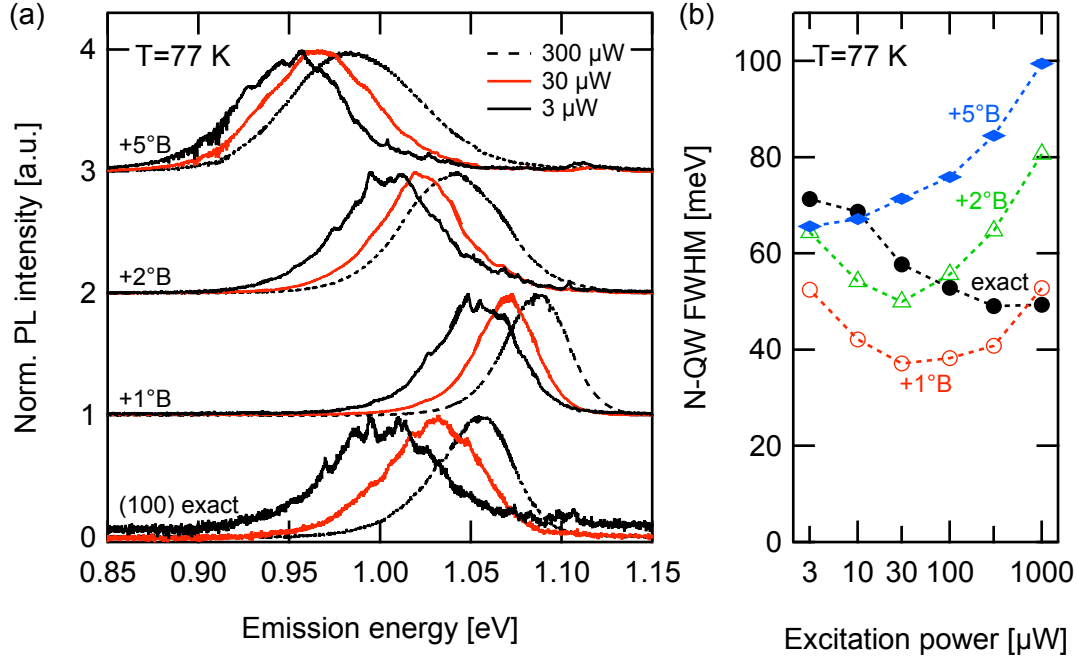


Figure 4.6: (a) Normalized μ PL spectra of 4 nominally identical N-containing QW grown on various substrate misorientations (exact, +1°B, +2°B, +5°B), using 3 excitation power levels (black, red, dashed black). (b) Emission FWHM of the N-containing QW shown in (a), as function of the excitation power. The evolution of the linewidths suggests a composite origin of the PL emission.

at various power levels. The N-QW emission exhibits a strong blueshift with increasing excitation power. The QW emission appears at first glance to be progressively shifted toward higher energies when the excitation power is increased. Some discrete spectral features can however be observed with unchanged energies. Thus, localized defects appear to have a major contribution to the low excitation power emission, and states with a wide distribution of energy coexist within the QW. With excitations above 100 μ W, the spectra develop an asymmetry at high energy, hinting at the filling of QW excited states.

The N-containing QW emission linewidth is displayed on Figure 4.6(b) as a function of the excitation power (as detailed in Chapter 3.3, 3 μ W can be estimated roughly equivalent to 100 W cm^{-2}). The FWHM appears oppositely correlated to the magnitude of the N-induced redshift: the +1°B sample with minimal redshift exhibits the narrowest emission, while the +5°B sample emission with the largest redshift is the broadest. The emission broadening can be consistently attributed to local potential inhomogeneities generated by the N incorporation in the QW. The FWHM evolution with excitation power differs from that of the InGaAs QW depicted in Figure 4.4(b). The minimal FWHM is observed at intermediate powers. The emission broadening at low power levels evidences the contribution of deep level defects to the QW emission. Those are the dominant contributions at low power, but become saturated and progressively negligible with respect to the QW global emission when the carrier density

is increased.

The power-dependent N-QW emission of a given sample was fitted with 2-Gaussian profiles with fixed peak energies as to tentatively reproduce the lineshapes of the QW and defects states, letting free the Gaussian widths and intensities. This fitting procedure was only poorly satisfying, indicating that the defect contribution originates from a whole distribution of states filling up progressively. By contrast, excellent fits were obtained by letting also free the 2 Gaussians central energies. Using such a fitting procedure, the central energies of the 2 Gaussian peaks were observed to shift in parallel to the blue when the excitation is increased. However, more valuable insights into the DOS of our QWR could be obtained by means of PLE or photoreflectance techniques.

The PL intensity of the N-containing QW is widely dependent on the observation conditions and on the history of illuminations of the probed location. Low power PL signals were observed to be improved by more than one order of magnitude after shining the sample with a high power beam of the same excitation wavelength (slightly higher than the maximal power shown on Figure 4.6(b)). This treatment notably decreases the activity of non-radiative traps for a few hours at least. The probed locations were therefore prepared before measurement using a certain illumination sequence so as to ensure the reproducibility of the observation conditions. As a general rule, the integrated intensity of the N-containing QW is quite comparable to that of the InGaAs reference, although the QW relative depths in the sample certainly affect the QW relative intensities. Remarkably, no clear correlation could be observed between the N-induced redshift and the relative PL intensities of the InGaAs and N-containing QWs. This is a very surprising observation, as the N-containing QW redshift is consistently attributed to the differences in N incorporation (correlation between linewidth and redshift, similar In amounts in the 2 QWs observed by SIMS in Section 4.4). This suggests that N is incorporated in larger concentration on misoriented substrates, but with no increase in the density of non-radiative recombination centers. Similar double-QW samples on wafers misoriented to the A direction were already characterized by Prof. D. Fekete and the author of this work [294]. The relative intensity ratios of the 2 QWs structure was monitored while varying the N content and substrate misorientation (toward the A direction). For a given substrate misorientation the relative intensity ratio was observed to regularly decrease when the N content is increased. For a given N content, the best PL intensities were obtained on misoriented substrates, which is consistent with the conclusion of this work.

The study of the PL emission of our double QW structures can be summarized as follow. Based on the emission FWHM, the linewidth of N-free InGaAs QWs is observed to be optimal in the 0.3-0.4°B substrate misorientation window, under our specific growth conditions. A large N incorporation can be obtained with our MOVPE system. The misorientation strongly affects the redshift of the N-containing QWs. The QW linewidth is correlated to the N-induced QW redshift. The PL intensity ratio of the 2 QWs is observed to be independent of the N-induced redshift, suggesting that the generation of non-radiative traps is not simply proportional to the N incorporation. Therefore, the use of misoriented substrates can help to simultaneously

optimize the N incorporation and the activity and/or concentration of non-radiative defects.

4.3 AFM interface characterization

A detailed knowledge of the growth template at the QW location is crucial to understand the strong influence of substrate misorientation on N incorporation. Actually, this interface can be reliably characterized by observing with AFM the GaAs cap surface immediately after growth. The sample surface is similar to the QWs lower interface as these GaAs layers were grown using the same conditions, and as the QWs were deposited after a growth interruption during which the reactor temperature was decreased. The QW lower interface is therefore very similar to the sample surface. The validity of this approach was already demonstrated in the case of GaAs/AlGaAs QW [296]. The surface of a series of QW samples was characterized by Dr. B. Dwir using a PSIA XE-100 AFM, within a few days after growth so as to limit the surface degradation. Representative topographic AFM images are shown on Figures 4.7(a)-(d), each representing a $500 \times 500 \text{ nm}^2$ region with the same color scale. The samples with a small miscut angle display a nice monoatomic step flow. However, the steps tend to stack to increasingly step bunches when increasing the misorientation. The multistep height evolution with substrate misorientation is shown on Figure 4.7(e), for miscuts toward A (red circles) and B (black crosses) directions. As a direct measurement of the step height proved difficult, we estimated the average number of terraces along a certain distance, and knowing the nominal substrate miscut angle we deduced the corresponding average multistep height. Measurements repeated over several AFM images are represented as individual symbols.

The step height evolves similarly on the samples oriented toward A and B direction, except for the $+5^\circ$ misorientation, which may result from insufficient statistics. The steps height regularly increases, and is indeed not negligible when compared to the QW thickness. In the luminescence spectrum, this translates into a broadening of the emission, as displayed on Figure 4.4(b). The carrier diffusion properties were not probed during this work, but strongly misoriented substrates would probably not be suitable for the fabrication of devices requiring efficient 2D in-plane diffusion.

The strong increase of N incorporation observed close to 2° substrate miscut can be explained by the evolution of the step height. On step-bunched surfaces the growth proceeds essentially by an advance of the multistep as a whole. This means that to completely cover the initial template, a layer is necessary that is as high as the multistep height. On highly misoriented substrates the multisteps become higher than the first stage of the 2-step growth method: the DMHy flux is strongly increased while some GaAs barrier material is still apparent on the growing surface. GaAs is well known to ease the N incorporation as compared to InGaAs alloys. This is a first indication that the additional N incorporation on strongly misoriented substrates is specifically located at the QW lower interface. Even if the thermally-assisted interatomic rearrangement following the initial incorporation draws closer the In and N distributions, we may still be able to observe by SIMS a shift of the N distribution compared to In, toward the

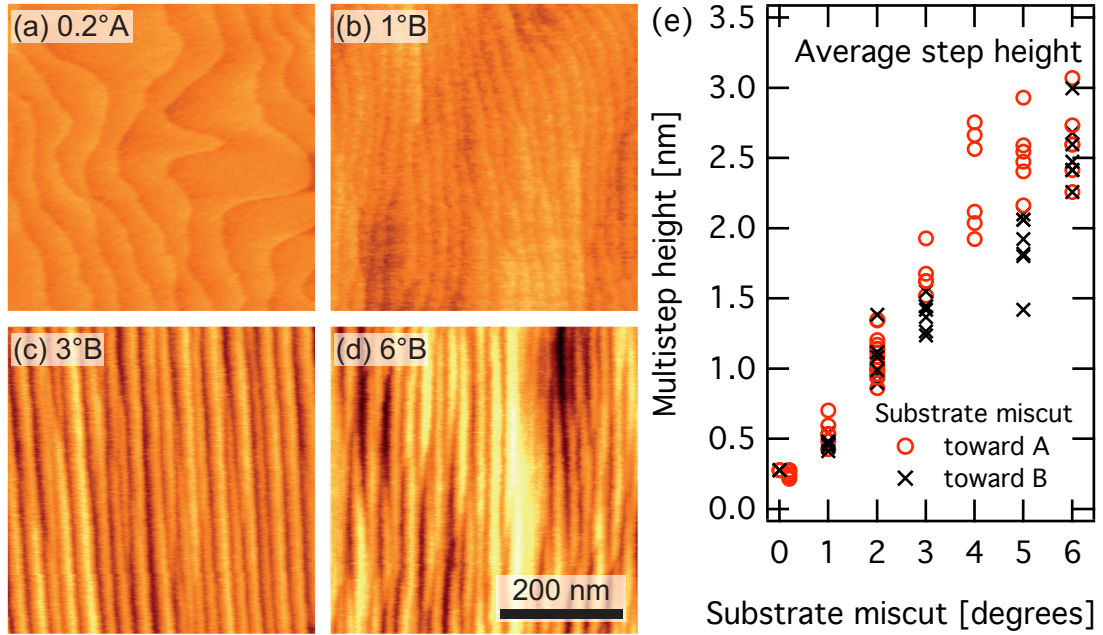


Figure 4.7: (a-d) 500 × 500 nm AFM topographic images of the surface of (a) +0.2°A, (b) +1°B, (c) +3°B and (d) +6°B QW samples, with identical color scales. The atomic steps progressively stack when increasing the misorientation. (e) Average multistep height observed by AFM on a series of QW samples as a function of the substrate misorientation. Above 2°, the multistep height becomes larger than 1.5 nm, a value that corresponds to the first QW deposition step with low DMHy flux.

QW deeper interface.

The AFM results provide evidences that the lower interface of our QWs is atomically smooth only when the substrate misorientation is below 1°. This is consistent with the lowest InGaAs QW FWHM obtained in the 0.3-0.4°B window. The improvement of the interface quality is due to the self-ordering of the atomic step, as was already evidenced in the AlGaAs/GaAs system using different MOVPE growth conditions [296]. Above 1° misorientation the surfaces present increasingly higher degree of step-bunching. Above 2°, the initial GaAs template is not fully covered when the second growth step proceeds with high DMHy flux, leading to an additional N incorporation at the QW lower interface.

4.4 SIMS characterization of N repartition

The N spatial distribution in QWs can be characterized using TEM-based methods [297, 298, 238], however such measurements are quite delicate. Some more direct insights can be obtained thanks to the secondary ions mass spectroscopy (SIMS) technique, where a mass spectrometer monitors the ions ejected from a sample that is eroded by an ion beam. This technique allows for determining the concentration profiles of several atomic species

simultaneously.

4.4.1 SIMS samples and measurement conditions

Two sets of samples were analyzed in two different SIMS facilities. The first set consisted in 4 samples issued from the same growth run with different substrate misorientations (+4°A, +5°A, +4°B and +5°B), using the growth procedure described in Section 4.1. The measurements were performed by Dr. C. Cytermann from the Surface Science Laboratory (Solid State Institute) in the Technion Institute of Technology (Israel), using a time of flight SIMS (*TOF.SIMS*⁵ from Ion-TOF GmbH). The sputter beam was 500eV Cs^+ . In negative mode the analysis beam was 25keV Bi_1^+ and the monitored signals were the ions H^- , C^- , O^- , As^- , In^- and Ga_2N^- . In positive mode the analysis beam was 25keV Bi_3^+ and the signals monitored were $CsGa^+$, $CsAs^+$, $CsIn^+$ and Cs_2N^+ . The nominal depth resolution is 1 nm, although drilling through the relatively thick GaAs cap also degrades this resolution. Two sample pairs were also characterized by the technical staff in Trento, Italy, grown using the same procedure on (100) exact and +5°B substrate misorientations. Each pair was composed of an as-grown sample, as well as a cleaved piece that was hydrogenated as to neutralize the effect of nitrogen on the electronic properties (details can be found in Chapter 2.2.5). The hydrogenation process was performed by Dr. M. Felici at Sapienza Università di Roma (Italy). To be able to discriminate the hydrogen signal from the background, the hydrogenation was performed using deuterium, a heavy isotope of hydrogen with almost identical electronic properties. The SIMS analysis was performed using Cs ions.

Figure 4.8(a) displays typical SIMS signals in negative mode acquired in Technion. The N-containing QW is visible on the left, and the reference InGaAs QW is on the right. On figure XXX(b) are displayed the SIMS signals acquired in Trento in positive mode, with In, N and D in log scale, and the Ga dip shown in linear scale. The QW peaks appear generally Gaussian, however both the instrumental resolution and the quite large depth at which the structures are buried participate in the distortion of the real profile. The D signal is only observed at the N-QW location, confirming the selectiveness of the hydrogenation process. The In tails above the QWs were only observed in that specific sample pair.

4.4.2 PL spectra and expected samples characteristics

The Figure 4.9 summarizes the (μ)PL spectra of the different samples that were SIMS-analyzed in Technion (black) and in Trento (red). The 2 samples series were grown using nominally identical growth runs. The luminescence of the samples sent in Trento has been characterized using a different, low-resolution setup, which partly explains the broader InGaAs QW lines. However several discrepancies appear immediately: when compared to the Trento series, the reference InGaAs QWs sent to the Technion are systematically redshifted (and the emissions broadened), and the N-induced redshift is reduced. Approximately one year separated the growth of the 2 series, and some MOVPE settings may have drifted meanwhile, or some non-

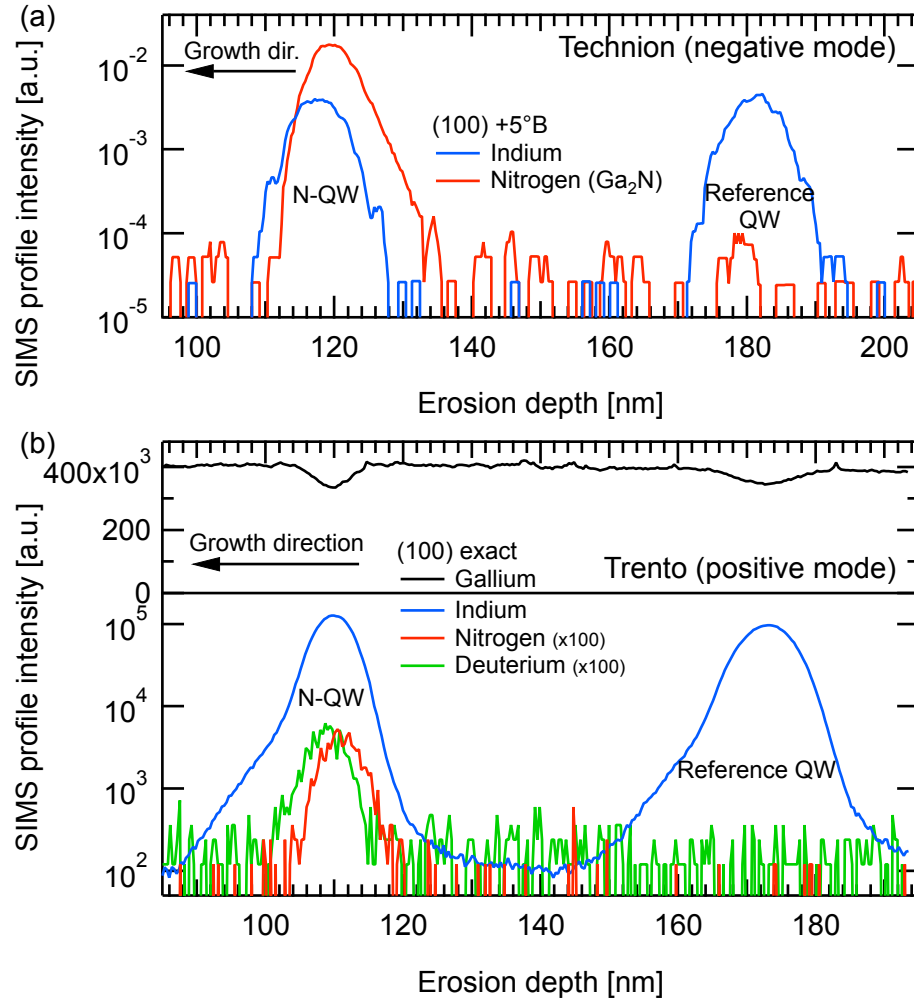


Figure 4.8: Typical SIMS profiles as function of the erosion depth. The data displayed here were acquired (a) in Technion in negative mode on a $+5^\circ\text{B}$ misoriented sample, as well as (b) in Trento in positive mode on a (100) exact sample. The In signal tail above the QW was only observed on that particular sample pair.

monitored MOVPE parameters (precursor bath temperature etc.) may have been modified. The exact origin of these discrepancies remains unclear. The analysis was performed by processing separately the 2 sets of samples, regarding the structures as similar but not identical. Nevertheless, the N-induced redshift increases when the substrate misorientation is increased, independently in the 2 series.

4.4.3 In distribution uniformity and In content

To start with the analysis we first characterized the In incorporation. The main question relates to the respective In content of the reference and N-containing QWs. The peak value is not a

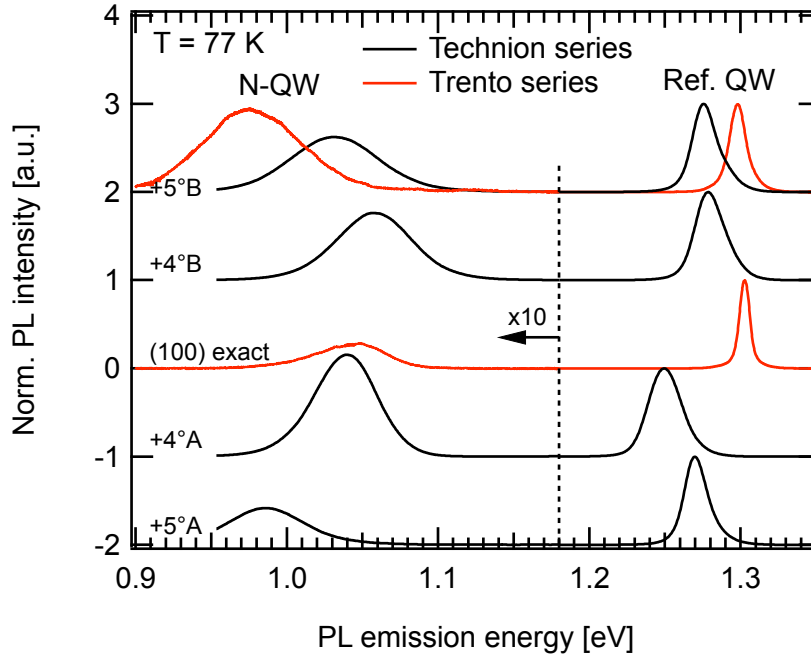


Figure 4.9: 77 K (μ)PL spectra of the different samples analyzed by SIMS in Technion (black) and in Trento (red), sorted according to the substrate miscut angle. The curves have been normalized to the reference InGaAs QW intensity, and for clarity the InGaAsN QW signals has been multiplied 10-fold.

good indicator as the reference QW SIMS signal is significantly broadened (FWHM of ~ 8 nm instead of ~ 7 nm for the N-QW), likely due to the respective QW depths that hinders the SIMS vertical resolution (the reference QW is ~ 200 nm below the surface). Instead, the total amount of In was characterized as the integral of a Gaussian fit to the In peak. The integrated In signal is displayed on Figure 4.10 as blue symbols. Similarly, the Ga profiles present a dip at the QW locations: the Ga dips were also fitted with Gaussian profiles; their integrals are shown as black symbols.

A detailed description is given here on the different symbols used consistently throughout this section dedicated to SIMS measurements. First the data points corresponding to the reference QW are depicted with empty symbols, while filled symbols refer to the N-QW. The symbol shapes are circles for data acquired in Technion (positive mode), diamonds for Technion data (negative mode), and squares for data from Trento (positive mode). Additionally, the black color refers to Ga, blue to In, red to nitrogen and green to deuterium. For the sake of visibility, the exact and $+5^\circ\text{B}$ hydrogenated samples observed in Trento are slightly shifted horizontally.

A closer look at the In peaks is displayed on Figure 4.11(a)-(b), where the left scales stand for the SIMS data and the right scales for the In content deduced from the reference QW PL emission energy. The vertical scales were adjusted so as to match the respective zero levels. Only data corresponding to the reference QW (open symbols) are shown.

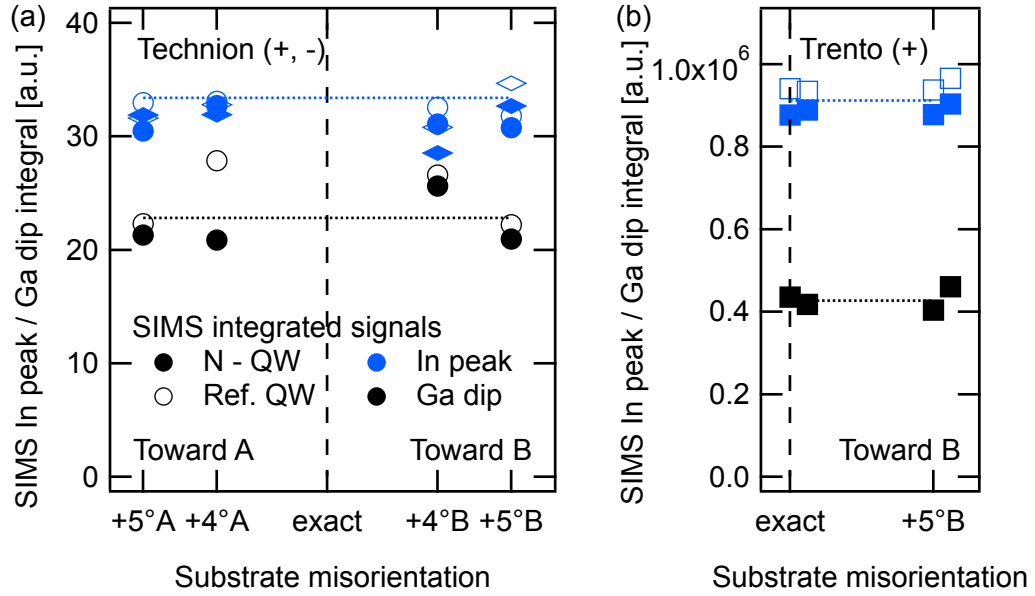


Figure 4.10: Integrated intensities of the In peaks (blue) and Ga dips (black) of the different samples as a function of the substrate misorientation, for both N-QW (full symbols) and reference InGaAs QW (open symbols). Data are shown, acquired (a) in Technion and (b) in Trento. The misorientation only marginally affects the In incorporation (the reduced In signals of the +4°B sample surprisingly correspond to larger dips in the Ga signal). Overall, the In content appears slightly higher in the reference QW than in the N-QW.

The direct In signal intensity and the amplitudes of the Ga signal dips agree on a slightly higher In content in the reference QW. This discrepancy can be translated into a 1 – 2 % In enrichment of the reference QW compared to the N-QW. We believe this is a real effect, but cannot rule out a measurement artifact. A signal distortion could be caused by the strength of the In-N bounds, more difficult to break than the Ga-N. Then, the monitored $CsIn^+$ ions may appear slightly less intense in the N-containing QW as compared to the reference QW. However a mis-calibration of the growth parameters appears a more likely cause of the different In concentrations observed.

4.4.4 N concentration

We were next interested in the qualitative determination of the N concentration, as well as its distribution within the QW. The N integrated signal is plotted as function of the substrate misorientation on Figure 4.12(a) (data acquired in Technion). The N-induced redshift of the N-QW is shown on the vertical right scale. Both the positive and negative SIMS N signals recorded in Technion present an increase with misorientation, consistent with the larger PL N-induced redshifts of the +5° samples.

Figure 4.12(b) shows the same data for the samples measured in Trento. The PL redshift is

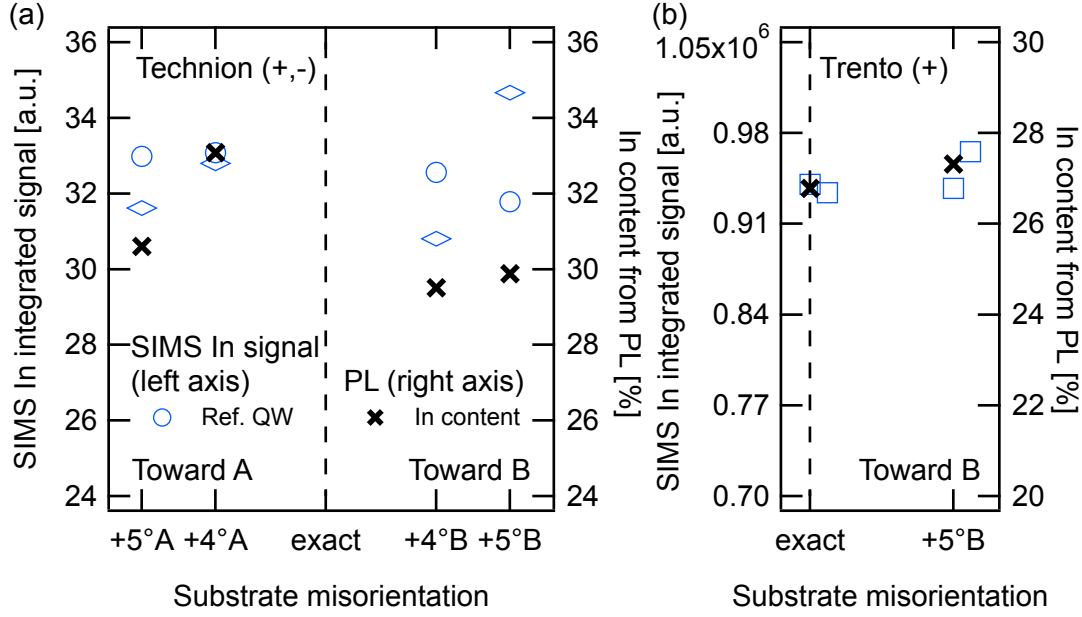


Figure 4.11: (a), (b) SIMS In peaks integrated intensities (left vertical scales) and comparison with the In content of the reference QW deduced from the μ PL emission (right scales), for the samples characterized (a) in Technion and (b) in Trento. The zeros of the vertical scales coincide in each graph.

increased in the +5°B sample as compared to the sample (100) exact. However, the nitrogen and deuterium signals measured in the +5°B sample are significantly lower, in contradiction with the PL results. The In signals recorded simultaneously are very similar for these 2 pairs of samples, ruling out the possibility of a modification of the setup sensitivity in-between the different measurement times. Although it is likely that an undocumented modification of the SIMS setup parameters took place, this contradiction between PL and SIMS signals acquired in Trento remains unexplained.

The samples analyzed in Trento present another interesting feature, possibly related to this contradiction. The N signal is observed reduced by 20 – 25 % on the hydrogenated samples when compared to the D-free counterpart. As the pieces characterized originate from the same sample, this implies that the N signal depends to a certain extent on the local atomic environment. Here the apparent reduced N content after hydrogenation is probably related to the rejection by the mass spectrometer of N atoms still bound to deuterium.

The N concentration can be quantitatively compared to the QW N-induced redshift. If the measurements performed in Technion do well agree with the PL results, the In and N contents measured in Trento are not consistent with the PL redshift.

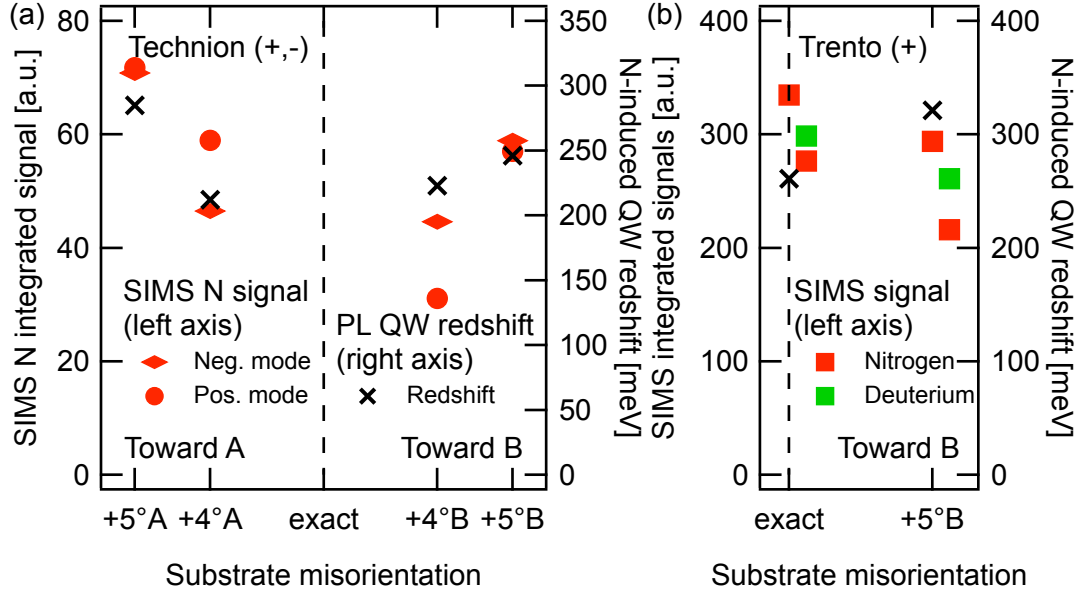


Figure 4.12: N integrated peaks intensities of the different samples characterized in Technion and in Trento. The redshifts of the corresponding PL peaks are overlaid as black crosses (right vertical scale), with the origins of vertical axes coinciding. (a) The data acquired in Technion evolve quite similarly to the PL redshifts. (b) The N signal of the samples analyzed in Trento appears weaker after the hydrogenation process (datapoints slightly horizontally shifted). The lower N signal in the +5°B samples is in contradiction with the emission redshift of the N-containing QW.

4.4.5 N distribution in the QW

The impressive spatial resolution of the SIMS technique allows the characterization of the In and N vertical distributions. Figure 4.13(a) and 4.13(b) show the SIMS In and N normalized profiles of the +5°B misoriented sample observed in Technion (negative mode). The N peak appears ~ 2 nm deeper than the In QW. It also appears asymmetric, presenting a tail into the GaAs QW lower barrier. Gaussian fits were used to monitor the different peaks locations and are shown as continuous lines.

Figure 4.14(a) summarizes the shifts of the N peaks (red) and Ga dips (black) relatively to the In peaks, as functions of the substrate misorientation. The Ga dip spatially matches quite well the In peak (with one exception, for which the Gaussian fit to the Ga profile is not satisfying). Conversely, the N peak appears systematically shifted, independently of the measurement conditions (in Technion using positive and negative modes, and in Trento). The shift especially increases with the substrate misorientation, starting from ~ 1.1 nm on the (100) exact sample, up to ~ 2.2 nm on the +5°B misoriented samples.

The vertical shift of N distribution is likely real but could also originate by a systematic measurement artifact (we remind here that the different profile data points are acquired alternately

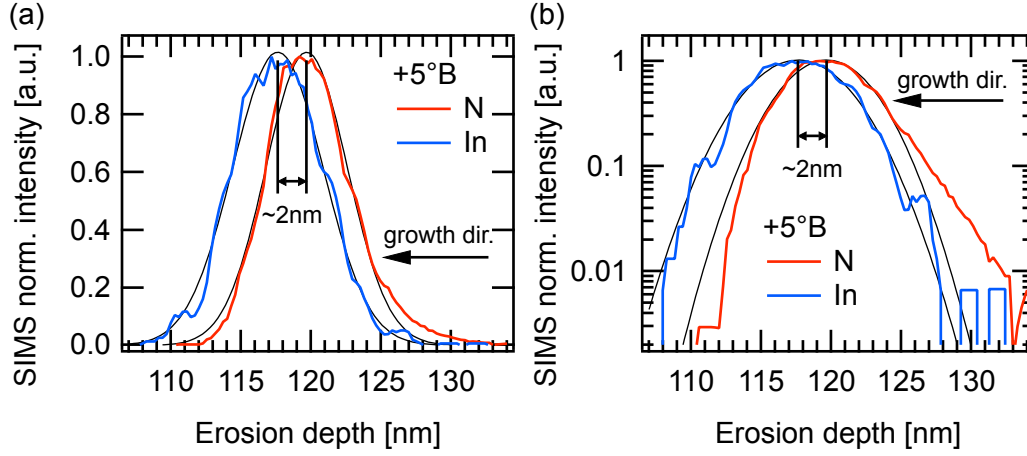


Figure 4.13: (a) linear and (b) logarithmic plots of the In and N peaks acquired in Technion (negative mode) on the +5°B sample, showing an asymmetric N peak located deeper in the sample than the In. Gaussian fits (black lines) were used to determine the peaks locations.

during the same erosion run). We cannot rule out an artifact, although some upper limit can be drawn using the following arguments. First, the Technion instrumental nominal vertical resolution is supposedly ~ 1 nm. Second as displayed on Figure 4.14(b), the D and N peaks appear shifted by ~ 2 nm, whereas the real distributions coincide. But D is a small, light atom occupying interstitial positions in the crystal, while the N is considerably heavier and strongly bound in the crystal matrix, thus causing the N-D shift. In and N are both heavy atoms embedded in the zincblende crystal (although respectively located on the III and V sublattices). We can safely assume that any measurement artifact causing shifts between the In and N distributions will be much less than 2 nm. The N distribution is very likely shifted even on (100) exact samples. Even if the 2-step growth method was specifically dedicated to tackle that issue [285, 294], our QW structures still suffer from a non-uniform N distribution and therefore needs further optimization. The growth interruption after the QW deposition may play a role in the systematic shift of the N to the lower QW interface, offering the possibility for N atoms close to the surface to be replaced by As.

The N distribution is also observed to extend deeper and deeper as the substrate misorientation is increased, with the N distribution centered more than 1 nm deeper in +5° as compared to exact samples. This is not a measurement artifact as such origin would consistently affect the different samples. As reported in a previous section 4.3, the atomic steps tend to stack and form multi-steps progressively higher (~ 2 nm on +5° samples) than the first of the 2 growth steps (1.5 nm). As the growth proceeds by a progression of the multistep as a whole, some GaAs material can be left uncovered when the DMHy flux is increased. We propose that the remaining GaAs surfaces are particularly favorable for N incorporation, as the presence of In is widely known to be particularly detrimental to N incorporation [204, 203]. This mechanism tends to generate high N content at the QW lower interface, and we propose that it is responsible for the larger N incorporation on misoriented substrates, shifted to the first QW interface. It also

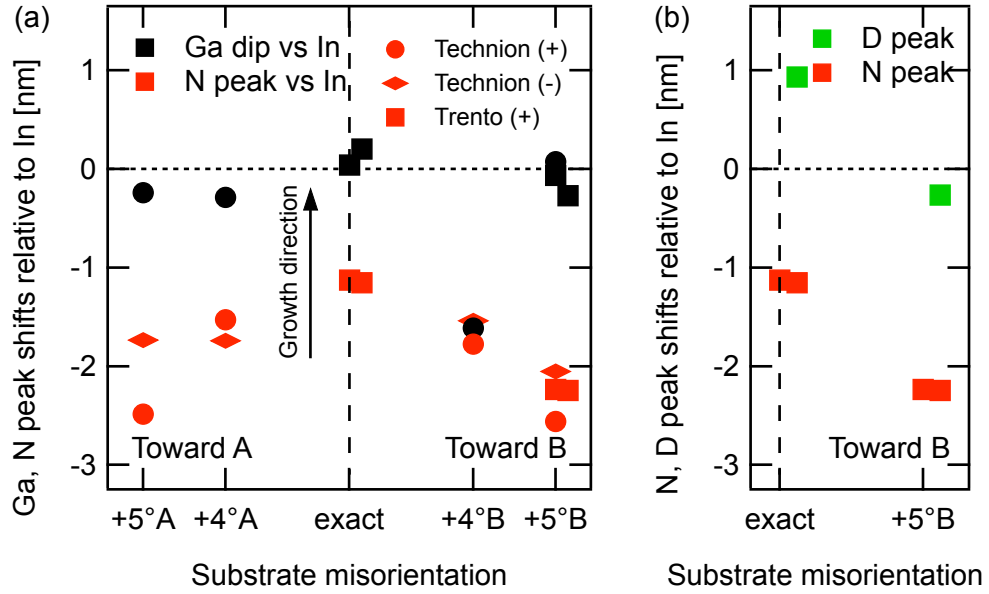


Figure 4.14: (a) Vertical shifts of the N peak (red) and Ga dip (black) relative to the In peak central location. If the Ga and In peaks match spatially, the N distribution is systematically observed closer to the lower interface. This tendency is increased on misoriented substrates. (b) Vertical shifts of the N and deuterium peaks of the samples characterized in Trento. The deuterium peak is shifted by a fixed distance (~ 2 nm) above the N. This distance seems independent from the substrate miscut.

results in a non-uniform N distribution throughout the QW. As the N content affects the optical quality and formation of defects, these results suggest that significant quality improvements could be obtained after a careful optimization of the profile of DMHy flux during the QW growth.

4.4.6 Photoluminescence of hydrogenated N-QWs

The N-containing QWs exhibit a sizeable blueshift upon hydrogenation, corresponding to ca. half to two thirds of the QWs energy separation. If, as suggested by the SIMS results, we assume an identical In content and profile in the N-containing and N-free QWs, the recovery of the emission energy is not complete. This is surprising as the hydrogenation process generally blueshifts the N-QW emission up to the energy of a N-free counterpart. The reference and N-containing QWs have very similar thickness: the SIMS In peak slight enlargement of the reference QW (~ 1 nm larger) is compatible with the loss of vertical resolution with increased erosion depth. Using a 5.6 nm-thick QW model, the In content of the reference QW can be estimated to be $[In] \sim 28\%$. If we assume that the emission energy of a fully hydrogenated N-QW matches that of a N-free counterpart, the In content in the N-QW should be estimated at $[In] \sim 44\%$. In this case the similar SIMS In signals in the 2 QWs has to be explained by a corresponding decrease in the extraction efficiency of the monitored In ions. It seems to

us very unlikely that the signals of both In^- and $CsIn^+$ decreases by a factor of more one third when a few percent of nitrogen is added in the matrix, corresponding exactly to the quite unrealistic In content suggested by the emission energy. Rather, we suppose that in our samples, the hydrogen irradiation process is not able to retrieve the emission energy of a N-free counterpart even when the maximum blueshift is achieved. We propose that the particular, highly non-uniform N distribution within our MOVPE-grown thin QWs is responsible for this particularity.

4.4.7 Summary of N incorporation effects

The SIMS measurements delivered rich data that can be summarized as follows. The amount of In incorporated in the reference InGaAs and in the N-containing QW are observed to be quite similar, suggesting the In content plays no role in the observed shifts of the PL emission. Secondly, the data acquired in Technion indicates a higher N content in misoriented substrates, corresponding to larger PL redshifts. However, data from Trento indicates a lower N concentration in misoriented substrates, but these SIMS data cannot account for the InGaAsN QW emission energies, suggesting the presence of an experimental artifact responsible for this contradiction. Third, the N is preferentially incorporated at the QW lower interface, and this tendency is strongly enhanced in misoriented substrates. The uniformity of the N distribution appears as a major issue concerning the dilute nitride alloys quality. We propose that the step bunching evidenced by AFM is the main effect responsible for the non-uniformity of N within the QW. Finally, the emission energies of hydrogenated samples suggest a large increase in the In content within the N-QW. However, the magnitude of this change and the contradiction with the SIMS results make us rather believe that the hydrogen irradiation process does not allow for retrieving the emission energy of the N-free QW counterpart. We believe that significant improvements in the QW quality could be obtained after a careful optimization of the DMHy flux profile during the QW growth.

4.5 Thermal annealing and S-shape behavior with temperature

The evolution with temperature of dilute nitrides compounds emission often reveals useful insights into the alloys quality. A double QW structure was analyzed, consisting of a pair of a N-free and a N-containing 5.6 nm QWs, with 30 % In nominal content, using a modified 2-step growth deposition (2.8 nm with a DMHy flux of 26 ccm, followed by 2.6 nm with 390 ccm). The substrate misorientation was +5°. In order to probe the effectiveness of annealing treatments on our nanostructures, a separated piece of the sample was subjected to a 25 min annealing at 750 °C under high arsine atmosphere. The same annealing conditions were applied to a QWR sample as presented in the next Chapter 5.4.2. The μ PL spectra were acquired using an HP 86140 spectrum analyzer, which was the best detector available at that time. A quite high excitation power was used so as to balance the quite low detector sensitivity, in order to observe signal even at high temperatures. The analysis was performed by fitting the spectra

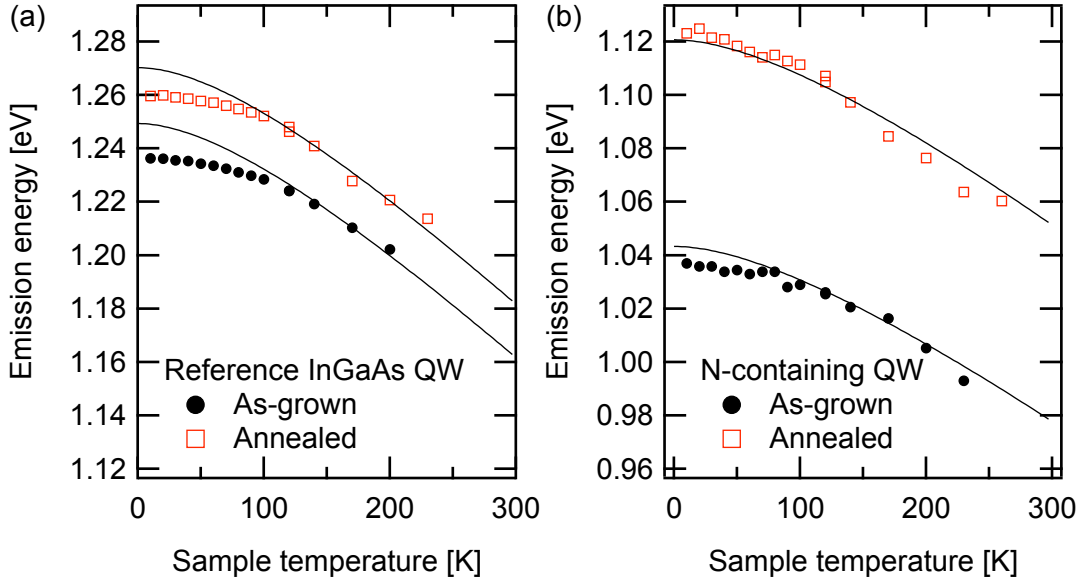


Figure 4.15: (a) Evolution of the emission energies of a nominally 5.6 nm, 30 % In InGaAs QW, prior to and after annealing ($P_{\text{exc}}=30\mu\text{W}$). QW models are shown as black lines (see text). (b) Emission energies of the corresponding N-containing QWs, showing a large QW blueshift upon annealing. The spans of the vertical scales of the two graphs are identical.

using an asymmetric lineshape (convolution of a Gaussian peak with an exponential function with a Boltzmann-type function $-\frac{\Delta E}{k_B T}$). The fit quality is very good as the exponential term reproduces well the broadening of the emission with temperature. The line maximum is reported on Figures 4.15 and 4.15(b) as the emission wavelength, showing the evolution of (a) the reference InGaAs and (b) the N-containing QW.

The emission energy of the reference QW experiences a blueshift of ~ 23 meV upon annealing, suggesting an overshoot in the annealing time or temperature, leading to alloy intermixing and atomic interdiffusion. By comparison, the N-containing QW is blueshifted by ~ 80 meV: in a first picture the additional ~ 55 meV can be associated with the effect of annealing on nitrogen. The blueshift is ~ 15 meV higher at low temperature when compared to $T > 150$ K. This suggests that a non-negligible amount of optically active deep level defects are cured upon annealing. The same annealing procedure was applied to a QWR sample as reported in Subsection 5.4.2. In that case, the 2-step growth procedure was not optimized for the 3 nm-thick top-QW structure, and a significant S-shape in the emission energy could be observed using an excitation power even 10-fold higher. In the adjusted 5.6 nm-thick QW structure, the S-shape is much less obvious: the 2-step growth procedure allows for a significant reduction of the quantity of defects incorporated in the N-containing layers.

A QW model based on literature [140, 158] detailed in Subsection 4.2.1 was used to draw the continuous lines on Figures 4.15(a) and 4.15(b). Assuming the nominal 5.6 nm QW thickness, the as-grown sample evolution is well reproduced by using a 34.5 % In content, slightly higher

than the nominal 30 % content. This enrichment is consistent with the higher In content similarly deduced in the previous sections (Sections 4.2 to 4.4). The InGaAs QW blueshift upon annealing was accounted for in the QW model by enlarging it and simultaneously lowering its In content by 14 %, so as to reproduce the effect of atomic interdiffusion and QW structural broadening. The In content determined in the reference QW allowed the estimation of an equivalent N concentration close to ~ 2 %. This value is reduced by ca. one third after annealing, evidencing the effect of N migration from Ga-rich to In-rich environment.

The reference N-free QW emission intensity is not observed to be improved after annealing. Oppositely, the N-QW exhibits an integrated PL intensity increased by a factor ~ 3 up to ~ 150 K. At higher temperatures the gain in intensity becomes progressively smaller.

4.6 Chapter summary

In this part of the work, QW pairs with or without nitrogen were grown on semi-insulating wafers using the so-called 2-step growth method. Large QW redshifts (>250 meV) were obtained for the N-containing QWs. It is shown that the N incorporation is significantly improved on misoriented substrates, pushing the emission close to $1.3\ \mu\text{m}$ at room temperature.

With identical growth conditions, the amount of N incorporated was found to be strongly affected by the substrate miscut angle in a quite complex evolution. The largest redshifts were obtained on $+5^\circ\text{B}$ misoriented substrates. The N incorporation was observed to be correlated to the regularity of the GaAs lower interface as characterized by AFM. A regular step-flow provides the lowest N-QW redshift, while strong step bunching promotes the N incorporation. A particularly large redshift is observed when the multisteps become higher than the thickness during the growth stage with low DMHy flux. Remarkably, for samples of various misorientation grown under fixed conditions, the N-containing PL intensity is found to be uncorrelated with the N-induced QW redshift. This suggests that the supplementary N incorporated on misoriented substrates does not generate additional non-radiative defects.

A SIMS analysis performed on a few samples confirmed the similar In content in the reference and N-containing QWs. The N distribution was observed systematically centered closer to the lower QW interface, a tendency enhanced on misoriented substrates. The PL spectra of hydrogenated samples suggest an increased In concentration in the N-QW, but we rather believe that in our particular structure, the hydrogenation process is unable to completely neutralize the effects of N on the band structure. The fabrication of dilute nitride QW with uniform N distribution appears as a major, non-trivial step in the optimization of the material quality.

The best InGaAs QW linewidths were obtained on slightly misoriented substrates ($+0.3^\circ$ to 0.4°B), for the specific conditions used here (growth interruption, temperature ramp, etc.). Like in the GaAs/AlGaAs system[296], the substrate misorientation determines the QW interfaces roughness, directly affecting the structural quality and the emission linewidth.

We demonstrated the successful N incorporation into QW grown on exact and vicinal planar (100) substrates. In the next chapters we will concentrate on incorporating N into nanostructures grown on non-planar substrates. The growth of V-groove QWR on (100) substrates proceeds essentially like that of regular QWs, with the additional phenomena of growth rate anisotropy and nano-capillarity. Later on, the QD in inverted pyramids introduces some new level of complexity in the nanostructure formation mechanism and in the nitrogen incorporation.

5 1D dilute-nitride nanostructures: V-grooves QWRs

The V-groove QWR is an interesting 1-dimensional system presenting excellent quality and homogeneity, and quite large design flexibility in terms of integration into photonic devices like V-groove waveguides and lasers [100], VCSELs-type structures [102, 103], photonic crystal cavities [111, 4], etc. However the GaAs-based V-groove QWRs suffer from the limited operating wavelength range granted by the InGaAs and GaAs active materials (roughly 700 nm to 1.1 μm). The shift of the operating range up to the optical silica fiber windows (1.3 and 1.55 μm) may open new perspectives to the V-groove technology. In this context, the huge bandgap shrinkage produced by the N incorporation into GaAs-based alloys [287] offers a solution for shifting the QWR emission up to these technologically relevant wavelengths. The incorporation of N into QWR formed using the T-shape formation scheme was recently reported [62, 63, 64]. However this QWR design relies on a simpler and quite well known formation mechanism, and does not offer the perspective of QD formation.

A second motivation for the study of dilute nitride V-groove QWRs is the perspective of N incorporation into QDs grown in inverted pyramids, a system that will be explored in Chapter 6. For that system the material limitations are quite similar, and the fabrication of QDs emitting at 1.3 μm would be highly desirable. The growth of dilute nitrides alloys on non-planar substrates is a new challenge, and the combined influence of growth rate anisotropy and capillarity on the nitrogen incorporation is yet unclear. Successive steps should better tackle this issue. Before proceeding the non-trivial QD growth on patterned (111)B substrates, the first studies are conducted on simpler (100) V-groove templates.

Figure 5.1 presents the typical cross-sectional structure of a InGaAs/GaAs V-groove QWR sample. The substrate, buffer and cap are shown in shades of grey while the confining InGaAs regions are depicted in black. During growth, the material deposits regularly on the different facets: {100}, quasi-{111}A and quasi-{311}. This later facet develops according to the growth conditions, especially favored at low reactor temperatures [299] like the ones used in this work. The effective growth rate is typically higher on the quasi-{111}A facets than on the {100}, which tends to narrow the groove bottom. A competing effect, the capillarity, leads to the establishment of a self-limited groove profile [98, 99]. The radius of curvature at the bottom

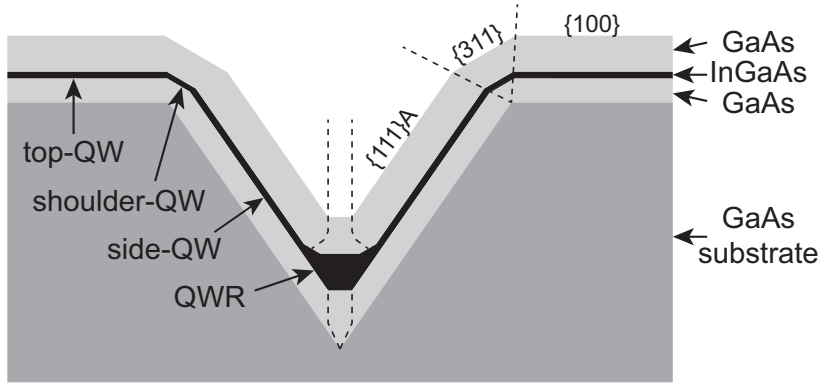


Figure 5.1: Schematics of the cross section of a V-groove QWR sample. The deposited layers stack regularly on the growing front, forming QWs of various thicknesses on the different facets: {100}, quasi-{311} and quasi-{111}. The self-limited profile of the groove apex is determined by a competition between growth rate anisotropy and capillarity, and depends primarily on the deposited chemical species: an InGaAs layer forms a crescent-shaped QWR at the groove bottom.

of the groove depends on the adatom diffusion length, and can be modified by tuning the chemical species, the temperature or the growth rate. In atoms have longer diffusion length than Ga ones, which in turn diffuse more extensively than Al. This allows the formation of various InGaAs/GaAs/AlGaAs QWR nanostructures at the groove bottom, a system now quite well known [99].

This chapter is organized as to address four main topics. First, the successful incorporation of N in InGaAs/GaAs QWR will be demonstrated. The PL emission spectrum will be described, based on etching and TEM experiments asserting the assignment of PL peaks to the proper nanostructures involved. The 1D behavior of the confined wavefunctions will be discussed relying on magneto-PL experimental results. The space of the different growth parameters will be explored, in view of optimizing the N-induced redshift and other emission properties. Finally, the QWR optical quality will be discussed, by probing the influence of defects on the emission, and by characterizing the QWR polarization properties. A fraction of this work was already published [300, 301, 302], but the present chapter presents more in-depth the research accomplished.

5.1 Incorporation of nitrogen into V-groove QWRs

Two samples will be characterized and discussed in detail in the forthcoming subsections. These samples were grown on a patterned (100) GaAs wafer with 1 μm and 10 μm pitch V-groove fields. The grooves width was ~ 350 nm. The fields covered only a small fraction of the sample, allowing formation of a regular QW on the planar regions. The growth of the first sample, labeled in the following as “N-QWR sample”, was as follows (see Figure 5.2). First, a 20 nm GaAs inferior cladding layer was deposited at 590 $^{\circ}\text{C}$ with a high arsine flux (As/III=43).

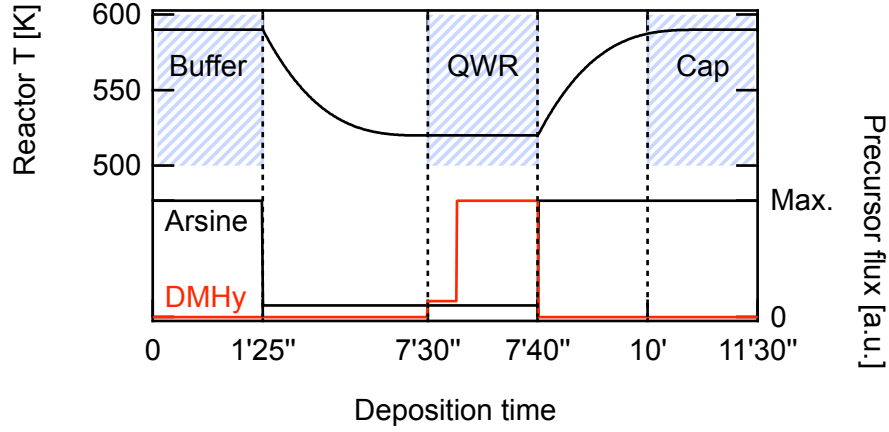


Figure 5.2: Schematics of the typical 2-step growth procedure used for the growth of our InGaAsN/GaAs V-groove QWR samples.

The growth was then interrupted for ~ 7 min to decrease and stabilize the temperature down to 520°C . Meanwhile, the arsine flux was decreased so as to ensure a low As adatom surface density at the onset of the QWR growth. The 3 nm-nominal $\text{In}_{0.25}\text{Ga}_{0.75}\text{As}(\text{N})$ active structure was grown at 520°C with reduced As flux ($\text{As}/\text{III}=3$), following the 2-step growth process described in the previous chapter (0.8 nm with 26 ccm DMHy, then 2.2 nm with 190 ccm). Finally, the growth was interrupted again with the sample kept under As atmosphere for 2 min while rising the temperature, before the growth of a 20 nm GaAs cap at 590°C took place.

The second sample ("N-free" reference sample) was grown similarly with the following differences: no DMHy valve opening, and constant, and high ($\text{As}/\text{III}=43$) As flux during active layer deposition and first growth interruption. This As/III ratio (and the associated growth rate calibration) was chosen according to the calibration of the MOVPE deposition performed on QWs by Prof. D. Fekete. That calibration ensures the deposition of InGaAs and InGaAsN QWs with identical thickness and In content. A high As/III ratio was needed as a low ratio results in a considerably altered and broadened PL emission (and to redshifted QWRs, see Figure 5.11). The QWR nominal thickness was chosen so as to target an effectively ~ 10 nm-thick QWR, by estimating the growth rate acceleration at the groove bottom. The DMHy fluxes were chosen according to the experiments performed on QWs in Chapter 4. The complex temperature profile is also similar to the one used for the QW growth, and should ensure both good GaAs quality when grown at 590°C , and a significant N incorporation at a growth temperature of 520°C . The temperatures given here are nominal. They are estimated to be overestimated by $\sim 20^\circ\text{C}$ at 520°C : the QWR growth thus actually proceeded at $\sim 500^\circ\text{C}$. The two samples were characterized by means of μPL , TEM and magnetopPL.

5.1.1 Photoluminescence spectra

The low-temperature PL spectra of the N-free reference sample (black lines) and the N-QWR sample (red lines) described above are shown on Figure 5.3. The spectra were acquired on

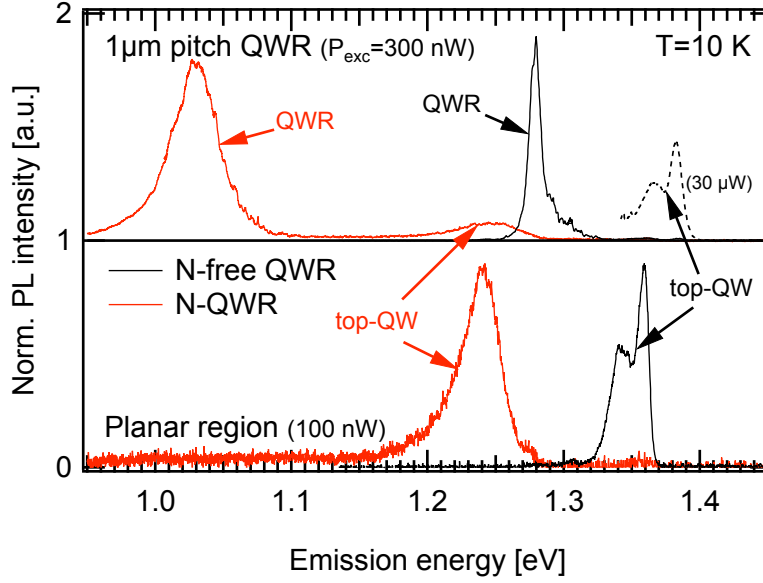


Figure 5.3: 10 K μ PL spectra of both reference N-free and N-QWR InGaAs(N)/GaAs samples, acquired on a 1 μ m pitch QWR (top) and on planar (bottom) regions. Two peaks are visible: the top-QW visible on both planar and patterned regions, and the lower energy QWR emission. A portion of a higher power spectrum of the N-free reference sample has been added on the upper panel (dashed line).

the 1 μ m pitch QWR field and on a planar (100) region of the same sample, located hundreds of μ m away from the QWR fields. Together with a (not shown) 10 μ m pitch QWR region, the identification of the lines in the PL spectra was based on comparisons with spectra of InGaAs/GaAs V-groove QWRs, and was confirmed by additional experiments.

A spectral line identified as due to recombination in the top-QW is present on both the planar and the patterned region of the reference N-free sample (black lines). As it is barely visible, a portion of a higher excitation power spectrum is also shown (dashed lines). The N-free top-QW emission consists in a double peak, with the low-energy component saturating with increasing excitation power. Its exact origin is unknown but probably originates from defects generated during the growth interruptions. This emission is slightly blueshifted (< 20 meV) in the QWR region, because of the preferential precursor decomposition on the highly reactive {111}A groove sidewalls, which in turn thins down the top-QW. The lower energy emission is identified as due to recombination at the QWR. The reference QWR line is ~ 9 meV wide (FWHM) at low excitation power, indicating good structural and optical quality. This linewidth is comparable to other state-of-the-art InGaAs QWR fabricated for achieving lasing in photonic crystal [4] or vertical Bragg [303] cavities. The low excitation spectrum is dominated by the QWR emission, indicating an efficient carrier capture process into the QWR, in spite of the large (1 μ m) inter-QWR spacing. The top-QW - QWR energy separation is ~ 60 meV. Based on the TEM observations presented later, the emission of the thinner side-QW is expected at higher energy than the top-QW, and is not observed on the spectrum of Figure 5.3.

The same identification can be performed in the N-containing QWR sample (Figure 5.3, red lines). The top-QW is visible on spectra acquired on planar regions. Introduction of DMHy during growth leads to a ~ 110 meV redshift of this line, suggesting significant N incorporation into the crystal; however, the exact amount is difficult to estimate reliably. The different As/III ratios used for the reference and N-QWR layers are not supposed to strongly affect the In content, as confirmed by the SIMS data of similar QW samples (however, this is disputed by the hydrogenation results, see Subsection 4.4.6). But even if the In content is identical in the two samples, the N distribution is likely to strongly differ from an ideal, square function. For these reasons, simple calculations are unlikely to give reliable estimates of the N contents and distribution across the QW layer.

The top-QW emission is also visible on the QWR field of the samples, being on this particular sample also slightly shifted to the blue. Here, the QWR emission is visible as an additional, intense peak at low energy. The N-induced redshift of the QWR line is very important, -250 meV relative to the reference N-free InGaAs QWR. The top-QW - QWR energy separation is here ~ 210 meV: this large energy separation suggests that the nitrogen is preferentially incorporated in the QWR parts than in any of the other planar parts of the structures. Finally, as in the reference sample, no side-QW emission is observed.

Figure 5.4 shows the spectra of the same samples, acquired on the $1\text{ }\mu\text{m}$ pitch QWR region, as a function of the excitation power. At low excitation the N-free QWR sample emission is dominated by the narrow spectral line of the QWR. A progressive band filling is visible upon increasing the excitation power, hinting at the population of QWR excited states. The top-QW is barely visible at low excitation, but as more and more carriers are injected into the system the QWR saturates and the top-QW emission becomes dominant.

A striking feature of the N-containing QWR is the progressive blueshift of the emission with increased excitation power. The low power spectrum presents several sharp features, signature of states strongly localized at local minima of the potential. With increasing power the QWR emission shifts to the blue, but some individual peaks can be recognized with unmodified energy. Oddly, the ensemble FWHM stays remarkably constant (~ 40 meV) up to intermediate excitation powers in spite of the spectral shift of the emission. This suggests that our N-samples have a disordered potential, with a relatively small density of states spread over a large energy span: at low excitation only the lowest energy states are filled (including the strongly localized ones), and with increased power the incoming carriers start filling higher energy states. A similar behavior was already reported in InGaAsN layers: the low excitation emission was attributed to deep-level transitions, and the emission energy only meets the bandgap at higher excitation level when the deep traps are saturated [219]. The density of states would be better characterized by photoluminescence excitation (PLE) technique, that requires a bright, tunable light source in the $1\text{--}1.3\text{ }\mu\text{m}$ wavelength range. Nevertheless an important spectral broadening is visible at higher excitation power ($> 30\text{ }\mu\text{W}$), prior to any broadening of the top-QW emission. As expected the QWR structure is easier to saturate than the planar, more extended QW structure.

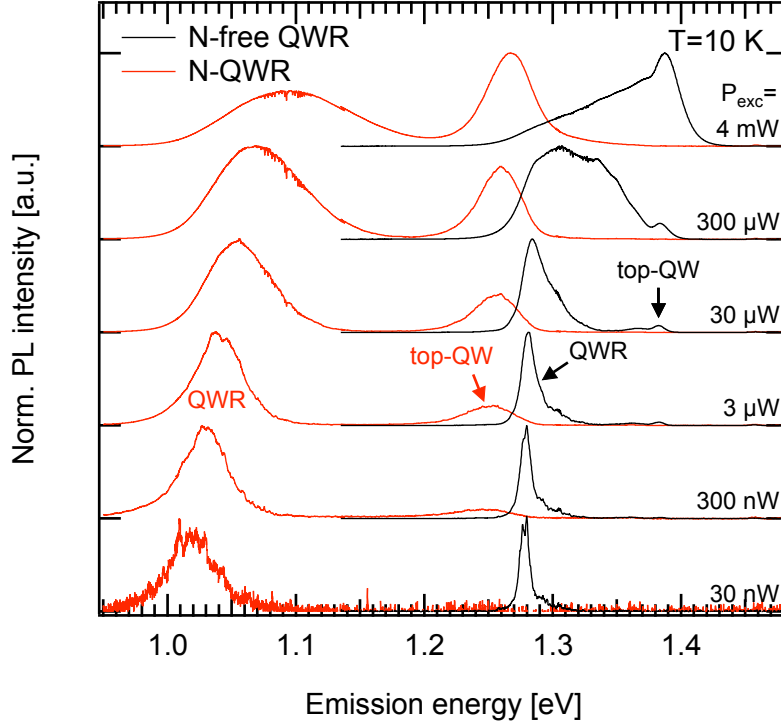


Figure 5.4: 10 K μ PL spectra of the samples presented on Figure 5.3, as function of the excitation power. The QWR dominates the low excitation power spectrum. The top-QW emission arises at higher excitation power, ultimately dominating the PL spectrum. Band filling effects are visible at high excitation power.

5.1.2 TEM cross sections

TEM is a powerful and quite versatile tool, especially adapted to the analysis of crystalline samples. Two V-groove QWR samples were analyzed through collaboration with the Interdisciplinary Centre for Electronic Microscopy (CIME, EPFL), with the experimental help of Dr. B. Bartova and Dr. M. Cantoni. First, we studied the reference InGaAs sample presented in the previous subsection, together with a N-containing sample identical to the one presented above but with slightly narrower grooves: ~ 270 nm instead of 350 nm, with the PL emission energy differing by less than 10 meV. The groove width of the reference sample is 350 nm. Figure 5.5 shows high-resolution TEM cross-section images of these samples, acquired in the $1\ \mu\text{m}$ pitch QWR field. The top-QW is visible on the ridge, with thicknesses matching closely the nominal values. Inside the grooves the thickest structure lies at the bottom, as expected. The sidewalls are observed to bow close to the ridge, forming $\{311\}$ facets. A slight thickening of the InGaAs(N) layer is observed at that position. A definitive confirmation that this region is not responsible for the lowest energy emission will be brought in the next subsection. A Fourier-transform analysis of the high-resolution images evidenced no dislocations in the examined area.

The two QWRs shown in Figure 5.5 have a slightly different shape: the measured thickness of

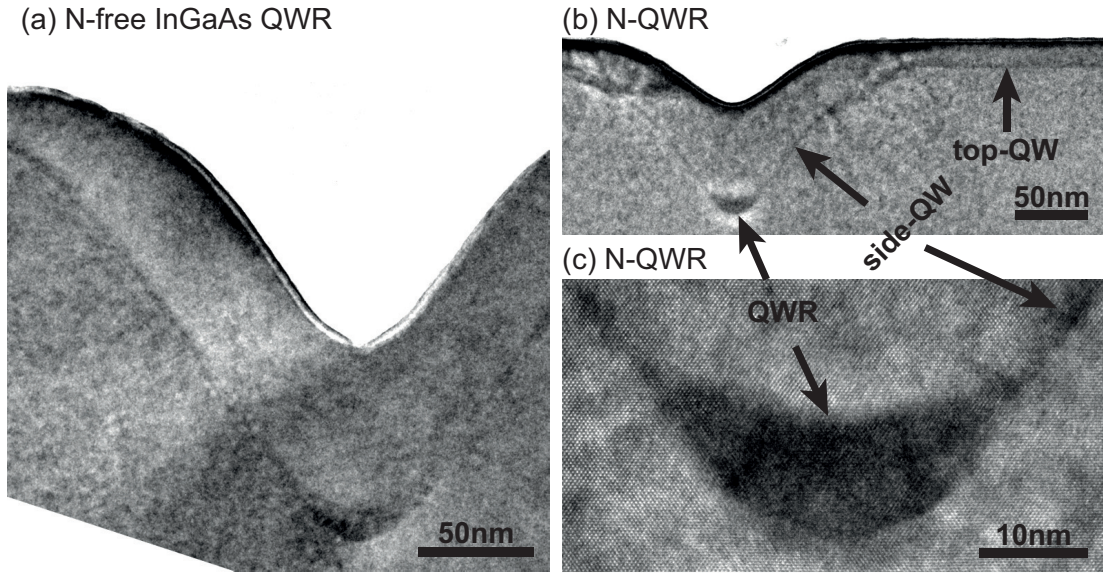


Figure 5.5: (a) TEM cross-section of a reference N-free V-groove QWR sample, of measured thickness 14 nm. The QWR is by far the thickness structure formed in the V-groove. (b) TEM cross-section of an InGaAsN V-groove QWR nominally identical to the reference sample, however with slightly narrower initial V-grooves. (c) Higher resolution image of the crescent of the same InGaAsN sample. The measured crescent thickness is 10.5 nm, i.e. less thick than the reference sample. Interface faceting is visible, especially below the QWR layer.

the QWR crescent in the reference sample is 13 nm, whereas the N-containing sample displays only 10.5 nm thick crescents. The crescent in the reference sample appears also slightly wider. The different initial widths of the grooves mentioned above may partly originate these discrepancies: the effective growth rate is increased in narrower grooves, which decreases the adatom diffusion length and results in smaller radii of curvature in smaller grooves. However, the similarity of the PL emission of the N-QWR sample with that having larger grooves tends to discard this hypothesis.

Instead, we propose that more significant differences in the growth conditions take place during the active layer growth itself. The reference sample As/III ratio was chosen much higher (As/III=43) than the N-QWR sample (As/III=3), because of the low quality of InGaAs samples grown with such ratios. As detailed in Subsections 5.3.1 and 6.1.1.1, low As/III ratios tend to increase the diffusion length of adatoms, thus promoting the mass transport to the QWR and enlarging the radius of curvature at the bottom of the V-groove. By contrast, the N-containing QWR grown in As-depleted conditions is thinner and narrower than the N-free QWR grown in As-rich conditions : the diffusion length seems actually lowered. This suggests that the massive presence of N atoms (a group-V element like As) and of DMHy decomposition by-products efficiently quenches the diffusion of Ga and In adatoms on the surface, limiting the mass transport to the QWR.

5.1.3 Chemical composition

Some more quantitative information is desirable about the In and N distribution within the V-groove structure. Such information is accessible by the use of the chemical-sensitive (002) reflection in dark field TEM mode [297, 298]. The In and N compositions of planar nanostructures can be simultaneously deduced when combining the data with measurement of the tetragonal distortion [304, 305]. However, the specific sample orientation required relative to the incident beam can only be met to a certain extent on 1D nanostructures [306, 307]. This method was therefore discarded due to our lack of intimate knowledge of the instrument capabilities and limitations. A variant is to use the so-called composition evaluation by lattice-fringe analysis (CELFA), which uses lattices fringes images instead of direct measurement of the tetragonal crystal distortion. This method can be combined with the EELS (Electron Energy Loss Spectroscopy) technique [308]. Here, the measured loss of the electron kinetic energy after inelastic collisions is a function of the nature of the collided atom, so the chemical composition can be retrieved [309]. However, the experimental setup available did not provide sufficient sensitivity to allow for N atoms observation. A third chemical-sensitive technique is EDX (Energy-Dispersive X-ray Spectroscopy). In this technique, a sample subject to high-energy electron beam excitation, as is the situation in a TEM instrument, emits X-rays with energy characteristic of its chemical composition. Monitoring the X-rays emitted while scanning the electron beam on the sample surface allows mapping the chemical composition.

In collaboration with CIME at EPFL, the N-QWR sample discussed previously was analyzed by EDX in a TEM facility located in Eindhoven, using a 200 kV electron beam. Figure 5.6(a) shows an EDX spectrum acquired in the QWR region. Several peaks can be identified, the most prominent ones due to As, Ga and In. Unfortunately, the N peak is barely visible and is spectrally located very close to other strongly emitting atoms like C. Figure 5.6(b) shows the mapping of the In peak intensity, acquired during a raster scan of the surface. The QWR shape is clearly visible, as well as the top- and side-QWs. A thickening of the InGaAsN layer is also visible on the groove shoulders, forming on the {311} top facets. This facet does not exist on the initial template, and develops upon growth depending on the relative growth rates the {100}, {311} and {111}A facets. Low-temperature growth is known to promote the development of these high-index features [299]. The existence of parasitic local heterostructure potential minima is to be avoided since it prevents diffusion of the trapped carriers to the QWR. Luckily, as confirmed in a later experiment, these thickenings do not efficiently emit light, at least in QWR samples grown on non-misoriented substrates. The contour of the In profile was extracted and super-imposed as a thin black line on the mappings corresponding to the emissions of Ga and N visible in Figure 5.6(c) and (d).

As visible on the images, the contents of In and N are maximal at the QWR location. The In and Ga signal show an expected In enrichment at the QWR center. The determination of chemical composition based on the In signal is not trivial since it relies on a sensitive calibration. It can be more satisfactorily deduced from the dip in the Ga signal at the corresponding location.

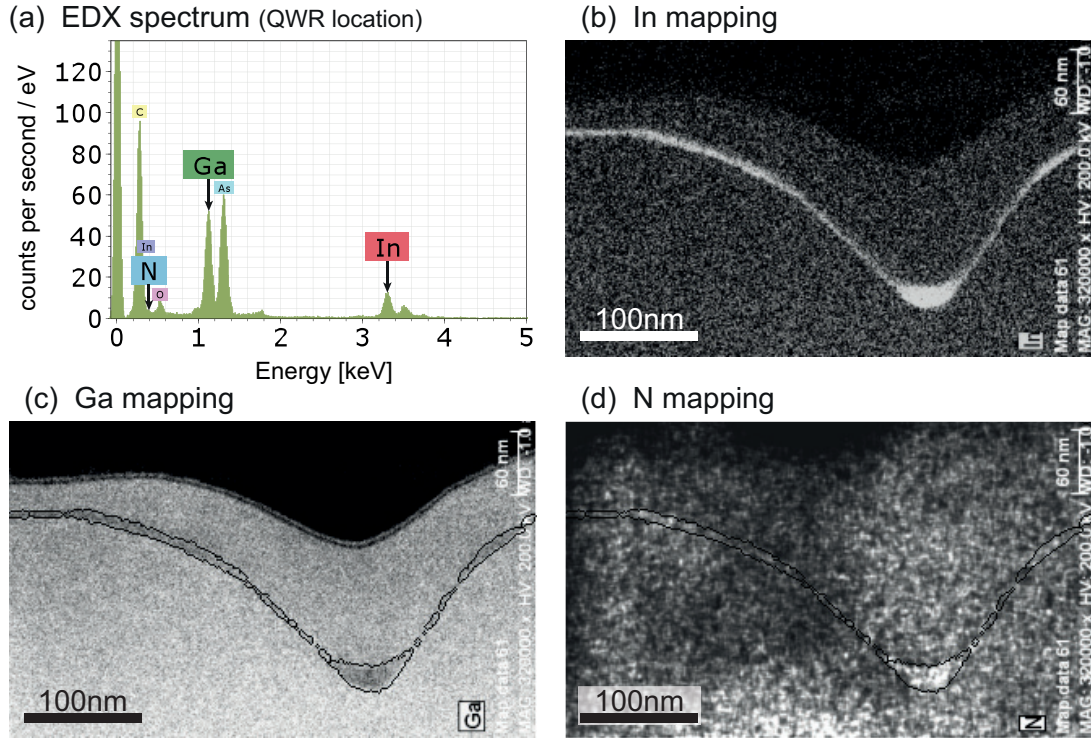


Figure 5.6: (a) TEM EDX spectrum acquired at the QWR location, with peaks associated to Ga, In and N evidenced. (b), (c), (d): Spatial mappings of the intensity of the peaks associated with (b) In, (c) Ga and (d) N. The contour of the In mapping was extracted and is depicted as a black line on the Ga and N images. A more pronounced Ga depletion is visible at the QWR center, indicating an In enrichment at the crescent center.

The intensity drop reaches slightly more than 30 % of its average value, yielding a 30-35 % In content in the QWR center. This is substantially larger than the 25 % In nominal content, indicating an In-enrichment at the QWR center as was already observed in InGaAs samples [123]. This enrichment originates from the longer diffusion length of the In adatoms compared to Ga ones, which renders them therefore more sensitive to the effect of capillarity. While the presence of N can be assessed at the QWR location, the N and As images signal-to-noise ratio are not sufficient to allow the determination of the N concentration in the QWR.

Another dataset was acquired at the same facility to obtain the atomic concentrations in the QWR core, along the growth direction. Figure 5.7(a) shows the line along which the scan was performed, and Figure 5.7(b) displays the atomic concentrations as calculated in by the operators in Eindhoven using a standard data processing software. The N signal rises above the background level, forming a broad peak that spatially coincides with the In distribution. The In and Ga concentrations also seem quite uniform in the QWR core. The atomic percentages are given with 100 % being the sum of group-III and group-V concentrations. If outside the QWR region the Ga and As concentration are as expected, $\sim 50\%$ each, in the QWR core the group-III and -V concentrations are not stoichiometric. As we did not have access to the

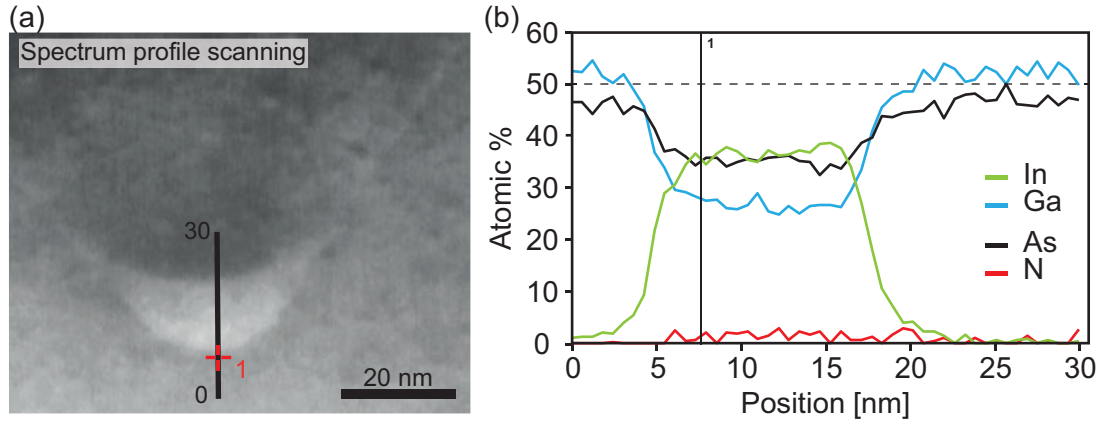


Figure 5.7: (a) TEM image of the QWR sample. (b) Atomic concentrations deduced from the EDX spectra acquired along the line shown in (a). A N signal is detected and duplicates spatially to the In distribution. However, these data processing resulted in unrealistic atomic percentages, illustrating the difficulty of a reliable measurement of the local concentration.

original data, and given the complexity of a proper data processing, we were not able to obtain trustworthy numbers for the atomic concentrations.

Finally, the measurements of QWR thickness and In concentration give some information on the N incorporation in the structure. A 12 nm-thick N-free GaInAs QW emitting at 1.05 eV at 10 K as our QWRs, should contain a high In concentration $[In] = \sim 49\%$, that is not reached even in the core of our QWR. This is another proof that nitrogen is actually incorporated and lowers down the bandgap.

5.1.4 QWR segmentation experiments

The TEM images of the QWR structures reveal a thickening of the InGaAsN layer located on the top- $\{311\}$ facets of the groove shoulders. μ PL experiments cannot discriminate these elongated structures from the actual QWR crescents because of their proximity (~ 100 nm). Charge carrier diffusion also limits the ability of cathodoluminescence to resolve these features. An independent confirmation was needed to formally link the long-wavelength emission to the QWR structure.

For this purpose, a single QWR located in a $10\mu\text{m}$ pitch field was isolated through mesa ICP-etching, as shown in the SEM images of Figure 5.8(a). The etching conditions led to a ~ 210 nm-mesa, passing through the top- $\{311\}$ shoulders. The photoluminescence of these nanostructures is quenched as the excited carriers are driven to the mesa surface where they recombine non-radiatively.

Figure 5.8(b) shows the μ PL spectrum of this structure (red line), as well as a spectrum acquired on a nearby single QWR located in an unetched region (black line). The spectra were acquired at room temperature, indicating good PL efficiency of the sample. The main, 1 eV low-energy

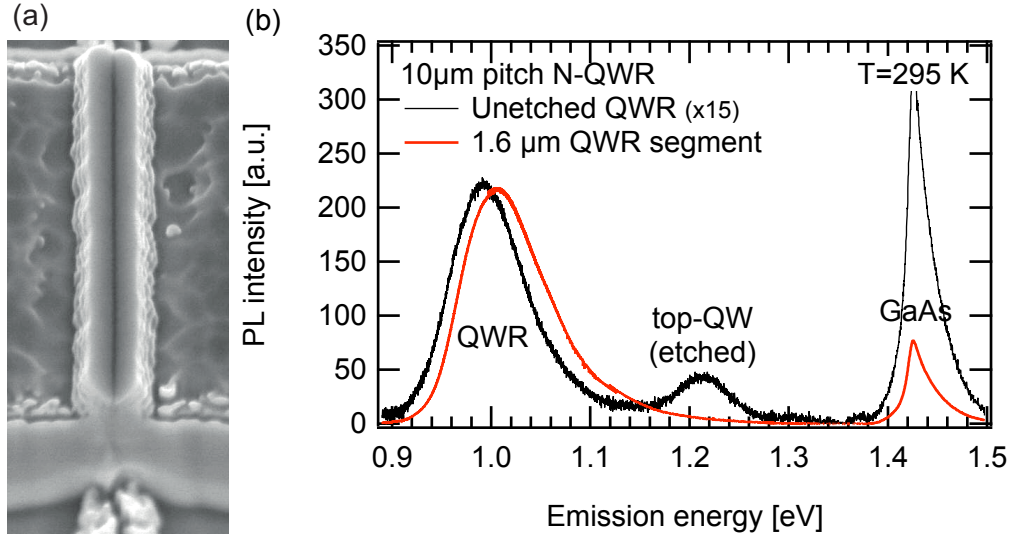


Figure 5.8: (a) SEM image (20° off from vertical axis) of a 1.6 μm long mesa processed on a 10 μm pitch N-QWR. The QWR is the only remaining structure as the top-QW and the top-{311} thickenings are etched away. (b) Room-temperature μPL spectra of the structure shown in (a) (red) and of a nearby unetched QWR (black). The strong, low-energy emission remains while the top-QW emission disappears. The long-wavelength peak is now attributed with certainty to the QWR nanostructure. The protruding shape of the mesa acts as a lens, enhancing the collected signal of the QWR segment.

emission is still present in the etched sample, but the 1.21 eV emission attributed to the top-QW disappears. A slight emission blueshift is visible, that may be explained by increased density of carriers, by the QWR inhomogeneities or by local strain or electric fields due to the proximity of the surface. As already mentioned, the {311} parts are cut by the mesa walls, hence should not emit light. This confirms the correctness of the peak identification performed on the sole comparison of planar and QWR regions spectra. The intensity of the isolated QWR was dramatically increased (15-fold), likely due to a strong light focusing effect related to the mesa geometry, improving the collection and maybe the excitation efficiency. We note that an increase in the excitation efficiency would also affect the QWR carrier density and explain the observed QWR blueshift.

To summarize this preliminary study, two N-containing and reference N-free QWR samples have been characterized in detail by means of PL before and after mesa etching, TEM and EDX. The V-groove structure is approximately as expected, with however marked thickening in the top-{311} facets. The presence of DMHy during the QWR growth shortens the adatom diffusion length, hindering the mass transport and leading to thinner QWRs. The top-QW and QWR emission have been identified in the PL spectrum with certainty. Nitrogen is successfully incorporated into these two nanostructures, inducing a strong redshift of the emission. The N-induced redshift is very pronounced especially in the QWR, while keeping a limited PL intensity degradation.

5.2 Quantum confinement in V-groove dilute-nitride QWRs

The first PL results as well as the TEM data show that the nanostructure named here “QWR” has a size and some characteristics ensuring the confinement of charges into a structure small enough to provide quantum confinement. However, if quantum confinement definitely occurs in our structures, the amplitude of the disorder as well as the free diffusion length of excitons remain unknown. The wavefunction are delocalized in ideal 1-dimensional nanostructures, but their extreme sensitivity to disorder causes strong localization effects. Actually, low temperature (< 50 K) diffusion length in the micron range is already a challenge in the cleaner GaAs/AlGaAs system [108], and the disorder introduced by presence of N atoms is likely to make the situation worse. It is therefore important to get some insight into the typical quantum confinement length, and to see to what extent the QWR characteristics differ from an ideal 1D structure.

5.2.1 Diamagnetic shift of PL spectra

A convincing evidence for the 1D-character of our QWR structure was brought by means of the magneto-PL technique. The samples were fabricated by the author of this work, and the hydrogen irradiation, measurements and subsequent data analysis were performed by Dr. Marco Felici and coworkers, a former colleague currently working at the University of Rome (La Sapienza). Measurements were acquired at the High Field Magnet Laboratory of the Nijmegen University (Netherlands). The findings briefly summarized here were already presented in a publication [301].

Measurement of diamagnetic shift is a tool allowing to determine the spatial extension of quantum-confined systems, as well as to calculate the electron effective mass. The experimental apparatus consisted in a low temperature (down to 4.2 K) μ PL setup, where the sample is placed in a strong magnetic field (up to 30 T). The variable field could be oriented along any of the three natural axis of the QWR structure, as sketched in Figure 5.9(a). The PL peaks are shifted by the additional confinement caused by the magnetic field as shown on Figure 5.9(b). Three samples were studied: the reference N-free and the N-QWR samples observed by TEM, as well as another piece of this last sample that underwent hydrogenation. As described earlier in Subsection 2.2.5, hydrogenation of dilute nitride samples leads hydrogen atoms to diffuse and fix in the immediate vicinity of nitrogen atoms, neutralizing the N effects on the band structure. The bandgap, strain and most of the PL efficiency are very generally recovered, reaching values of an N-free counterpart.

The PL spectra of the three samples are displayed on Figure 5.9(c). The hydrogenation process significantly blueshifts the QWR emission, however not reaching the energy of the reference sample as was expected after such processing. This may be partly explained by the different As/III ratios used for the growths, leading to modified diffusion lengths and In concentration. The modified strain field due to the N and H atoms presence may also be partly responsible of this discrepancy. Nevertheless, the results on planar QW structures (see Subsection 4.4.2)

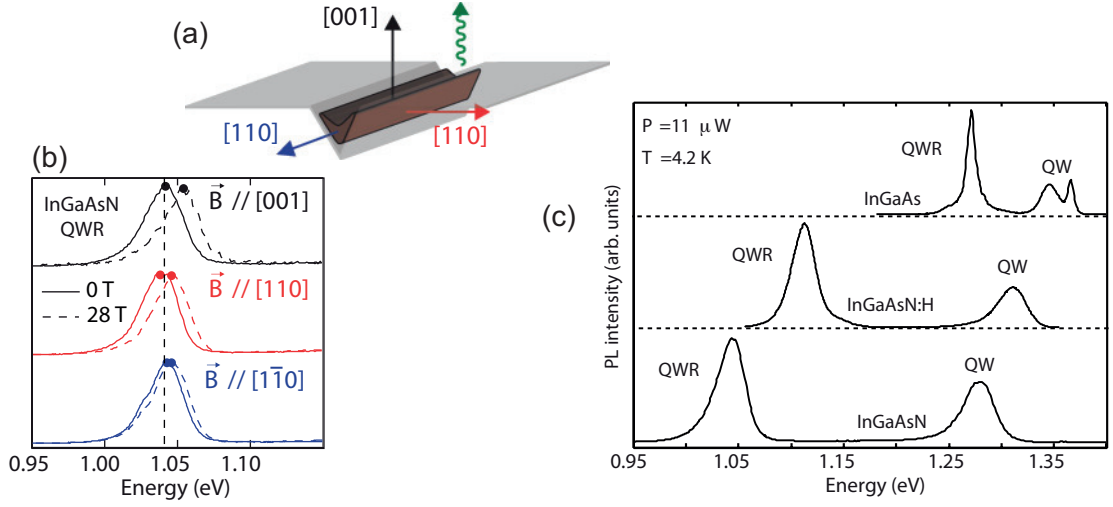


Figure 5.9: (a) Schematics showing a QWR in a V-groove, with the associated crystallographic axes. (b) PL spectra of the N-QWR sample, showing shifts between the zero and strong magnetic field conditions, with the field oriented along the three proper QWR axis. (c) PL spectra of the three samples analyzed, displaying the QWR and top-QW emission. The InGaAs and InGaAsN samples are the ones observed by TEM (see Figure 5.5). A part of this last sample was hydrogenated to neutralize the effect of nitrogen, and is labeled InGaAsN:H. Graphs from [301].

suggest the full recovery of the emission energy is not achieved in N-containing nanostructures structures, possibly due to the local, non-trivial N atoms distribution in the heterostructure.

The magneto-PL results shown on Figure 5.10 were interpreted by modeling the QWR as a 2-dimensional parabolic potential [310]. Using as model parameters values found in the literature (see Ref. [301] and references therein), the QWR effective width and height were fitted from the magneto PL data of the reference and hydrogenated samples. The obtained thicknesses $L_{[001]}$ and widths $L_{[110]}$ were found to be in excellent agreement with values measured on TEM cross-section images of the corresponding samples, thus validating the approach. The extracted effective QWR size was used as a parameter in the model to fit the electron effective mass in the N-QWR sample data, which in turn was found in good agreement with the effective nitrogen content estimated from the blueshift of the hydrogenated sample ($\sim 1\%$).

The remarkable agreement of the data and the model used confirms the one-dimensional character of the wavefunction. Moreover, the QWR width and height are found in excellent agreement with values independently obtained with the TEM analysis. The hydrogenation results finally suggest that the N-QWR samples are enriched in In as compared to their reference counterpart, although similar findings on our planar QW structures that are contradicted by SIMS measurements leave the question open.

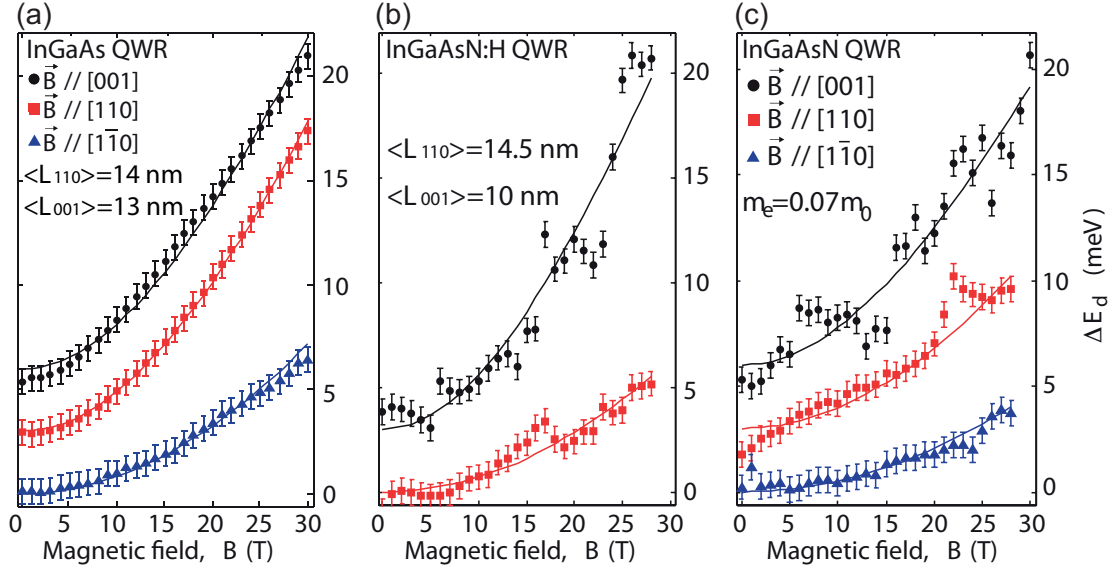


Figure 5.10: (a), (b), (c): PL emission shift as a function of the applied magnetic field, for the three samples. The curves have been vertically shifted for clarity, and the continuous lines are the best fit to the data. The deduced QWR thicknesses, QWR widths and electron effective mass are displayed on the graphs. Graphs from [301].

5.3 Influence of growth and structural parameters on nitrogen incorporation

In the previous subsections the detailed characterization of an N-containing QWR samples has been presented. Nitrogen can be successfully incorporated in the QWR structure, and important emission energy shifts (> 200 meV) of the QWR peak are achieved. The QWR size determined by the emission diamagnetic shift is in excellent agreement with the TEM direct measurements, signature of a significant spatial extension of the carrier wavefunctions along the QWR axis.

Following this demonstration, a growth study is presented summarizing our findings on the nitrogen incorporation into the QWR structure. The aim of this study is the fabrication of QWR samples emitting at $1.3\mu\text{m}$ wavelength at room temperature, while keeping good PL efficiency. First, the somewhat non-trivial choice of the reference sample is discussed. Then, the influence of several growth parameters is explored: substrate misorientation, QWR thickness, growth temperature, DMHy flux, growth rate, and deposition of a GaAs cap layer before the second growth interruption. The “B” substrate misorientation corresponds to atomic steps perpendicular to the groove axis.

The standard pattern consists of 350 nm -wide grooves in fields of 1 and $10\mu\text{m}$ pitch, on a GaAs substrate of exact (100) orientation. First, a 20 nm GaAs buffer is deposited at 590°C nominal substrate temperature. After a 7 min growth interruption to cool the reactor down

5.3. Influence of growth and structural parameters on nitrogen incorporation

to $T_{\text{QWR}}=520^\circ\text{C}$, a $L_{\text{QWR}}=3\text{ nm}$ $\text{In}_{0.25}\text{Ga}_{0.75}\text{AsN}$ layer is deposited at 0.278 nm s^{-1} according to the 2-step procedure (0.8 nm with 26 ccm DMHy flux followed by 2.2 nm with 190 ccm), using a gas-phase ratio $\text{As/III}=3$. After a 3 min growth interruption, a 20 nm GaAs cap is deposited at 590°C . Table C.5 in Appendix C summarizes the different QWR samples studied in this work, together with their main characteristics and the figures associated. Growth and structural parameters are given when differing from the “standard” procedure summarized above.

At the time the study was conducted only a non-optimal detector was available (optical spectrum analyzer HP 86140). Unless specified otherwise, the PL graphs presented in the following actually display spectra acquired in a later stage of the work with a more efficient detection setup, most of the time at room temperature. The peaks energy shifts, shapes and relative intensities are always found in good agreement with the lower quality data previously obtained at low temperature. The above-barrier excitation was provided by a CW Ti:saph set at 735 nm or by a laser diode emitting at 650 nm.

5.3.1 Choice of a proper reference sample

When exploring something new, one needs a reference point, that can be a known sample or some theoretical prediction. In the specific case of GaAs-based dilute nitride alloys, theoretical predictions are hard to obtain and even the choice of a proper reference sample can be somewhat tricky. Ideally the reference and the N-containing samples should only differ by the presence of N atoms in the crystal. This requirement can be met in the case of QWs, and this can be asserted by means of SIMS or TEM-variants.

However, the N precursor flux ratio exceeds by orders of magnitude the final N crystal concentration, and the massive presence of DMHy, N-subunits, N and by-products is likely to affect the growth dynamics in multiple ways (undesired cross-reactions, modification of the surface adatom diffusion lengths, etc.). This last property assumes a crucial importance in the case of patterned substrates growth, as the nanostructure shape is determined by the capillarity effect. The V/III ratio is one of the parameters affecting the adatoms diffusion length (see also Subsection 6.1.1.1). So assuming a N-containing sample grown with known arsine and DMHy fluxes, what should be the corresponding arsine flux of the N-free reference sample? Keeping constant the As/III ratio is not the good answer: this means assuming that neither the DMHy nor the N atoms affect the growth dynamics. If the total V/III ratio is the key parameter, then which N concentration is to be considered, the gas-phase, the crystal-phase or some intermediate value? This discussion also neglects the fact that the different nanostructures (top-QW, side-QW, QWR) do not experience the same growth conditions. The reference growth conditions thus differ for every different region of the structure. A satisfactory answer could be reached after a trial and error process, involving TEM-EELS shape and local concentration analysis. As this appeared prohibitively expensive both in time and money, the effort was directed to a few growths and PL characterizations that are able to circumvent these difficulties.

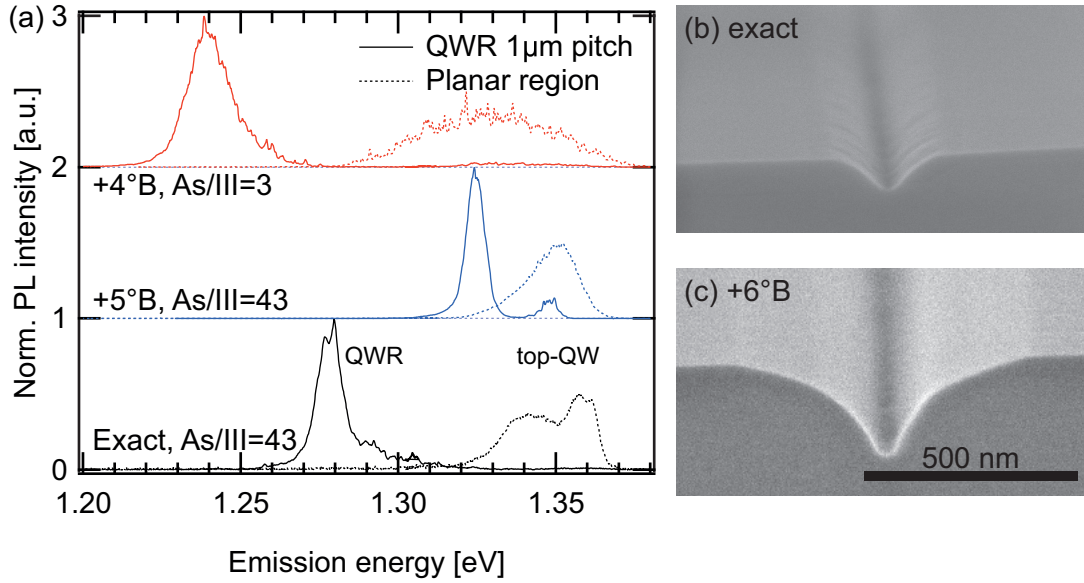


Figure 5.11: (a) 10 K μ PL spectra of three N-free reference samples with various misorientations and As/III ratio, measured on both 1 μ m pitch QWR (solid lines) and planar (dashed lines) regions. The following parameters were implemented: exact As/III=43 (black), misoriented +5°B, As/III=43 (blue), and misoriented +4°B, low As/III=3 (red). The curves have been normalized for clarity. (b), (c) SEM side-views of QWR samples grown on exact and +6°B misorientation (the view is tilted 8° away from the cleaved facet axis).

A few N-free samples were grown with various As/III and GaAs off-(100) substrate misorientations, to match the substrates used for the growth of N-containing samples. Figure 5.11 displays μ PL spectra of three N-free samples for both planar and QWR 1 μ m pitch regions. Two samples were grown on exact and misoriented (+5°B) substrates, with a moderate As/III=43 ratio. A second misoriented (+4°B) substrate was grown with a lower As/III ratio corresponding to that used for the growth of N-samples.

At high As/III ratio the substrate misorientation only marginally affects the top-QW emission wavelength, as expected of InGaAs QWs. The low growth temperature being largely below the InGaAs optimum probably explains the large linewidth as well as the low-energy component of the peak. The QWR emission experiences a 40 meV blueshift when increasing the miscut angle from 0 to +5°B. Alternatively, the high substrate misorientation strongly reduces the QWR - top-QW lines energy spacing. This surprising result calls for some comments. The substrate misorientation indeed affects the growth process in the V-groove. As demonstrated in the GaAs/AlGaAs system [311], the use of misoriented substrates leads to a comparatively larger development of the top-{311} facets, corresponding to the rounding visible on the TEM images. The lower temperature used in the work especially favors the development of those {311} top facets [299]. On Figure 5.11(b)-(c) are displayed side-view SEM images of samples grown on exact and misoriented (+6°B) (100) GaAs substrates, illustrating the effect of misorientation on the final groove size. The resulting misoriented groove is much larger than the exact

5.3. Influence of growth and structural parameters on nitrogen incorporation

counterpart. The changes induced in the surface dynamics may trigger a modification of the emission energy. A second point is that the latter sample was grown more than 1 year after the other experiments of the QWR project, together with the low-As reference sample: some drift of the MOVPE parameters may have occurred meanwhile.

The optical quality of the sample grown under the low As/III ratio is strongly deteriorated, the spectrum being much broader and exhibiting spikes, signature of carrier localization (see Figure 5.11(a)). This is not surprising since the low As/III=3 ratio is well below the optimal growth conditions. The slight miscut difference cannot be the origin of the strong discrepancies when compared with the misoriented reference, grown during the same period of time. The surface is likely Ga-rich, a situation with unpredictable consequences. The low As flux increases the adatom diffusion length during growth, and by capillarity yields larger, In-enriched QWRs: the low As, +4°B exhibits a sizeable –75 meV redshift when compared to the +5°B sample grown under high As partial pressure. We stress out that this QWR emission is still ~ 210 meV above that of N-containing QWRs grown with the same As/III=3 ratio. The same evolution is observed in InGaAs QDs grown with various As/III ratios (see Subsection 6.1.1.1), but the presence of DMHy changes this regime, as observed in Subsection 5.1.2. We observe that the optical quality of the N-free top-QWs is worse than that of top-QWs grown with nitrogen. The massive presence of DMHy, N and other decomposed products has a positive influence on the epitaxial growth mode in the As-depleted conditions.

5.3.2 QWR pitch and groove-groove interaction

Differences in the luminescence spectrum can be spotted when comparing QWR fields of various pitches. Figure 5.12(a) and (b) show spectra acquired on planar regions, as well as 10 and 1 μm pitch QWR fields, for both N-free and N-containing QW samples. If the top-QW is only marginally perturbed in the 10 μm pitch groove fields, both QWR and top-QW are systematically observed to be blueshifted when the pitch is decreased from 10 to 1 μm . Interestingly, the N-containing sample exhibits similar shifts as the N-free sample, indicating that the N incorporation rate is sensitive to the same physical phenomena.

This blueshift is primarily caused by the significant increase of the surface to be covered if the substrate is corrugated, in conjunction with the limited amount of material available for growth. For example, the surface of a 1 μm pitch, 350 nm-wide V-groove is 15 % larger than a corresponding (100) planar. This is a first reason why the top-QW tends to be thinner, hence to emit at higher energy, in V-groove fields. The magnitude of this effect is strongly diminished in the 10 μm pitch QWR fields, as the relative increase in surface area is much lower.

But a more subtle difference needs to be explained in some details, and is related to the adatoms diffusion length on the growing surface. The precursor last decomposition steps preferentially occur on the {111}A grooves facets, these effectively acting as a net source of adatoms. The decomposition products then diffuse over a few hundreds of nanometers, spreading out of the groove and perturbing the step flow in the vicinity of the groove. An

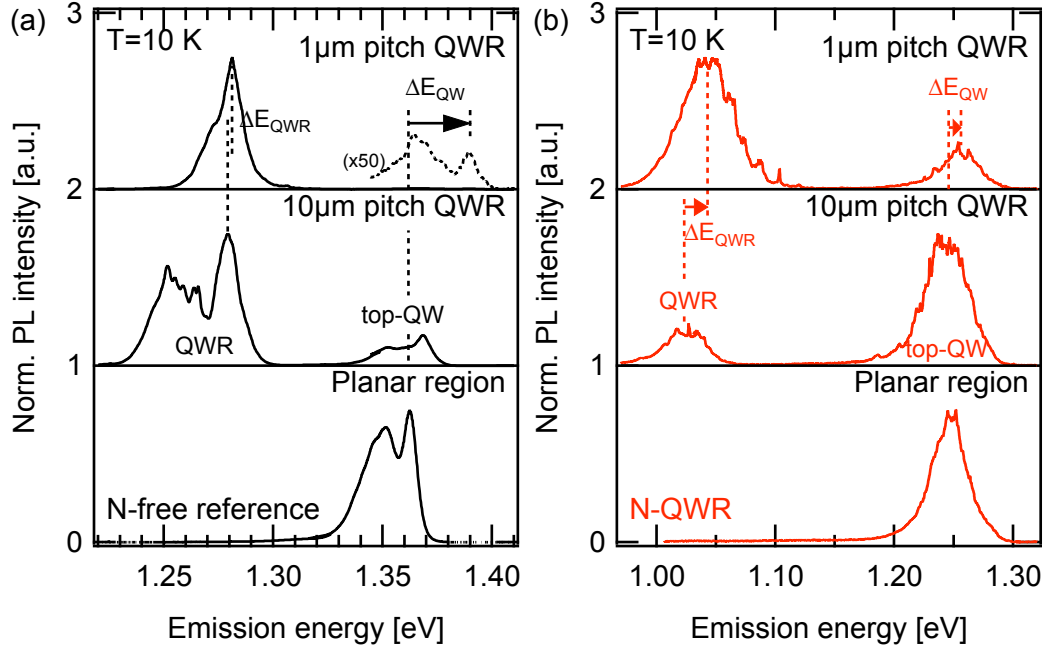


Figure 5.12: 10 K μ PL spectra of the N-containing and reference N-free samples introduced in Subsections 5.1.1 and 5.1.4, acquired on planar region as well as 1 and 10 μ m pitch QWR fields. A blueshift of the top-QW and QWR emissions are observed on the 1 μ m pitch field when compared to the 10 μ m pitch and planar regions.

omega-shape of the step flow front was already observed and reproduced by numerical simulations [312]. This effect is illustrated in Figure 5.13, showing a SEM picture of a 10 μ m pitch QWR sample grown on a +4°B misoriented substrate. The step-flow perturbation extends over 750 nm from the groove axis, establishing a lower bound to the adatoms diffusion length on the (100) surface.

This means that 10 μ m and 1 μ m pitch grooves do not experience the same growth regime. 10 μ m pitch V-grooves can be considered as independent (considering the adatoms diffusion). The isolated V-groove is merely a perturbation to the existing top-QW, and each QWR is able to catch material by capillarity from a quite large region surrounding the groove. On the contrary, in 1 μ m pitch fields, adatoms can diffuse from one groove to the next. Small-pitch V-grooves are thus in direct competition for decomposing the precursor molecules, and the QWRs are also competing to attract adatoms. Thus, the small-pitch QWR are thinner and emit at higher energy. This more intense competition for the available resources also depletes the top-QW that displays emission at a higher energy.

5.3.3 Effect of substrate misorientation

The effect of substrate misorientation on the N incorporation in planar QWs was discussed in detail in Chapter 4. Through PL, AFM and SIMS analysis, the N incorporation was shown

5.3. Influence of growth and structural parameters on nitrogen incorporation

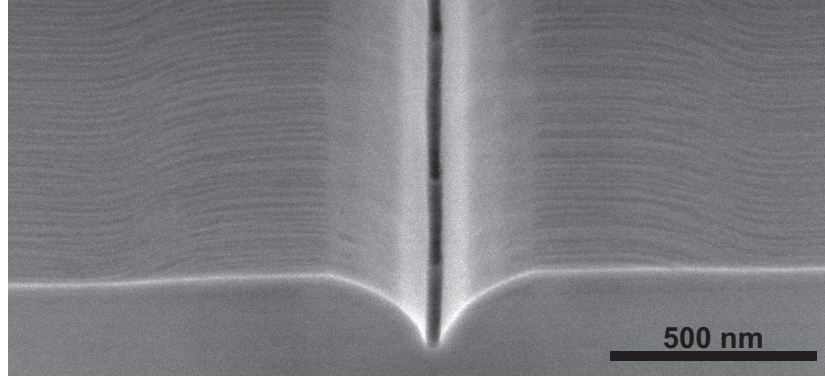


Figure 5.13: SEM side view of a cleaved +4°B misoriented QWR sample in the 10 μm pitch field, acquired 30° from the cleaved surface normal direction. The groove width after growth is ~ 500 nm. The step flow perturbation extends over ~ 750 nm away from the groove axis, meaning that grooves separated by 1 μm are interacting.

to be enhanced on misoriented-(100) GaAs substrates, promoted by the presence of atomic multisteps of increasing height. A parameter so easy to tune and with such a dramatic effect had thus to be checked in the QWR system as well. A second motivation is that GaAs/AlGaAs V-groove QWRs grown on misoriented substrates showed increased homogeneity when compared with their exact-(100) counterpart [108, 311]. The QWR emission FWHM was found reduced, together with a partial disappearance of the sharp features in the μPL spectrum, indicating a reduction of the disorder at the length scale of excitons and above.

To probe the effect of the substrate miscut angle, 4 samples were grown simultaneously using substrates of various misorientation (exact-(100), +4°B, +5°B and +6°B). The misoriented samples are tilted with respect to the (100) plan along the axis of the grooves. The 4 samples considered here have a very similar groove width, slightly larger than the sample imaged by TEM. The growth procedure is otherwise identical to the N-QWR samples presented above. Figure 5.14 displays the room temperature spectra of the 4 samples acquired in the planar (top-QW) as well as the 1 and 10 μm pitch QWR regions. The spectra were normalized for clarity but have quite similar PL intensities.

As already observed in Chapter 4, the N incorporation in the top-QWs strongly increases with misorientation. It is worth mentioning that the thicknesses of the 2 growth steps (0.8 + 2.2 nm) are not optimized so as to cover the multisteps formed during growth. Parts of the GaAs surface remain uncovered as the second growth step proceed with high DMHy flux. The redshift is consequent, -75 meV for the +6°B sample compared to exact-(100), and the spectral linewidth is also broadened.

By contrast, the QWR appears only slightly affected by the misorientation. Their emission spectra present a small shift to the blue in the 1 μm pitch field, while no appreciable shift is observed on the 10 μm pitch region. This different behavior indicates that the N incorporation in the QWR is only marginally influenced by the substrate misorientation. The numerous steps

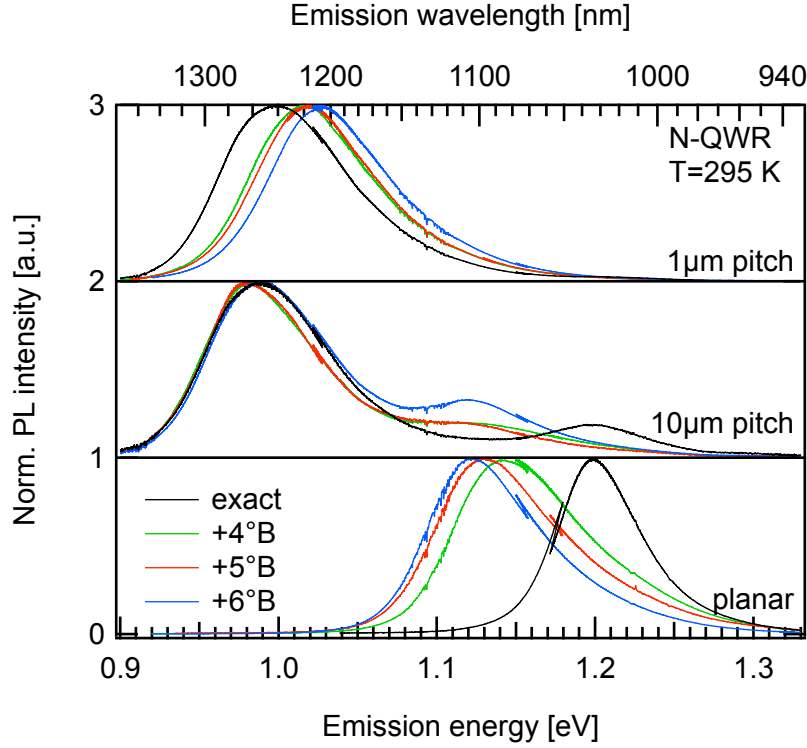


Figure 5.14: Room temperature spectra of 4 V-groove QWR samples grown side-by-side, acquired on a planar (top-QW) region as well as 1 and 10 μm pitch QWR fields ($P_{\text{exc}}=300\mu\text{W}$). Misorientation: exact-(100) (black), $+4^\circ\text{B}$ (green), $+5^\circ\text{B}$ (red) and $+6^\circ\text{B}$ (blue). The N incorporation into the top-QW is favored on misoriented substrates. By contrast the QWR emission appears only marginally affected by the miscut.

and multisteps already existing at the groove bottom probably enhance the N-incorporation like the steps on a planar misoriented surface, whatever the sample actual substrate misorientation is. The groove-to-groove influence and the modification of the V-groove shape upon growth probably explain the variation of the QWR emission with pitch.

It is known that the shape of a V-groove undergoes modifications when increasing the substrate misorientation. V-groove QWRs grown on exact wafers tend to preserve quite well the original groove shape, even if the top- $\{311\}$ facets expand significantly thanks to the low reactor temperature. With increased misorientation, the top- $\{311\}$ facet extends increasingly inwards and outwards, eventually consuming the initial quasi- $\{111\}$ A facet as observed by Moret *et al.* [311].

As depicted on Figure 5.11(b)-(c), if the groove final width is $\sim 300\text{ nm}$ on an exact-(100) orientation, it extends over $\sim 500\text{ nm}$ on a $+4^\circ\text{B}$ and even $\sim 650\text{ nm}$ on a $+6^\circ\text{B}$ substrate. The groove enlargement is due to the extension of the top- $\{311\}$ facets. In all our samples the $\{111\}$ A facets still exist after the growth of the cap. The modification of the groove shape and of the surface ratio between top-QW and QWR affects the distribution of InGaAsN material

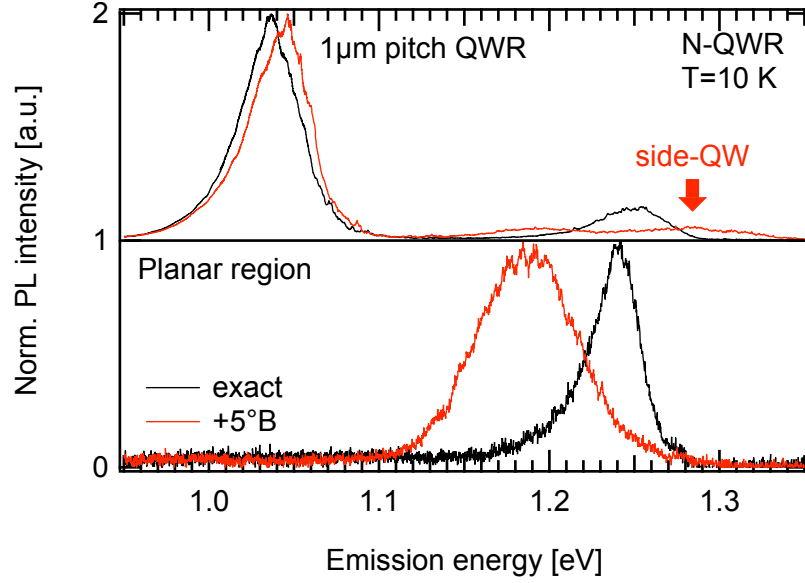


Figure 5.15: Low-temperature PL spectra of the exact-(100) (black) and +5°B (red) misoriented N-QWR samples, acquired on planar region ($P_{\text{exc}}=100$ nW) and 1 μm pitch QWR field (1 μW excitation). The red arrow points to an additional peak present on the misoriented-substrates V-groove QWR spectra.

and modifies the QWR and top-QW emission energies. This effect becomes obvious when the groove pitch is small (1 μm). This mechanism was already observed in the GaAs/AlGaAs system [311]. The same work also reported a reduced disorder in QWR grown on misoriented substrates. The sole linewidth criterion does not allow us to determine if it also improves the InGaAsN QWR quality. The misoriented top-QW is however severely degraded, as expected from a thin QW grown on a step-bunched template.

Finally, the red arrow on Figure 5.15 points to an additional peak detected on misoriented substrates. We tentatively identify this peak to a QW-like structure formed on the top-{311} facets. A thicker QW was evidenced by TEM on samples grown on exact-(100) substrates, although the associated luminescence was not observed. The much larger spatial extension of these structures on misoriented substrates is likely to increase the intensity of the luminescence signal.

As substrate misorientation is of limited influence on the N incorporation in the QWR, the following studies were conducted on wafers of various misorientations. The substrate mis-cuts are systematically indicated and the samples presented in this subsection are used as references.

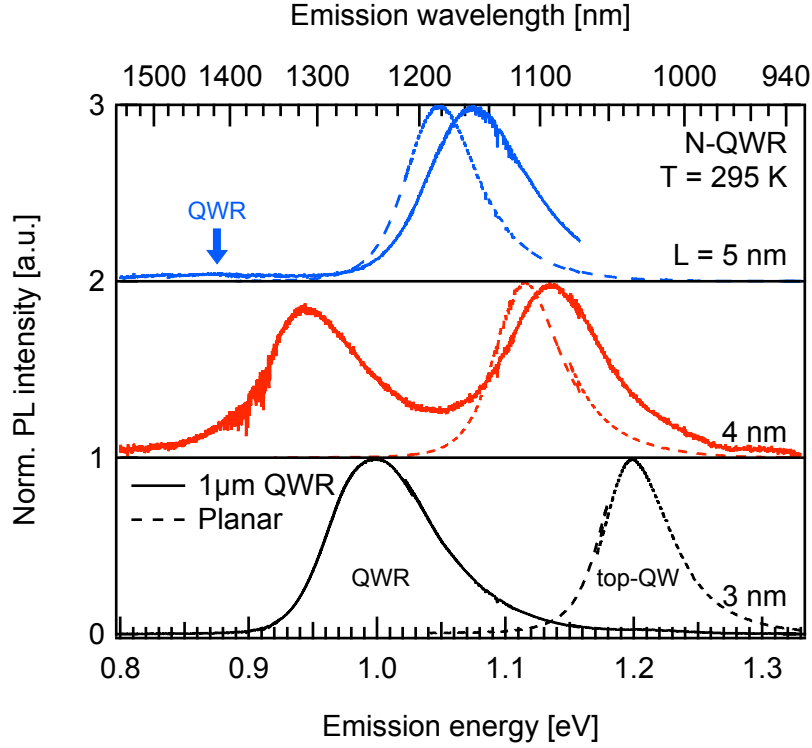


Figure 5.16: Normalized RT μ PL spectra of V-groove QWR samples grown with various nominal QWR thicknesses ($L = 3, 4$ and 5 nm), while keeping constant the first of the 2 growth steps with low DMHy flux (0.8 nm). Spectra were acquired both on a planar region (dashed) and on $1\ \mu\text{m}$ pitch QWR regions (continuous) ($P_{\text{exc}}=300\ \mu\text{W}$). The top-QW is strongly redshifted with increased thickness, and its intensity remains quite constant. The QWR emission is also redshifted but its intensity dramatically drops.

5.3.4 QWR thickness

The longest room temperature emission wavelength of InGaAsN V-groove QWR achieved in the experiments mentioned above was 1265 nm, close to but not reaching $1.3\ \mu\text{m}$. Longer wavelengths are desired and thicker QWR structures are potentially good candidates for such purpose. The QWR nominal thickness was varied in two samples and compared with the N-QWR sample already presented (see Section 5.1). The nominal thicknesses were $0.8 + 3.2 = 4$ nm and $0.8 + 4.2 = 5$ nm compared to the $0.8 + 2.2 = 3$ nm of the existing sample, grown on substrates with zero nominal miscut.

The room temperature μ PL spectra of the three samples are displayed on Figure 5.16. Both planar regions (dashed line) and $1\ \mu\text{m}$ pitch QWR fields (solid line) were characterized. The top-QW experiments a sizeable redshift when increasing the layer thickness (1.2 eV for the 3 nm, 1.05 eV for the 5 nm QW). The QWR emission is also strongly redshifted in the last samples: the 5 nm QWR emits at $1.38\ \mu\text{m}$ wavelength. Simultaneously, the QWR intensity dramatically drops down, depicted on Figure 5.17(b). The thickest QWR is fainter by ca. 2 orders of magnitude,

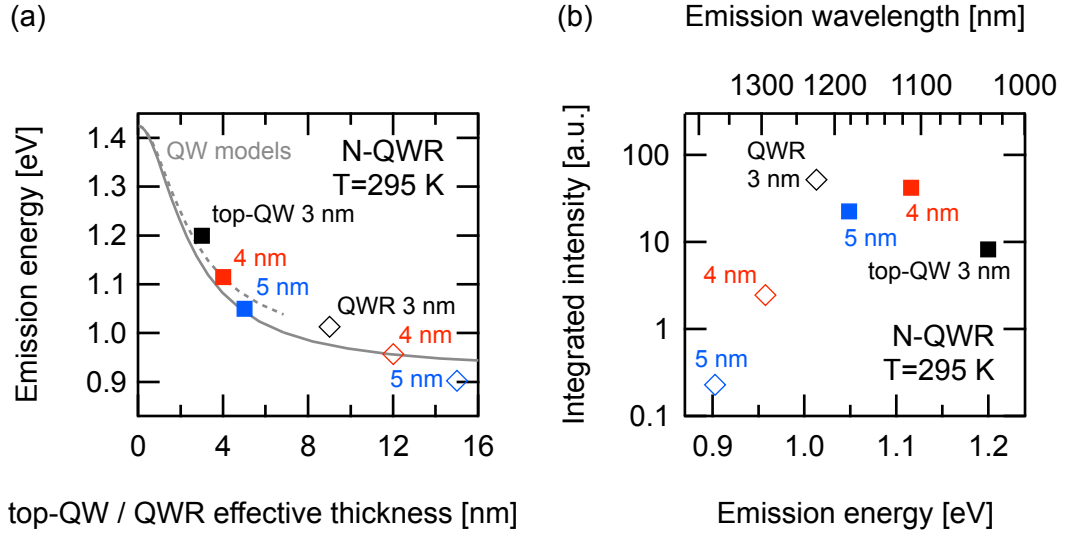


Figure 5.17: (a) Emission energies of the top-QW (squares) and QWR (open diamonds) as functions of the expected heterostructure thicknesses, for the three samples shown on Figure 5.16. The solid lines represent the emission energy of two InGaAsN/GaAs QWs models of composition estimated to be grossly similar to our nanostructures (see text). (b) Integrated intensities of the top-QW (squares) and QWR (open diamonds) as function of the peak emission energy. In opposition to the top-QW, the QWR experiments a dramatic decrease in intensity.

similar at low and room temperature. Such a dramatic decrease in emission intensity is likely to make these structures unsuitable for most of potential applications.

The magnitude of the emission redshift is surprisingly high considering the small changes in the nominal layer thickness. The emission energies of the top-QW measured in planar regions are displayed on Figure 5.16(a) (squares) as a function of the nominal deposition. The black line represents the emission energy calculated with a QW model described in Subsection 4.2.1, with parameters picked up from the literature [140, 158]. A square potential InGaAsN/GaAs QW structure was considered, with In content $[In] = 25\%$ and with N composition adjusted to the data ($[N] = 1.8\%$). The QWR energies (measured at identical power levels) are also reported on the graph (diamonds) as a function of their expected thicknesses, calculated as 3x the nominal value (the measured acceleration factor is 3.5). This lower value was chosen to take into account the non-uniform thickness of the crescent-shaped QWR. The continuous line represents a QW model with increased In content (30%) and identical N content. A 1D-confined QW model is certainly not suitable to calculate the energy levels of a QWR. However, as the vertical confinement is stronger than the in-plane, this simple picture is sufficient to estimate the QWR ground state energy.

The top-QW and QWR emission energies do not follow the curves of the ideal QW model. Instead, the evolution of both QWR and top-QW prove more abrupt than predicted by the model. Small changes in the model element concentrations or parameters would not account for this

discrepancy of behaviors, since the curve shape is mostly determined by the confinement strength, i.e. the structure thickness.

It may be that the plotted thicknesses are bad estimates for the width of the square potential of the model. The interfaces may be less sharp than expected as a result of some atomic interdiffusion. But the steeper dependency of the data suggests the widths have been overestimated, which is not consistent with a possible structural enlargement.

The discrepancy is more probably due to differences in the In and N composition between samples, and/or to a non-uniformity of the element distribution within the structures. Due to segregation effects, In QWs tend to present relatively smooth interfaces [203], but there is no reason to suspect variation in the In content of the three samples. A stronger N incorporation in the thicker structures is a more likely hypothesis. The N distribution can fluctuate according to location (first/second interface, core, etc.) and from sample to sample. The strong influence of In on N incorporation, the 2-step growth method as well as the growth interruption after QWR deposition may lead to variations in the average N concentration, probably linked to a non-uniformity of the N distribution within a single sample. As more N implies more defects, the drastic reduction in QWR PL efficiency for the thicker structures supports this conclusion.

Two main origins of the stronger N incorporation in thicker structures can be mentioned here. First, the thicknesses and fluxes of the 2-step growth process described earlier may not be optimal for the QWR structures considered here. The SIMS results obtained in Chapter 4 indicate an accumulation of N at the QW lower interface. In this framework a thicker structure only extends the region where the N content is low. Hence the 5 nm structures should have an overall lower N content than the 3 nm, in contrast to the tendency observed. This suggests another scenario, where the N of the upper part of the QWR actually desorbs after being incorporated. This desorption would occur during the 2 min of growth interruption required to raise the reactor temperature up to 590 °C. A high arsine flux is maintained during that period to partly prevent the mass transport occurring on the surface. The numerous As atoms diffusing on the surface can then replace the N atoms located close to the surface via As-N exchange, depleting the N content of the first few angstroms of material near the surface. In this scenario a 3 nm-thick structure would be significantly depleted, while the thicker 5 nm-thick layers would maintain an overall higher N content. Additionally, the residual mass transport occurring at the sample surface tends to drive more material into the QWR region. In this scenario, the upper few MLs of the QWR layer are likely to be composed of pure InGaAs, and the average N concentration to be higher in thicker QWRs.

In summary, we compared the emission of QWRs of different thicknesses and observed a pronounced redshift of the thicker structures, associated with a degradation of the optical quality. Combining these two observations suggests a larger N incorporation in thicker structures, explained by the N-As exchange during the second growth interruption, as well as by the composition of the material transported during this phase. These phenomena could be prevented if a small cap was deposited immediately after the QW layer before the interruption, hindering the mass transport and group-V atoms exchange phenomena. This possibility is further explored in the next subsection.

5.3.5 GaAs cap layer on QWR

The 2-step procedure used to grow the QWR includes 2 growth interruptions, right before and right after the InGaAsN QWR layer deposition. The purpose of these interruptions is to allow the reactor temperature to be adjusted and stabilized between the 590 °C suitable for the GaAs growth, and the lower 520 °C necessary for N incorporation. The interruptions were respectively 3 and 2 min long during which the reactor was kept under arsine atmosphere to prevent surface degradation, as well as to limit mass transport processes on the non-planar surfaces.

If growth interruptions are an essential step of Stranksi-Krastanow (SK) nucleation, it is seldom used in more regular epitaxy processes. Its effects can be summarized in a few points. First, the same surface adsorbs contaminants for a long time, generating a layer with a high density of defects. This degradation can be postponed in the case of GaAs by maintaining the wafer under arsine atmosphere. An increase of the surface roughness with interruption time was reported [313], even if short interruptions of a few seconds were also observed to improve the quality of InGaAs QWs prior to such degradation [314]. A second effect relates to far-from-equilibrium alloys like dilute nitrides. The interruptions let the fresh material exposed to the As-rich atmosphere, leading to group-V atoms exchange and N desorption from the layer. A last important point is the mass transport occurring on the surfaces. This can be used for example to control the SK QD size distribution. In MOVPE growth on non-planar substrates, the sharpness of the recess profile is affected by a combination of growth rate anisotropy and capillarity (mass transport). When the growth is stopped, the profile tends to flatten and widen, thus enlarging and thinning the nanostructure. Following Biasiol et al. [99], the radius of curvature of the QWR lower interface can be estimated to increase two-fold after a 3 min growth interruption at constant temperature.

A sample was dedicated to the exploration of the nitrogen desorption during the 3 min growth interruption following the QWR layer deposition. Its structure was based on the usual recipe, except for a 3 nm GaAs cap deposited immediately after the QWR layer, i.e. before the second growth interruption. The As/III ratio was high 100 like in the barriers, and TMGa was used as Ga precursor in spite of its known tendency to incorporate carbon and form defects at low temperature [315]. The sample was grown on a +6°B misoriented substrate. During the interruption the mass transport drives more material to the QWR due to its strong surface curvature. As the higher-mobility In atoms are also preferred, the resulting QWR is wider, thicker and In-enriched. The deposited cap quenching this mechanism, a blueshift of the capped QWR emission is expected, as long as nitrogen incorporation is not affected.

Room temperature spectra of this sample are shown on Figure 5.18 together with that of the corresponding sample grown without cap, for both planar and 1 μm pitch QWR regions. The relative intensity of each pair of curves was preserved to allow direct visual comparison of the luminescence efficiencies. The same changes in the spectrum are observed at low and room temperature.

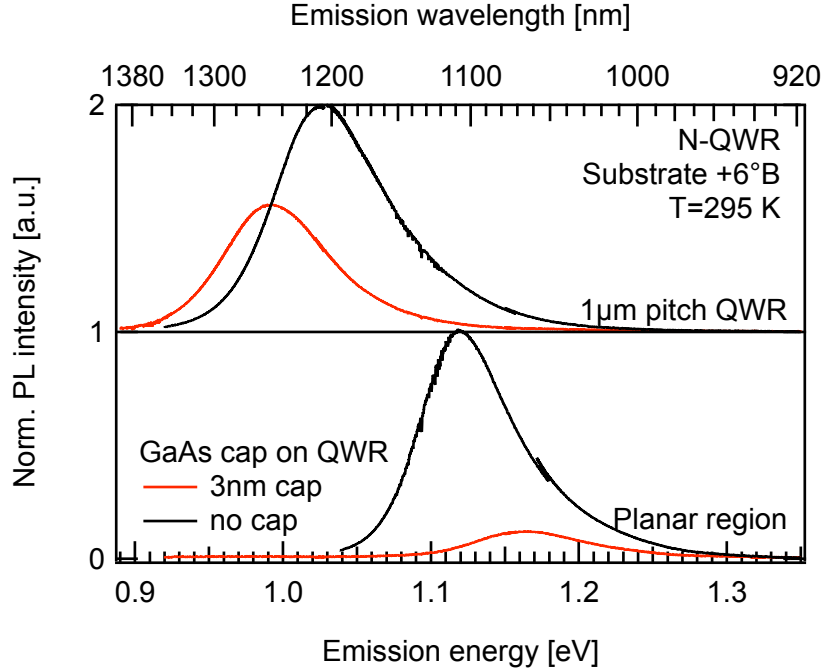


Figure 5.18: Room temperature μ PL spectra of two samples grown on wafers of same misorientation ($+6^\circ\text{B}$), nominally identical except for the deposition of a 3 nm GaAs cap immediately on the QWR layer after its deposition ($P_{\text{exc}}=300 \mu\text{W}$). Spectra were acquired on both $1 \mu\text{m}$ pitch QWR array and planar regions. To allow visual comparison the PL intensities, the relative intensity of each pair of curves was preserved. The quenching of N atoms desorption is evidenced by the QWR emission redshift of -40 meV . Defects incorporated during the 520°C GaAs growth strongly degrade the top-QW emission of the capped sample. The QWR PL efficiency is comparatively better preserved.

The top-QW emission experiences a strong decrease in intensity together with a blueshift. The intensity decrease suggests a degraded crystal quality in the vicinity of the active layer, due to the use of TMGa as Ga precursor at low reactor temperature. The origin of the energy shift is less clear. It may be that the high As flux used for the cap growth allows for group-V atoms exchange, but more probably the cause resides in the deposition of bad quality GaAs over the active layer. A growth repetition on non-misoriented substrates may allow deciding between these hypotheses.

By contrast, the QWR emission is significantly redshifted (-40 meV), evidencing the effectiveness of the cap in preventing the N-escape during the growth interruption. The redshift induced by the mass transport is more than compensated by the quenching of nitrogen desorption by the cap. The small decrease of PL intensity shows a limited negative influence of the cap deposition on the crystal quality. That may be originated by a lower probability of carrier trapping on non-radiative impurities, related to the low dimensionality of the wavefunctions. Also, the chemically more active $\{111\}\text{A}$ facets may assist the precursor proper decomposition and help forming a better crystal quality at the groove center. Indeed, the reduction in PL in-

tensity may be exclusively due to defects associated with the presence of the higher N content in the QWR, responsible for the observed redshift.

5.3.6 Growth temperature

The modification of the reactor temperature has multiple effects on the growth mechanisms. Some thermally activated processes do not occur below a certain critical temperature, and the kinetics of many more are strongly dependent on the actual temperature. A decreased reactor temperature is generally observed to enhance the nitrogen incorporation efficiency, in GaAsN but mostly in GaInAsN alloys [203]. In this latter case the evolution with temperature suggests an underlying thermally activated process triggering N desorption from surface: a low temperature ($< 550^{\circ}\text{C}$) is to be preferred. On the other hand such temperatures degrades the quality of GaAs-based alloys. A degradation of the crystal quality appears unavoidable below 500°C . TMGa also experiences an incomplete decomposition at lower temperatures [191, 128], resulting in a lower level of control on the growth rate and incorporation of defects. Consequently, the optimal reactor temperature is generally held in the 520 to 530°C window [200].

As previously mentioned all the reactor temperatures stated in this work are nominal and differ from the actual values of the surface temperature of the substrate. The 590°C temperature used for the growth of GaInAs nanostructures is estimated to be actually close to 560°C . The 520°C temperature was chosen during the QW optimization process performed by Prof. D. Fekete during his stay in our Laboratory, and is estimated close to 500°C . This last temperature is lower than the 520 - 530°C commonly reported optimal for the MOVPE growth of GaInAsN, but the presence of the $\{111\}\text{A}$ facets in the V-grooved substrates may facilitate the decomposition of precursors as compared with $\{100\}$ surfaces. The crystal quality could be preserved in the recesses as opposed to planar heterostructures, as hinted by the results obtained on the QWR samples capped with GaAs at low temperature.

In order to explore the effect of temperature and increase the emission wavelength of our QWR samples, two growth runs were performed at nominal 500°C (20°C lower than usual), on exact- (100) and $+4^{\circ}\text{B}$ misoriented substrates. The expected effect of this lower reactor temperature can be described as follow. First, less N desorption from the surface should occur [223], which would shift the emission to the red. Second, reducing the temperatures lowers the species surface diffusion lengths, and so hinders the mass transport to the QWR. However the results of Biasiol *et al.* [99] suggest that a 20°C difference should not lead to dramatic modification of the radius of curvatures and emission energies. Finally, a partial decomposition of TMGa precursor leads to thinner, In-enriched nanostructures. As long as N is not involved, such a nanostructure would emit at lower energy when considering the parameters range used here. But the increased In concentration may favor the N desorption, which would in turn blueshift the emission.

Figure 5.19 shows room temperature normalized μPL spectra of QWR samples grown at 520°C

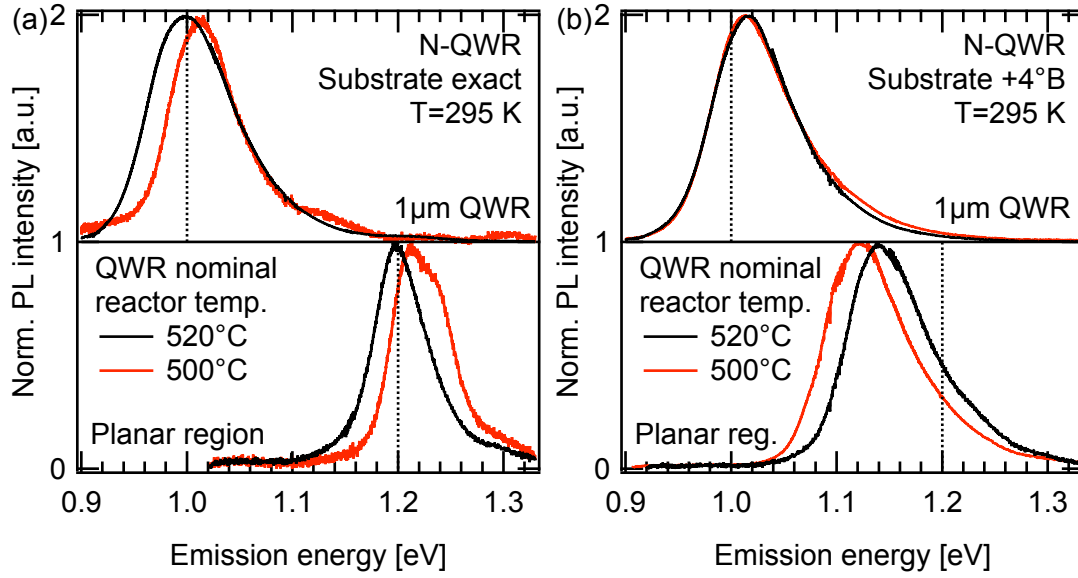


Figure 5.19: Room temperature spectra of InGaAsN QWR samples grown nominally at 500 °C (red) and 520 °C (black), acquired on planar and 1 μm pitch QWR regions at 300 μW excitation power. Samples grown on (a) exact and (b) +4°B misoriented substrates were characterized. To ease comparison, vertical dashed lines are placed on both graphs at same energy. A low reactor temperature increases the QW shift with misorientation. If the 1 μm pitch QWR grown at 520 °C are affected by misorientation (see Subsection 5.3.3), the sample grown at 500 °C are more similar.

and 500 °C, on both planar and 1 μm pitch QWR regions. Spectra for samples grown on exact-(100) substrates are displayed in Figure 5.19(a), while the case of +4°B substrates is shown in Figure 5.19(b). To ease comparison, vertical dashed lines are added on both graphs at the same energies. The top-QW is more strongly affected by the change of substrate misorientation on samples grown at 500 °C than at 520 °C. In the two cases the underlying GaAs was deposited at 590 °C before the growth interruption, so the growth template should be similar. The cause of the increased sensitivity to substrate misorientation remains unclear, as multiple effects occurs, affecting the N incorporation in one way or the other.

As reported in Subsection 5.3.3, the 1 μm pitch QWR array grown at 520 °C emits at different energies depending on the substrate misorientation, while the 10 μm pitch structures show similar spectra. This was explained by the modification of the groove shape associated with the groove-to-groove interaction, affecting the surface fluxes towards the QWR. The QWR emission energies of the samples grown at 500 °C are similar, both on 10 and 1 μm pitch V-groove arrays. This can be explained by a reduction in the adatom surface diffusion caused by the temperature decrease, making the groove-to-groove interaction less important. The sample grown on exact-(100) substrate shows a strong (10-fold) decrease in PL intensity as compared to the counterpart grown at 520 °C. The PL intensity decrease is also observed, although less marked, on the misoriented substrate. It may that the presence of multi-steps

5.3. Influence of growth and structural parameters on nitrogen incorporation

promotes the proper TMGa decomposition and therefore helps to prevent the incorporation of impurities in the crystal.

However, the main motivation of tuning the reactor temperature was to achieve longer emission wavelength. Although emission energy changes are indeed observed, the intended redshift did not occur.

5.3.7 DMHy flux

The most obvious way to increase the N content and shift the emission wavelength is to increase the DMHy precursor flux in the reactor. The N content is however not satisfactorily determined by the group-V gas-phase ratio, as it was reported that a super-linear incorporation was observed while all the other parameters were kept constant [203].

To probe the effect of the group-V gas-phase ratio, a sample with increased DMHy flux was grown on a +6°B misoriented substrate. The flux was only increased during the second growth step so as to prevent any excessive N accumulation at the first interface, which could otherwise induce defects. The value of the DMHy flux used (290 ccm) is close to the limits of our MOVPE reactor.

Figure 5.20 displays room temperature μ PL spectra of this sample and of another one grown with the usual DMHy flux. Spectra acquired on planar region as well as 1 and 10 μ m pitch QWR fields are shown. The top-QW and QWR emissions are systematically redshifted, however by a limited amount (ca. 15 to 20 meV), while the DMHy flux was increased by almost a factor 1.5 during most of the deposited thickness. If (as an over estimation) assuming a linear N incorporation with DMHy flux and an initially uniform N distribution in the nanostructures, this suggests a fairly low initial N incorporation (60 to 80 meV redshift). The small emission redshift confirms the previous indications of a non-constant N distribution in our nanostructures, with a high N incorporation close to the lower interface and a smaller content at the upper one. If the PL intensity is comparable in the two samples with different DMHy flux, the emission linewidth is observed largely increased in the second. The top-QW RT FWHM is increased from 75 to 96 meV, and the 1 μ m pitch QWR linewidth increases from 85 to 136 meV. This broadening appears independently of the excitation power level, and was confirmed by measurements performed in different locations.

To summarize, if increasing the DMHy flux increases the N incorporation in our nanostructures, a significant degradation of the emission linewidth is simultaneously observed in the spectra. A probably more effective bandgap tuning could be achieved by increasing the DMHy flux during the first growth step, at the risk of generating more defects.

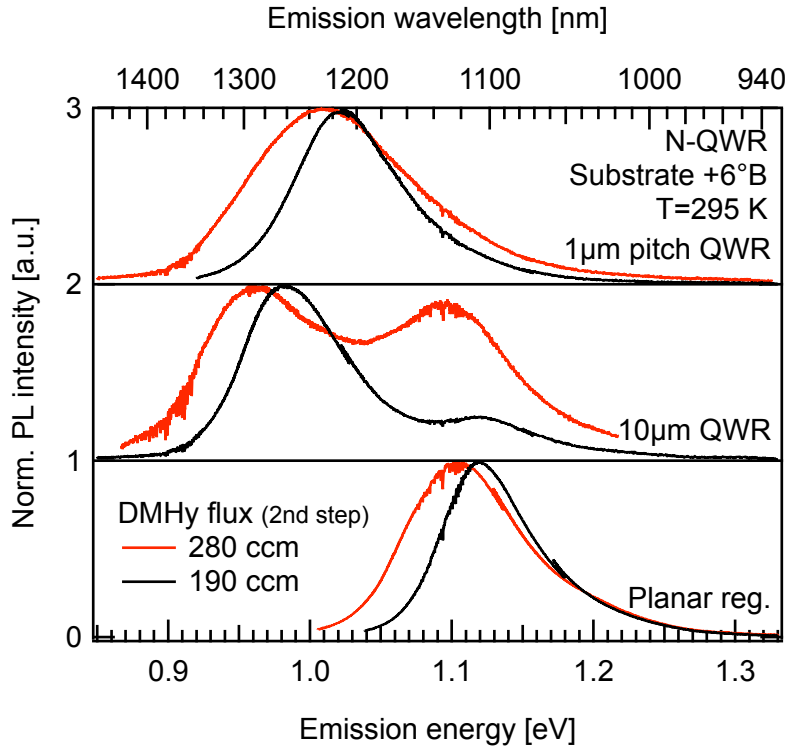


Figure 5.20: Room temperature spectra of samples grown with usual and increased DMHy flux during the second growth step, acquired on planar parts and on 1 and 10 μm pitch QWR regions. The QWR layer was nominally 0.8 nm thick and was deposited with a DMHy flux of 26 ccm, followed by 2.2 nm with 190(280)ccm of DMHy. The excitation power was 100 μW for the QWR and 300 μW for the top-QW. The emissions of the DMHy-rich sample are slightly redshifted but also significantly broadened.

5.3.8 Growth rate

As a general rule, a decreased growth rate allows more time for the N atoms to desorb and/or be replaced by As atoms diffusing on the crystal surface. If some contradictory results are reported for the GaAsN alloy [203, 129], a linear increase of the N incorporation with growth rate is observed in the case of GaInAsN [203]. On the other hand, the growth rate also substantially affects the QWR shape. A slower growth rate of the InGaAsN layer increases the adatoms surface diffusion length, thus enhances the mass transport to the groove bottom. The self-limited radius of curvature (not reached in the case of the QWR upper interface) follows a power law $\rho_{sl} \sim R^{-1/3}$, meaning that a 2-fold slow down of the growth rate should increase the radius of curvature by a factor 1.25 [99]. A slower growth rate may result in a redshift of the QWR emission if the mass transport is the stronger mechanisms, or in a blueshift if the N incorporation is dominant.

A new sample was fabricated with a growth rate during the QWR deposition diminished 2-fold as compared with the usual recipe: 139 nm s^{-1} instead of 278 nm s^{-1} . As the growth rate

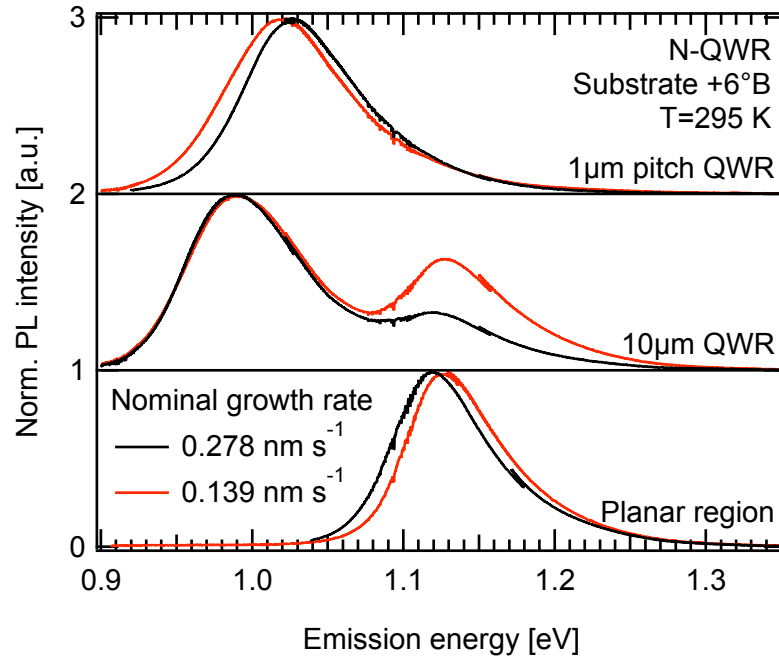


Figure 5.21: Room temperature μ PL spectra of two InGaAsN/GaAs V-groove QWR samples grown on $+6^\circ\text{B}$ misoriented substrates, with different growth rates during the QWR growth stage, acquired on planar region and 1 and 10 μm pitch QWR fields, with 100 μW as excitation power. The 10 μm pitch QWR shows no shift in emission energy, while the 1 μm pitch emits at a slightly lower energy.

was only changed during the QWR layer growth, the template at the beginning of the QWR growth is expected to be identical in both samples. The DMHy flux was also diminished by a factor 2, so as to maintain a constant DMHy/III gas-phase ratio. However, the arsine flux was kept constant, attempting to maintain a similar QWR shape. Therefore, the DMHy/As ratio is decreased by a factor 2, which should further decrease the N content.

Figure 5.21 displays room temperature μ PL spectra of these two samples together with that of a reference sample, acquired in a planar region as well as on 10 and 1 μm pitch QWR fields. The top-QW of the sample with slow growth rate shows a slight emission blueshift (~ 7 meV). Both the reduced growth rate and the lower DMHy/As ratio could generate this shift by reducing the N content. In that perspective, it is surprising that the top-QW shift is not much more pronounced. However, the QW growth conditions are different from the bulk situation owing to the template surface, as the strong substrate misorientation ($+6^\circ\text{B}$) generate multisteps almost as high as the thickness (3 nm) of the QW layer.

As the QWR structure is definitely thicker than the possible multisteps created on its lower interface, the blueshift of the slow growth rate sample should be pronounced due to the combined effects of the nitrogen desorption and of the lower DMHy/As ratio. However, the 10 μm -pitch QWR spectra look very similar, as the tiny energy difference between the two samples lies within the reproducibility error. This suggests that the expected lower N content is

counterbalanced by another effect, likely the enhanced mass transport toward the QWR. As the growth rate is increased, the atoms on surface have less time to diffuse before incorporation, which enhances the capillarity strength, attracting more material to QWR location. This results in a thicker, In-enriched QWR. As the QWR is only ~ 11 nm at its thickest point, a few additional nm can compensate for a significantly reduced N concentration. As an example, the ground state of a 1.5 % N, 30 % In 10 nm-thick QW closely matches the one of a 13.5 nm QW with 1.2 % N.

The $1\text{ }\mu\text{m}$ pitch QWR array situation is somewhat different, with the sample with reduced growth rate shifting less to the blue than the other when compared to the $10\text{ }\mu\text{m}$ pitch emission. As evidenced by SEM, the $1\text{ }\mu\text{m}$ pitch grooves do not evolve independently as the adatoms diffusion length is comparable to the pitch. The QWR blueshift when reducing the pitch is explained by the increased competition between QWRs to attract the material available. In that perspective, the increased diffusion length for the slow growth rate sample should make the $10\text{ }\mu\text{m}$ and $1\text{ }\mu\text{m}$ pitch cases even more dissimilar. This is opposite to the effect actually observed, as the 1 and $10\text{ }\mu\text{m}$ pitch QWRs emit at closer energies when decreasing the growth rate. Some unclear effects are responsible for the discrepancy, limiting the validity of the conceptual framework used to interpret the energy shifts of our N-containing QWRs.

The growth rate proved itself an inefficient parameter to shift the emission wavelength of V-groove QWR, because of its counterbalancing effects on the QWR thickness and N incorporation efficiency. The influence of the growth parameters is quite well understood in InGaAs structures. While the adjustment of growth parameters is already a non trivial task in N-containing QWs, N incorporation in non-planar heterostructures adds an additional degree of complexity. Variations of a single growth parameter can have multiple effects in the shape, thickness and composition of the resulting nanostructure.

5.3.9 Summary

To summarize, the influence on the InGaAsN QWR emission spectrum of a wide range of growth and structural parameters was explored. Room temperature $1.3\text{ }\mu\text{m}$ emission from GaInAsN QWR has been obtained, as shown on Figure 5.22. Several sets of growth parameters indeed allow for reaching this technologically relevant spectral window, with a certain tolerance on the thickness, composition and cap deposition on the QWR. Two examples are given: 4 nm-thick QWRs grown on a $+5^\circ\text{B}$ misoriented wafer without cap, and 3.5 nm-thick QWRs on $+0.3^\circ\text{B}$ misoriented wafer covered by a 3 nm TEGa cap. These two samples have comparable PL efficiencies. Capping with TEGa seems as effective as with TMGa, with the advantage of an improved top-QW PL intensity. A further analysis is difficult as the latter sample was the only one growth with such capping, and its QWR thickness does not match that of any other sample. Another example of $1.3\text{ }\mu\text{m}$ QWR emission is visible on Figure 5.16. The QWR long-wavelength PL efficiency can probably be improved by optimizing the growth procedure and parameters. However, while not definitely excluded, the fabrication of high-quality QWR emitting in the

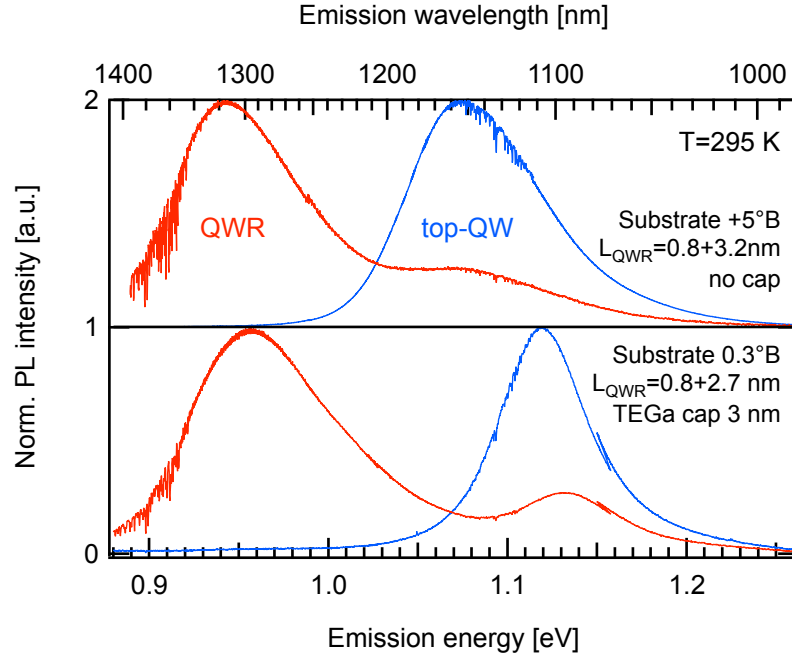


Figure 5.22: Room temperature μ PL spectra of InGaAsN/GaAs V-groove QWRs samples grown under various conditions indicated on the figure. Spectra were acquired on planar regions (top-QW, blue) and on $1\ \mu\text{m}$ pitch QWRs (red) emission, with $\sim 100\ \mu\text{W}$ as excitation power. The QWR emission wavelength lies at or above $1.3\ \mu\text{m}$.

$1.55\ \mu\text{m}$ telecommunication window appears very challenging.

5.4 QWR disorder characterization

In the previous section, different ways were explored to shift the QWR emission energy to longer wavelengths. In the following, the quality of the layers and the defects incorporation are discussed, by evaluating the magnitude of the so-called S-shape of the bandgap energy with temperature, and the influence of sample annealing on the optical properties. The emission from short ($\sim 1\ \mu\text{m}$) QWR segments fabricated by mesas etching is also characterized to help the interpretation of the results.

5.4.1 Defects incorporation determined by PL temperature dependence

The large amplitude of the electronic potential fluctuations in (In)GaAsN heterostructures leads to a particular temperature dependence of the emission energy, diverging from the usual behavior based on the empirical Varshni law. At low temperature, the charge carriers diffuse to and recombine in the electronic potential dips, acting as carriers traps: the PL signal is dominated by the emission from impurities. When the temperature is increased the bandgap progressively shrinks, but the carriers are simultaneously allowed to escape from the

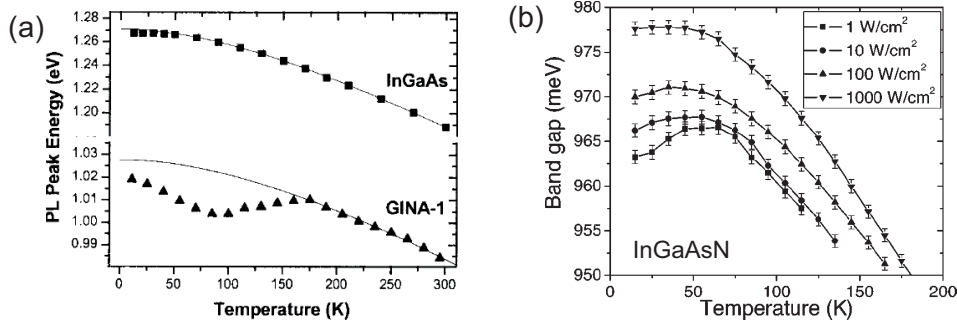


Figure 5.23: (a) PL energy of MBE grown InGaAs and InGaAsN (GINA) samples. The continuous lines are Varshni fits, evidencing the S-shape evolution of InGaAsN. Graph adapted from [217]. PL emission energy of an MBE-grown InGaAsN QW sample as a function of the sample temperature, using 4 different excitation power densities. The S-shape becomes more apparent as the excitation power is decreased, since originated from deep electronic traps. Graph from [218].

traps (defects ionization). The usual emission energy decrease is therefore reduced, cancelled or even reversed at temperatures below ~ 100 K, forming the so-called S-shape [316, 218] temperature dependence visible on Figure 5.23. A reduced S-shape effect is a sign of good sample quality, as it contains less deep defects that are optically active.

To probe the quality of our QWR samples, a N-containing QWR sample grown on a exact-(100) GaAs substrate was studied versus temperature in view of characterizing the amplitude of its S-shape. The excitation power was chosen constant and quite high to allow signal detection at room temperature (only a low sensitivity optical spectrum analyzer HP 86140 was available at that time). The power density equivalent to the $300 \mu\text{W}$ used for the experiment can be estimated to be close to $\sim 10\,000 \text{ W cm}^{-2}$ if assuming a $2 \mu\text{m}$ spot diameter (thus taking into account the carrier diffusion, as detailed in Section 3.3). The excitation energy was chosen well above the GaAs barrier bandgap (1.69 eV) to avoid parasitic effects related to variations of the absorption efficiency. The slightly asymmetric spectra were fitted with a Gaussian convoluted with an exponential of decay $\frac{\Delta E}{kT}$, and the bell shape maximum was reported as the emission energy. The emission evolution with temperature is displayed on Figure 5.24, for both the $1 \mu\text{m}$ pitch QWR array (red) and the top-QW (black). The calculated results, based on the QW model detailed in Subsection 4.2.1, are also shown as continuous lines. The top-QW emission is compared with a 3 nm-thick $\text{Ga}_{0.75}\text{In}_{0.25}\text{AsN}$ QW model with $[N] = 1.25\%$ (nominal thickness and In content, and N content adjusted to fit the data), and the QWR data are compared to a 9 nm-thick $\text{Ga}_{0.7}\text{In}_{0.3}\text{AsN}$ QW with $[N] \sim 1.475\%$. The energy spans of the two graphs are similar. As visible, the QWR follows quite well the expected dependency, suggesting a rather good structural quality. The observed redshift from 10 K to room temperature is $\sim 55 \text{ meV}$ at constant power. Oppositely, the top-QW displays a reduced energy dependency, with $\sim 45 \text{ meV}$ redshift only. A plateau at low temperature is especially visible, with almost no shift up to $\sim 120 \text{ K}$.

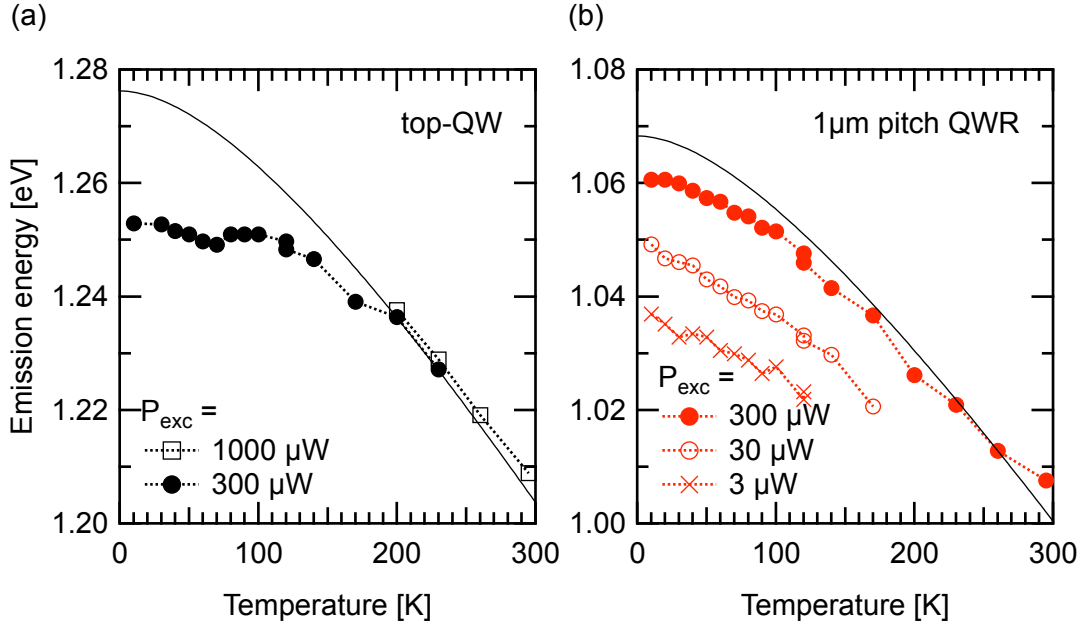


Figure 5.24: (a) top-QW and (b) QWR μ PL emission energies as function of sample temperature ((100) substrate, $P_{\text{exc}} = 300 \mu\text{W}$). Symbols are the experimental data and solid lines stand for a QW model (see text). The top-QW diverges from a QW model at low temperatures in a S-shape-type evolution, while the QWR better follows the model. The top-QW curve is extended by data points acquired at a slightly higher power. The low-temperature QWR emission energies using 10- and 100-fold lower excitation power are also depicted, showing no sign of S-shape behavior.

A few comments are needed to interpret these data. First, the carrier diffusion is strongly hindered in QWRs when comparing to QWs, as small perturbations in a 1D potential tend to localize the charges. The carriers in QWRs may recombine radiatively in potential local minima that do not have the same nature as the structural defects hosting most of the QW low temperature recombinations. Thus the broadening of the low excitation emission in the QWR spectra may hide the S-shape energy evolution.

As a second comment, the carrier density plays an important role when considering the trapping on impurities. When the carriers density is increased the traps contribution to the carriers' recombination becomes minor since electronic traps can only host a certain number of charges at a time. The strong luminosity of the QWR related to its small volume implies the carrier density is notably higher in the QWR than in the top-QW. Also, the lifetime of carriers is notably extended in QWRs compared to QWs. While InGaAs QWs exhibit carrier lifetime below 100 ps, values of 880 ps were reported for InGaAs V-groove QWRs [4]. The carrier's lifetime is also increased with temperature [108]. Although not tested on our samples, this tendency probably holds true in N-containing structures. The carrier density is therefore increased in the QWR as compared to the top-QW, thus masking the possible S-shape behavior.

A third comment is related to the high excitation power level used for these measurements, required by the lower sensitivity of the detector available at the time of measurements. We first note that evolution of the top-QW markedly differs from that of the model at the high power level used, indicating a deteriorated quality and the presence of defects. The deviation of the QWR remains much smaller at the same power level. This may be due to the 2 growth steps, not adjusted for a 3 nm QW. As presented in Section 4.5, a 5.6 nm-thick QW grown using an adjusted 2-step growth procedure exhibited no S-shape behavior when using a 10-fold lower excitation power. By comparison, this confirms the intrinsically lower quality of the non-adjusted top-QW layer present on the QWR samples. Let us finally mention that same thicknesses variations lead to much larger variations in the potential in thin structures than on thick ones; this participate in the high sensitivity of the top-QW to disorder and make it prone to a marked S-shape behavior.

Besides, more testing is needed on the QWR emission. The low-temperature behavior with 10- and 100-fold lower power is depicted on Figure 5.24(b) as open circles and crosses. Although shifted to the red, these spectral evolutions with temperature are consistent with the high power trend, showing no hint of an S-shape behavior. A more detailed comparison between 10 K and room temperature spectra was also performed when a more sensitive detector became available. Figure 5.25 displays μ PL spectra of the top-QW and QWR at low and room temperatures, with excitation power corresponding to the previous experiment (black) as well as 30-fold lower power level (red). The spectral shifts between these temperatures remain essentially constant with power level, and correspond to the energy span observed in the first experiment.

As quality assessment based on the S-shape should be performed at similar carriers densities, the QWR quality cannot be certified comparatively better than the top-QW. Lower excitation power, at which spikes become visible in the spectra, would probably allow for evidencing an S-shape evolution of the QWR energy with temperature. Such measurements could be performed at temperatures below 100 K using the new detector. Nevertheless, if the data available do not ensure a better material quality in the QWR compared to the top-QW, we managed to definitely assert the lesser sensitivity of QWR to the defect-dominated regime.

5.4.2 Sample annealing

Sample annealing is often reported to dramatically improve PL efficiency of both MBE [236] and MOVPE [223] grown samples. As an example, alloys intended for multijunction solar cells applications require ~ 1 eV GaAs lattice-matched epilayers that can be achieved with $[N] = \sim 3\%$ and $[In] = \sim 9\%$. Such layers are generally found of quite poor optical quality, and PL intensity increases by orders of magnitude can be obtained after appropriate post-growth thermal treatment [241]. In alloys with composition closer to the ones used in this work, the benefits are less impressive, but up to 10-fold PL intensity increases were reported [234, 223]. This performance improvement however comes with a sizeable blueshift of the emission, in

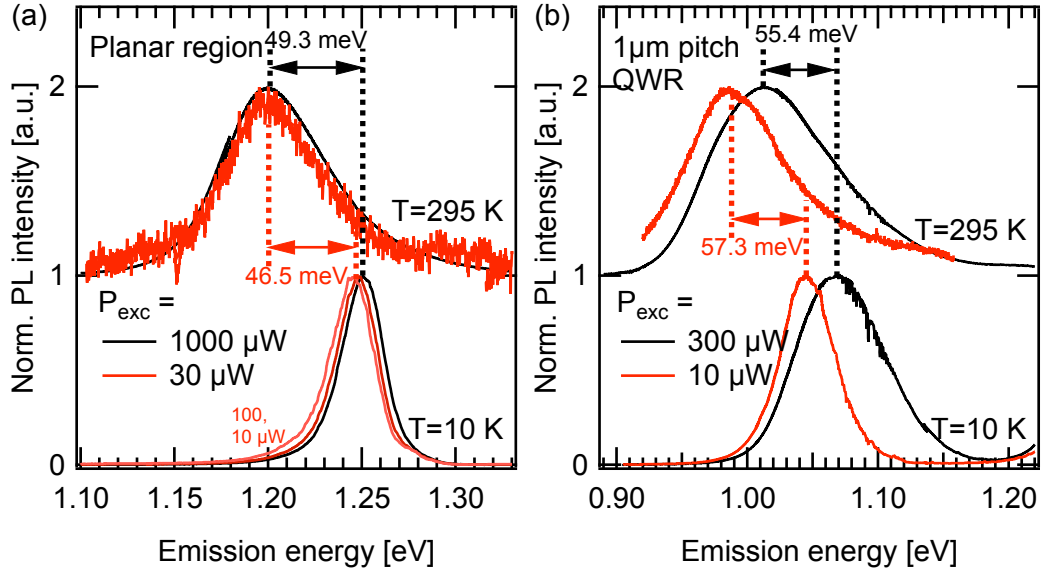


Figure 5.25: A more sensitive detector allowed for checking the (a) top-QW and (b) QWR redshifts between low and room temperature at lower excitation power. While the black curves reproduce the power densities used for the first experiment of Figure 5.24, the red line spectra were acquired with a 30-fold lower power. The temperature-induced redshifts are almost identical for these two power levels, and correspond to the previous experiment observations.

the 20 to 100 meV range.

Various phenomena happen during the annealing process at the microscopic level [234, 317] (see also Subsection 2.2.2.5). Some of the crystal defects incorporated during the low temperature growth can be cured. Existing N clusters may also dissolve, making the alloy more homogeneous and relaxing the strain field. Due to the surface activation energies, the low temperature growth favors formation of Ga-N bonds on the growing surface, whereas in the bulk N-In bonds are preferred. The annealing yields an atomic rearrangement favoring In-N pairs as nearest neighbors. This reduces the local strain field, interesting for solar cells applications but also for nanostructures. This also changes the electronic properties of the material causing the observed annealing blueshift. These structural modifications explains why N-rich, In-poor alloys highly benefit from annealing, while the improvement is more limited in In-rich, N-poor alloys like ours.

The samples presented in this chapter so far were not subjected to any annealing process. Indeed the growth process involves a ~ 2 min growth interruption after the active layer deposition, and a subsequent growth of a GaAs cap at the nominal 590°C temperature. As this nominal temperature is known to be overestimated by $\sim 30^\circ\text{C}$, the samples have been heated for some minutes at $\sim 560^\circ\text{C}$ after the QWR deposition under arsine-rich atmosphere. One would not expect In-rich alloys to experience dramatic changes with such treatment, as 600°C temperatures are usually required to bring significant changes [223]. To explore the influence

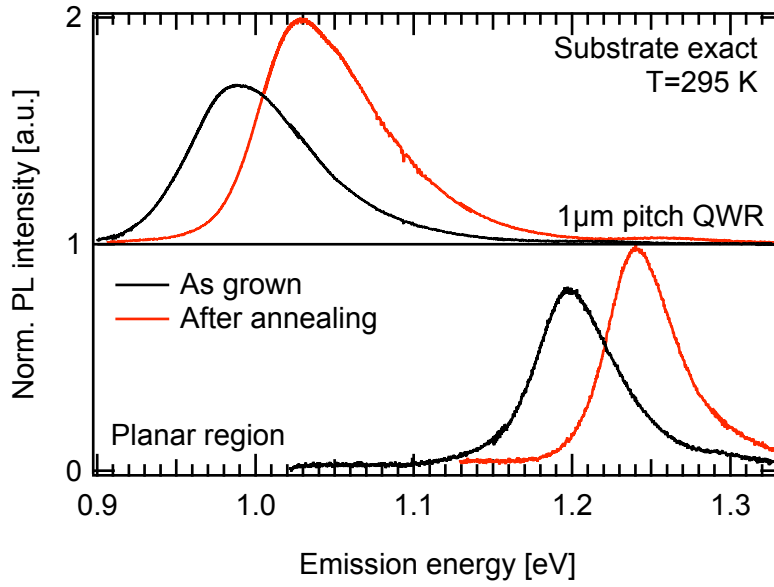


Figure 5.26: Room temperature μ PL spectra of a N-QWR sample acquired before and after a 25 min annealing at 750 °C nominal (~ 710 °C real) under arsine atmosphere. The excitation power is 30 μ W (QWR) and 100 μ W (top-QWR). A sizeable blueshift is observed on both the QWR emission (~ 40 meV) and the top-QW (~ 42 meV) after annealing. The luminescence efficiency is moderately enhanced (less than 2-fold).

of annealing in our structure, a sample was maintained at 750 °C nominal (~ 710 °C real) for 25 min under high arsine atmosphere.

Figure 5.26 shows power-dependent spectra of a QWR sample grown on a (100) substrate, before and after annealing. The 1 μ m pitch QWR array and the planar regions were characterized. Upon annealing the emission is shifted to the blue by a sizeable amount (~ 40 meV for the QWR, ~ 42 meV for the top-QW). The FWHM simultaneously exhibits a slight narrowing (84 versus 88 meV for the QWR displayed, 50 versus 58 meV for the top-QW), but this remains quite a marginal improvement. The 1 μ m pitch QWR array spectrum hints to a peak substructure, suggesting an actual line narrowing masked by emissions from several different states. However, measurements performed at low temperature using the old detection setup did not reveal any improvement in the 10 K emission FWHM. Finally, a moderate improvement of the PL intensity signal is observed, up to 2-fold according to the location and excitation power.

While some improvement of the emission quality is obtained through the annealing process, the strong blueshift associated tends to negate the advantages of N incorporation. Improvements may certainly be obtained after a careful optimization of the annealing parameters, among others the use of an As-depleted atmosphere. However, the low temperature emission of the QWR samples is quite satisfactory when compared to N-free samples, and does not need extensive post-growth processing before emitting a decent intensity.

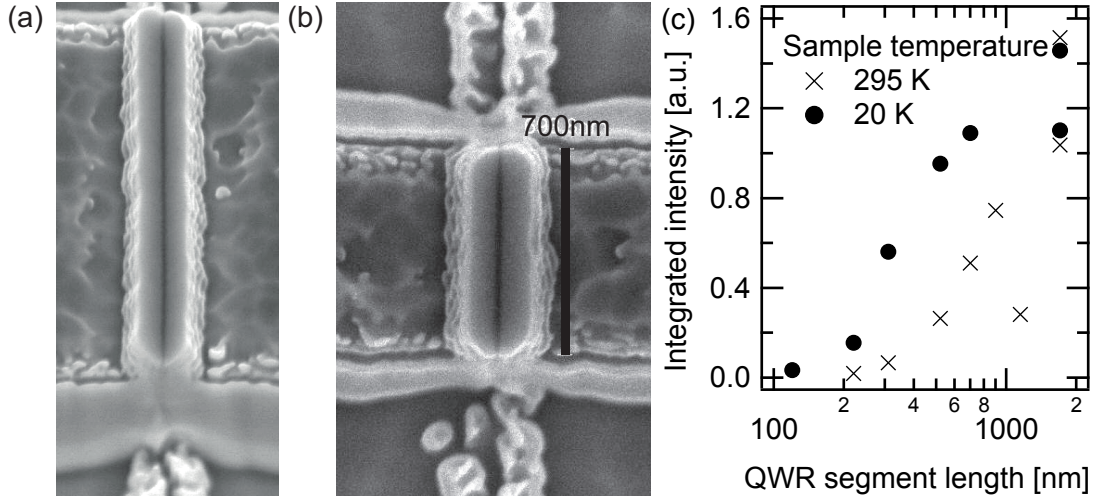


Figure 5.27: (a), (b): SEM side (top)-view of 1600(700) nm-long mesa containing a single InGaAsN QWR. The fabrication process was used to etch away the top-QW, as well as the structures formed on the groove {311} top facets, leaving only the QWR as a long-wavelength emitter. (c) QWR integrated intensities of the same series of QWR segments, at low and room temperature. The data series have been vertically scaled to match the intensities of the 1.7 μm -long segments. The QWR emission intensity is strongly enhanced on longer mesas.

5.4.3 QWR segments measurements

The spatial resolution of a microscope setup is primarily diffraction-limited to ca. the wavelength of interest, depending on the numerical aperture of the objective lens. The μPL setup effective resolution is also limited by the diffusion of carriers before recombination. To get new insights into the local shape of the electronic potential, more advanced techniques are required, like for example surface near-field optical spectroscopy (SNOM) [318]. Sample post-processing can also deliver some new information. This last solution was implemented by etching large trenches on a 10 μm pitch QWR field, in such a way that QWR segments are conserved and the surrounding material etched away. The resulting mesas are ~ 220 nm wide. Due to the high sensitivity to structural disorder, QWR can be generally seen as a chain of connected QDs. Thus by attributing the low-temperature peaks to local minima of the electronic potential, one can get some insight into the QWR roughness and carrier diffusion length.

SEM side- and top-view images of mesas containing a single QWR segment of different lengths are shown on Figures 5.27(a) and 5.27(b). As previously demonstrated (see Subsection 5.1.4), the QWR emission can be observed by μPL experiments while the top-QW emission is absent from the spectrum. μPL spectra of QWR segments of different sizes were acquired both at 20 K and room temperature. PL emission can be detected out of 220 nm-long QWR segments at room temperature. The low- and room-temperature PL integrated intensity is shown on Figure 5.27(c), for a series of mesas of different length, using above-barrier excitation. The intensity evolution is not discussed at length here since it depends on numerous phenomena

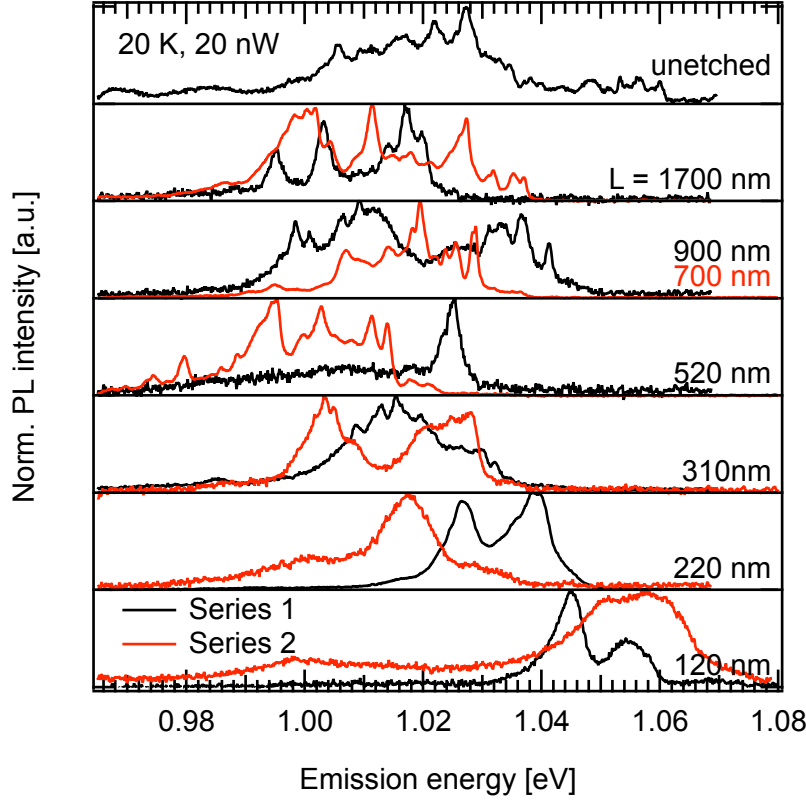


Figure 5.28: 20 K normalized μ PL spectra of QWR segments of various lengths L , etched on two different isolated QWR (red and black series, $P_{\text{exc}}=20$ nW). The emission from segments with $L < 300$ nm are systematically blueshifted and the emission lines are broadened. The emission intensity is also much weaker. A complex emission spectrum can still be seen on 300 nm-long segments.

like localization of carrier generation, diffusion to the QWR or the surfaces, light extraction efficiency, etc. However, the PL intensity increase occurs for mesas twice as long at room temperature than at 20 K. This indicates significant carrier diffusion in the QWR at room temperature.

The 20 K μ PL spectra of QWRs of different length are presented on Figure 5.28. The QWR luminescence can be tracked down to 120 nm-long mesas. The emission of the shortest segments ($L < 300$ nm) is observed to be blueshifted and significantly broadened. This is certainly due to the close vicinity of the mesa walls on which free carriers are trapped, generating a local, fluctuating electric field. However, the number of active recombination centers is visibly quite stable on long mesas until reaching the same length scale. This suggests that the QWR disorder characteristic length is far shorter than 300 nm, probably below 50 nm.

5.4.4 QWR emission polarization

InGaAs/GaAs QWRs exhibit a strong anisotropy of the ground state emission polarization in favor of the groove axis direction, caused by the carrier wavefunctions lateral confinement [319] combined with the triaxial strain field [320]. The holes confinement plays a key role in the origin of the emission anisotropy. As those remains quite insensitive to the introduction of nitrogen in GaInAs, it is not surprising that the degree of polarization of GaInAs and GaInAsN QWRs is similar at low temperature (degree of linear polarization $\sim 25 - 30\%$ in our structures).

The detailed study was conducted on the polarization properties of a couple of identical N-containing QWR samples, with one having been irradiated with hydrogen as to passivate the effect of its nitrogen. The hydrogen selectively diffuses to the immediate vicinity of N atoms, forming N-H complexes. This cancels the effect of N on the electronic properties, and shifts the emission energy up to that of the N-free counterpart. Additionally, the arrival of new atoms modifies the layer strain field. In In-rich alloys like in our QWRs, the N incorporation releases a fraction of the compressive In-induced strain. Hydrogen irradiation then increases the compressive strain, to a higher value than the N-free counterpart would exhibit [274]. The effect of hydrogenation is presented more in-depth in Subsections 2.2.5 and 5.2.1.

Dr. M. Felici, a former colleague, performed the following measurements and analysis while at La Sapienza University of Rome. The results were summarized in a publication [302] from which the figures and part of the content of this subsection are taken from. The author of this work fabricated the samples, contributed to the redaction of the publication and personally acquired some data on the QWR polarization behavior that indeed support the findings and conclusions of that publication.

The anisotropy is generally experimentally characterized by the degree of linear polarization (DOP) given by the $\rho = \frac{I_{\parallel} - I_{\perp}}{I_{\parallel} + I_{\perp}}$, expression where I_{\parallel} stands for the emission intensity linearly polarized along the QWR and I_{\perp} is the component perpendicular to it. The same quantity can also be retrieved by fitting of the angle-dependent intensity with the expression $I(\theta) = \frac{1}{2} [1 + \rho \cos(2\theta)]$.

The QWR polarization anisotropy spectra are asymmetric and the maxima do not correspond to the PL maximum intensity (especially for the InGaAsN QWRs). This suggests that multiple QWR states are responsible for the emission: regions exist with higher N concentration and lower strain level, which become passivated upon hydrogenation. To reproduce this, a 2-Gaussian fit procedure was elaborated as depicted in Figure 5.29(c)-(d). The PL spectra were fitted as the sum of two Gaussian peaks, representing the QWR ground, respectively higher-energy states. The energies and widths of the Gaussian peaks were kept constant for the two polarizations. The intensity of corresponding Gaussians fits of the two orthogonal polarizations are compared to extract the DOP values at low (ρ_1) and high (ρ_2) energy.

The ρ_1 (grey circles) and ρ_2 (empty circles) values extracted from the two Gaussian peaks fit are plotted on Figure 5.30(b) and (c). Some data points are not shown, where the relative intensity

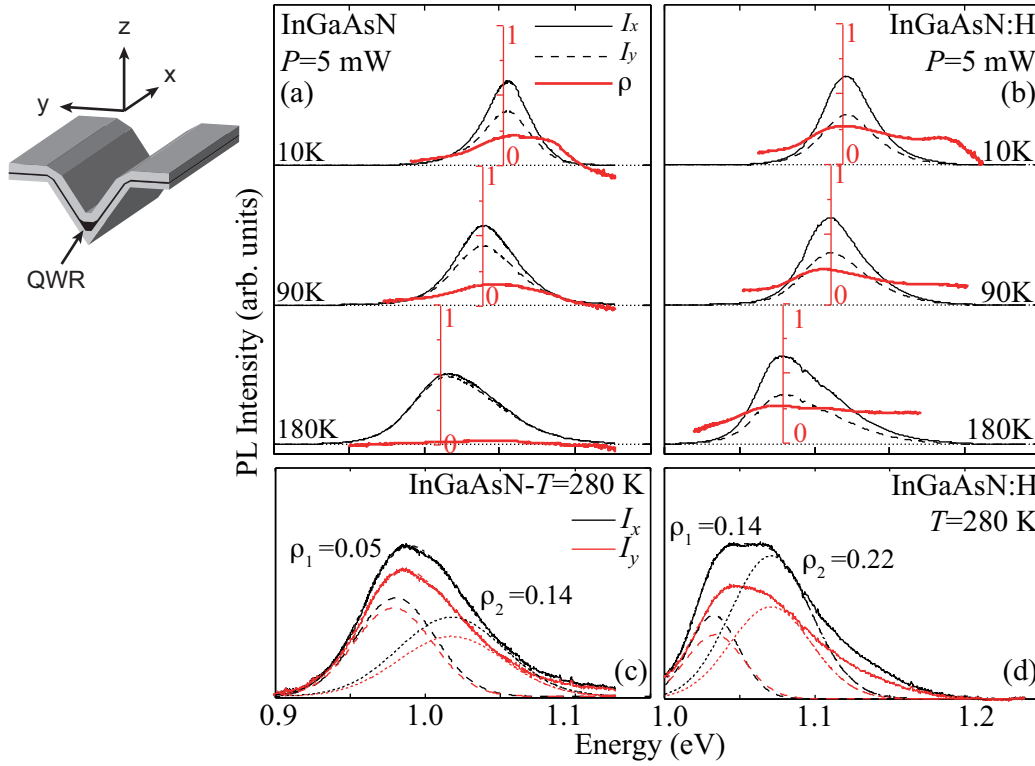


Figure 5.29: PL spectra of the (a) as-grown and (b) hydrogenated QWRs, recorded at different temperatures for polarization parallel (continuous) and perpendicular (dashed) to the wire. The degree of linear polarization ρ is shown as a thick red line. (c) and (d) Fitting procedure used to extract the value of the degree of linear polarization of the main QWR and of the higher-energy transitions ρ_1 and ρ_2 , together with the associated fits. The curves relative to the polarization parallel (perpendicular) to the QWR are displayed in black (red). Two Gaussian peaks (dashed and dotted lines, respectively) are employed to fit the PL spectrum corresponding to each polarization. For the higher-energy transition, energy and linewidth of the Gaussian peak are kept constant for the two polarizations. Graphs from [302].

ratio of the Gaussians exceeds 5. The maximum of the energy-dependent DOP spectra is also displayed as crosses, to assert the validity of the fit procedure. Figure 5.30(a) emphasizes the ρ_1 value, representing the QWR ground state polarization anisotropy. The polarization of the untreated QWR sample exhibits a strong decrease already below 100 K, and is close to zero at temperatures higher than 180 K. The ground state polarization of the hydrogenated sample is comparatively stronger at both low and high temperature. A marked decay only occurs above 200 K. The ground state keeps a high DOP even at room temperature.

The findings on the QWR polarization can be summarized as follow. First, the QWR exhibits a significant polarization anisotropy at low temperature (DOP = $\sim 25 - 30\%$). The comparison of the temperature dependencies of two identical InGaAsN QWR samples, but one hydrogenated, evidenced the strain-related origin of the anisotropy. The increase of compressive strain level in the QWR further splits the holes subbands, which strengthens the polarization anisotropy

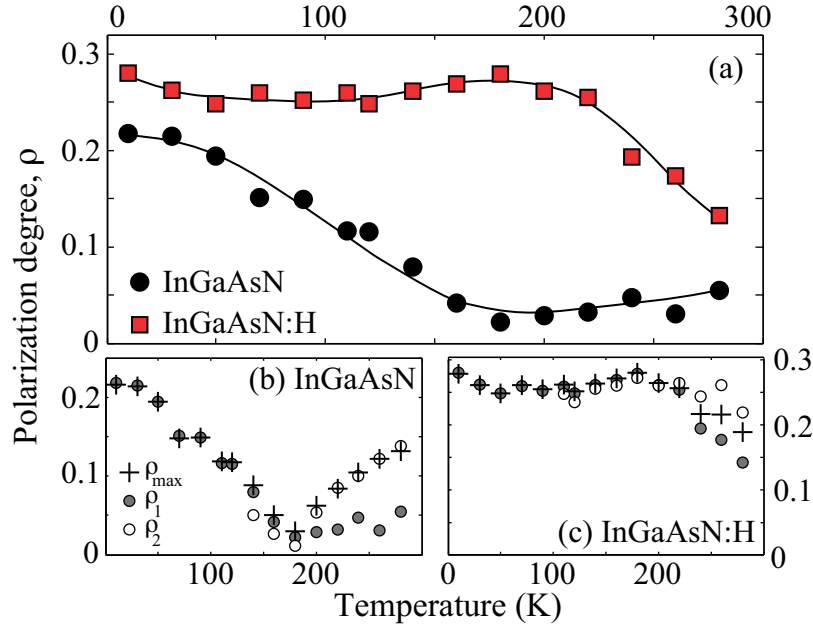


Figure 5.30: Temperature dependence of the degree of linear polarization of the main QWR transition (the lower-energy peak) in the spectra of Figure 5.29, estimated from the fitting procedure outlined in Figures 5.29(c) and 5.29(d). Data relative to the untreated (hydrogenated) GaInAsN QWR samples are reported as black-filled circles (red-filled squares). Solid lines are guide to the eye. (b), (c) Comparison between the maximum value (ρ_{max} , black crosses) of the energy-dependent degree linear of polarization presented in Figures 5.29(a) and 5.29(b) and the polarization degree of the lower- (ρ_1 , grey circle) and higher-energy (ρ_2 , empty circles) QWR transition, as estimated from the fitting procedure described in Figures 5.29(c) and 5.29(d). For ρ_2 only those datapoints for which the intensity is at least one fifth of the low-energy transition intensity are shown. Graphs from [302].

and improves its thermal stability.

5.5 Chapter summary

To summarize the present chapter, we successfully demonstrated nitrogen incorporation into capillarity-driven, MOVPE-grown V-groove QWR nanostructures. Room temperature QWR PL emission is obtained in the technologically relevant 1.3 μm band, an emission wavelength that can be achieved by several sets of growth parameters.

Our InGaAsN QWRs were grown at low temperature through an intricate procedure leaving room for significant quality improvement. The QWR morphology is comparable to that of the InGaAs counterpart, although the diffusion length of adatoms appears quenched by the large presence of N and of the DMHy decomposition by-products. The strong, low-energy PL signal detected is unambiguously attributed to the QWR structure located at the groove center. Measurements of the diamagnetic shift are in excellent agreement with the nanostructure size

measured by TEM, and confirm the spatial extension of the carrier wavefunctions along the QWR axis.

The influence of several growth and structural parameters on the N incorporation is studied, amongst those the substrate misorientation, the QWR thickness, the presence of a cap grown immediately on top of the QWR, the growth temperature, the DHMy flux and the growth rate. Our results suggest that the N distribution is not uniform throughout the QWR. The N content concentration appears to be higher in the vicinity of the lower interface, in spite of our 2-step growth method intended to avoid such distribution. A uniform N distribution may hopefully allow reaching long wavelength emission while avoiding the formation of high N-content layers that are sources of defects.

The temperature dependence of the emission energy reveals a significantly improved quality of the QWR when compared to the surrounding top-QW. The rather strong decay of the room temperature luminescence is essentially due to the thermal holes escape from the nanostructure, and could be prevented by various bandgap engineering techniques (deposition of delta-doping layers or use of AlGaAs barriers). The embedded strain generates a significant PL polarization anisotropy up to 150 K. A hydrogenation process enhances the strain level, which increases the energy spacing of the holes subbands, and allows for maintaining a strong anisotropy up to room temperature.

Although not ruled out, a 1.55 μm emission does not seem realistic if a satisfactory crystal quality is to be maintained. However, the key point of this chapter is the possibility of N incorporation into nanostructures formed by capillarity. The nitrogen content is comparable if not slightly enhanced in the QWR as compared to the surrounding top-QW structure. This opens the way to the fabrication of N-containing QDs in inverted pyramids, for which the growth mechanisms are essentially similar to that of QWR.

6 0D-nanostructures: dilute nitrides quantum dots

Semiconductor quantum dots (QD) are of prime interest for the realization of current and future optoelectronic devices. In particular, decisive advantages are foreseen due to the better temperature behavior and the reduced power consumption of QD-based light emitting devices [321, 322, 323]. But the most interesting perspectives arise from the quantum nature of the fully confined electronic states: QDs can act as light sources with non-classical photon statistics (emission of single photon [324, 14] or entangled photon pairs [17, 67, 66, 68]). Quantum electrodynamics experiments in a solid-state environment [12] can be performed using QDs embedded into photonic crystal cavities, for example the observations of the vacuum Rabi splitting [9, 8] or photon blockade [11]. Amongst the major challenges of these technologies is the need for simultaneous control of QD location and emission energy, necessary for placing the QD at the right position inside optical cavities in a scalable manner [92]. As detailed in Subsection 2.1.2, such requirements are met by QDs grown in inverted pyramids [112, 113, 325], but remain a major challenge for self-assembled QDs [326]. Another desirable feature is achieving photon emission in the 1.3 μm and 1.55 μm optical fiber spectral windows, important for potential applications in optical fiber communication.

The fabrication of 1.3 μm -emitting In(Ga)As QDs formed by the strain-induced Stranski-Krastanov (SK) growth mode is possible, although not straightforward [327]. For such structures, the addition of N would help further red shifting the emission wavelength. As early as the year 2000, the fabrication of N-containing QDs emitting at 1.5 μm was reported [328]. However, the strong lattice mismatch introduced by the N atoms perturbs the SK formation mechanism, affecting the island size, composition, morphology and areal density [329, 330, 331, 332]. A bimodal size distribution of InGaAsN SK QDs was predicted [333] and observed [334, 335]; the formation of dislocations in this system was also reported [330, 335]. With the addition of N, the SK formation becomes very sensitive to the growth parameters [336]. Cross-sectional STM measurements evidenced the diffusion of N atoms in the GaAs matrix and their incorporation close to the wetting layer [337]. Nevertheless, a satisfactory control of 1.5 nm-emitting QDs made with this system can be achieved [338, 339]. A possibility to overcome these limitations is to incorporate N in the capping layers and not necessarily in the QD itself [340, 341, 342].

The fabrication of N-containing InGaAsN SK-QDs by MOVPE was also demonstrated [128]. Several publications focused on the theoretical properties of such N-containing SK-QDs [343, 344, 345, 346]. However, the SK-QD approach suffers by design of three major drawbacks when compared to QDs formed in inverted pyramids: (i) a lack of control on the formation site; (ii) a relatively low homogeneity of the QD properties; and (iii) the absence of a natural symmetry that might guarantee vanishing of the FSS.

The emission wavelength of QDs grown in inverted pyramids is limited to the 0.7 - 1 μm range. Yet an extension of their emission to longer wavelengths may open the possibility for their applications in devices operating in the silica optical fiber windows (1.3 and 1.55 μm). The optical quality of photonic devices depends in particular on the size of lithographic imperfections, and may benefit from scaling up the device size. In this context, the N incorporation offers a promising path toward long wavelength emission of QDs, supported by the successful 1.3 μm QWR emission properties presented in Chapter 5. N incorporation into pyramidal QDs was reported quite recently also by another research group [347, 348, 349], although the high growth temperature (730 $^{\circ}\text{C}$) employed and the ambiguous QD redshift cast some doubts on the actual presence of N in these QD. We suggest instead that, in that case, DMHy or the decomposition products generate structural and/or compositional modifications to the QDs, responsible for the observed characteristics.

We successfully demonstrated in Chapter 5 the N incorporation into QWR grown on non-planar substrates. We will here focus on the N incorporation into pyramidal QD nanostructures. Part of this study was the object of a brief publication [350]; the present chapter presents our results in a much more detailed way. The pyramidal QD system offers rather large flexibility in the emission energy. In view of this, the first section is dedicated to the characterization of the effect of the As/III ratio, buffer thickness and pyramid size on the emission energy of pyramidal InGaAs QDs. Next, the successful incorporation of nitrogen is presented, including a brief study of the influence of growth and structural parameters on the emission spectra. The subsequent section focuses on the emission properties of isolated pyramidal QDs. Finally, the polarization properties of N-containing QDs will be presented in detail.

6.1 Growth of InGaAs pyramidal QD

The (111)B GaAs substrates were patterned as detailed in Section 3.1, with fields of 500 nm pitch triangular arrays of pyramids, surrounded by big ($\sim 10 \mu\text{m}$) pyramids so as to slow down the growth rate. Fields with different pyramid size S_{pyr} were systematically explored, ranging from 200 to 400 nm depending on the designs. Dr. A. Rudra and Dr. P. Gallo performed the growths, while the author conducted the sample preparation, data acquisition and analysis.

The growth of QDs in inverted pyramids proceeds essentially like that of QWRs described in Chapter 5, with the deposition of a strained InGaAs layer in-between GaAs barriers. A major difference is that the precursor decomposition is quenched on the (111)B substrate surface. This causes the effective growth rate to dramatically increase in the pyramids. The formation

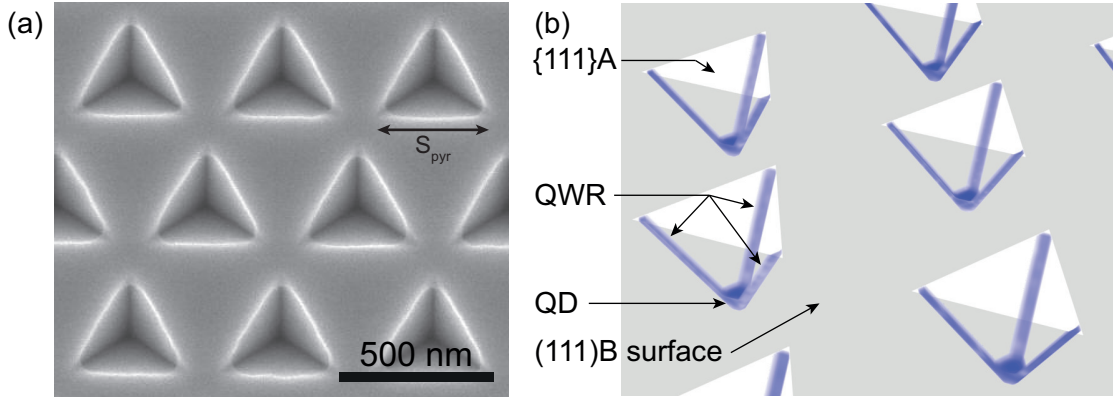


Figure 6.1: (a) SEM top-view image of a (111)B GaAs substrate patterned with $S_{pyr}=400$ nm pyramids, before Si-oxide removal. (b) Schematics of the different nanostructures resulting from the deposition of a thin InGaAs layer in the inverted pyramids. The initial recess openings are depicted in white. The InGaAs QD (at the pyramid apex) and the lateral InGaAs QWRs (at the wedges) are shown in blue.

mechanism of the nanostructures is similar to the case of QWR, with a competition between the nano-capillarity and the growth rate anisotropy between the {111}A pyramid sidewalls, the {100} wedges and the (111)B apex. The In adatoms are more sensitive to capillarity because of their longer diffusion length. This causes an anisotropic deposition of the InGaAs layer. A QD forms at the pyramid apex, which presents the strongest local surface (concave) curvature. QWR structures are also deposited in the three wedges of the pyramid. The QWs grown on the sidewalls are very thin and no associated emission is observed. Figure 6.1(a) shows a SEM top-view image of a substrate patterned with 400 nm-side pyramids after etching. On Figure 6.1(b) is represented a schematics of the different nanostructures formed inside the pyramids. The lateral QWs are not shown since they are very thin as compared to the other structures.

The MOVPE growth process employed is as follow. $L_{deox}=1.3$ nm GaAs is deposited during the deoxidation step. The temperature is then set to 590°C for the $L_{buffer}=5$ nm GaAs buffer deposition. This deposition proceeds with a slow growth rate (0.01 nm s^{-1}) using a high arsine flux (ratio As/III= ~ 2640). The growth is then interrupted for 3 min to lower the reactor temperature down to $T_{QD}=520^{\circ}\text{C}$, while keeping a high arsine flux during the first 2 min and lowering the flux for the last minute as to offer a low As surface concentration when the QD deposition begins. The QD nominal thickness is $L_{QD}=0.5$ nm, with 30 % In nominal concentration. The N-containing QDs were deposited using the 2-step growth procedure as 0.1 nm with 21 ccm DMHy flux, followed by 0.4 nm with 150 ccm DMHy. Unless specified otherwise, the arsine flux was such as As/III=250. The growth is again interrupted during 1 min to increase the reactor temperature up to 590°C , before the deposition of a 10 nm GaAs cap using a high As/III ratio. This typical growth sequence is reported on Table C.6 in Appendix C.

This growth sequence differs by several aspects from these of N-containing QWs and QWRs

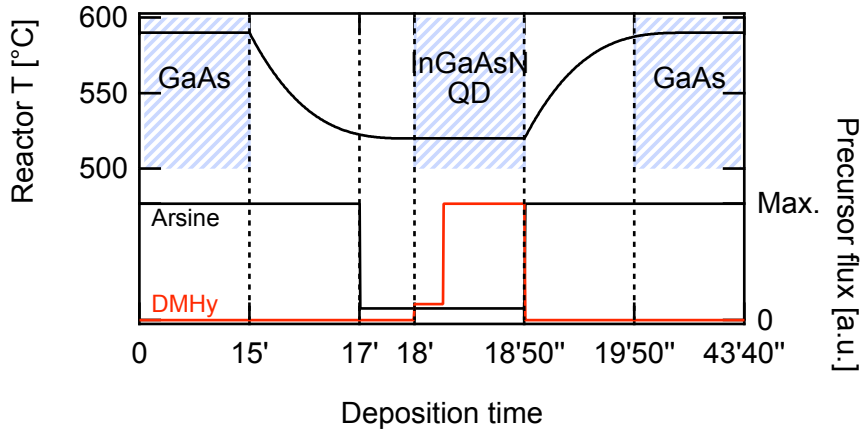


Figure 6.2: Schematics of the temperature and precursor fluxes during the MOVPE growth of the pyramidal QDs. The horizontal time axis is not uniform.

described in Chapters 4 and 5. The growth interruptions were here set to 3 and 1 min, while the longer interruptions (6 min to 7 min) of the QWs and QWRs growth were triggered by setpoints assigned to the reactor temperature controller. The high As/III ratios used here were chosen based on existing processes for InGaAs pyramidal QDs delivering excellent results. For this reason the arsine flux was only lowered during the last minute of the first growth interruption so as to prevent the surface degradation. The slow nominal growth rates are necessary to prevent the “closing” of the pyramid upon growth. We remind the reader that the effective growth rate in the pyramid is considerably higher than the nominal value and is strongly dependent on the pyramid size and pitch (growth rate enhancement is about 10-fold in our structures). Therefore the effective As/III ratio at the QD location may be considerably lower than the nominal value.

In Table C.7 in Appendix C are reported different QD growth runs, together with the specificities of the sample as compared to the base recipe detailed in the previous paragraph. References to figures showing μ PL spectra of the samples are also reported. The wafers were cleaved into sixths (like a circular tart), and then again in two in order to obtain central (triangular) and external (elongated) pieces. The samples are grown in the corresponding position in the reactor, either external (labeled “A” in Table C.7), or central (“B”). Some growth runs were performed on two separate pieces patterned with pyramids of different sizes (“AB”).

Spectra of a representative InGaAs pyramidal QD ensemble are shown on Figure 6.3 as function of the excitation power ($L_{\text{buffer}}=5$ nm, $L_{\text{QD}}=0.5$ nm, As/III=107, $S_{\text{pyr}}=300$ nm). The QDs emit at the lowest energy and their emission spectral line consists in a multitude of sharp peaks. The pyramidal QWRs emit at higher energy and become the dominant emission at high power, due to their larger volume and density of states. As detailed in the next subsections, the QWR and QD emission energies strongly depend on the growth conditions and structural properties of the sample.

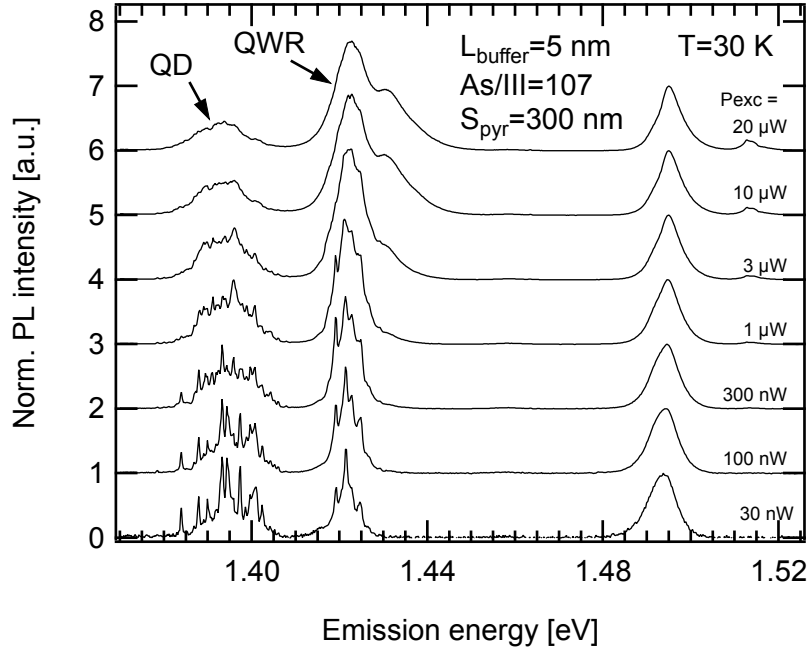


Figure 6.3: Low temperature μ PL spectra as function of excitation power of a QD ensemble (~ 10) grown in 300 nm-side pyramids with a 5 nm buffer and a As/III=107 ratio. The spectra were normalized to the peak intensity of the 1.49 eV GaAs C impurity. The QD emission is observed at the lowest energy, while the QWRs emit at higher energy and become dominant at high excitation power.

6.1.1 Influence of growth parameters

The pyramidal QD emission energy can be tuned with the help of various parameters: QD and buffer thicknesses, nominal alloy concentration, As/III ratio, growth rate, temperature, size and pitch of the recess. The high degree of freedom can be used to engineer the QD energy levels, and to control of the in-plane emission anisotropy [351]. In the present work, a special attention is set on the influence of the As/III ratio during the QD deposition, as As atoms compete with N for incorporation [203]. The influence of the pyramid size is also detailed as this parameter is given “for free” by etching additional recesses of different sizes. The influence of the buffer thickness is also explored, in order to characterize the lower bound of InGaAs QD emission energies. The influence of the QD thickness is finally briefly discussed.

6.1.1.1 As/III ratio

The use of high As/III ratios improves the quality of pyramidal InGaAs QDs: values are commonly in excess of 1000 [352]. Such ratios are certainly not compatible with efficient incorporation of nitrogen, so there is a need to probe the effect of lower As/III ratios during the growth of such dots. The As/III ratio can be kept high during the growth of the QD barriers. Several QDs samples were grown varying the As/III ratio during the QD deposition (and accordingly during

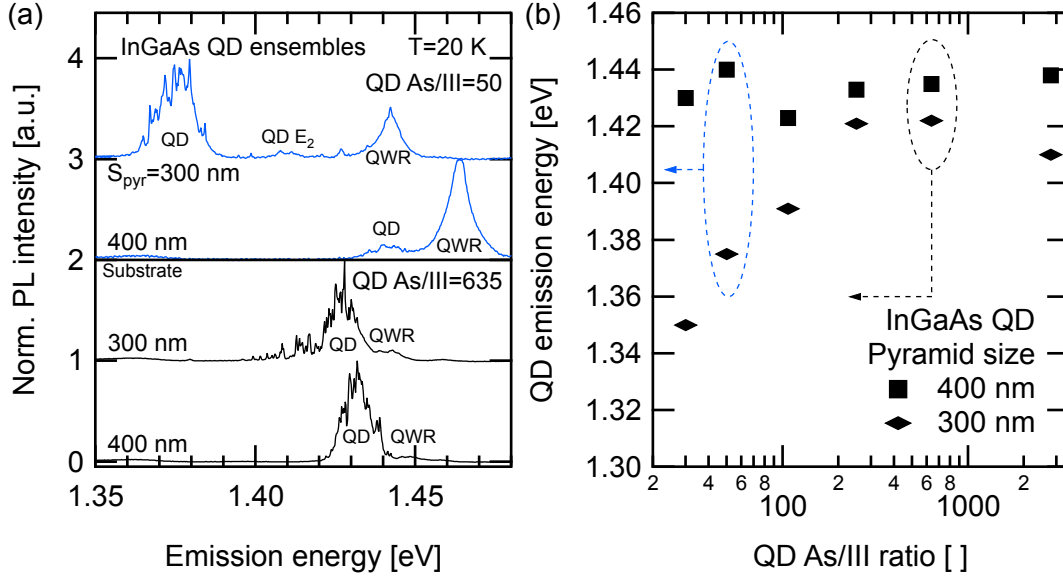


Figure 6.4: (a) Low temperature μ PL spectra of two InGaAs QD samples grown with As/III=635 and 50, respectively. The emissions from 300 nm- and 400 nm-side pyramids are shown. (b) Emission energies of InGaAs QD as functions of the As/III ratio employed during the QD deposition, with all other deposition steps kept unchanged ($L_{\text{buffer}}=5$ nm). The emission energies of QDs grown in 300 nm and 400 nm recess are reported. The data points corresponding to the spectra shown in (a) are evidenced. A drastic change in emission energy is noticed for small pyramids at low As/III ratios.

the last minute of the growth interruption), by tuning the arsine flux. The other parameters were kept identical, including the As/III ratio for the barriers and the substrate patterning procedure. The samples were all grown in an external position in the MOVPE reactor. Figure 6.4(b) summarizes the emission energies of QDs grown in 300 nm- and 400 nm-side pyramids as a function of the As/III ratio, while representative spectra are shown on Figure 6.5(a).

The pyramid size only marginally affects the QD emission energy under standard, high arsine flux conditions. Moreover, QDs grown in large (400 nm) recesses seem unaffected by changes in the arsine flux down to the lowest ratios employed in this experiment. The fluctuations in the emission energies are partly due to the growth-to-growth MOVPE repeatability, and partly to fluctuations of the recess size introduced during the electron beam substrate patterning. By comparison, QDs grown in smaller recesses (300 nm) are strongly affected by changes in the As/III ratio. Several effects can contribute to this evolution. The dominant mechanism is probably related to the surface density of As adatoms, determined by the arsine flux. As adatoms in large concentrations act like a “glue”, hindering the surface mobility of group-III adatoms, which in turn modifies the capillarity-driven mass transport to the QD formation site. Lowering the As/III ratio can therefore increase the QD thickness by favoring the mass transport to the QD location. A second effect may be that the TMGa decomposition at 520 °C could be affected by changes in the surface conditions related to the modifications of the

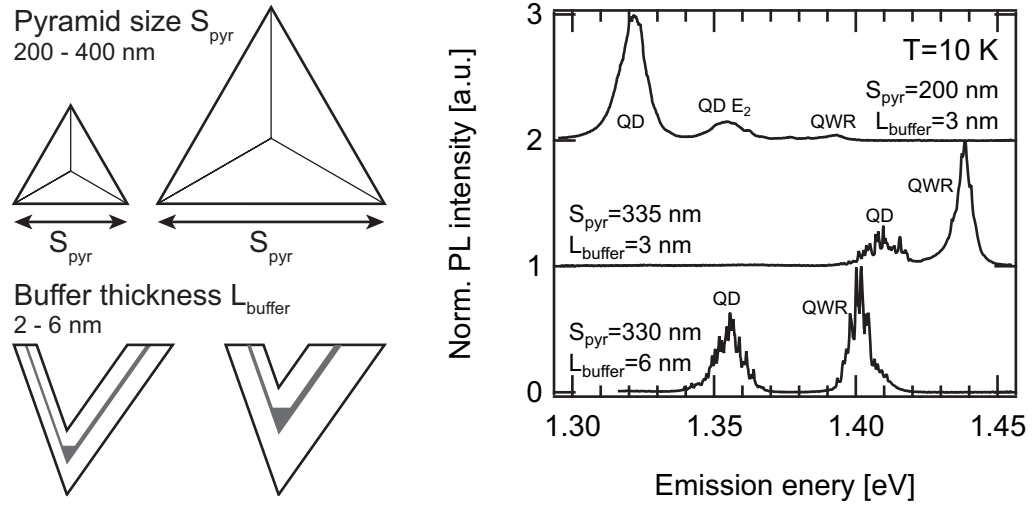


Figure 6.5: Schematics of the pyramid size S_{pyr} and of the buffer thickness L_{buffer} , together with low temperature μPL spectra of selected QD ensembles illustrating the influence of S_{pyr} and of L_{buffer} , on the emission properties.

arsine flux, thus modifying the QD thickness, composition and emission energy.

6.1.1.2 Pyramid size and buffer thickness

The pyramid size deeply influences the QD emission energy, as it determines the effective growth rate within the pyramid. The buffer thickness, i.e. the thickness of GaAs barrier material deposited prior to the active layer, affects the QD geometry in a quite similar way to the pyramid size. A large pyramid largely filled with material, becomes geometrically similar to a smaller one filled with a thinner buffer. To explore the range of accessible QD emission energies, a series of four samples was grown with nominal buffer thickness ranging from 2 nm to 6 nm (NB: an additional 1.3 nm is deposited during the substrate deoxidation and is not included in these values). The samples were patterned with pyramid of size ranging from 200 to 400 nm, and the growths were conducted within a short period of time to ensure MOVPE conditions stability. Representative spectra of these samples are shown on Figure 6.5, and the QD emission energies are reported on Figure 6.6.

The QD emission regularly decreases when the buffer thickness is increased and the recess size diminished, corresponding to previously reported results [109, 351]. When S_{pyr} is reduced, the surface available for growth decreases (no deposition proceeds on the top (111)B surface). Meanwhile the adatoms incoming flux remains quite constant, due to the effective precursor decomposition on the {111}A sidewalls, and to the inter-recess diffusion of adatoms allowed by the small pitch. Therefore the effective growth rate increases, resulting in thicker QDs emitting at longer wavelength. Similarly, the geometry of the large recess filled with a consequent buffer is quite similar to that of a smaller recess filled with a thinner buffer. The effective growth rate accelerates during the growth, resulting in thicker QDs if deposited on a thicker buffer.

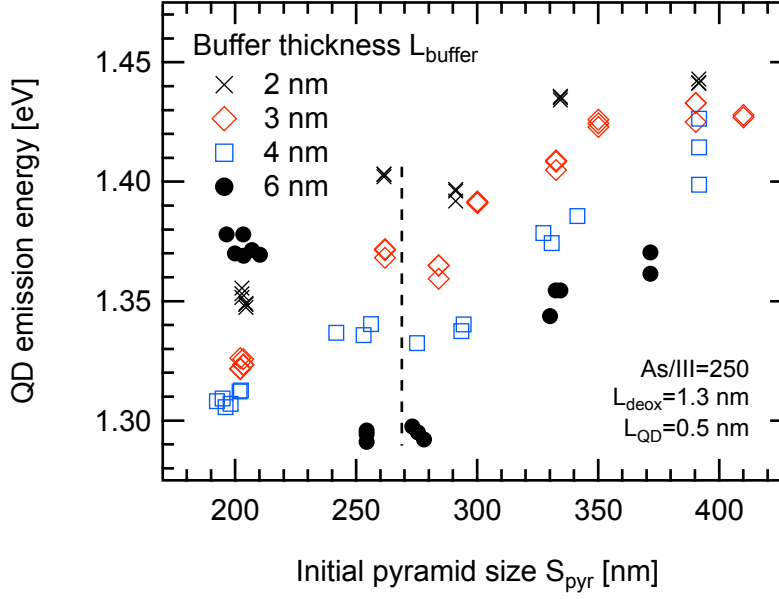


Figure 6.6: Emission energies of nominally 0.5 nm-thick InGaAs/GaAs QD ensembles, as functions of the etched pyramid size and GaAs buffer thicknesses. The energy decreases with increased buffer thickness and with decreased pyramid size. The deposition of large buffers in small pyramids leads to a change in the QD growth mode.

This explanation is supported by the analysis of the growth rate acceleration presented in Appendix B.

The longer emission wavelengths obtained with our parameter range were observed close to 1.295 eV (960 nm). This value is close to that obtained during other studies [351]. A change in the growth mode is evidenced for the smallest pyramids in which a 6 nm buffer was deposited: the emission wavelength dramatically blueshifts, and this is associated with a decrease of the PL intensity and an absence of sharp emission lines. We did not perform a growth run in order to characterize the recess morphology after a $L_{buffer}=6$ nm buffer deposition in $S_{pyr}=200$ nm pyramids, but based on SEM post-growth images, we estimate that in these conditions, the recesses to be nearly filled when the QD is deposited. Besides, the sidewalls of our pyramids become more and more vertical as the growth proceeds, a process known as “pyramid closing”. A modified template geometry may generate QDs with peculiar electronic properties. The drastic reduction in the total {111}A surface areas due to the filling of the pyramid may also hinder the precursor decomposition, thus affecting the QD formation.

In our case, the emission energy was observed to attain a minimum at 1.295 eV, but can probably be pushed a bit further to lower values by increasing the QD thickness, by limiting the growth interruptions and by increasing the In concentration.

An irregularity in the energy evolution with pyramid size can be observed close to 270 nm-size, marked by a dashed vertical line in Figure 6.6. Pyramids initially smaller than this value were

grown near the center of the susceptor in the reactor, while larger pyramids were grown close to the reactor edge. The latter positioning affects the QD emission energy quite similarly to a ~ 20 nm decrease in the pyramid size, due to variations in growth rates across the susceptor.

The electronic structure of QDs emitting at a given energy only marginally depends on the actual combination of the pyramid size and the buffer thickness. We observed bright excited transitions at a fixed energy ((33 ± 4) meV) above the ground state transition for all variants used in the above-mentioned experiments. The only exceptions are when the QWRs emit below or close to that energy, and the pathological $L_{\text{buffer}}=6$ nm, $S_{\text{pyr}}=200$ nm combination. These transitions originate from excited electronic states and are labeled as E_2 in Ref. [351]. The energy separation was observed to be remarkably independent of the GaAs buffer thickness, the initial pyramid size and the emission energy. This indicates that only a fraction of the parameter space was probed during our short survey: the pyramidal QDs can be engineered with a wide range of energy state spacings [351]. There are probably growth conditions producing QDs emitting at longer wavelengths. We also emphasize the robustness of the energy state separation with respect to fluctuations in the pattern parameters, an advantage for devices based on intraband transitions as was demonstrated recently [122].

6.1.1.3 QD thickness

A redshift of the QD emission wavelength can be obtained by increasing the QD thickness. To explore this possibility, two growth runs were performed, depositing QDs of 0.8 nm nominal instead of 0.5 nm, on GaAs buffer layers 3 and 5 nm thick. The pyramid size was between 300 and 400 nm. However, the samples comparison proved uneasy, as the samples with thicker dots were grown at a different (central) position in the MOVPE reactor. At the moment of the experiments, the sensitivity of our fabrication process with respect to this parameter was not precised. Nevertheless, the redshift associated with the thickening of the dots can be estimated to be ~ 20 meV, with QDs emitting at or above 1.35 eV. Whenever visible, the $E_1 - E_2$ energy separation was observed to be surprisingly unchanged.

We reached ~ 1.295 eV (~ 960 nm) emission out of InGaAs QD, with depositing a thick buffer ($L_{\text{buffer}}=6$ nm) in small pyramids ($S_{\text{pyr}}=\sim 260$ nm). This late QD deposition proceeds in shallows pyramids with an increased effective growth rate. In order to lower the emission energy of our InGaAs QDs, we propose to characterize more extensively the influence of QD thickness on the emission energy, focusing on growth conditions that delivered ~ 1.3 eV QD emission. We can also imagine increasing the nominal In content, slowing down the growth rate (enhancing diffusion, thus creating wider, thicker, In-enriched QDs). However, these options may have an adverse effect on a future N incorporation into these long-wavelength QD.

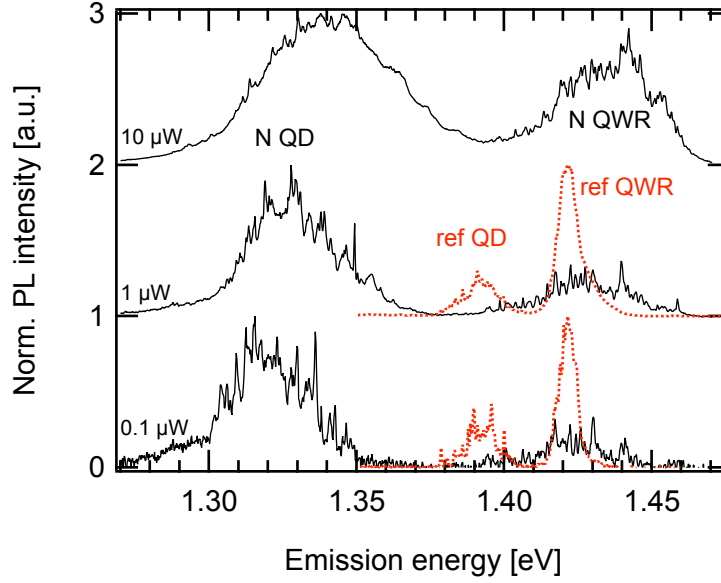


Figure 6.7: Comparison of low temperature μ PL spectra of QD ensembles (~ 10 QDs) grown with and without N, at different levels of excitation power. The initial pyramid size is 300 nm and the ratio As/III=107 during the QD deposition.

6.2 Nitrogen incorporation in InGaAs/GaAs pyramidal QDs

Based on the results of the preliminary growth studies described above, a few QD samples were grown while incorporating nitrogen. The GaAs buffer thickness was chosen to 5 nm and the As/III ratio as 250 for the initial experiments, as these parameters were best characterized and still in a regime seemingly unperturbed by the low As/III ratio. Two samples were grown with increasing DMHy flux, using 2-step growths with 0.1 nm with 7 ccm DMHy followed by 0.4 nm with 50 ccm, respectively 0.1 nm with 21 ccm followed by 0.4 nm with 150 ccm. These samples provided a sizeable redshift, but a QD emission energy still above 1.35 eV. As further increases in the DMHy flux proved unpractical, two further samples were grown with lower As/III ratios (107 and 50 respectively), with unchanged DMHy flux (0.1 nm with 21 ccm followed by 0.4 nm with 150 ccm). This situation corresponds to an effective increase in the DMHy/As (or V/V) ratio, which is also known to promote the N incorporation, by redistributing the group-V competition for incorporation.

Figure 6.7 displays low temperature μ PL spectra depending on the excitation power, for a pair of samples grown with and without DMHy flux, using As/III=107. The pyramid size is 300 nm. The QDs grown under those conditions exhibit the largest N-induced redshift of our collection, close to 75 meV. The QD emission is strongly broadened, with no less than 35 meV emission ensemble FWHM compared to ~ 10 meV for the N-free sample. A multitude of individual spectral lines were observed with $\sim 300 \mu\text{eV}$ linewidth, whereas the InGaAs counterpart commonly shows resolution limited lines ($< 100 \mu\text{eV}$). The QWR emission surprisingly exhibits a large emission broadening in spite of its almost unchanged energy.

The redshift of the QD emission alone is not sufficient to confirm the successful incorporation into the QDs. As suggested in Ref. [349], just the presence of DMHy with no actual N incorporation can significantly change the QD emission properties, by acting on the precursor decomposition kinetics and the surface adatoms diffusion. Therefore, the N incorporation cannot be reliably inferred from the observed redshift.

Another evidence of the effective N incorporation is the broadening of the QD ensemble emission, signature of the fluctuating number of N atoms embedded into a single QD. Some ~ 10000 atoms compose a given QD of the size we are dealing with. The emission redshift suggesting a N concentration in the 1 % range, the number of N atoms contained in a single QD can be estimated to be only ~ 100 . Such small numbers are subject to large statistical fluctuations, leading to significant dot-to-dot bandgap variations. Moreover, the QD emission energy is certainly influenced by the local configuration of N atoms within the nanostructure. The broadening of QD individual lines is also consistent with the nitrogen incorporation, as a signature of a degraded crystal quality and of the presence of charges in the QD environment.

The N incorporation efficiency strongly depends on the growth conditions and on the pyramids structural parameters. Emission energies of QDs grown in 300 and 400 nm-size pyramids are reported on Figure 6.8, as function of the As/III ratio. Are depicted N-free samples (filled black symbols, as in Figure 6.4), and samples grown with moderate (open green symbols) and high DMHy flux (lined open red symbols). The redshift regularly increases with increasing DMHy flux for the samples grown with As/III=250, suggesting N incorporation primarily driven by the precursor fluxes. Based on the emission energies of N-free QD, these growth conditions can be characterized as arsine rich. The maximal redshift is obtained with a lower As/III=107 ratio, evidencing the group-V competition for incorporation. The N-free QDs are redshifted when the As/III ratio is decreased, the growth progressively switching to an As-depleted regime with increased adatoms diffusion length. The surprisingly small redshift of the QDs grown with As/III=50 is probably related to a change in the growth mode, due to the As-depleted growth conditions.

The QD and QWR emission energies generally decrease when the pyramid size is increased [109]. A crude approximation can be made by assuming that the same amount of material is deposited on the substrate, independently of the pyramid size. This leads to an enhanced effective growth rate in smaller pyramids, and accounts for the progressive growth rate acceleration that is observed in large pyramids (See Appendix B.1.2.2). Larger growth rates take place in small pyramids, forming thicker structures emitting at lower energies. Such a trend is observed in our N-free structures and is depicted on Figure 6.9(b) (dashed black lines), representing the QD and QWR emission energies as functions of the pyramid size. On the same figure are also depicted the emission energies of the corresponding N-containing sample (red continuous lines). If the N-containing QD follow the expected trend, the QWR emits at higher energy in smaller pyramids. Such an evolution inversion is observed on the 3 samples containing the most nitrogen. Representative μ PL spectra of this evolution are shown on Figure 6.9(a), depicting the emission of QD arrays with three different pyramid sizes.

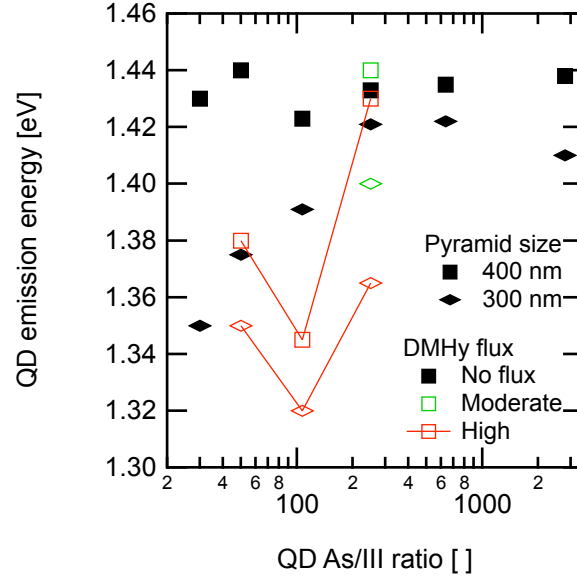


Figure 6.8: Emission energies of QD ensembles grown in 300 and 400 nm-size pyramids as a function of the As/III ratio used during the QD deposition. Are displayed data for N-free (solid black symbols, identical to Figure 6.4(b)) and N-containing samples grown with moderate (open green) and high (open red symbols and continuous line) DMHy fluxes.

This effect can be tentatively attributed to a preferential accumulation of N adatoms at the pyramid apex rather than at the wedges, due to the stronger capillarity flux toward this location that presents the highest local curvature. In this hypothesis, the QD efficiently captures most of the N atoms in small pyramids, while the capillarity effect is not efficient enough to completely deplete larger pyramids. This leads to a gradient of N concentration in the QWRs, notably contributing to the emission broadening. The diffusion length of the N adatoms in the pyramids can thus be estimated to be in the order of magnitude of ~ 200 nm.

Another effect involved might be the smaller effective As/III ratio at the QD site, caused by the small diffusion length of As. This would favor the N incorporation at the QD location by limiting the surface desorption [203]. The reduction in Ga-In atoms intermixing during capping, induced by the presence of nitrogen [332], could be an additional factor involved.

We stress out that QD emission can be pushed to significantly longer wavelength as compared to this first study. For example, in a preliminary study, N-containing QDs emitting at ~ 1.2 eV ($>1 \mu\text{m}$) were obtained in micron-sized pyramids. However the growth conditions proved unreliable and decision was made to switch to smaller pyramids.

6.3 Single pyramidal QD emission spectra

Obtaining single QD spectra is of prime importance for characterizing the emission properties of these fully-confined quantum structures. This section presents general QD emission characteristics of several samples containing single InGaAs and InGaAsN pyramidal QD. A

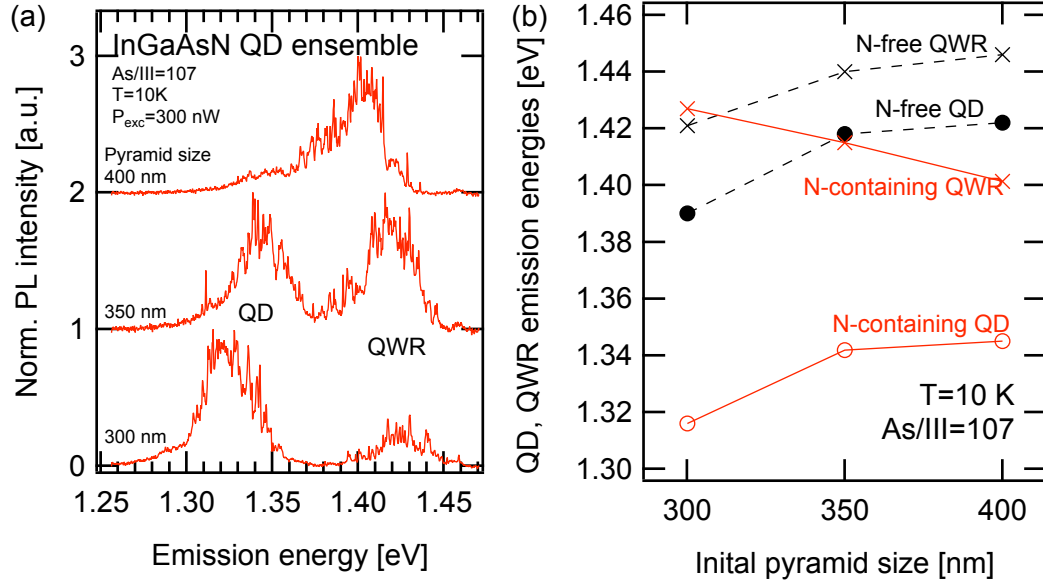


Figure 6.9: (a) Representative μ PL spectra of InGaAsN QD ensembles as function of the pyramid size, with the QD and QWR emissions evidenced. (b) QD and QWR emission energies in pyramidal structures as function of the initial pyramid size, for N-free and N-containing (high DMHy flux) samples grown with ratio As/III=107. Decreasing the pyramid size lowers down both the QD and QWR energies of the N-free sample. The trend is reversed in the case of N-containing QWR.

deterministic isolation of single QD was achieved thanks to the high accuracy of electron beam writing, with which the location of each QD was determined. The QD isolation was implemented by a $\sim 1 \mu\text{m}$ deep etching performed by ICP dry etching. A first design implemented drilling holes at the positions of the pyramids except for that of the selected dot. This design is shown on Figure 6.10(a). Observed from above, this pattern looks like a photonic crystal cavity, but no resonances are expected due to the absence of vertical confinement (no membrane structure is present) and the lack of resonant modes. Nevertheless, the polarization of the PL signal perpendicular to the substrate surface can be affected by the geometry of the etched structure. For polarization-resolved measurement a second, cleaner design was used, consisting in circular mesas of diameter roughly corresponding to the array pitch. On Figure 6.10(b) is shown such a mesa, with the residual recess barely visible at the center of the pillar.

On Figure 6.11 are displayed μ PL spectra of a collection of single InGaAs QDs (black lines), as well as a spectrum of an as-grown QD ensemble (red line). The QDs were grown in 300 nm-size pyramids on top of a 5 nm GaAs buffer layer, using a As/III=250 ratio, and were isolated with design (a) of Figure 6.10. The broad, spiky emission spectra below 1.43 eV can be attributed to the QDs while the smoother component above 1.43 eV originates from the QWRs. A quite broad distribution of the QD energies can be observed, significantly larger than the state-of-the-art distribution of pyramidal QD energies [110]. This is because pyramids of different

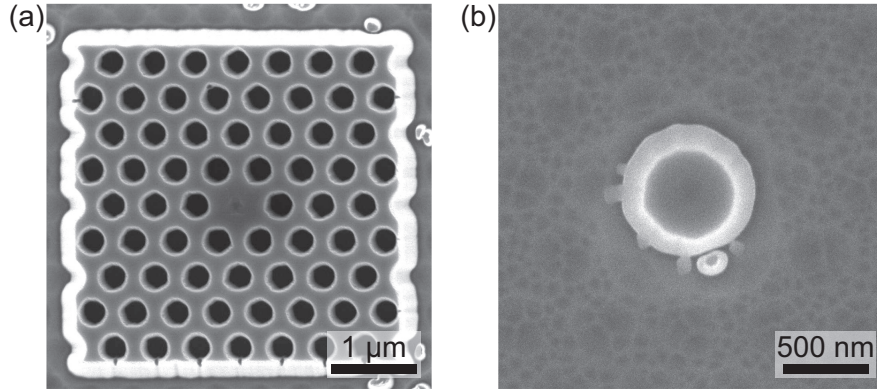


Figure 6.10: SEM top-view images of etched structures for QD isolation, showing (a) the early design with holes drilled at pyramid positions except for the central one, and (b) a circular mesa containing a single pyramid.

sizes were etched on the same substrate, at the cost of overshooting the etching time of the smallest pyramids presented here. An etching time longer than required results in a small but uncontrolled etching of some of the {111}A facets, possibly initiated at imperfections of the crystal-oxide contact. The pyramid size distribution is therefore significantly broadened, which results in an increased variation of the QD emission energy.

More surprising is the dot-to-dot variation of the spectral features. QDs in inverted pyramids typically share a reproducible pattern of excitonic lines with fixed energy separations, making the peak identification an easy task [110, 352]. In the case of our InGaAs QDs, we observed up to 4 lines with intensity varying almost linearly with the excitation power. The energy separation between the different lines was found to vary, but ~ 7 meV was a recurring energy span. This suggests an identification as X^- (low energy) and X (high energy peak) by similarity to the results in the above-cited references, although the energy spacing appears larger. Peaks with superlinear evolution with excitation power can be attributed to biexcitons and biexcitonic complexes. These features are generally, but not always, observed at lower energies than the peaks identified as excitons. The cause of the dot-to-dot dissimilarities is yet unclear. The growth interruptions set before and after the QD deposition may individually alter the QD shape. The low As/III ratio may also give rise to such effect. The QD shape was not characterized, and we do not exclude that the dot may be significantly wider and flatter than the usual pyramidal QDs, strongly affecting the emission spectrum.

The circular mesa isolation (design shown on Figure 6.10(b)) procedure was conducted on a sample containing N, grown with identical As/III=250 ratio (sample 4275, DMHy flux (21,150)ccm). Spectra are displayed on Figure 6.12, representing a QD ensemble as well as isolated QD grown in 300 nm-size pyramids. The QD emission is centered at 1.365 eV and presents a still quite narrow QD ensemble linewidth (~ 15 meV). The individual QD low power emission generally consists in 1 to 3 peaks that can be tracked up to a quite high excitation power. As will be presented in Section 6.4, the magnitude of the degree of linear polariza-

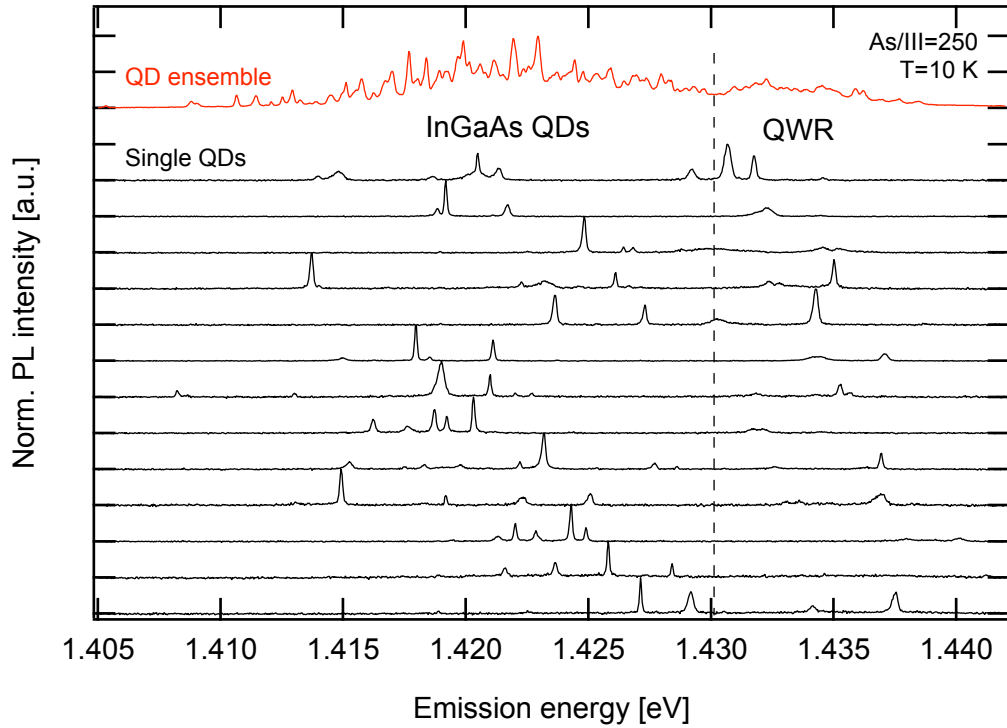


Figure 6.11: Low temperature, low power μ PL spectra of a collection of isolated InGaAs QDs (black) as well as of a QD ensemble (red). The low power emission consists in a collection of sharp lines. Peak identification of specific features can be conducted on some QDs, based on the excitation power dependency, and on linewidth comparison [352]

tion (DOP) and of the fine structure splitting (FSS) are significantly higher in this sample as compared to the N-free counterpart ($34 \mu\text{eV}$ average FSS instead of $12 \mu\text{eV}$). The individual QD features linewidth is degraded compared to the N-free counterpart, but a significant proportion of the lines were observed below $200 \mu\text{eV}$, hinting at a still good QD electronic environment. Power- and polarization-dependant PL spectra of the QDs marked with labels “A” to “E” are shown in Section 6.4.

The last N-containing sample (4280) was grown with a decreased As/III=107 ratio and the same (21,150)ccm DMHy fluxes. Spectra of a QD ensemble as well as of isolated QDs grown in 300 nm-size pyramids are shown on Figure 6.13. With $\sim 35 \text{ meV}$ spectral width, the QD ensemble spectrum is much broader than that of the other samples. This originates from a broader QD energy distribution (inhomogeneous broadening), but also from the large energy separation between the lines emitted by each single QD.

It is difficult to describe general characteristics of the emission in this case, as every QD behaves somewhat differently. Nevertheless, some features are shared by a fairly large number of QDs. The low power spectra are often dominated by quite broad spectral features emitting at low energy. These features are generally observed to spectrally shift when varying the excitation power. This behavior corresponds to that of QDs placed in a slightly charged

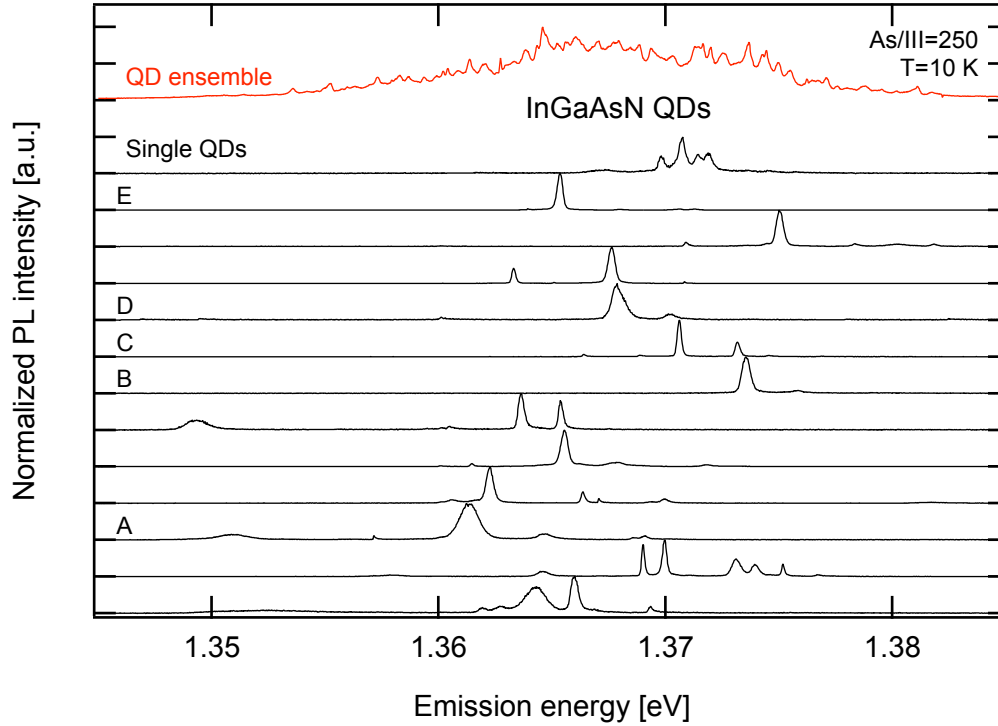


Figure 6.12: Low temperature PL spectra of N-containing QD ensemble (red) and of a collection of isolated single QDs (black). The samples were grown with a ratio As/III=250. Narrowest linewidths are typically less than 200 μeV .

environment, a situation where the excitation power can effectively control the number of net charges in the QD [353]. The fluctuating number of charges inside and close to the QD is responsible for the broad emission linewidth. In our case, a residual background is probably incorporated together with nitrogen, an issue common to all DMHy-grown dilute nitride materials.

As expected, the broad spectral features tend to disappear at higher power levels, overcome by sharper transitions ($\sim 300 \mu\text{eV}$) that become dominant at power levels corresponding to the exciton saturation on the N-free InGaAs QDs. These transitions are most probably the exciton and single-charged exciton lines.

We observed the regular presence of a narrow set of transitions located 10 - 15 meV above the lowest-energy sharp transitions, behaving supralinearly with power. By comparison with Refs. [354, 355], we suggest that these transitions originate from biexcitonic lines with dominant light-hole character.

On Figure 6.14(a)-(d) are shown 10 K power-dependent PL spectra of four selected isolated QD. While Figures 6.14(a) to 6.14(c) show QDs with relatively simple low power emission spectra, Figure 6.14(d) depicts a less clear situation more representative of the majority of QDs. The low-power emission from the QD depicted on Figure 6.14(a) consists in a single line. But several other peaks and complexes rise with power, revealing a complex electronic

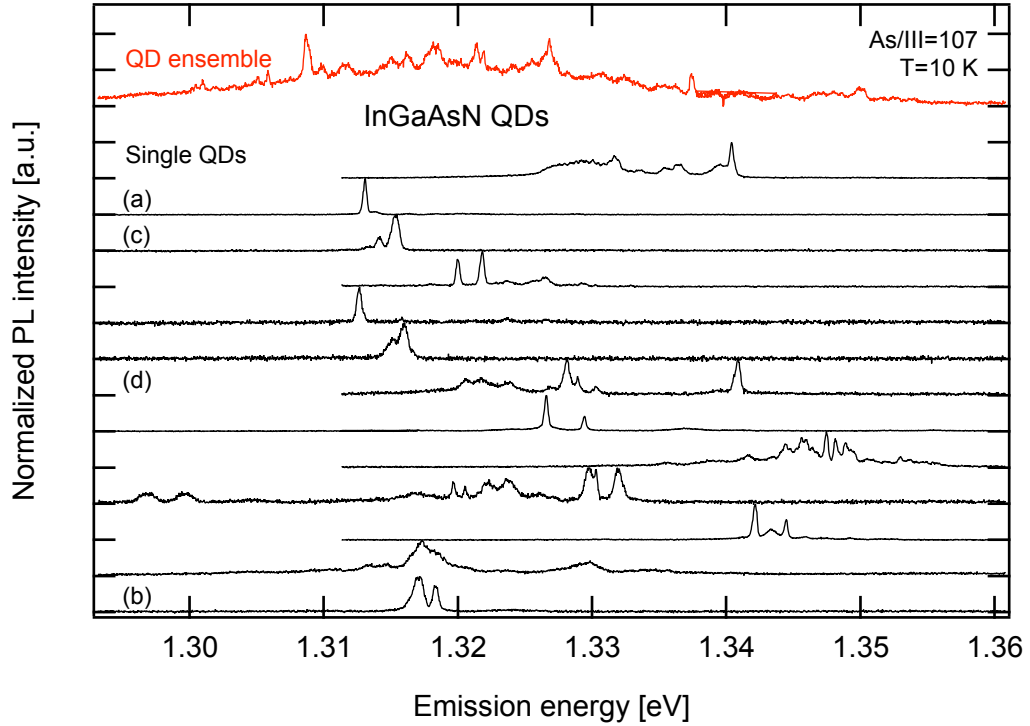


Figure 6.13: Low temperature PL spectra of a N-containing QD ensemble (red) and of a collection of isolated single QDs (black). The samples were grown with a ratio As/III=107. The distribution of QD emission is further broadened as compared to the sample grown with As/III=250 (see Figure 6.12). The low power spectra are often dominated by the low energy, broad spectral features. Power-dependent spectra of the QDs labeled (a), (b), (c) and (d) are shown on the corresponding panels of Figure 6.14.

structure. The two lines visible on Figure 6.14(b) behave like exciton and biexciton lines with power. However the broad low-energy peak seems to be composed of two or three separate contributions whose weight varies with excitation power. Like on Figure 6.14(a), a group of peaks rise with power at an energy ~ 10 meV higher, probably related to excited hole states.

The low-power spectra depicted on Figure 6.14(c) also show what seems like an exciton-biexciton pair, with a reversed binding energy when compared to Figure 6.14(b).

Finally, Figure 6.14(d) shows a more common situation where a whole set of relatively broad emission lines dominates the low-power emission spectrum. The relative intensities of the peaks change with the excitation power. Sharper lines arise at intermediate power levels. In general, we observed a large variety in the arrangement of QD emission lines and variation with power level.

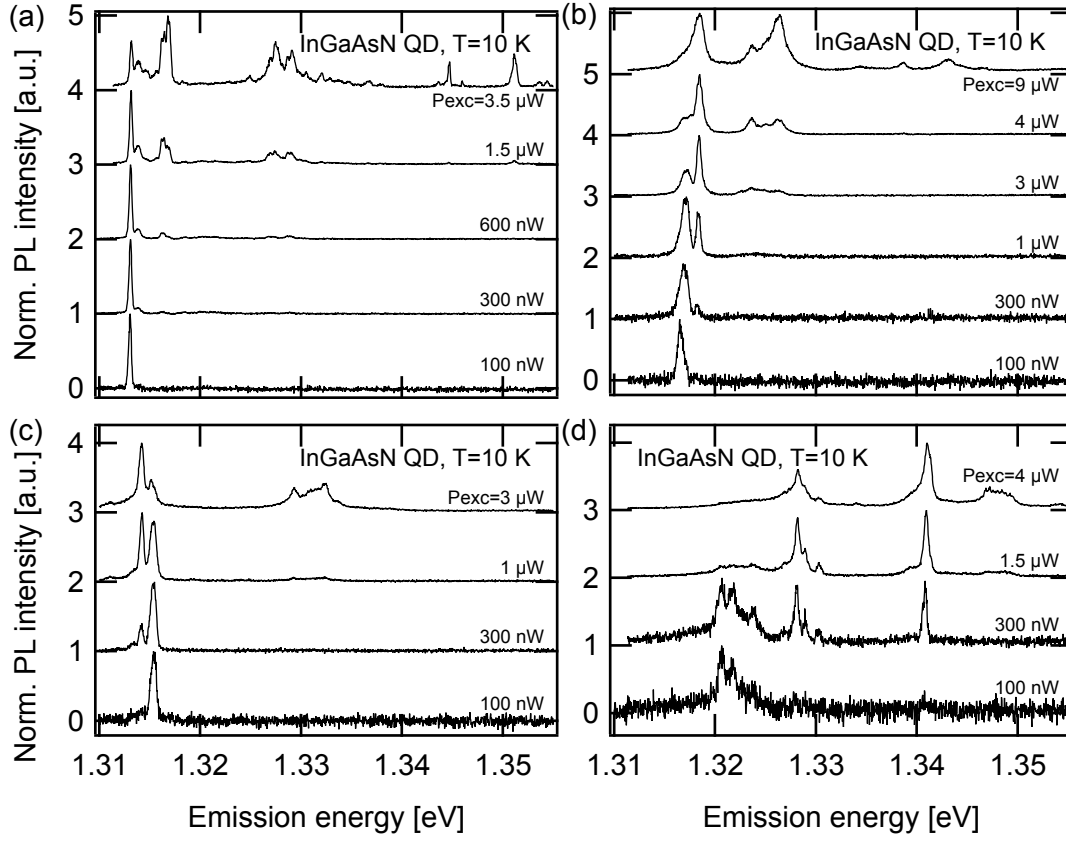


Figure 6.14: Power-dependent low temperature spectra of four isolated N-containing QD grown using a low arsine flux ($\text{As}/\text{III}=107$). The horizontal axis is identical in each graph. The sharpest lines present $\sim 300 \mu\text{eV}$ spectral linewidths.

6.4 Polarization properties of InGaAsN pyramidal QDs

In ideal, symmetric QD, states with opposite spin are degenerate, hence they emit at the same energy. The out-of-plane emission consists in two independent components, circularly polarized in the right, respectively left direction. However, if the QD symmetry is not perfect, this degeneracy is lifted and the emission peak splits into two components with slightly different energy, linearly polarized according to the QD asymmetry. The energy difference between the two states defines the fine structure splitting (FSS). The two orthogonal states often have different intensities, such that a degree of linear polarization (DOP) can also be measured ($\frac{I_{\max}-I_{\min}}{I_{\max}+I_{\min}}$ as detailed in Section 5.4.4). The emission of entangled photon pairs can be obtained from the biexciton-exciton recombination cascade, at the condition that the QD is symmetric enough to exhibit a vanishing FSS, enabling the preservation of the quantum state at least during the time separating the successive recombinations [17, 67, 66, 68]. In the present Section, we analyze the emission of our QDs in terms of linear DOP and FSS, as to characterize the dots symmetry. Values as low as possible are desired, as only vanishing values indicate QDs potentially suitable for the emission of entangled photon pairs.

6.4.1 Methodology

As the QD emission can be polarized in a possibly random orientation, spectra were acquired while regularly rotating a $\frac{\lambda}{2}$ plate placed in front of a fixed polarizer (see Section 3.3). The light was rotated by a full 360° turn, providing two maxima in order to check for the signal stability. The DOP signal plotted on the Figure 6.15 was calculated as follow. The intensity of each pixel was fitted with a sine wave as function of the polarization angle. The degree of linear polarization $\frac{I_{max}-I_{min}}{I_{max}+I_{min}}$ is deduced from the fit according to the formula :

$$I(\theta) = \frac{1}{2} I_0 [1 + \text{DOP} \cos(2(\theta - \theta_0))]$$

The preferential emission axis is at this point a free fit parameter (the phase θ_0 of the sine wave). If no preferential direction can be observed (case of the QD ensembles, see Figure 6.15), θ_0 is kept as a free parameter and the DOP ranges from 0 to 1 (a negative amplitude of the cosine is alternatively described by a phase shift). In the case of isolated QDs, preferential directions were generally observed. In such cases the fit was performed again with θ_0 fixed at the best value, and the DOP ranges as usual from -1 to 1.

Some peaks were observed to spectrally shift with polarization, which is interpreted as a signature of a fine structure splitting. The magnitude of the shift was generally small enough to prevent evidencing the individual contribution of the orthogonal states. The FSS was characterized by: (1) fitting the peak with a waveform on every spectrum, (2) reporting the central energy $E(\theta)$ as function of the polarization angle and (3) fitting the evolution $E(\theta)$ with a sine wave $E_0 + 0.5\text{FSS} \sin(\theta)$. The FSS is taken as twice the sine amplitude.

A non-vanishing FSS prevents computing the DOP using the procedure described above. The DOP value of a large number of individual lines was also calculated based on the peak integrated intensity.

The experimental setup used for polarization measurements was optimized for ~800 nm operation, and induces a slight polarization anisotropy at the wavelength of interest (DOP ~0.04 according to the specifications of the beamsplitter extracting the signal from the microscope column). The data were processed without correcting this artifact, as it was observed generally weaker than the QD intrinsic polarization anisotropy. Nevertheless, the intensity of the polarization labeled as 0° should be increased by ca. 8% to properly take care of this artifact. The signal polarization induced by other optical elements at the wavelength of interest is not known, but is believed small thanks to the positioning of the polarization optics close to the cryostat.

6.4.2 Polarization properties of QD ensembles

In a first step the polarization properties of as-grown InGaAsN pyramidal QD ensembles were characterized, to avoid effects related to the presence of mesas in the vicinity of the

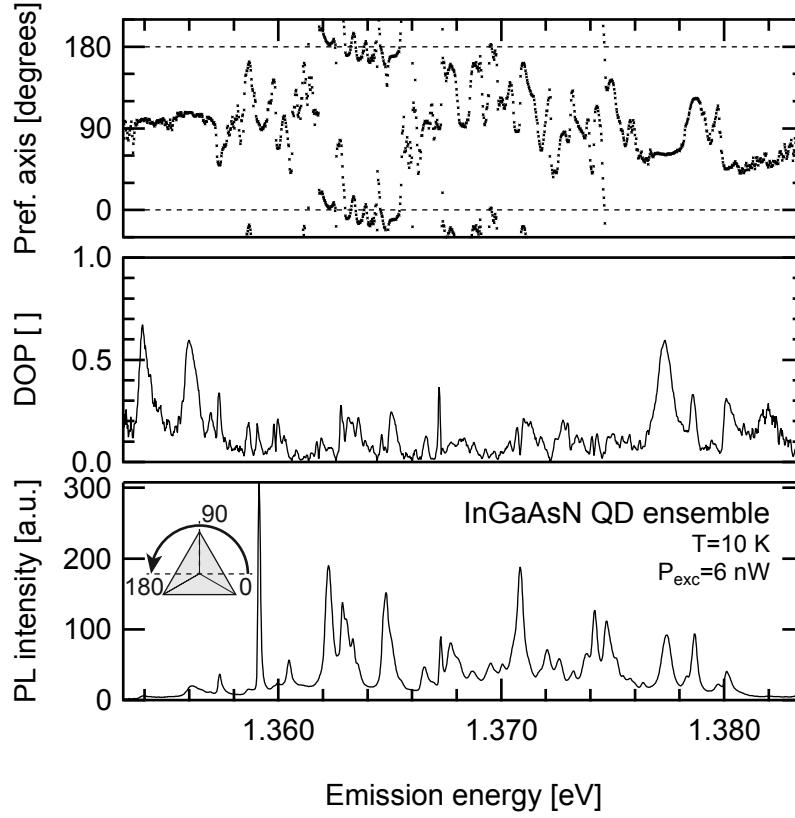


Figure 6.15: Linear polarization of a N-containing QD ensemble (As/III=250). Top: θ_0 phase of the preferential axis (values out of the 0-180° interval are symmetries). Center: degree of linear polarization, ranging from 0 to 1 (negative values are alternatively described by a dephasing). Bottom: PL intensity I_0 . The inset indicates the polarization axis relatively to the pyramid orientation.

light emitters (extraction of anisotropy or resonances). Figure 6.15 shows the polarization properties of such an ensemble, grown with high DMHy flux and high As/III ratio (As/III=250). Each panel shows a free fit parameter of the DOP equation: from top to bottom, the preferential anisotropy direction θ_0 , the DOP (ranging from 0 to 1 as a negative value is accounted for by a phase shift), and the average PL intensity I_0 .

A preferential axis (associated with a weak DOP) can be observed close to the 90° direction, and matches the anisotropy induced by the beamsplitter. This axis is especially preferred on the low and high-energy edges of the emission. The preferential emission direction of the main peaks appears quite random, and both the DOP and the phase exhibit sudden changes.

To obtain some statistical information on the distribution of DOP and FSS values over the emission peaks, we characterized individually the QD lines of polarization-resolved spectra acquired on different locations. The lines were fitted on each spectrum by a waveform, generally a Gaussian peak. The evolution of the integrated intensity of the waveform was used to calculate the DOP, and the shift in the central energy to estimate the FSS. The quality

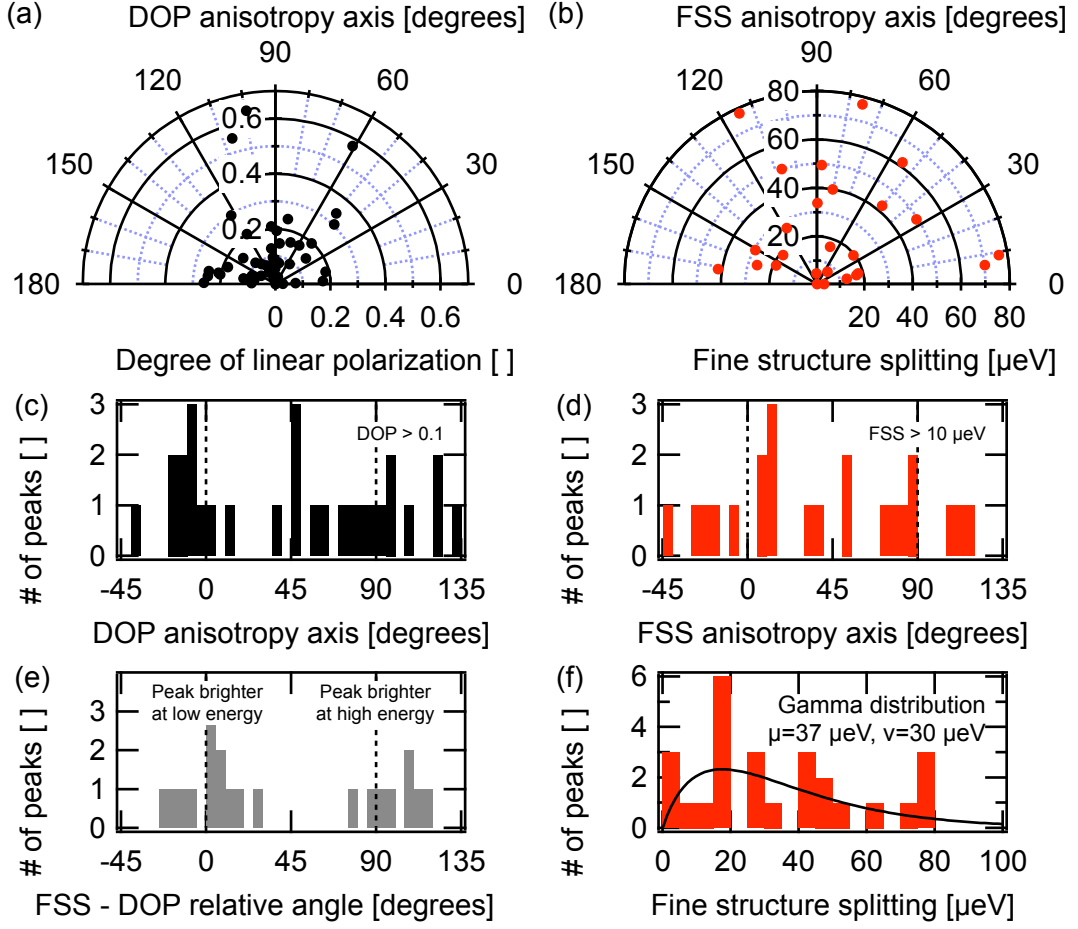
N-containing InGaAsN QD polarization properties


Figure 6.16: Polarization properties of individual lines in ensemble spectra of InGaAsN QDs (As/III=250). (a) Polar representation of the DOP of peaks in a QD ensemble, as a function of the anisotropy direction. (b) Polar representation of the magnitude of the FSS of the same series of peaks, as a function of the anisotropy direction. (c), (d) Histograms of the anisotropy axis of the (c) DOP and (d) FSS, revealing no clear preferential direction. Small anisotropies were excluded from the histograms. (e) Histogram of the angular difference between the DOP and FSS anisotropy axis, showing a clear (anti-)correlation between the DOP and FSS anisotropy axis. (f) Histogram of the FSS values, fitted with a Gamma probability distribution.

of the waveform fit, that of the intensity evolution as well as that of the spectral shift, were systematically controlled, and inconsistent data were discarded. However, as the waveform accounts for the background emission in addition to the analyzed peak itself, the DOP value obtained by this method is only a lower estimate of what would be measured if the QD had been isolated (i.e. if the spectra presented no background emission). The reliability on the FSS shifts is estimated better than $10 \mu\text{eV}$.

Figures 6.16(a) and 6.16(c) reports the preferential anisotropy direction of the emission inten-

sity, represented (a) on a polar plot with the DOP as radial coordinate, and (c) on a histogram plot (restricted to peaks with $\text{DOP} > 0.1$). For most of the individual lines the DOP is smaller than 0.2, but large values are also found. Due to the data processing method, the DOP values are only lower estimates. The real values are certainly higher. The histogram plot reveals no significant alignment of the preferential axis along the 30° , 90° and 150° directions, which point toward the QWR and pyramid wedges. Similarly, no clear alignment can be linked with the 0° and 90° axes, which could be induced by the setup.

On Figures 6.16(b) and 6.16(d) are shown the preferential FSS directions, presented in (b) as a polar plot with the FSS shift as radial coordinate, and in (d) on a histogram plot (where only QD lines with a FSS $> 10 \mu\text{eV}$ are represented). Again, no clear alignment of the FSS is observed along the natural axis of the setup or along the pyramid symmetry axis. The FSS has a quite wide distribution, extending up to $80 \mu\text{eV}$ for the spectral lines sampled. Figure 6.16(f) shows an histogram of the FSS values, that was fitted with a Gamma probability distribution ($f(x; k, \theta) = \theta^{-k} (\Gamma(k))^{-1} x^{k-1} \exp -\frac{x}{\theta}$, for $x > 0$ and $k, \theta > 0$ and with Γ the gamma function). The average (median) value deduced from the fit is $37(30) \mu\text{eV}$, comparable to the experimental values (34 and $27 \mu\text{eV}$). These values are larger than for comparable InGaAs pyramidal QDs grown without nitrogen (see below).

On Figure 6.16(e) is shown the angular difference between the anisotropy axes of the DOP and of the FSS. A clear correlation is observed, evidencing that the DOP and FSS as were characterized in this work, arise from the same origin. For the majority of QD lines, the two characteristics are correlated: the brighter polarization is that at low energy. In this survey a significant proportion of the QD lines present an inverse behavior, i.e. the brightest polarization is that at high energy. A similar correlation is observed on mesa-isolated QDs (not shown). The preferential axis of FSS is statistically observed correlated to that of DOP. The low-energy line is generally brighter than the high-energy one and the opposite situation less common.

The polarization properties described above can be compared with that of the N-free InGaAs pyramidal QD sample grown without DMHy, using the same As/III=250 ratio. The same data processing was performed on polarization-resolved spectra acquired on that sample, and the results are summarized on Figure 6.17 with a layout identical to that of Figure 6.17. A significantly lower average DOP value was observed (below 0.05 over the spectrum, instead of 0.17 for the InGaAsN sample), but the characterization procedure may preclude this comparison, as the background was not properly separated from the signal. The FSS is less sensitive on measurement artifacts and conditions, and again the N-free QD are more symmetric. The average (median) FSS shift is $10(9) \mu\text{eV}$ in the case of N-free QDs, while $37(30) \mu\text{eV}$ are observed in the case of N-containing QDs. This demonstrates that the introduction of nitrogen contributes to breaking of the natural QD symmetry, and introduces a sizeable emission anisotropy. The FSS of a significant proportion of QD lines of the N-free sample was actually too weak to be reliably estimated. Especially, most of the peaks were excluded from the histograms on Figures 6.17(c)-(e) because of their low FSS or DOP magnitude. A more extensive set of data

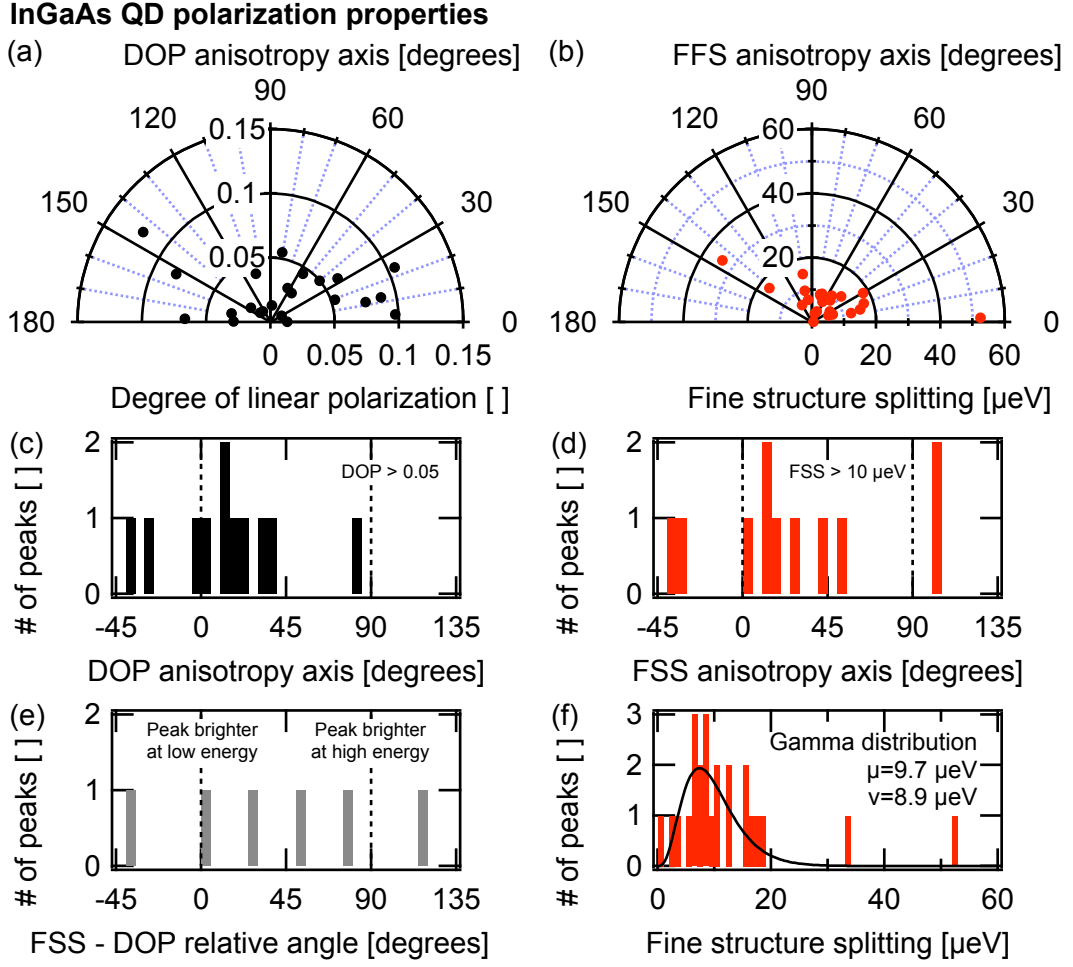


Figure 6.17: Polarization properties of individual lines in ensemble spectra of InGaAs QDs. (a) Polar representation of the DOP of peaks in a QD ensemble, as a function of the anisotropy direction. (b) Polar representation of the magnitude of the FFS of the same series of peaks, as a function of the anisotropy direction. The anisotropies are weaker than for InGaAsN QD. (c), (d) Histograms of the anisotropy axis of the (c) DOP and (d) FFS, revealing no clear preferential direction. Small anisotropies were excluded from the histograms. (e) Histogram of the angular difference between the DOP and FFS anisotropy axis: the small number of peaks with both significant FFS and DOP preclude any conclusion. (f) Histogram of the FSS values, fitted with a Gamma probability distribution.

would be required to analyse more in detail the preferential anisotropy axis.

The polarization properties of the pyramidal QD ensembles can be summarized as follows. The values of both linear DOP and FFS are observed to be significantly increased in N-containing samples as compared to the N-free counterparts. The FFS of N-containing QDs is generally non-vanishing ($\sim 30 \mu\text{eV}$ on average), indicating that the N significantly disturbs the QD natural symmetry. We observed no clear alignment of the DOP or FFS along any of the pyramid

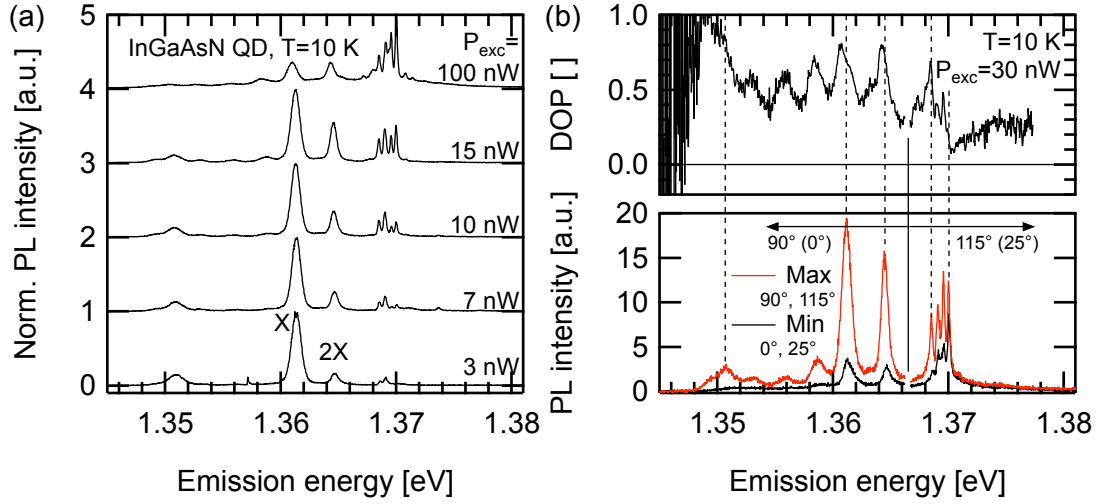


Figure 6.18: Low temperature spectra of the isolated QD labeled “A” on Figure 6.12, as function of (a) the excitation power density, and (b) linear polarization. The degree of linear polarization is also shown and is above 0.5. The preferential emission angle is slightly tilted for the high-energy spectral lines.

symmetry axes, or along the measurement setup axis. However, a clear correlation is observed between the preferential axes of the DOP and the FSS. Most of the lines are brighter when shifted at low energy, while a small proportion behaves oppositely.

6.4.3 Polarization properties of isolated QD

In the following subsection the emission features of 5 N-containing QDs (As/III=250, DMHy flux=(21,150)ccm) are presented in detail. The QDs were isolated by circular mesa etching. Spectra are shown as function of excitation power and linear polarization. To acquire the polarization data, the excitation power was chosen such as the lines that can be attributed to the X and 2X transitions show comparable intensities. The preferential polarization direction, or anisotropy axis, of the QD lines will be systematically commented on. The purpose is to present some of the variety of emission lines patterns we met, and to show in more details the influence of nitrogen incorporated on the QD polarization properties.

Figure 6.18(a) shows the power-dependent spectrum of the isolated QD labeled “A” on Figure 6.12. The presence of several peaks is noted on the low-energy side of the spectrum. In InGaAs QDs, such peaks arise when multiple charges get trapped into the QDs. This type of recombination becomes dominant at low excitation power when a slight residual background doping surrounds the QD [353]. In our case, a slight residual doping is probably incorporated together with the N. Alternatively, the etched surfaces may host impurities and trap charges. The evolution of peak intensities with power is consistent with assigning the 1.361 eV peak to the X, the 1.365 eV peak to the 2X ($E_{2X}^B = -3.3$ meV) and the series of peaks at 1.37 eV to

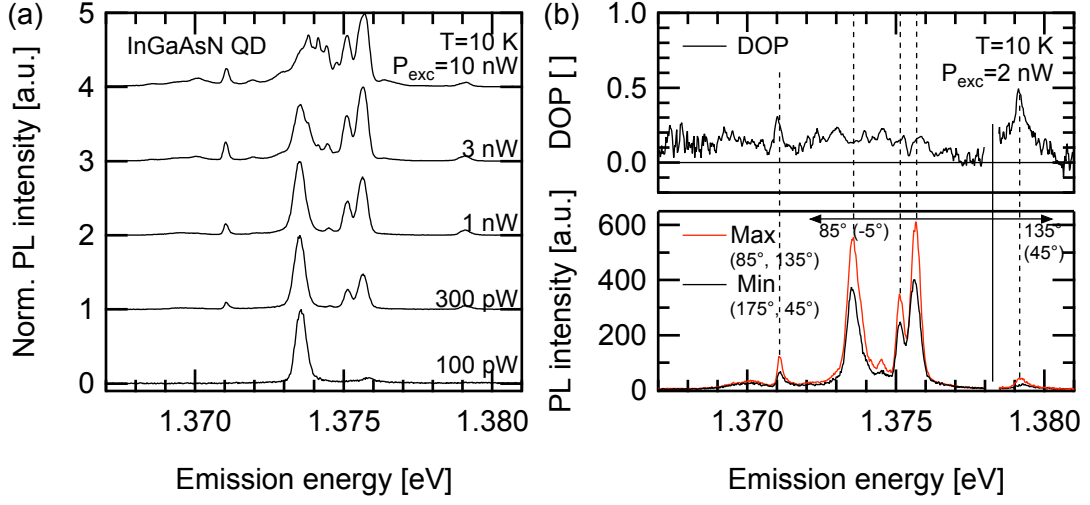


Figure 6.19: Low temperature spectra of the isolated QD labeled “B” on Figure 6.12, as function of (a) the excitation power density, and (b) linear polarization. The degree of linear polarization stays below 0.5. The preferential polarization direction of the 1.379 eV line is tilted with respect to that of the other lines.

biexcitonic lines with a dominant light-hole character [354, 355], although this remains speculative.

The DOP is large, ≥ 0.5 for most of the peaks. The peaks with dominant heavy-hole character (emitting at lower energy) exhibit a preferential polarization axis at 90° . However the series of peaks attributed to light-hole biexcitonic transitions are polarized along a slightly different direction, 115° . We quite commonly observed QDs with most of the transitions sharing the same preferential polarization axis, while a single or a group of lines present a different preferential axis.

Figure 6.19 shows the power-dependent and the DOP spectra of the isolated QD labeled “B” on Figure 6.12. Several sets of lines successively rise with excitation power. With the exception of the 1.379 eV line, all peaks share the same preferential polarization orientation. The DOP is close to ~ 0.2 for every peak.

Figure 6.20 shows the power-dependent and the DOP spectra of the single QD labeled as “C” on Figure 6.12. The DOP is large (in the 0.4-0.5 range when properly characterized). All the lines share the same preferential anisotropy axis. The presence of a non-negligible FSS leads to large changes in the DOP spectrum displayed on Figure 6.20(b). The peaks are asymmetric, and present a high-energy tail that is less polarized than the QD line itself. The FSS of the 3 main low-energy states is small ($< 20 \mu\text{eV}$) and the peak low-energy polarization component is brighter.

The emission can be divided into 3 pairs of lines with similar behavior with power (power exponent and saturating power), with the lines within each pair separated by an equal energy span (2.55 meV). The central pair remaining at low excitation power is likely emitted by an

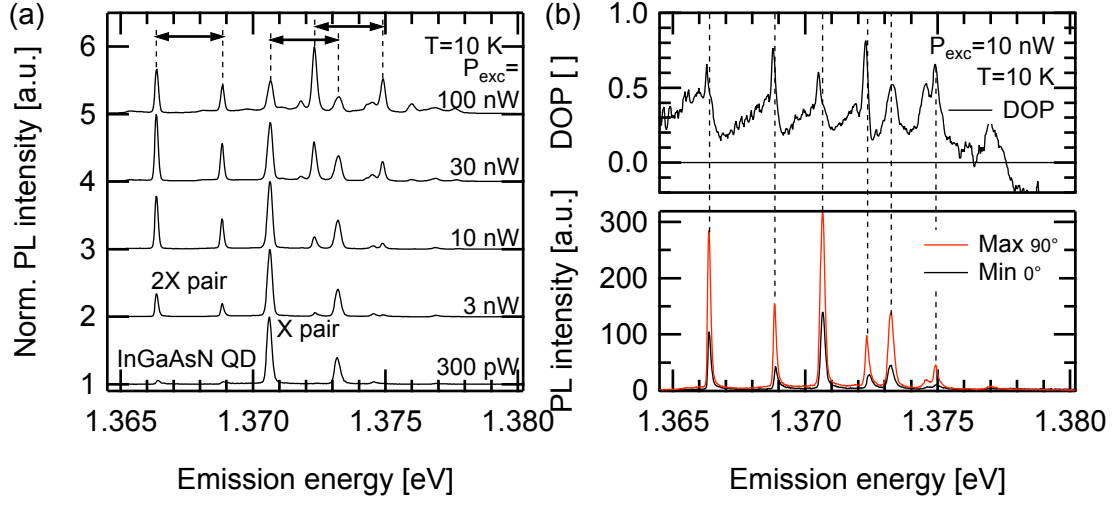


Figure 6.20: Low temperature spectra of the isolated QD labeled “C” on Figure 6.12, as function of (a) the excitation power density, and (b) linear polarization. The different spectral features are highly polarized (~ 0.5), all in the same direction. 3 pairs of peaks with identical energy spacing and behavior with power are evidenced in (a).

exciton and a charged exciton. The intensity of the low energy pair rises with power like a biexciton (power exponent ~ 1.2 versus ~ 0.6 for the first pair) and we propose to assign its origin to a neutral, respectively charged biexciton ($E_{2X}^B = 4.3$ meV). The last pair appears at high power with an even higher power exponent (~ 1.6) and we propose a neutral, respectively charged multiexcitonic origin.

On Figure 6.21 are depicted the power- and polarization- dependent spectra of the QD labeled “D” on Figure 6.12. This is a more complex situation, where three distinct preferential polarization directions can be identified throughout the spectrum. Additional, broad transitions seem to appear in the low-power spectrum, modifying the shape of the main peak.

Figure 6.22 depicts the power- and polarization- dependent spectra of the QD labeled “E” on Figure 6.12. The two low-energy peaks behave with power like an exciton and a biexciton ($E_{2X}^B = 2.6$ meV), and exhibit opposed FSS: while the high-energy polarization of the X transition is brighter, the low-energy 2X polarization is brighter. This behavior is expected for any X-2X recombination cascade.

This QD is one of the few cases where a simple reversal of the DOP can be seen. The more common situation is when the preferential polarization direction of different lines is slightly tilted. Here we observe close to 1.372 eV a tilt of the preferential polarization direction by 90° , translated here by conserving the same direction and computing a negative DOP.

The emission features of several pyramidal InGaAsN QDs were presented above in some details. For a given QD, the majority of the spectral lines exhibit linear polarization aligned along the same anisotropy axis. It is however common that the preferential polarization direction of

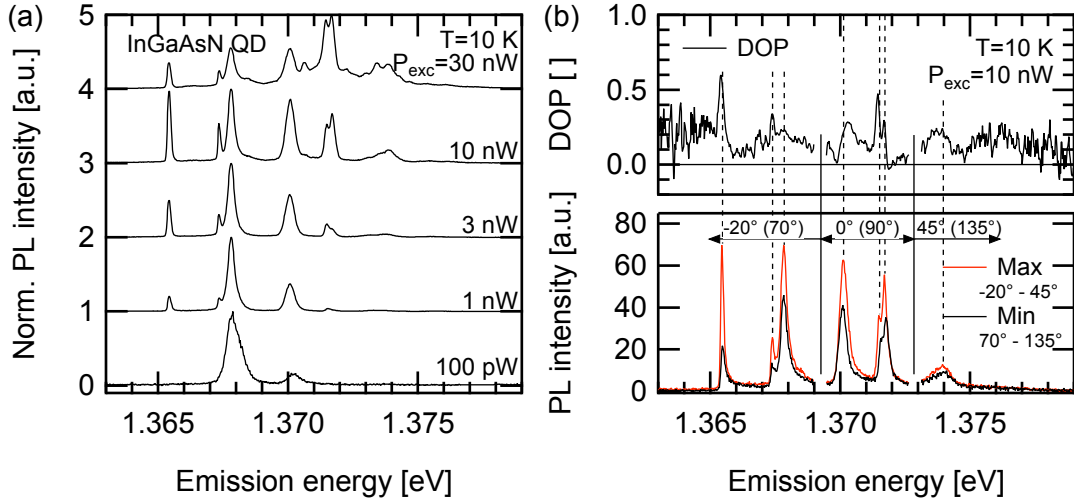


Figure 6.21: Low temperature spectra of the isolated QD labeled “D” on Figure 6.12, as function of (a) the excitation power density, and (b) linear polarization.

a set of high-energy lines is slightly tilted with respect to that of the low energy peaks. We were able to tentatively attribute some emission peaks to the X and $2X$ transitions, and these transitions are located on the low-energy side of the QD emission spectrum. The X and $2X$ transitions quite generally share the same preferential polarization direction. In some cases, the change in the anisotropy axis of high-energy peaks seems related to a possible change from heavy- to light-hole character of the transitions.

6.5 Chapter summary

We demonstrated the successful incorporation of nitrogen into InGaAs/GaAs QDs grown in inverted pyramids. A 75 meV redshift of the QD emission was achieved as a result of N incorporation. The characteristics of QD emission were discussed in detail, including on the characteristics of the emission polarization.

The influence of the crucial parameters As/III, GaAs buffer thickness and pyramid size was systematically explored, in order to determine the window of parameters most favorable for N incorporation. The QD emission wavelength is strongly affected by these parameters, showing a strong redshift when decreasing the pyramid size and lowering the As/III ratio. InGaAs QDs emitting at energies as low as 1.295 eV were obtained, and some further redshift is possible, although limited.

Isolated InGaAs QDs obtained with our growth procedure exhibit sharp emission peaks, a significant proportion of the lines being resolution-limited ($<100 \mu\text{eV}$). However, in contrast to previous studies that revealed an extreme dot-to-dot similarity in the emission spectra [356, 110, 352], in our case we were not able to identify a clear, reproducible pattern in the

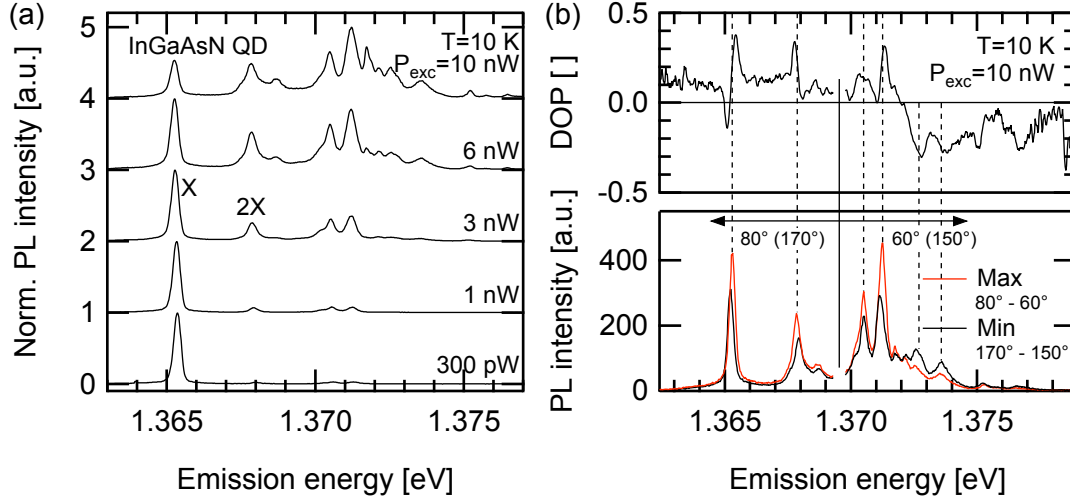


Figure 6.22: Low temperature spectra of the isolated QD labeled “E” on Figure 6.12, as function of (a) the excitation power density, and (b) linear polarization.

energy separations between discrete QD lines. The degradation of the reproducibility may arise from several origins. Irregularities in the substrate patterning are introduced by the recess over-etching required to place pyramids of different sizes on the same substrate. More likely, the QD interfaces are modified during the growth interruptions set before and after the QD deposition, thus affecting the QD states energies. The low As/III ratio may also adversely affect the QD shape or alloy purity in the QD or in its vicinity. Finally, the QD shape was not characterized and may be significantly flatter than usual pyramidal QD, a shape that would alter the electronic states.

The first growths of N-containing QD were conducted with an As/III=250 ratio that produces N-free QDs with an almost unchanged energy when compared to the usual, high ratio. The redshift is significant and increases with the DMHy flux (~ 55 meV with a high DMHy flux in 300 nm-size pyramids). It is difficult to separate the effect of N on the bandgap bowing from that of the presence of DMHy on the MOVPE surface kinetics. We are however most confident in the actual presence of N in the QD. Peaks are observed with ~ 200 μ eV linewidth, still good but already degraded when compared to the resolution-limited lines of the N-free sample (< 100 μ eV). The DOP and FSS are significantly increased compared to the N-free counterpart (FSS average value of 34 μ eV instead of 12 μ eV). Within a single QD, the axis of polarization anisotropy of each peak are generally aligned; it is however common that the axis of some high-energy lines are slightly tilted to a different direction. Some QDs present broad transitions on the low-energy side of the spectrum, which can be attributed to multi-charged QD states. This behavior is commonly observed when the QD sample presents a slight residual doping [353].

Next, the As/III ratio was lowered to As/III=107 as to favor N in the group-V competition for incorporation. A further redshift (~ 75 meV) was thus obtained, leading to a 1.32 eV emission

energy. On this sample, a large N-induced redshift was also achieved on larger pyramids (400 nm). The QD linewidth is further degraded, with a few lines exhibiting a 300 μeV linewidth. The disorder is also increased in the pattern of spectral lines. Broad, low-energy transitions often dominate the low-power spectrum, indicating a slightly doped environment in the QD surrounding. This may be caused by the DMHy-induced residual doping, but also by the low As/III ratio used for the QD deposition, which is known to be too low for the fabrication of high-quality QDs.

A sizeable deterioration of the QD optical quality is already noticeable with a 80 meV redshift. As a consequence, high-quality QDs can only be grown with a relatively limited N content, and the emission wavelength is therefore closely related to that of the InGaAs QD counterpart. As it is difficult to grown InGaAs pyramidal QDs emitting above 1 μm , the fabrication of high-quality N-containing QDs emitting at 1.3 μm appears difficult.

The N incorporation appears non homogeneous in the different pyramidal nanostructures (QD, QWRs). A reversed evolution of the QWR emission energy with pyramid size was observed in the samples grown with high DMHy flux. We propose a tentative scenario explaining this behavior. In small pyramids, the high local curvature and growth rate at the QD location efficiently depletes the N in the whole recess, whereas in large pyramids the limited N diffusion length limits the trapping efficiency, letting a significant amount of N to be incorporated in the QWR. This scenario explains the unusually lower QWR emission energy in large pyramids. The large QWR linewidth also finds a satisfactory explanation by the formation of a gradient of N concentration in the QWR, according to the distance to the QD.

It appears that if N can be used satisfactorily to shift the emission of QWs and QWRs up to the 1.3 μm telecommunication window, the N incorporation into pyramidal QDs contributes to break the natural C_{3V} dot symmetry. The degradation of the emission linewidth and symmetry is already effective when a relatively small redshift (~ 75 meV) is achieved. The detailed characterization of our N-free QDs confirms that a large room exists for quality improvement. It does nevertheless seem unrealistic to expect emission of entangled photon pairs at 1.3 μm out of dilute nitride GaAs-based QD grown in pyramids.

7 Conclusions and outlook

The present research forms a coherent ensemble, focusing on the study of nitrogen incorporation in QW, QWR and QD nanostructures. The main goal in view of applications is the fabrication of nanostructures formed by capillarity emitting at $1.3\text{ }\mu\text{m}$ wavelength, relevant for devices related to glass optical fiber telecommunication. Such emission wavelength cannot be achieved with alloys like InGaAs, GaAs or AlGaAs on GaAs substrates without undesired 2D-3D growth mode transitions. The introduction of small amounts of nitrogen in GaAs-based nanostructures materials is seen as a unique opportunity to shift their emission spectrum close to $1.3\text{ }\mu\text{m}$.

The research work is structured based on a regular progression. It starts from the quite well documented growth of dilute nitride QW on planar substrates, then concentrates on incorporating nitrogen into the related V-groove QWR system, and finally studies the influence of nitrogen on the optical properties of QDs grown in tetragonal pyramids. The main findings of our work can be summarized as follow.

In Chapter 4 we reported the growth of dilute nitride QW using the so-called 2-step growth method. Large QW redshifts were achieved ($> 250\text{ meV}$), pushing the emission wavelength close to $1.3\text{ }\mu\text{m}$ at room temperature. The effect of substrate misorientation is studied, showing large variations in the N incorporation efficiency according to the substrate misorientation and to the surface corrugations. SIMS measurements evidenced the preferential accumulation of N at the lower QW interface, actually suggesting a significant N incorporation into the GaAs lower barrier on the substrates with a large misorientation. Meanwhile, we observed no correlation between the redshift achieved by varying the substrate misorientation with the intensity of the corresponding PL signal. Our results especially emphasize the importance of a homogeneous N incorporation in QWs. The performances of MOVPE-grown QWs is usually inferior to those grown by MBE, and part of the discrepancy may be due to an inhomogeneous N incorporation leading to the formation of a defect-rich layer at the lower interface, hindering the overall device performance. The use of misoriented substrates in future devices may permit a non-negligible redshift of the optical transitions of dilute nitride QW, this hopefully without negatively affecting the PL efficiency.

In the same chapter we evidenced the effect of misorientation on N-free InGaAs QWs. The narrowest linewidths were observed for small miscut angles ranging from $0.3 - 0.4^\circ$, quite analogous to what was observed in GaAs/AlGaAs QWs. The optimal angle depends on the surface diffusion of adatoms, promoted in our case by the growth interruptions: other conditions may lead to different optimal substrate miscuts.

The incorporation of nitrogen into QWRs grown in V-grooves is presented in Chapter 5. The introduction of N slightly affects the QWR structure by decreasing the adatom surface diffusion length. The identification of the PL emission peaks is performed rigorously, and confirmation is brought about the 1D character of the carrier's wavefunctions. We proceeded to a detailed growth study, determining the influence of several growth parameters on the N incorporation efficiency. The top-QW emission energy is affected by substrate misorientations in a similar way as the QWs presented in the previous chapter; by contrast the QWR emission energy is only marginally affected by the substrate miscut. Room temperature $1.3\text{ }\mu\text{m}$ wavelength emission is demonstrated, achievable by several combinations of growth parameters. The N content seems larger in the vicinity of the first interface, in spite of the 2-step growth process. The evolution of the PL spectrum with temperature shows that the top-QW is more strongly affected by defects and presents a more pronounced S-shape than the QWR and than the optimized QWs presented in the previous chapter, hinting at the effectiveness of the 2-step growth method to improve the material quality. A study of the QWR polarization properties is also reported, emphasizing the role of strain on the anisotropy buildup. Hydrogenated QWR samples maintain a strong anisotropy of the QWR ground state even at room temperature. If we successfully demonstrated $1.3\text{ }\mu\text{m}$ room temperature emission, the $1.55\text{ }\mu\text{m}$ telecommunication window may not be achievable while conserving the desired level of material quality. Future works may focus on embedding QWRs into photonic crystal cavities operating at long wavelengths, with several advantages. First the emission wavelength shifts away from the GaAs absorption tail. Second, such cavities need to be scaled-up to accommodate longer wavelength resonances, while the size of lithographic defects remains unchanged: the quality factor of long-wavelength photonic crystal devices should be improved.

A growth study of pyramidal InGaAs QDs is presented in Chapter 6, in view of identifying the window of parameters best suitable for N incorporation. The primordial influence of the As/III ratio on the emission energy is especially demonstrated, in addition to better-known parameters such as the buffer thickness, recess size and QD thickness. The longest N-free QD emission achieved during this short survey was $\sim 960\text{ nm}$, but this wavelength is not the upper bound for QD emission. This wavelength is well above that of similar QD embedded into photonic crystal cavities [113]. Yet these structures still require improvements before entering the strong coupling regime in the QD-cavity interaction. We suggest the QD emission to be shifted to longer wavelengths, migrating further away from the absorption tail of GaAs defects. We point out that a broad emission below 1.37 eV originating from the GaAs substrate is consistently noticed in our setup (see Figure 6.4). If the QD were shifted to these energies, the corresponding states related to this tail may absorb light, possibly affecting the effectiveness of the optical resonator.

We successfully achieved nitrogen incorporation into pyramidal QDs. The QD emission is shifted to the red, and the QD inhomogeneous broadening is progressively increased as more nitrogen is incorporated. The evolution of the emission energy of the lateral QWRs as function of the pyramid size is reversed: a tentative explanation is provided, which involves a long diffusion length of N adatoms, but this point demands a further confirmation. The polarization behavior of individual dots is extensively studied. In addition to the linewidth broadening of the individual QD peaks, the emission becomes also anisotropic. We quantify the increases in the degree of linear polarization (DOP) and in the fine structure splitting (FSS) values related to the nitrogen incorporation. The deterioration of the QD emission quality becomes significant and detrimental to possible applications when a limited redshift is achieved (75 meV). Future works may focus on the interaction of excitons with incorporated nitrogen atoms in the confined space of the QD.

The use of dilute nitride alloys as active materials into nanostructures formed by capillarity proposed new challenges related to the epitaxial growth, the sample characterization and the comprehension of the underlying physics.

The epitaxy of dilute nitride materials does not proceed like that of more usual alloys. For example, high-quality layers of AlGaAs or InGaAs can be grown on GaAs, with chemical compositions almost proportional to the precursor fluxes. By contrast, the fabrication of dilute nitride alloys is a much more intricate problem, far more complex than that straightforward picture. The epitaxy must be performed far from thermodynamic equilibrium due to the very low solubility of N into GaAs; and the incorporation heavily depends on surface effects and chemistry, making the final N concentration very sensitive on the growth conditions. Moreover, N is a member of the group-V family, and as such competes with the arsenic for incorporation. The arsine level is usually kept very large during the growth of QWR and QD nanostructures formed in recesses, in order to saturate the surface with As and improve the purity of the electronic properties. Such arsine-rich conditions cannot be adopted to the epitaxy of dilute nitride alloys, which requires new and unexplored MOVPE conditions.

The dilute materials with concentration in the percent range also do not behave like usual alloys. Dilute nitrides especially share some similarities with doped materials, due to the low atomic concentration and to the electronic properties of N atoms that strongly differ from those of arsenic. In this context the research work performed on structures with different dimensionalities offers new insights in the interaction of charge carriers and excitons, with individual N atoms. In bulk materials the charges carriers tend to diffuse, which averages the properties of the local environment. Any measurement will average the effect of thousands of nitrogen atoms. This remains mostly true in the case of QWs, where the diffusion of carriers still largely occurs.

In the 1-dimensional space offered by the QWR, even shallow irregularities in the electronic potential can prevent the diffusion of the charge carriers, which become trapped in local minima of the fluctuating potential that is associated with specific N local concentrations. This is even more striking when the quantum confinement of charges is further extended in a

QD to the 3 spatial directions. At this point, the electronic properties are determined by the exact location of the nitrogen atoms within the QD. A quantum dot containing nitrogen is a completely different object than the corresponding InGaAs QD.

The optical quality of dilute nitride alloys suffers from defects, non-radiative recombinations and broad emission linewidths. We were indeed able to fabricate QWR structures emitting at $1.3\text{ }\mu\text{m}$, and this wavelength can probably be achieved with QWs as well after minor changes in the growth conditions (only the influence of misorientation was presented in detail). The fabrication of QWs or QWRs emitting at $1.55\text{ }\mu\text{m}$ while keeping good luminescence efficiency appears very challenging, but this is no real surprise.

The PL emission homogeneity and intensity can be improved by incorporating antimony in addition to nitrogen, forming InGaAsNSb alloys. The addition of Sb is known to improve the material quality of N-containing materials by releasing the strain level and preventing the incorporation of defects, and introduces a further bandgap redshift by acting on the valence bands [261, 262]. We strongly suggest future works on dilute nitride materials to focus on this material offering improved devices performances [257, 258].

Nevertheless, it seems unlikely that GaAs-based dilute nitride materials may one day replace lower-bandgap semiconductors such as InGaAs/InP in light-emitting or sensor devices related to silica optical fiber communication.

Contrary to the QW and QWR systems, the QD ground state energy achieved leaves little hope that dilute nitride pyramidal QDs may one day emit at $1.3\text{ }\mu\text{m}$, and a fortiori emit single and entangled photon pairs. Nevertheless, the same mechanism of nanostructure formation may also proceed satisfactorily using other material systems, especially on InP substrates. In spite of early reports, we believe it is possible to grow InP-based QWRs and QDs emitting at longer wavelengths. We indeed initiated some efforts in that direction before the redaction of the present document. This preliminary study is reported in Appendix A, and show promising results with the InGaAs/InAlAs alloys nearly lattice-matched to InP.

A QD grown in inverted pyramids on InP substrates

The 1.3 and 1.55 μm wavelength telecommunication windows are no easy targets for GaAs-based QDs grown in pyramids. As presented in Chapter 6, our dilute nitride InGaAsN/GaAs QD failed to reach the wavelength of interest, and even if able to do so would probably not meet the requirements of QD symmetry and reproducibility. InP-based materials may provide a solution to this problem, as these, and especially the lattice-matched InGaAs compound, exhibits a bandgap compatible with emission in the telecommunication windows. Heterojunctions can be considered, using InP or the lattice-matched InAlAs as barrier material, and InGaAs as active medium.

Numerous attempts were performed in the 1990's to fabricate InP-based V-groove QWRs, a 1D nanostructure with a formation mechanism identical to that of QD grown in pyramids (see Chapter 5). The growth of InGaAs/InP V-groove QWR was already reported using MOVPE [135, 136, 137, 138] and gas-source MBE [139]. However, InP was observed not well suitable for the preservation of a sharp V-groove tip, required to strongly laterally confine the carriers. The formation of nanostructures was nevertheless demonstrated.

For this project, growths were performed in the production reactor of our MOVPE facility by Dr. A. Mereuta, Dr. A. Rudra and Dr. P. Gallo. The author performed the substrate patterning as well as the SEM characterization. The growth study on planar (111)A substrates was performed by the growers.

A.1 Brief review of the InP-based system

InP is a pure III/V material that can be grown with a high quality on conventional substrates. This material presents no segregation effects in the case of non-planar growth. The surface adatom diffusion length is very long, according to the images of Ref. [135, 136, 137].

The InAlAs alloy lattice-matched to InP presents a bandgap quite similar to InP, with however some band offsets. This material is a possible candidate for the growth of the QD barriers. In segregation is expected at the apex of pyramids filled with InAlAs, leading to the formation of an

In-enriched vertical QWR analogous to that formed in the GaAs/AlGaAs pyramid system [124, 117]. This vertical QWR would be strained, and could possibly emit at very long wavelengths: the lower bound being the bandgap of pure InAs. The alloy composition should be (nearly) lattice-matched on InP, and this may require adjustment of the actual group-III gas-phase precursors ratio from that determined on (100) surfaces. This alloy generally presents a poor luminescence efficiency.

The GaInAs lattice-matched to InP is the candidate for the QD material. As a ternary material, segregation effects are also expected here. Those would probably be not detrimental; this would only increase the In content and redshift the QD emission. The longest emission wavelength would anyway be due to the QD. The QD strain could be released by increasing the nominal Ga composition. In an ideal scheme, the GaInAs would be the thickest at the QD location. The characterization of an InP-based structure must be performed carefully, as the emission could be shifted out of the range of the detector presented in our measurement system (~ 1620 nm as mentioned in Chapter 3).

A.2 Substrate patterning

The patterning of (111)B InP substrates was performed using the same lithographic processes as in the case of GaAs substrates (see Chapter 3). The Br:Methanol solution proved efficient and provides excellent crystallographic selectivity. InP appears to resist better than GaAs to etching times largely exceeding the targeted value.

The selectivity of the ICP recipe using a BCl_3/N_2 gas mixture intended for GaAs etching proved sufficient to fabricate alignment marks, although the etching rate of InP is about half that of GaAs. Thicker SiO_2 masks should be deposited if ICP etching recipes optimized for GaAs are to be used.

A.3 Determination of the best material for barrier composition

The proper choice of the barrier material is crucial as it determines the shape of the QD formation site. The candidate materials are InP and InAlAs. Two growths runs were performed on InP substrates patterned with fields of $1\text{ }\mu\text{m}$ pitch pyramids of size ranging from 0.6 to $0.9\text{ }\mu\text{m}$. The growths consisted in the deposition of two layers of same nominal thickness: InP on InAlAs (Figure A.1(a)), respectively InAlAs on InP (Figure A.1(b)). The growth rate of InP was 0.08 nm s^{-1} , and that of InAlAs was 0.16 nm s^{-1} . The evolution of the pyramidal template was characterized by means of side-view SEM on freshly cleaved substrates, owing to a weak chemical contrast. Such images are shown on Figure A.1, with the inner interfaces emphasized with white dashed lines.

InP presents irregular growth on the (111)A facets of the recesses, and offers only a flat pyramid apex unsuitable for the formation of a QD. Moreover, qualitative differences in the profile are

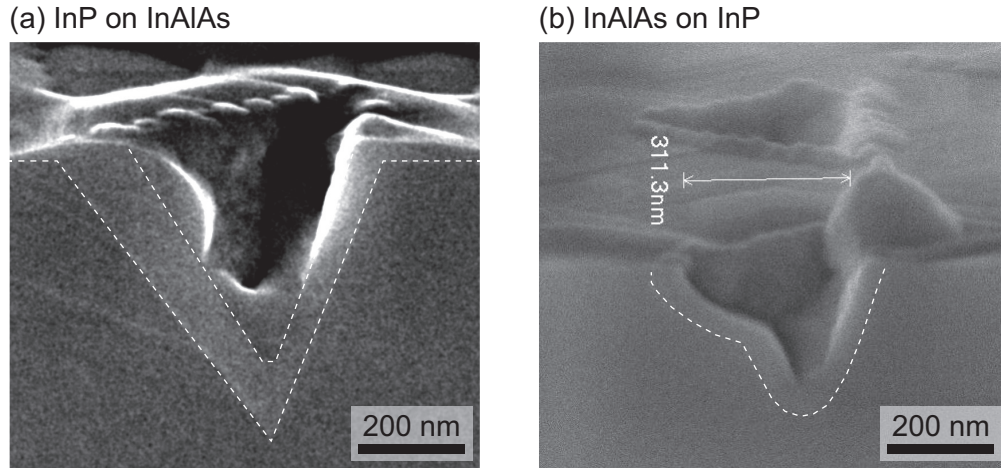


Figure A.1: SEM side-views of patterned InP substrates, after the successive deposition of (a) InP on top of InAlAs, and (b) InAlAs on top of InP. InP produces an irregular shape and deforms the pyramidal template. InAlAs seems to be a promising candidate owing to the smooth surfaces and sharp pyramid apex.

observed when comparing neighboring pyramids. Similar problems were already reported in the case of growth of V-groove InP-based QWRs [135, 136, 137, 138]. A much lower growth temperature and a faster growth rate may, or may not, overcome this latter difficulty. But the irregular surfaces are to be imperatively avoided.

InAlAs appears as a better candidate for the barrier material. A vertical In-rich QWR can be guessed on Figure A.1(a) as a dark vertical line. The actual alloy composition of the QWR has not been determined. The pyramidal template starts to close, evidenced on Figure A.1(a) by the steeper second interface. This image also evidences the robustness of the recess shape regarding the high temperature during sample deoxidation. InAlAs appears a candidate much more promising than InP for the barrier material.

Only thin, irregular growth is observed on the (111)B ridge. This material generally arranges itself into triangular islands either flat or pyramidal-shaped with a small slope angle. Figure A.2 shows an optical microscope top-view image acquired in dark-field mode, evidencing fields of pyramids (white regions) as well as the triangular islands. Their size is up to $\sim 2 \mu\text{m}$, and their density shrinks close to the pyramid fields: the long-diffusing precursors molecules are preferably decomposed on the (111)A pyramid facets, depleting the neighboring regions. As visible on Figure A.1, thicker structures also form on the (111)B surface in the immediate vicinity of the pyramids. These originate from the adatom diffusion out of the pyramids, after the decomposition of precursors on the chemically active (111)A sidewalls. These structures may act as radiative recombination centers and may require removal by a well-established post-growth etching, as for the GaAs/AlGaAs on GaAs pyramid system.

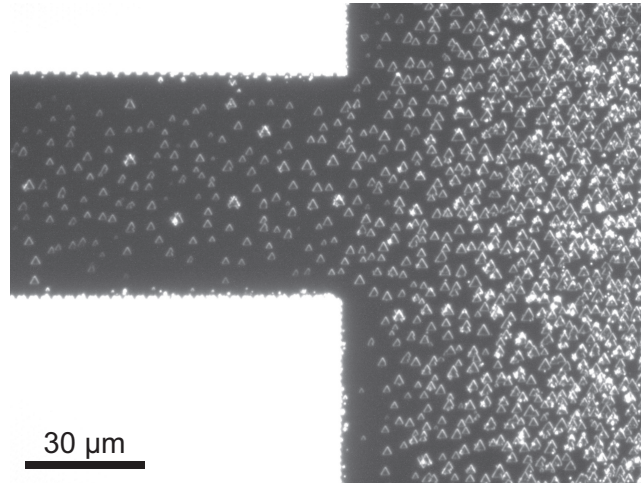


Figure A.2: Top-view optical microscope dark-field image of an InP substrate patterned with square arrays of pyramids (white regions on the left), after the deposition of an InAlAs layer. Residual growth can be observed on the (111)B ridge in the form of triangular islands.

A.4 Detailed morphology of InAlAs growth in pyramids

To facilitate the sample preparation and characterization, growth runs were performed also in larger pyramids ($3\text{ }\mu\text{m}$ pitch). The effective growth rate is reduced in larger pyramids, which helps to reduce the pyramid closing evidenced on Figure A.1(a). Figure A.3 shows a pyramid filled with a 80 nm -thick InAlAs layer. The surface is rough, exhibiting faceted corrugations. A closer look on this type of corrugations is shown on Figure A.3(b), displaying a SEM side-view image of a sample where multiple InAlAs layers were deposited, separated by InGaAs spacers.

A few growth runs were performed with varying the growth conditions (alloy composition, reactor temperature), in order to try improving the morphology. The optimization process is however much easier if performed on planar InP (111)A surfaces, substrates that were ordered meanwhile.

A.5 Growth study of InAlAs on InP (111)A substrates

A growth study was performed by the growers on InP (111)A substrates. The density, size and thickness of the corrugations were evaluated by phase contrast optical microscopy. The aim was to achieve a smooth surface after the deposition of a relatively thick InAlAs layer on InP (111)A surfaces. Such a condition also implies that the alloy is close to being lattice-matched to InP. If this criterion is satisfied, there are fair chances that the growth in pyramidal recesses also produces smooth interfaces.

Some satisfactory InAlAs surfaces have been obtained when increasing the growth temperature from $600\text{ }^{\circ}\text{C}$ to $700\text{ }^{\circ}\text{C}$ (nominal value), using a growth rate of 0.2 nm s^{-1} and a ratio $\text{As}/\text{III}=150$.

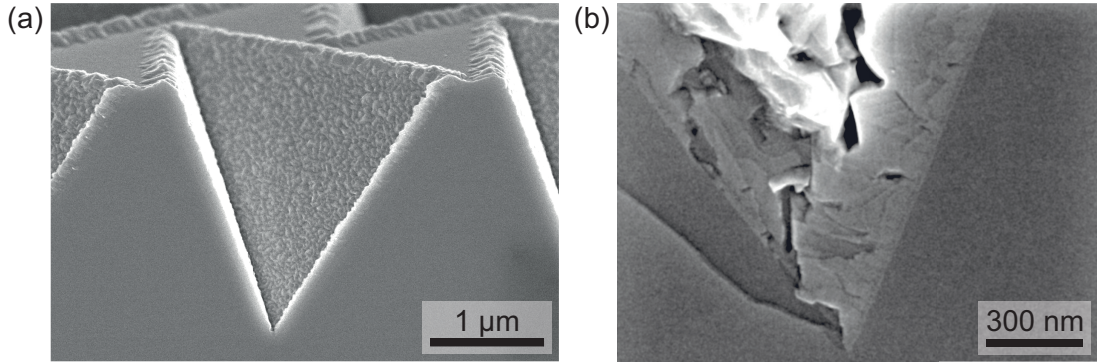


Figure A.3: (a) SEM side-view image of an 80 nm-thick InAlAs layer grown on InP pyramid template. The material covers the entire pyramid surface, but presents a microscopic structure. (b) SEM side-view zoom-in on the pyramid apex. Multiple InAlAs layers were deposited, separated by InGaAs spacers (dark lines), evidencing the progressive formation of faceted irregularities.

In the future, the growth on patterned substrates can resume, using these improved growth conditions.

A.6 Outlook

This project is interrupted at the moment. We believe to be on the edge of successfully fabricating long-wavelength QDs in inverted pyramids, with a fabrication scheme providing a natural C_{3v} symmetry. The growths may be quickly resumed on patterned substrates using the improved growth conditions.

The first step would be to control the morphology of a thick InAlAs layers with the help of SEM studies. If satisfactory, the sample photoluminescence has to be characterized before and after the sample surface etching. This etching is performed by depositing some resist on the substrate, then partly removing it using a controlled plasma etching in order to leave some resist only inside the recesses. A subsequent wet etching removes the ridge as well as the structures formed on the edges of the recess. The contribution of the vertical QWR to the PL emission is to be identified by comparing the spectra before and after etching. Some long-wavelength emission may also originate from the InP-InAlAs interface, due to the different material band offsets. At this point a next sample could be grown, with inserting a thin InGaAs layer at the middle of the InAlAs layer, to form the QD and the lateral QWRs. Again, comparing the PL spectra would allow to identify the contributions of the QD and QWRs to the PL spectrum.

B Kinetic Monte Carlo simulations of growth in pyramidal recesses

In this appendix we present numerical simulations of the epitaxial growth in pyramidal recesses. Dr. A. Surrente and the author of this work conducted a joint study of the recess morphology upon growth. Dr. A. Surrente performed the sample processing and AFM and PL characterization, while the author of this work wrote the numerical simulation code and performed the numerical experiments. This appendix can be seen as a complement to Chapter 3 of the PhD thesis of Dr. A. Surrente [44]. The code was implemented in the Matlab programming language, and run on Apple desktops as well as on the EPFL Vega cluster. In the following, we first give some details on the algorithm itself, and then present the results in two separate sections. The first one is dedicated to the interaction between the atomic steps on the substrate ridge, and the second one focuses on the evolution of the recess morphology.

B.1 Kinetic Monte Carlo algorithm

Numerical simulations are able to overcome the limitations of the analytical description of physical systems, and became an essential tool in many areas of contemporary physics. The choice of the type of numerical simulations depends on the desired level of detail, as well as on the constraints in memory and computation time.

The epitaxial growth of semiconductors can be simulated on different scales. An example of small-scale simulation is the determination of the local conformations and binding energies of atoms at the surface of a crystal [357, 213]. This type of methods delivers useful results, as well as valid approximations feeding larger-scale models like the kinetic Monte-Carlo method [358, 312, 359]. This type of models can simulate the diffusion of individual atoms on a lattice. Analytical models of terraces [360], or recess shape evolution [98, 99, 361, 362], take a broader perspective, and introduce mesoscopic and macroscopic concepts (capillarity, entropy of mixing, etc.) to effectively take into account the neglected microscopic phenomena.

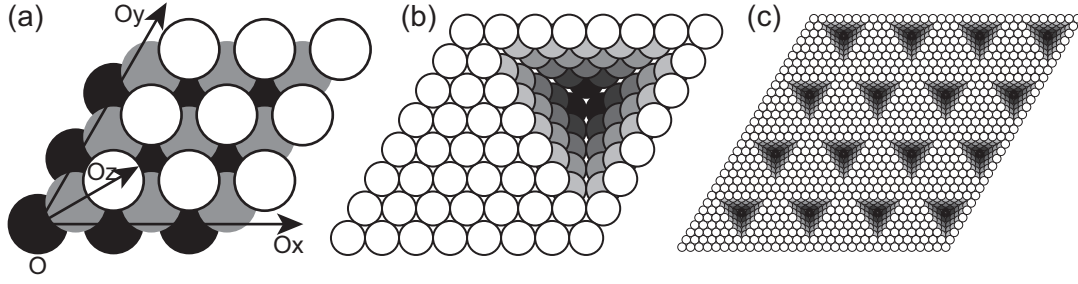


Figure B.1: (a) Position of the sites on a FCC lattice, as stored in a $(3 \times 3 \times 3)$ matrix. The color shade represents the atom z coordinate. The vector basis is not orthogonal. (b) Top-view representation of a $(8 \times 8 \times 6)$ lattice where a pyramid was “etched”. Only the sites located at the surface of the numerical sample are shown. (c) Periodic conditions allow for paving the Oxy plane and simulating an infinite field of pyramids.

B.1.1 General description of the algorithm

The Monte-Carlo method is a very general algorithm for conducting a numerical experiment reproducing the evolution of a physical system. The system evolution must to be formulated as a succession of events, chosen randomly. The rate, or probability, of realization of every event is calculated from the inputs of the simulation, and cannot be explicitly predicted by the simulation. These requirements are met by a wide class of physical systems, ranging from statistical physics to the price evolution of financial markets. In the Kinetic Monte-Carlo variant, the evolution of time is estimated by adding an increment equal to the inverse of the sum of the rate of each individual event, at every iteration.

The numerical experiments proceed by iterating the following loop:

- (1) List (and update!) every possible event and associated rate r_i ($i = 1, \dots, N$).
- (2) Calculate the list of cumulative sums of the rates $R_i = \sum_{j=1}^i r_j$.
- (3) Chose a random number u in the $(0, R_N]$ interval.
- (4) Realize the event i such that $R_{i-1} < u \leq R_i$.
- (5) Increment the time by $\Delta t = R_N^{-1}$. Then resume step (1).

B.1.2 Model description

In our work we modeled the deposition and diffusion of adatoms on a face-centered cubic (FCC) crystallographic lattice (or cubic closely packed) that initially reproduce the geometrical shape of an inverted pyramidal recess. The FCC lattice is the simplest that reproduces the crystallographic planes of our pyramid: the (111)B substrate surface, the three (111)A pyramids sidewalls and the (100) planes located on the three pyramid wedges. The FCC lattice actually reproduces the group-III sublattice of a GaAs zinc-blende crystal.

The occupancy of the lattice sites is stored in a 3D matrix, generally of size $(n \times n \times m)$, with n, m natural integers. The Oxy plane represents a (111)B-type dense plane, with the Oy

direction tilted by 60° from Ox . The vector basis Ox , Oy and Oz is therefore not orthogonal. In the plane, the $(1,1,0)$ position is in contact with the sites $(2,1,0)$, $(1,2,0)$, $(0,1,0)$, $(1,0,0)$, but also $(0,2,0)$ and $(2,0,0)$. The $(0,0,1)$ site is located at equal distance of the $(0,0,0)$, $(1,0,0)$ and $(0,1,0)$ locations as depicted on Figure B.1(a). A pyramid can be “etched” by removing atoms from a block matrix so as to form a tetragonal recess, as represented on Figure B.1(b). Periodic boundary conditions in the Oxy plane allow simulating an infinite pyramid field as shown on Figure B.1(c). No boundary condition is set on the vertical axis, as this would be meaningless. Vicinal surfaces can be simulated by connecting layers with different z -coordinates in the boundary conditions. In the following, we note the length S of the pyramid side and P the pitch (lateral size n of the matrix), in units of interatomic distance.

B.1.2.1 Atomic diffusion

The atoms are modeled by setting the corresponding lattice position to the “occupied” state. The diffusion of atoms takes the form of nearest-neighbor hops. The target lattice site must be empty, and have at least one other nearest-neighbor occupied site. The direct exchange of two atoms, or second-nearest-neighbor hops, is not permitted. As a consequence, only atoms located on the “surface” of the crystal can move, and no diffusion is permitted in buried structures. The nearest-neighbor hopping rate of an atom at position site i to an empty site j is given by the Arrhenius equation:

$$v_{i,j} = v_0 \exp - \frac{E_{B,tot}}{k_B T},$$

where T stands for the absolute temperature and $v_0 = \frac{2k_B T}{h} \approx 10^{13} \text{ s}^{-1}$ the adatom vibration frequency. The exponential term makes the diffusion process very sensitive to temperature. $E_{B,tot}$ is the bounding barrier the atom must overcome to move, and is calculated as $E_{B,tot} = 0.1 + 0.3n$ eV, with n the number of occupied nearest-neighbor lattice sites. This formulation takes naturally into account arbitrary local configurations where the crystallographic orientation cannot be precisely defined. In the case of an isolated atom diffusing on a (100) surface, the contribution of the 4 nearest-neighbor atoms of the lower level can be separated, and the bounding barrier rewritten as $E_{B,tot} = 0.1 + 0.3 \cdot 4 + 0.3n_{lat} = 1.3 + 0.3n_{lat}$ eV, with n_{lat} the number of occupied lateral sites ranging from 0 to 4 like in a cubic lattice. This expression and the numerical values match those usually reported in the literature [358, 312, 359].

B.1.2.2 Atom incorporation in the crystal

The incorporation of new atoms into the growing crystal is accounted for by switching an empty lattice site into an “occupied” state. Any empty lattice site is eligible for atom deposition, as long as at least one nearest-neighbor position is occupied. An additional requirement is set: as the growth rate on the (111)B surfaces is negligible, sites at the z level, that have only 3 nearest-neighbor all located at the $z - 1$ level, are not eligible for atom deposition.

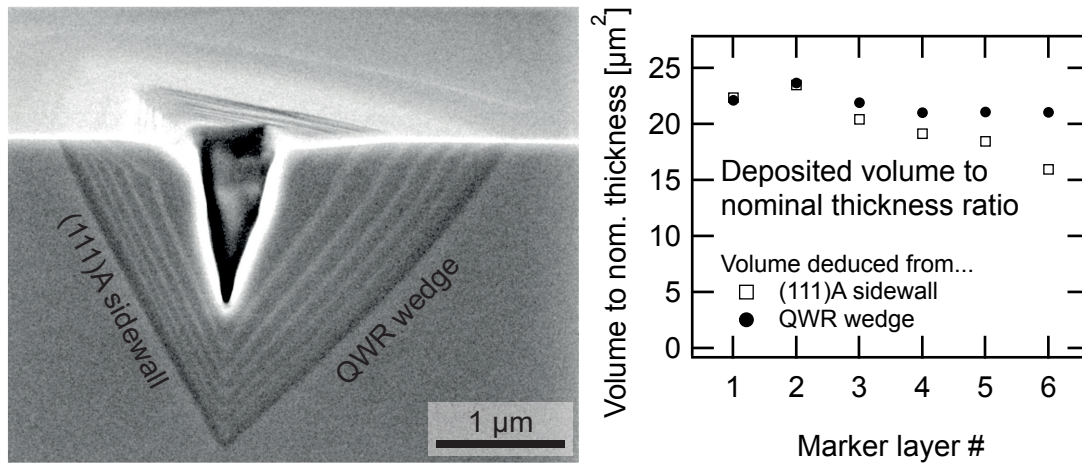


Figure B.2: (a) SEM side-view of a cleaved 3 μm pyramid filled with alternate AlGaAs and GaAs layers (courtesy from J. Szeszko). (b) Ratio of the deposited volume estimates to the nominal thickness of layers, in-between each marker layer. The volume of material effectively deposited appears linear with the nominal thickness, and quite independent from the filling of the pyramid.

The nominal growth rate ML/s is one of the simulation parameters. The time is monitored while atom diffusion events realize. Deposition of new atoms occurs when the time reaches multiples of a fixed value, calculated by dividing the time required for the deposition of a single ML by the number of sites contained in a horizontal lattice plane. This time is constant throughout the simulation. This leads to a pronounced acceleration of the growth rate while the pyramid is filling up, due to the rapidly shrinking number of lattice sites eligible for deposition (the (111)B-type lattice sites on the ridge are particularly not counted). This approach was chosen in order to reproduce the growth rate acceleration observed in real pyramids.

We first wanted to assess the validity of the hypothesis that the deposited volume stays constant with time. On Figure B.2(a) is shown a SEM side-view image of a cleaved micrometre-size pyramid, filled with alternate GaAs and AlGaAs layers (courtesy of J. Szeszko). The growth rate is high enough for the pyramid aperture to progressively close upon growth. We approximated the successive GaAs/AlGaAs interfaces with tetrahedrons, vertically stretched to account for the pyramid closing. The tetrahedrons could be reconstructed using the angles measured on the left side of the image (pyramid sidewall), or on the right side (QWR wedge). The volume effectively deposited during each cycle was estimated as the volume difference between those of successive tetrahedrons. Figure B.2(b) shows the ratio between the volume effectively deposited, and the nominal deposited thickness (given for a (100) surface). The two data series correspond to tetrahedrons reconstructed from the pyramid sidewall, and from its QWR wedge.

The volume effectively deposited in the pyramid appears to vary quite linearly with the nominal thickness, and this independently from the pyramid progressive filling. The growth rate

acceleration appears to be essentially due to the decrease in the surface in the recess: a larger thickness is needed to accommodate the same volume on a smaller surface. This observation validates our choice to “deposit” new atoms on the surface at a constant time rate, independent of the recess size and of the number of lattice sites eligible for the creation of new atoms. This result also suggests that a non-linear growth rate, evolving as the inverse of the remaining pyramid volume, should lead to more homogeneous vertical QWRs (Ga-enriched vertical 1D structure formed at the centre of the pyramid when AlGaAs is grown).

B.1.3 Diffusion length of adatoms

The simulation proceeds by depositing a single atom, and then performs a fairly high number of diffusion steps in order to cover the time separating two atom depositions. The exact number of steps depends of the successive time increments, which calculation is detailed in Appendix B.1.1. The square root of the average number of diffusion steps between subsequent atom depositions corresponds to the effective atom diffusion length (random walk on a 2D lattice), and was commonly in the range of 50-100 interatomic distances. This effective diffusion length averages the situations of atoms that are very mobile or almost fixed, and does not correspond to that of a single atom on a flat surface. As expected, no formation of islands is observed on vicinal surfaces, unless the effective diffusion length is significantly shorter (~ 10 -fold) than the terrace width. The effective diffusion length is controlled by the temperature and the growth rate. The temperature was generally set so as to reproduce the one of our MOVPE reactor and set to 843 K unless specified otherwise. We simulated the evolution of misoriented, non-patterned surfaces, and checked that, using that temperature, the border of the atomic terraces were similarly smooth when proceeding to diffusion only, or to growth using typical conditions (the terraces become more irregular when simulating lower temperatures).

B.1.4 Comments on the model assumptions

A few comments can be made on the hypotheses of the model states above.

No explicit distinction is made between atoms located in the bulk and on the surface. Especially, we ignored the effect of surface reconstruction on the atom diffusion and deposition. It can be argued that such effects are empirically accounted for through the values of the bounding barrier coefficients. Nevertheless different coefficients should be used for different surfaces.

The model only favors low-index surfaces like (111) or (100). Atoms diffusing on such planes have an especially low number of nearest-neighbors, and quickly diffuse to the boundary of the terrace. Oppositely, no mechanism stabilizes or favors higher-index surfaces like (311), commonly evidenced by TEM observations. Therefore the simulations will fail to form these intermediate planes, and tend to form sharp angles between different low-index facets.

The Ehrlich-Schwoebel barriers are ignored. This additional term to the bounding barrier accounts for the difficulty for an adatom to descend an atomic step and diffuse to the lower

terrace [363]. Our model will systematically favor step-flow situations.

The effect of strain is ignored. The model is suitable for reproducing (Al)GaAs heterostructures. Although the nanostructure formation mechanism does not depend primarily on strain, great care should be taken if extrapolating the results to strained InGaAs nanostructures.

B.2 Step flow interaction with the recesses

The atomic steps are perturbed by the presence of the pyramidal recesses. These act simultaneously as a source of atoms (due to the precursor decomposition in the pyramid) and as traps (due to the capillarity-induced attraction of adatoms). The dominant role may vary according to the simulation settings. The following simulations focus on the evolution of atomic terraces in the presence of neighboring recesses. As detailed in Subsection B.1.2.2, no deposition of atoms was allowed on the (111)B-type top surface, but eligible lattice sites exist at the borders of atomic terraces, that are not (111)B surface sites.

B.2.1 Terraces curving and bending

The AFM images demonstrated a marked influence of the recesses on the atomic terraces, which appear pinched by the recesses. Figure B.3(a) shows an AFM topographic image of a pyramid array, with numerous atomic steps curved and bent. We simulated the evolution of the pyramidal recesses on misoriented surfaces, by adapting the boundary conditions. The initial configuration implemented a straight monoatomic step in-between the pyramids, representing a small substrate miscut. Some simulation runs implemented actual growth while some others simulated only diffusion. The simulations confirmed the role of the recesses as traps for diffusing atoms, depleting the neighboring atomic terraces. The distance between recesses determines the trapping efficiency.

Figure B.3(b) depicts the simulated step pattern in a field of large pyramids, with a zero growth rate ($S = 145$). The dashed white line indicates the initial position of the terrace, and the red arrows represent the flux of material diffusing from the step into the recesses. The step propagates backwards, depleted by the pyramid. The influence of the distance between recesses is evidenced on Figures B.3(c) and B.3(d), where smaller ($S = 35$) pyramids are disposed with a lateral pitch of 50, respectively 200. Only the region of the terrace in the immediate vicinity of the recess is depleted; but if the recesses are dense enough, a given terrace is quickly depleted and can move backwards through several rows of pyramids. We observed the backward motion speed of the terraces to be inversely proportional to the distance separating recesses, but a more detailed study should confirm this observation.

When a sufficiently fast growth rate is set, the terraces adopt the expected forward propagation. However, the recesses still act as traps for diffusing atoms, significantly hindering the step progression. The trapping efficiency increases when the recesses are close, when the curvature of the terrace edge is increased, or when the growth rate is lowered (due to the increased

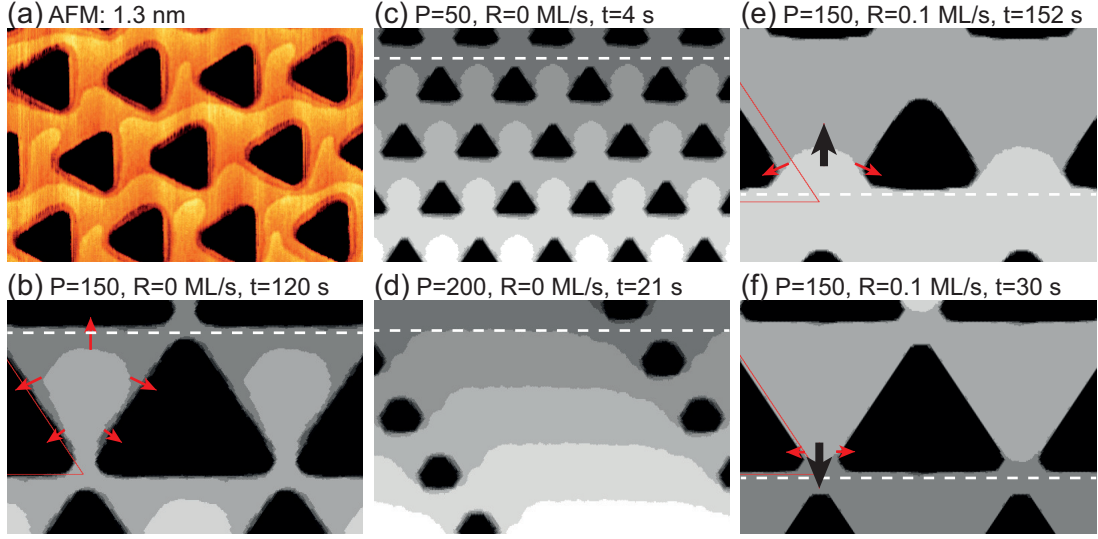


Figure B.3: Interaction between the step flow and the pyramidal recesses. (a) AFM topographic image of a pyramid array (size 175 nm, pitch 350 nm), showing perturbed monoatomic terraces on the (111)B ridge (step height ~ 0.33 nm). (b) Omega shapes of the steps can be retrieved by simulating pure diffusion ($S = 145$, $P = 150$, $R = 0$ ML/s). The initial step front is marked by a dashed white line, and the red arrows indicate the material desorption flux from the terrace to the pyramids. The shade of grey indicates the topographic level. (c), (d) Simulations of smaller pyramids with various pitches ($S = 35$, lateral pitch $P = 50$, resp. 200, $R = 0$ ML/s). The recesses are fed by the diffusion from the terraces, more efficiently when the pitch is small. (e) In presence of a finite growth rate, the terrace progression is hindered by the presence of the recesses. When the distance between recesses is below a certain threshold, no progression of the step in between the pyramids is possible. The black arrow represents the step forward progression. (f) This configuration induced a backward step progression at the onset of the simulation, before stabilization in the depicted situation.

diffusion length). Figure B.3(e) depicts a terrace on the ridge, with $R = 0.1$ ML/s. For a while the step could not move, and the deposited atoms only fed the pyramids. But as the pyramids fill up, the distance between the recesses increases, as does the deposition rate of atoms on the terrace edge (due to the decreasing number of eligible sites for atom deposition). At $t = 152$ s, the situation is such that the step finally starts its forward propagation with almost unperturbed speed. At that moment, the effective atom diffusion length is almost equal to the distance separating the two recesses. Figure B.3(f) depicts the situation with opposite substrate miscut angle. At the beginning of the simulation, the terrace fluctuated and broke when meeting the recess, initiating an initial backward propagation due to the strong atom diffusion toward the recesses. In the situation depicted, the forward propagation is blocked until the recesses shrink sufficiently to allow passage.

The bending and pinching of the atomic terraces by the recesses is asserted by our numerical simulations, which emphasize the role of the recesses as traps for diffusing atoms. We evidenced a net mass transport from the atomic terraces to the interior of the pyramids. This

contribution primarily depends on the terrace edge curvature, which directly depends on the distance between recesses.

B.2.2 Stability of a depletion centered on the pyramid

In order to study the deformation of the pyramid pattern during growth, a sample was placed in the MOVPE reactor and submitted to the usual deoxidation temperature under arsine atmosphere, but with no growth actually taking place. This sample presented monolayer-deep depletions centered on the pyramids, as depicted on Figure B.4(a). These depletions can also be observed on samples submitted to a brief deposition during deoxidation process (see Figure B.3 (a)), but then quickly disappears upon further growth.

To reproduce this effect, we performed some simulations where the pyramid was initially surrounded by a monolayer-deep depletion area, as depicted on Figure B.4(b). Simulations were performed using various growth rates. The situation for a $R = 0.1$ ML/s simulation at $t = 25$ s is shown on Figure B.4(c): the depletion vanishes, starting with the areas along the pyramid facets. This suggests that the ML step progresses not only thanks to the direct atom deposition on it, but is also fed by atoms diffusing out of the pyramid.

Figure B.4(d) shows as continuous lines the deposition rate of atoms on the sides of the depletion, for the $R = 0.1$ and 0.3 ML/s simulations. The deposition rate on the border is quite stable up to $t = \sim 30$ s, but then drastically evolves to a lower value as the depletion vanishes ($t = 35 - 40$ s).

The symbols indicate the effective incorporation rate of atoms on the depletion edge. The high initial values are related to the initial pyramid profile, far from the later quasi-equilibrium. The regular increase up to $t = 25$ s is related to the approach of the depletion edge closer to the recess, favoring the diffusion from the pyramid to the step edge. The final decrease is related to the contact and merging of the depletion with the pyramid.

The net incorporation rate of atoms on the edge is larger than the sole contribution of deposition, evidencing a significant contribution of atoms diffusing out of the pyramid to the depletion area.

A confirmation for this effect is brought by the weak, but non-vanishing, net contribution from the pyramid in the case of $R = 0$ ML/s (blue symbols, ~ 12 on average). This is surprising as the pyramid apex and wedges are strongly attractive locations.

The depletion evolution can be compared when tuning the effective diffusion length by changing the growth rate. The curves and symbols of the $R = 0.3$ ML/s simulation (red) were multiplied ($\div 3$) and horizontally stretched ($\times 3$) to allow direct comparison with the $R = 0.1$ ML/s experiment (black). The black symbols appear systematically higher than the red ones, evidencing a larger contribution of atom diffusion when the effective diffusion length is increased. Accordingly, the black continuous curve is lower, and evolves faster to the limit value, as the faster-shrinking depletion offers fewer sites for atom deposition.

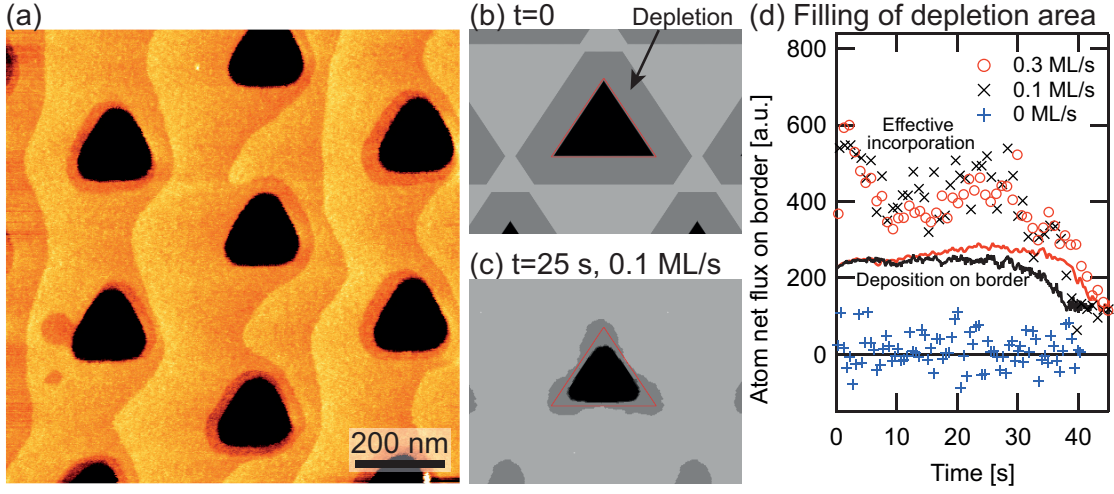


Figure B.4: (a) AFM topographic image of a patterned substrate after annealing (pitch 400 nm, size 100 nm, no deposition), showing a ML-deep depletion surrounding the recesses. (b) Initial configuration of a simulation, reproducing the template revealed by AFM. (c) Evolution of the simulation at $t = 25$ s ($R = 0.1$ ML/s), showing the shrinkage of the depletion, partly fed by adatom diffusion out of the pyramid. (d) Comparison of the depletion shrinking rates with 3 different growth rates (symbols, $R = 0, 0.1, 0.3$ ML/s). The vertical axis is proportional to the number of atoms incorporating on the border of the depletion. The continuous lines show the rate of atom deposition on the depletion side, deduced from the growth rate and from the ratio of sites eligible for atom deposition. The difference between the effective incorporation and the nominal atom deposition comes from atom diffusion from the recess. To allow comparison with the $R = 0.1$ ML/s simulation, the curve and symbols corresponding to $R = 0.3$ ML/s were multiplied ($\div 3$) and horizontally stretched ($\times 3$).

The net contribution of atoms diffusing out of the pyramid seems contradictory with the results obtained in Subsection B.2.1, where a net flux of atoms from the step to the recess was evidenced. Here, the terrace only offers its lower edge to the recess: atoms diffusing out of the pyramid are quite efficiently incorporated when arriving at the step. Moreover, the curvature is here concave, thus limiting the atom desorption.

If the KMC simulations are unable to reproduce the formation of the initial depletion area, we successfully demonstrated their relative stability when no growth is taking place, as well as their disappearance when a finite growth rate is set. We also evidence a net flux of atoms from the pyramid to the depletion edge.

B.3 Evolution of the pyramidal recesses

After the presentation of some results obtained on the interaction between the recesses and the step-flow, we take a closer look at the morphology evolution of the pyramids.

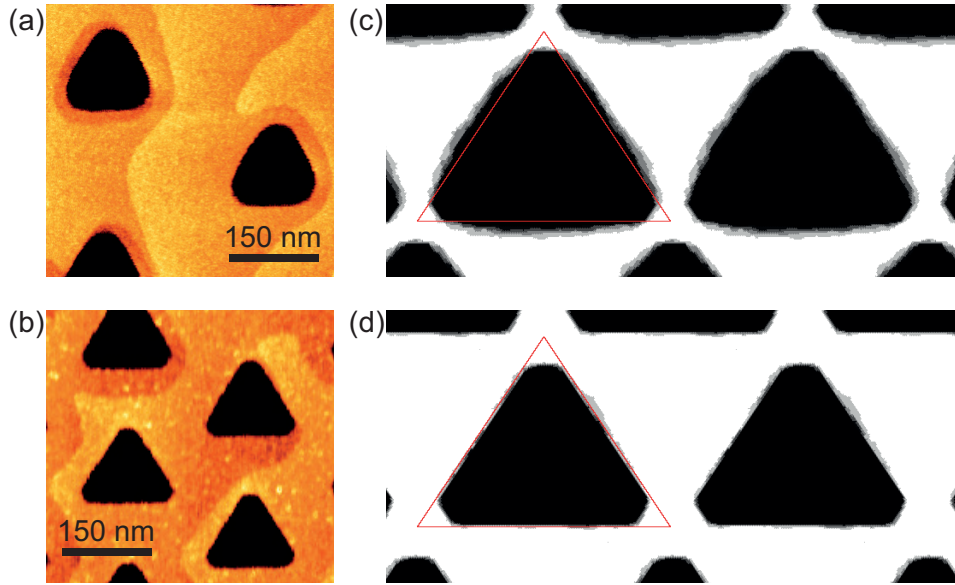


Figure B.5: (a), (b): AFM topographic images of initially 100 nm pyramids of (a) 400 nm pitch after deoxidation (no deposition), and (b) 300 nm pitch after 3.8 nm nominal deposition. Monoatomic terraces are visible on the ridge. (c), (d) Top-view representations of KMC experiments with no growth ($R = 0$ ML/s, $t = 300$ s) and a small growth rate ($R = 0.01$ ML/s, $t = 300$ s). The initial recess is depicted in red.

B.3.1 Apparent pyramid rounding

AFM and top-view SEM images commonly reveal recesses larger than the initial etched pyramids, when only a small amount of material was deposited. In more details, if no growth took place, the initial triangle evolves to a more rounded shape; but the triangular shape is recovered upon growth, truncated at the QWR wedges. Figures B.5(a) and B.5(b) depict this evolution, showing initially 100 nm pyramids after deoxidation (without any deposition), and after the growth of 3.8 nm (nominal thickness) GaAs.

Figures B.5(b) and B.5(c) represents the surface of simulated patterned substrates, with (c) $R = 0$ ML/s ($t = 300$ s), and (d) a reduced growth rate ($R = 0.01$ ML/s, $t = 300$ s). In the first case, the recesses appear enlarged and rounded, owing to the smoothening of the initial sharp angles of the recess. Mass transport occurred from the (111)B-(111)A wedges, to the pyramid apex and to the QWR wedges. By contrast, a low growth rate successfully stabilizes the pyramid sharp top interface. At $t = 300$ s, the recess is still barely filled, and the growth was concentrated at the apex and on the QWR wedges of the pyramid (Figure B.5(d)). When evidencing the substrate surface, the pyramid appears only as large as the initial recess, but exhibits truncated corners. Other simulations, proceeding to the deposition of atoms after a long period of pure diffusion, evidenced a quick recovery of a truncated triangular shape, comparable to that shown on Figure B.5(d).

However, the simulations do not satisfactorily reproduce the enlargement of the pyramid,

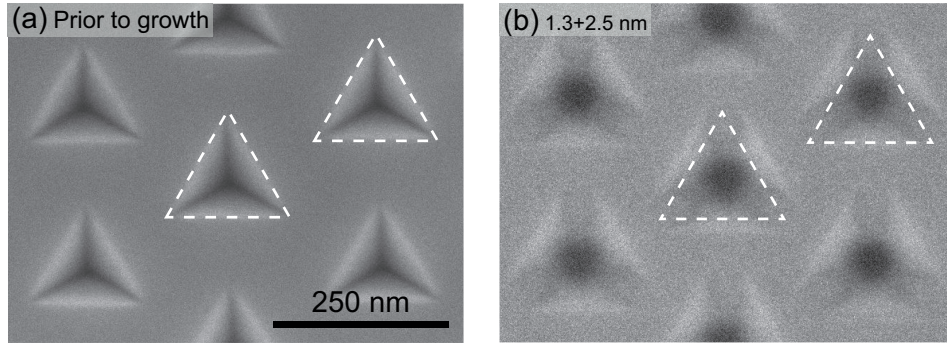


Figure B.6: SEM top-view images of a patterned substrate (125 nm pyramids with 250 nm pitch), (a) prior to growth, and (b) after the deposition of 1.3 + 2.5 nm nominal.

that is due to the formation of stable, high-index facets at the boundary between the (111)B and (111)A planes. These facets can also be evidenced by top-view SEM images: Figure B.6 represents 125 nm pyramids with 250 nm pitch, prior to growth and after the deposition of 3.8 nm nominal, respectively. The initial pyramid size is reported with dashed white lines. The high-index facets appear as light regions, and extend significantly beyond the initial recess. This extension of the recess is quite resistant to further deposition, as it can be still observed after the deposition of 1.3 + 6.2 nm nominal, a thickness sufficient to host a QD. The SEM images cannot distinguish details close to the recess apex, only showing a dark spot.

For relatively small deposited thickness, the recesses are observed to be larger than the initial pyramids. This is due to mass transport from the recess top boundaries to the inner regions, and to the formation of quite stable high-index facets at these locations. The recess boundaries initially evolve toward a quasi-circular shape, but a (truncated) triangular shape is quickly recovered upon growth. Our numerical simulations correctly reproduce this evolution.

B.3.2 QWR wedge tapering

In this subsection we detail how the atoms are incorporated into the pyramid, with the help of Figure B.7 that shows cross-sections and top-view representations of a filling pyramid. At first, the material is only incorporated on the QWR wedges (Figures B.7(a) and B.7(c), $t = 1.3$ second). The sharp wedges are extremely favorable positions, initially able to capture diffusing atoms before these can reach the apex. This scheme carries on as long as the curvature of the wedges remains far from the self-limited profile. Figure B.7(d) depicts the situation at $t = 25$ s: the wedges are nearly self-limited, and terraces develop on the (111)A sidewalls (red arrows), initiated at the wedges. The strong 2D-curvature of the pyramid apex retards the development of this terrace close to the center. Figure B.7(e) shows the situation at $t = 35$ s: the first (111)A terrace is complete, with the exception of a ML-deep depletion close to the apex (red arrows). This depletion originates from the strong local curvature of the recess apex that efficiently traps the diffusing atoms. The QWR wedges are also perturbed, depleted close to the apex. Due to the crystallography, a slope in the wedge corresponds to a variation of its width. On

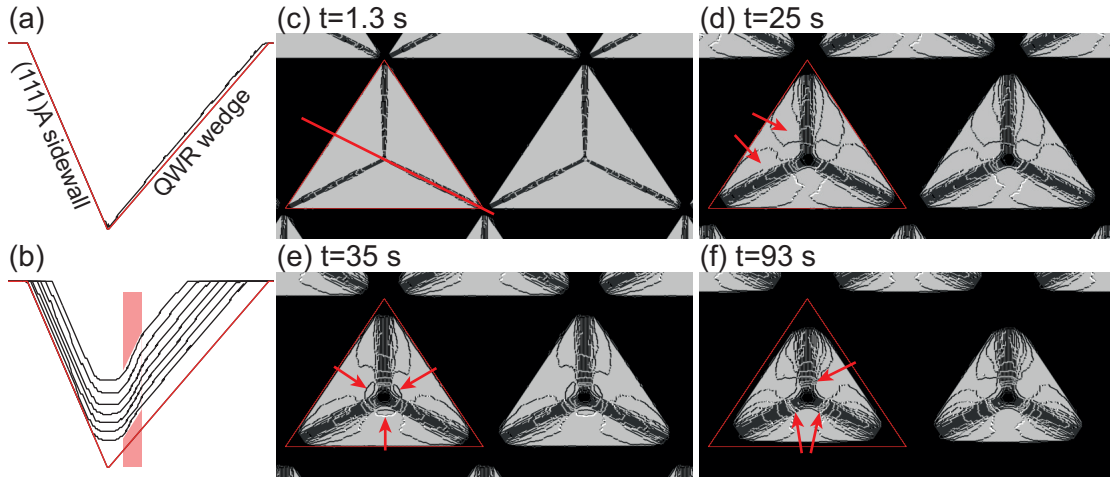


Figure B.7: Numerical simulation of the filling of a pyramidal recess ($R = 0.1 \text{ ML/s}$). (a) Profile cross-section of the initial (red) pyramid shape. The black line evidences the profile after $t = 1.3 \text{ s}$. (b) Successive profiles with fixed time intervals ($\Delta t = 25 \text{ s}$). The red region evidences the tapering of the QWR wedge. (c), (d), (e), (f) : Top-view representations of the simulation at different times. Are evidenced in red : (c) the cross-section plane, (d) the growing terraces on the (111)A sidewalls, (e) the depletion in the (111)A terrace close to the apex, and (f) the QWR wedge tapering zone.

Figure B.7(f) are evidenced series of atomic steps (red arrows) on the otherwise near-flat QWR wedge, corresponding to a change in the wedge width. The QWR wedge tapering is maybe better evidenced in the cross-section profile shown on Figure B.7(b). The initial profile is depicted in red, and the black curves are successive pyramid profiles with equal time interval of growth between them ($\Delta t = 25 \text{ s}$). The QWR wedge is tilted in the region evidenced in red when compared to the upper region. This tilt is a signature of the attraction of the pyramid apex for diffusing atoms.

The tapering of the QWR wedge tends to elevate the symmetry of the QD formation site, from the initial C_{3V} point-group symmetry, toward a hexagonal symmetry.

B.3.3 From triangular to hexagonal pattern

The tapering of the QWR wedge leads to an evolution of the QD formation site from a triangular toward a hexagonal shape. A 3D reconstruction is shown on Figure B.8(a), depicting a pyramidal recess partly filled, with tapered QWR wedges. Above is reported the QD formation site, exhibiting a hexagonal symmetry.

To obtain a representation of what could look like a QD, a simulation was conducted using standard conditions ($S = 145$, $R = 0.1 \text{ ML/s}$) for $t = 100 \text{ s}$. To simulate the deposition of a QD, a 50 % - 50 % alloy was then deposited, with the second species having lower diffusing barriers. The binding energy was $\sim 0.263 \text{ eV}$ per nearest-neighbor pair of the second specie,

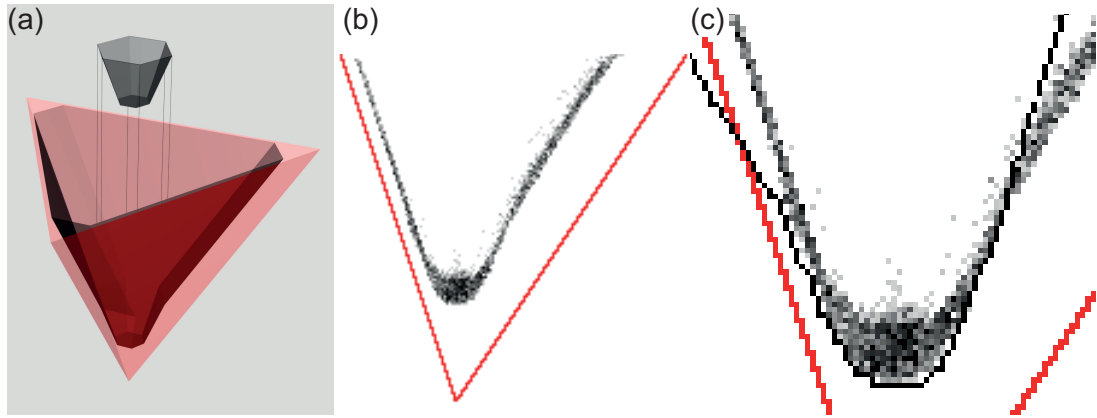


Figure B.8: (a) 3D reconstruction of a hexagonal QD formation site, obtained by inclining the QWR wedge in the vicinity of the QD. (b) Cross-section of a simulated pyramid (initial profile set in red), with an alloy layer representing a QD, composed of 50 % nominal with a longer-diffusing atomic specie. (c) Zoom-in on the simulated pyramid, with the additional black line representing the mirror symmetry of the QD lower interface, evidencing the symmetrization of the QD formation site induced by the tapering of the QWR wedge.

corresponding to $0.3 * 1.73 / 1.53 \text{ eV}$ as suggested in Ref. [358] in order to simulate In atoms. The binding energy of mixed atom pairs was the arithmetic average of 0.3 eV and of the previous value. The lower diffusing barriers lead to a significant increase in the diffusion length (and of the calculation time). The same growth rate was kept for 20 s while depositing the 50 % alloy. Finally, the deposition of the initial atomic species was resumed. The cross-section of this numerical experiment is shown on Figure B.8(b), with the color scale indicating the local alloy concentration, and the red line the initial pyramid profile. The QD center exhibits an average alloy concentration well above the nominal 50 %. On Figure B.8(c) is depicted a closer look on the cross-sectional composition. The black line represents the mirror image of the QD lower interface, and emphasizes the symmetrization of the QD formation site: a hexagonal pattern must present a symmetrical profile on a cross-section plot.

When increasing the alloy concentration, we also observed the formation of thicker QDs: the richer alloy has a longer overall diffusion length, promoting the efficiency of the QD capture of adatoms and further depleting the surrounding regions.

B.4 Appendix summary

In this appendix we presented in some details the algorithm and some results obtained with a Kinetic Monte Carlo algorithm, implementing atomic diffusion and incorporation of atoms on a patterned FCC lattice. A more complete analysis of the evolution of the real shape of pyramids can be found in Ref. [44].

Atomic terraces on the substrate ridge are observed to interact with the recesses, these some-

times acting as an atom source, or as an atom well. Atomic steps on vicinal substrates acquire an omega-shape, depleting by the recesses when there is no deposition. When some growth rate is set, dense recesses can block the forward progression of atomic terraces.

The monolayer-deep depletion observed by AFM on samples exposed to high temperatures is observed to be quite stable with time. When some growth proceeds, the depletion is quickly filled, with a significant contribution of atoms diffusing out of the pyramid.

The deformation of the recess observed by AFM was reproduced by the numerical simulations. When no growth proceeds, the triangular pattern evolves toward a more rounded profile, but the (truncated) triangular shape is quickly recovered as soon as some growth proceeds. Due to the simple assumptions, the model does not reproduce the formation of the high-index planes located in the upper regions of the recesses, which cause an apparent widening of the pyramids.

The filling of the recess initiates by QWR wedges and the apex. Upon growth, terraces develop on the (111)A sidewalls, initiated at the wedges. The large curvature of the apex attracts atoms in its vicinity, depleting the nearby (111)A sidewalls as well as the lateral QWR wedges. This leads to a tapering of the wedges of several ML. As a result, the QD formation site evolves towards a hexagonal shape, possibly more robust to inhomogeneities than the initial C_{3v} symmetry.

This model can be extended to simulate the formation of QWRs in V-grooves on (100) substrates, by only modifying the boundary conditions. The easiest implementation is to place the QWR along the Oz axis of Figure B.1. The limitation on the depositions on (111)B surfaces should also be dropped. Some simulations were performed in this sense. The QWR formation mechanisms requires a growth rate anisotropy between the (111)A and (100) planes. A growth rate anisotropy is induced by the distance separating successive monolayers measured perpendicular to the growth direction, which is twice as large on (111)A sidewalls than on the (100) surface ($r_{(111)A}/r_{(100)} = 2$). Although insensitive on temperature, this value is quite realistic and corresponds to values reported in the case of MOVPE at temperatures close to 930 K [364, 361].

The KMC simulation method allows reproducing most of the physics involved at the surface of a growing semiconductor. However, it is difficult to set the initial parameters so as to obtain reliable quantitative values of physical quantities, like the radius of surface curvature. By running our simulations, we observed the radius of curvature of the QWR wedges to be significantly smaller than the values observed on real substrates. We stress that if KMC methods can qualitatively catch the physics, quantitative data may be delicate to extract.

The size of the pyramids simulated in this work was generally $S = 145$, corresponding to 58 nm. This means that only very small pyramids were effectively simulated, but this is maybe effectively compensated by the smaller-than-expected radii of curvature. The main limitation of this method is the computation time, measured in days. We recommend future implementations of the KMC algorithm to translate the code in a programming language executing faster than Matlab (provided the algorithm make little use of the highly optimized matrix

calculations). The simulation of QWR structures is less computationally demanding, and may allow for deducing a scaling of the results. We also recommend the simulation of strain-free GaAs/AlGaAs nanostructures, with diffusing barriers adapted for example from Ref. [362].

C List of Tables

In this Appendix are reported the details on the substrate patterning processes, as well as the epitaxial sequences of the different samples presented throughout this work.

C.1 Substrate patterning

In Table C.2 are compiled technical details on the processing steps leading to the fabrication of patterned substrates. A textual description of these steps can be found in Section 3.1.

C.2 QW samples

The sample design consists in a double QW structure, with the InGaAsN structure on top of the InGaAs QW layer. The standard deposition sequence is as follow. First, a thick (~235 nm) GaAs buffer is grown at 590 °C. After a growth interruption to decrease the temperature down to 520 °C, the 5.6 nm-thick $\text{In}_{0.25}\text{Ga}_{0.75}\text{As}$ reference QW is deposited and the temperature is brought back to 590 °C. During this process the arsine flux is kept high ($\text{As}/\text{III}= 100$ when relevant). A ~ 60 nm GaAs layer is then deposited before interrupting again the growth to lower the reactor temperature. The $\text{In}_{0.25}\text{Ga}_{0.75}\text{AsN}$ QW is deposited using the 2-step growth method intended to prevent the N accumulation at the first growth interface. The InGaAsN is deposited in 2 successive layers: 1.5 nm with moderate DMHy flux (26 ccm) followed by 4.1 nm with higher flux (190 ccm). The $\text{As}/\text{III}=8$ ratio is kept low during the N-containing QW deposition, and a similar arsine flux is used during the last minutes of the preceding growth interruption. The temperature is finally increased to 590 °C to depose a ~ 120 nm GaAs cap. The deposition sequence is summarized in Table C.2

The different QW samples mentioned in Chapter 4 are summarized in Table C.3, together with the specificities and the different figures related.

Appendix C. List of Tables

Table C.1: Substrate patterning processes.

Step	V-grooves/pyramids	Alignment marks/mesas
SiO ₂ deposition	PlasmaLab system 100 PECVD 40 nm	150 nm
Resist deposition	PMMA A4, 30 s @ 6000 rpm 2 min bake @ 160 °C	PMMA A8, 30 s @ 6000 rpm 5 min bake @ 160 °C
E-beam lithography	Vistec EBPG5000	
PMMA reveal	1 min developer 15 s isopropanol rinse	Ibid.
Pattern transfer	Oxford Plasmalab system 80 plus RIE, O ₂ , CHF ₃ /Ar 80 W 7 s, 3 min 20 s	10 min instead of 3 min 20 s
Resist removal	Acetone US bath 3 min 30 % Isopropanol rinse	Ibid.
Plasma O ₂	5 min	Ibid.
Surface cleaning	Ar plasma 15 s prior to etching	Ibid.
Recess etching	QWR: HBr:Br:Meth 40:1:100 QD: Br:Meth 0.03-0.1:180 (depending on recess size)	Sentech ICP-RIE SI 500 ICP etching, BCl ₃ /N ₂
Control	SEM	SEM
SiO ₂ removal	HF 40 % 1 min	HF 40 % 1 min
Native oxide removal	HF 40 % 5 min	

Table C.2: Standard QW epitaxial sequence as described in Chapter 4.

Layer	Content	Thickness [nm]	In [%]	DMHy [ccm]	Growth rate [nm s ⁻¹]	T [°C]	As/III ratio
Substrate							
Buffer	GaAs	117.6	0	0	0.236	590	100
T ramp						~ 7 min	
QW	InGaAs	5.6	25	0	0.278	520	100
T ramp						~ 3 min	
Buffer	GaAs	58.8	0	0	0.236	590	100
T ramp						~ 7 min	
QW	InGaAsN	1.5 4.1	25	26 190	0.278	520	8
T ramp						~ 3 min	
Cap	GaAs	235	0	0	0.236	590	100
Surface							

C.3 QWR samples

The epitaxial sequence of the QWR samples contain a single active layer, and the layer thicknesses differ from that of the QW depositions. The standard pattern consists of 350 nm-wide

Table C.3: Growth runs, substrate misorientations and specificities of the QW samples.

Growth Id.	Substrate misorientations	Specificities
3640	+4°A, +5°A, +4°B, +5°B	Characterized by SIMS in Technion. Figure 4.15, In 30 %, 2.6 nm (26 ccm) + 2.6 nm (390 ccm)
3788	+5°A	
3920	+2°A, exact ^{*†} , 0.2°A [§] , +1°A	
3921	+2°A, +3°A, +4°A, +5°A(n)	
3923	+2°A, +2°B, +3°B [§] , +5°B	
3925	+2°A, +6°A, +1°B [§] , +6°B [§]	
3968	+2°A, +1°B*, +3°B, +5°B ^{*†}	
3971	+2°A, +0.2°B(n), +2°B*, +6°B	
4006	+2°A, +0.3°B, +0.4°B, +0.6°B	
* :	Presented in more details on Figures 4.2, 4.4(b), 4.6.	
§ :	AFM topographic image on Figure 4.7(a).	
† :	Characterized by SIMS in Trento.	
(n) :	Doped substrates, discarded from the analysis.	

grooves in fields of 1 and 10 μm pitch, on a GaAs substrate of exact (100) orientation. The typical procedure is as follow. First, a 20 nm GaAs buffer is deposited at 590 °C nominal substrate temperature. After a ~ 7 min growth interruption to cool the reactor down to $T_{\text{QWR}}=520$ °C, a $L_{\text{QWR}}=3$ nm $\text{In}_{0.25}\text{Ga}_{0.75}\text{AsN}$ layer is deposited at 0.278 nm s^{-1} according to the 2-step procedure (0.8 nm with 26 ccm DMHy flux followed by 2.2 nm with 190 ccm), using a gas-phase ratio As/III=3. After a ~ 3 min growth interruption, a 20 nm GaAs cap is deposited at 590 °C. This sequence is summarized in Table C.4.

Table C.4: Standard QWR epitaxial sequence as described in Chapter 5.

Layer	Content	Thickness [nm]	In [%]	DMHy [ccm]	Growth rate [nm s ⁻¹]	T [°C]	As/III ratio
Substrate							
Buffer	GaAs	20	0	0	0.236	590	100
T ramp						~ 7 min	
QWR	InGaAsN	0.8 2.2	25	26 190	0.278	520	3
T ramp						~ 3 min	
Cap	GaAs	20	0	0	0.236	590	100
Surface							

Table C.5 summarizes the different QWR samples studied in this work, together with their main characteristics subsections associated.

Appendix C. List of Tables

Table C.5: Growth runs, specificities of the QWR samples and Subsections associated.

QWR sample	Substrate misorientation and specificities		See Subsection
3615	exact	Grooves 270 nm	5.1.2, 5.1.3, 5.2.1
3648	+5°B	$L_{\text{QWR}} = 0.8+3.3$ nm	5.3.9
3768	exact, +4°B, +5°B and +6°B		5.1.1, 5.1.4, 5.3.3
3774	exact	Nitrogen-free, As/III=43	5.1.1, 5.1.2, 5.2.1, 5.3.1
3826	exact	$L_{\text{QWR}}=0.8+3.2$ nm	5.3.4
3827	exact	$L_{\text{QWR}}=0.8+4.2$ nm	5.3.4
3853	exact	$T_{\text{QWR}}=500$ °C	5.3.6
3857	+4°B	$T_{\text{QWR}}=500$ °C	5.3.6
3900	+6°B	DMHY flux 26+280 ccm	5.3.7
3945	+6°B	TMGa cap 3 nm before 2 nd G.I.	5.3.5
3947	+6°B	Growth rate 0.139 nm s ⁻¹	5.3.8
4003	+0.3°B	$0.8+2.7$ nm, TEGa cap 3 nm before G.I.	5.3.9
4548	+4°B	Nitrogen-free, As/III=3	5.3.1
4549	+5°B	Nitrogen-free, As/III=43	5.3.1

C.4 QD samples

The MOVPE sequence of the QD growth is as follow. During the deoxidation step $L_{\text{deox}}=1.3$ nm GaAs is deposited. The temperature is then set to 590 °C for the $L_{\text{buffer}}=5$ nm GaAs buffer deposition. This deposition proceeds with a slow growth rate (0.01 nm s⁻¹) using a high arsine flux (ratio As/III= ~ 2640). The growth is then interrupted for 3 min to lower the reactor temperature down to $T_{\text{QD}}=520$ °C, while keeping a high arsine flux during the first 2 min and lowering the flux for the last minute as to offer a low As surface concentration when the QD deposition begins. The QD nominal thickness is $L_{\text{QD}}=0.5$ nm. The N-containing QDs were deposited using the 2-step growth procedure as 0.1 nm with 21 ccm DMHy flux, followed by 0.4 nm with 150 ccm DMHy. Unless specified otherwise, the arsine flux was such as As/III=250. The growth is again interrupted during 1 min to increase the reactor temperature up to 590 °C, before the deposition of a 10 nm GaAs cap using a high As/III ratio. This process is summarized on Table C.6.

Finally, Table C.7 summarizes the different QD samples fabricated in this work, together with the specificities of the sample as compared to the base recipe detailed in the previous paragraph. References to figures showing μPL spectra of the samples are also reported. The wafers were cleaved into sixths (like a circular tart), and then again in two in order to obtain central (triangular) and external (elongated) pieces. The samples are grown in the corresponding position in the reactor, either external (labeled "A" in Table C.7), or central ("B"). Some growth runs were performed on two separate pieces patterned with pyramids of different sizes ("AB").

Table C.6: Standard QD epitaxial sequence as described in Chapter 6.

Layer	Content	Thickness [nm]	In [%]	DMHy [ccm]	Growth rate [nm s ⁻¹]	T [°C]	As/III ratio
Substrate							
Deoxidation	GaAs	1.3	0		0.01	570	2640
Buffer	GaAs	5	0		0.01	590	2640
T ramp						2 min 1 min	high flux low flux
QD	InGaAsN	0.1 0.4	30	21 150	0.013	520	3
T ramp						1 min	high flux
Cap	GaAs	10	0		0.01	590	2640
Surface							

Table C.7: QD samples growth ID, with the sample characteristics relatively to the standard deposition (see text).

InGaAs QD	Specificities	Figures
4209	B, As/III=665, T _{QD} =590 °C	
4215	A, As/III=2800	
4222	B, As/III=7. No QD signal.	
4253	A, As/III=635	6.4
4258	A, As/III=250. Reference for N-containing samples.	6.11, 6.17
4263	A, As/III=107	6.7
4266	A, As/III=50	6.4
4309	B, L _{QD} =0.8 nm	
4317	A, L _{buffer} =3 nm	
4319	B, L _{buffer} =3 nm, L _{QD} =0.8 nm	
4341	AB, L _{buffer} =2 nm	
4345	AB, L _{buffer} =3 nm	6.5
4380	AB, L _{buffer} =4 nm	
4411	A, As/III=25	
4413	AB, L _{buffer} =6 nm	6.5
InGaAsN QD	Specificities	Figures
4273	B, As/III=250, (7, 50) ccm DMHy	
4275	A, As/III=250, (21, 150) ccm DMHy	6.12, 6.15, 6.16, 6.18-6.22
4280	B, As/III=100, (21, 150) ccm DMHy	6.7, 6.9, 6.13 6.14
4281	B, As/III=50, (21,150) ccm DMHy	

Bibliography

- [1] S. Richard, F. Aniel, and G. Fishman. Energy-band structure of ge, si, and gaas: A thirty-band k center dot p method. *Physical Review B*, 70(23), 2004.
- [2] Y. Akahane, T. Asano, B. S. Song, and S. Noda. High-q photonic nanocavity in a two-dimensional photonic crystal. *Nature*, 425(6961):944–947, 2003.
- [3] O. J. Painter, A. Husain, A. Scherer, J. D. O’Brien, I. Kim, and P. D. Dapkus. Room temperature photonic crystal defect lasers at near-infrared wavelengths in ingaasp. *Journal of Lightwave Technology*, 17(11):2082–2088, 1999.
- [4] K. A. Atlasov, M. Calic, K. F. Karlsson, P. Gallo, A. Rudra, B. Dwir, and E. Kapon. Photonic-crystal microcavity laser with site-controlled quantum-wire active medium. *Optics Express*, 17(20):18178–18183, 2009.
- [5] S. Noda. Seeking the ultimate nanolaser. *Science*, 314(5797):260–261, 2006.
- [6] S. Strauf, K. Hennessy, M. T. Rakher, Y. S. Choi, A. Badolato, L. C. Andreani, E. L. Hu, P. M. Petroff, and D. Bouwmeester. Self-tuned quantum dot gain in photonic crystal lasers. *Physical Review Letters*, 96(12), 2006.
- [7] S. Strauf and F. Jahnke. Single quantum dot nanolaser. *Laser & Photonics Reviews*, 5(5):607–633, 2011.
- [8] T. Yoshie, A. Scherer, J. Hendrickson, G. Khitrova, H. M. Gibbs, G. Rupper, C. Ell, O. B. Shchekin, and D. G. Deppe. Vacuum rabi splitting with a single quantum dot in a photonic crystal nanocavity. *Nature*, 432(7014):200–203, 2004.
- [9] J. P. Reithmaier, G. Sek, A. Löffler, C. Hofmann, S. Kuhn, S. Reitzenstein, L. V. Keldysh, V. D. Kulakovskii, T. L. Reinecke, and A. Forchel. Strong coupling in a single quantum dot-semiconductor microcavity system. *Nature*, 432(7014):197–200, 2004.
- [10] K. Hennessy, A. Badolato, M. Winger, D. Gerace, M. Atatüre, S. Gulde, S. Falt, E. L. Hu, and A. Imamoglu. Quantum nature of a strongly coupled single quantum dot-cavity system. *Nature*, 445(7130):896–899, 2007.

Bibliography

- [11] A. Faraon, I. Fushman, D. Englund, N. Stoltz, P. Petroff, and J. Vuckovic. Coherent generation of non-classical light on a chip via photon-induced tunnelling and blockade. *Nature Physics*, 4(11):859–863, 2008.
- [12] J. L. O’Brien, A. Furusawa, and J. Vuckovic. Photonic quantum technologies. *Nature Photonics*, 3(12):687–695, 2009.
- [13] Veeco Instruments Inc., 2013.
- [14] P. Michler, A. Kiraz, C. Becher, W. V. Schoenfeld, P. M. Petroff, L. D. Zhang, E. Hu, and A. Imamoglu. A quantum dot single-photon turnstile device. *Science*, 290(5500):2282–+, 2000.
- [15] P. Michler, A. Imamoglu, M. D. Mason, P. J. Carson, G. F. Strouse, and S. K. Buratto. Quantum correlation among photons from a single quantum dot at room temperature. *Nature*, 406(6799):968–970, 2000.
- [16] M. H. Baier, E. Pelucchi, E. Kapon, S. Varoutsis, M. Gallart, I. Robert-Philip, and I. Abram. Single photon emission from site-controlled pyramidal quantum dots. *Applied Physics Letters*, 84(5):648–650, 2004.
- [17] O. Benson, C. Santori, M. Pelton, and Y. Yamamoto. Regulated and entangled photons from a single quantum dot. *Physical Review Letters*, 84(11):2513–2516, 2000.
- [18] Dirk Bouwmeester, Artur K. Ekert, and Anton Zeilinger. *The Physics of Quantum Information*. Springer, Berlin, 2000.
- [19] N. Gisin, G. G. Ribordy, W. Tittel, and H. Zbinden. Quantum cryptography. *Reviews of Modern Physics*, 74(1):145–195, 2002.
- [20] M. Kroutvar, Y. Ducommun, D. Heiss, M. Bichler, D. Schuh, G. Abstreiter, and J. J. Finley. Optically programmable electron spin memory using semiconductor quantum dots. *Nature*, 432(7013):81–84, 2004.
- [21] X. Q. Li, Y. W. Wu, D. Steel, D. Gammon, T. H. Stievater, D. S. Katzer, D. Park, C. Piermarocchi, and L. J. Sham. An all-optical quantum gate in a semiconductor quantum dot. *Science*, 301(5634):809–811, 2003.
- [22] Hyochul Kim, Ranojoy Bose, Thomas C. Shen, Glenn S. Solomon, and Edo Waks. A quantum logic gate between a solid-state quantum bit and a photon. *Nat Photon*, advance online publication, 2013.
- [23] Y. Qiu, S. A. Nikishin, H. Temkin, N. N. Faleev, and Y. A. Kudriavtsev. Growth of single phase $\text{GaAs}_{1-x}\text{N}_x$ with high nitrogen concentration by metal-organic molecular beam epitaxy. *Applied Physics Letters*, 70(24):3242–3244, 1997.
- [24] D. Schlenker, T. Miyamoto, Z. Pan, F. Koyama, and K. Iga. Miscibility gap calculation for $\text{Ga}_{1-x}\text{In}_x\text{N}_{y+1-y}$ including strain effects. *Journal of Crystal Growth*, 196(1):67–70, 1999.

-
- [25] R. Schwabe, W. Seifert, F. Bugge, R. Bindemann, V. F. Agekyan, and S. V. Pogarev. Photoluminescence of nitrogen-doped vpe gaas. *Solid State Communications*, 55(2):167–173, 1985.
- [26] X. Liu, M. E. Pistol, L. Samuelson, S. Schwetlick, and W. Seifert. Nitrogen pair luminescence in gaas. *Applied Physics Letters*, 56(15):1451–1453, 1990.
- [27] M. Weyers, M. Sato, and H. Ando. Red shift of photoluminescence and absorption in dilute gaasn alloy layers. *Japanese Journal of Applied Physics Part 2-Letters*, 31(7A):L853–L855, 1992.
- [28] M. Kondow, K. Uomi, K. Hosomi, and T. Mozume. Gas-source molecular-beam epitaxy of ganxas_{1-x} using a n radical as the n-source. *Japanese Journal of Applied Physics Part 2-Letters*, 33(8A):L1056–L1058, 1994.
- [29] M. Kondow, K. Uomi, A. Niwa, T. Kitatani, S. Watahiki, and Y. Yazawa. Gainnas: A novel material for long-wavelength-range laser diodes with excellent high-temperature performance. *Japanese Journal of Applied Physics Part 1-Regular Papers Short Notes & Review Papers*, 35(2B):1273–1275, 1996.
- [30] S. H. Wei and A. Zunger. Giant and composition-dependent optical bowing coefficient in gaasn alloys. *Physical Review Letters*, 76(4):664–667, 1996.
- [31] K. D. Choquette, J. F. Klem, A. J. Fischer, O. Blum, A. A. Allerman, I. J. Fritz, S. R. Kurtz, W. G. Breiland, R. Sieg, K. M. Geib, J. W. Scott, and R. L. Naone. Room temperature continuous wave ingaasn quantum well vertical-cavity lasers emitting at 1.3 μ m. *Electronics Letters*, 36(16):1388–1390, 2000.
- [32] M. C. Larson, M. Kondow, T. Kitatani, K. Nakahara, K. Tamura, H. Inoue, and K. Uomi. Gainnas-gaas long-wavelength vertical-cavity surface-emitting laser diodes. *Ieee Photonics Technology Letters*, 10(2):188–190, 1998.
- [33] M. Fischer, M. Reinhardt, and A. Forchel. A monolithic gainasn vertical-cavity surface-emitting laser for the 1.3- μ m regime. *Ieee Photonics Technology Letters*, 12(10):1313–1315, 2000.
- [34] F. Alexandre, E. Gouardes, O. Gauthier-Lafaye, N. Bouadma, A. Vuong, and B. Thedrez. Nitride-based long-wavelength lasers on gaas substrates. *Journal of Materials Science-Materials in Electronics*, 13(11):633–642, 2002.
- [35] R. Fehse, S. Tomic, A. R. Adams, S. J. Sweeney, E. P. O’Reilly, A. Andreev, and H. Riechert. A quantitative study of radiative, auger, and defect related recombination processes in 1.3- μ m gainnas-based quantum-well lasers. *Ieee Journal of Selected Topics in Quantum Electronics*, 8(4):801–810, 2002.
- [36] S. Tomic and E. P. O’reilly. Optimization of material parameters in 1.3- μ m ingaasn-gaas lasers. *Ieee Photonics Technology Letters*, 15(1):6–8, 2003.

- [37] W. Shockley and H. J. Queisser. Detailed balance limit of efficiency of p-n junction solar cells. *Journal of Applied Physics*, 32(3):510, 1961.
- [38] S. R. Kurtz, A. A. Allerman, E. D. Jones, J. M. Gee, J. J. Banas, and B. E. Hammons. Ingaasn solar cells with 1.0 ev band gap, lattice matched to gaas. *Applied Physics Letters*, 74(5):729–731, 1999.
- [39] M. Wiemer, V. Sabnis, and H. Yuen. 43.5 *High and Low Concentrator Systems for Solar Electric Applications Vi*, 8108, 2011.
- [40] F. Schattiger, D. Bauer, J. Demsar, T. Dekorsy, J. Kleinbauer, D. H. Sutter, J. Puustinen, and M. Guina. Characterization of ingaas and ingaasn semiconductor saturable absorber mirrors for high-power mode-locked thin-disk lasers. *Applied Physics B-Lasers and Optics*, 106(3):605–612, 2012.
- [41] M. Guina, T. Leinonen, A. Harkonen, and M. Pessa. High-power disk lasers based on dilute nitride heterostructures. *New Journal of Physics*, 11, 2009.
- [42] C. E. Max, S. S. Olivier, H. W. Friedman, K. An, K. Avicola, B. V. Beeman, H. D. Bissinger, J. M. Brase, G. V. Erbert, D. T. Gavel, K. Kanz, M. C. Liu, B. Macintosh, K. P. Neeb, J. Patience, and K. E. Waltjen. Image improvement from a sodium-layer laser guide star adaptive optics system. *Science*, 277(5332):1649–1652, 1997.
- [43] C. F. Blodi, S. R. Russell, J. S. Pulido, and J. C. Folk. Direct and feeder vessel photocoagulation of retinal angiomas with dye yellow laser. *Ophthalmology*, 97(6):791–797, 1990.
- [44] A. Surrente. *Epitaxial Growth and Optical Properties of Dense Arrays of Pyramidal Quantum Dots*. Ph. d., 2013.
- [45] W. Seifert, M. Borgstrom, K. Deppert, K. A. Dick, J. Johansson, M. W. Larsson, T. Martensson, N. Skold, C. P. T. Svensson, B. A. Wacaser, L. R. Wallenberg, and L. Samuelson. Growth of one-dimensional nanostructures in movpe. *Journal of Crystal Growth*, 272(1-4):211–220, 2004.
- [46] J. M. Ulloa, P. M. Koenraad, D. Fuster, L. Gonzalez, Y. Gonzalez, and M. U. Gonzalez. Self-assembling processes involved in the molecular beam epitaxy growth of stacked inas/inp quantum wires. *Nanotechnology*, 19(44), 2008.
- [47] H. Akiyama, M. Yoshita, L. N. Pfeiffer, and K. W. West. One-dimensional excitonic states and lasing in highly uniform quantum wires formed by cleaved-edge overgrowth with growth-interrupt annealing. *J. Phys.: Condens. Matter*, 16:S3549–S3566, 2004.
- [48] M. D. Kelzenberg, S. W. Boettcher, J. A. Petykiewicz, D. B. Turner-Evans, M. C. Putnam, E. L. Warren, J. M. Spurgeon, R. M. Briggs, N. S. Lewis, and H. A. Atwater. Enhanced absorption and carrier collection in si wire arrays for photovoltaic applications. *Nature Materials*, 9(3):239–244, 2010.

- [49] M. T. Bjork, B. J. Ohlsson, T. Sass, A. I. Persson, C. Thelander, M. H. Magnusson, K. Depert, L. R. Wallenberg, and L. Samuelson. One-dimensional heterostructures in semiconductor nanowhiskers. *Applied Physics Letters*, 80(6):1058–1060, 2002.
- [50] J. Johansson, L. S. Karlsson, C. P. T. Svensson, T. Martensson, B. A. Wacaser, K. Deppert, L. Samuelson, and W. Seifert. Structural properties of (111)b-oriented iii-v nanowires. *Nature Materials*, 5(7):574–580, 2006.
- [51] T. A. Langdo, C. W. Leitz, M. T. Currie, E. A. Fitzgerald, A. Lochtefeld, and D. A. Antoniadis. High quality ge on si by epitaxial necking. *Applied Physics Letters*, 76(25):3700–3702, 2000.
- [52] J. Z. Li, J. Bai, J. S. Park, B. Adekore, K. Fox, M. Carroll, A. Lochtefeld, and Z. Shellenbarger. Defect reduction of gaas epitaxy on si (001) using selective aspect ratio trapping. *Applied Physics Letters*, 91(2), 2007.
- [53] Peter Krogstrup, Henrik Ingerslev Jorgensen, Martin Heiss, Olivier Demichel, Jeppe V. Holm, Martin Aagesen, Jesper Nygard, and Anna Fontcuberta i Morral. Single-nanowire solar cells beyond the shockley-queisser limit. *Nat Photon*, 7(4):306–310, 2013.
- [54] H. X. Li, Q. D. Zhuang, X. W. Kong, Z. G. Wang, and T. Daniels-Race. Self-organization of wire-like inas nanostructures on inp. *Journal of Crystal Growth*, 205(4):613–617, 1999.
- [55] C. Walther, W. Hoerstel, H. Niehus, J. Erxmeyer, and W. T. Masselink. Growth, structural, and electrical investigation of self-assembled inas quantum wires on (001)inp. *Journal of Crystal Growth*, 209(4):572–580, 2000.
- [56] J. M. Garcia, L. Gonzalez, M. U. Gonzalez, J. P. Silveira, Y. Gonzalez, and F. Briones. Inas/inp(001) quantum wire formation due to anisotropic stress relaxation: in situ stress measurements. *Journal of Crystal Growth*, 227:975–979, 2001.
- [57] Y. C. Chang, L. L. Chang, and L. Esaki. A new one-dimensional quantum well structure. *Applied Physics Letters*, 47(12):1324–1326, 1985.
- [58] A. R. Goni, L. N. Pfeiffer, K. W. West, A. Pinczuk, H. U. Baranger, and H. L. Stormer. Observation of quantum wire formation at intersecting quantum-wells. *Applied Physics Letters*, 61(16):1956–1958, 1992.
- [59] W. Wegscheider, L. N. Pfeiffer, M. M. Dignam, A. Pinczuk, K. W. West, S. L. McCall, and R. Hull. Lasing from excitons in quantum wires. *Physical Review Letters*, 71(24):4071, 1993.
- [60] M. Yoshita, S.-M. Liu, M. Okano, Y. Hayamizu, H. Akiyama, L. N. Pfeiffer, and K. W. West. T-shaped gaas quantum-wire lasers and the exciton mott transition. *J. Phys.: Condens. Matter*, 19:295217, 2007.
- [61] H. Akiyama, M. Yoshita, L. N. Pfeiffer, K. W. West, and A. Pinczuk. One-dimensional continuum and exciton states in quantum wires. *Appl. Phys. Lett.*, 82(3):379, 2003.

- [62] P. Klangtakai, S. Sanorpim, R. Katayama, and K. Onabe. Photoreflectance study of strained gaasn/gaas t-junction quantum wires grown by movpe. *Inec: 2010 3rd International Nanoelectronics Conference, Vols 1 and 2*, pages 402–403, 2010.
- [63] P. Klangtakai, S. Sanorpim, R. Katayama, and K. Onabe. Movpe growth and optical characterization of ingaasn t-shaped quantum wires lattice-matched to gaas. *Physica Status Solidi a-Applications and Materials Science*, 207(6):1418–1420, 2010.
- [64] Pawinee Klangtakai, Sakuntam Sanorpim, and Kentaro Onabe. Optical study of gaas-n/gaas and ingaasn/gaas t-shaped quantum wires grown by movpe. *Journal of Crystal Growth*, 370(0):200–203, 2013.
- [65] X.L. Wang and V. Voliotis. Epitaxial growth and optical properties of semiconductor quantum wires. *Applied Physics Reviews*, 99:121301, 2006.
- [66] N. Akopian, N. H. Lindner, E. Poem, Y. Berlatzky, J. Avron, D. Gershoni, B. D. Gerardot, and P. M. Petroff. Entangled photon pairs from semiconductor quantum dots. *Physical Review Letters*, 96(13), 2006.
- [67] R. M. Stevenson, R. J. Young, P. Atkinson, K. Cooper, D. A. Ritchie, and A. J. Shields. A semiconductor source of triggered entangled photon pairs. *Nature*, 439(7073):179–182, 2006.
- [68] R. Hafenbrak, S. M. Ulrich, P. Michler, L. Wang, A. Rastelli, and O. G. Schmidt. Triggered polarization-entangled photon pairs from a single quantum dot up to 30k. *New Journal of Physics*, 9, 2007.
- [69] K. Eberl, M. Lipinski, Y. M. Manz, N. Y. Jin-Phillipp, W. Winter, C. Lange, and O. G. Schmidt. Self-assembling inas and inp quantum dots for optoelectronic devices. *Thin Solid Films*, 380(1-2):183–188, 2000.
- [70] J. Drbohlavova, V. Adam, R. Kizek, and J. Hubalek. Quantum dots - characterization, preparation and usage in biological systems. *International Journal of Molecular Sciences*, 10(2):656–673, 2009.
- [71] I. N. Stranski and V. L. Krastanow. *Akad. Wiss. Lit. Mainz. Math-Natur*, K1(Ilb 146):797, 1939.
- [72] M. Bayer and A. Forchel. Temperature dependence of the exciton homogeneous linewidth in in_{0.60}ga_{0.40}as/gaas self-assembled quantum dots. *Physical Review B*, 65(4), 2002.
- [73] N. N. Ledentsov, M. Grundmann, N. Kirstaedter, O. Schmidt, R. Heitz, J. Bohrer, D. Bimberg, V. M. Ustinov, V. A. Shchukin, A. Y. Egorov, A. E. Zhukov, S. Zaitsev, P. S. KopEv, Z. I. Alferov, S. S. Ruvimov, A. O. Kosogov, P. Werner, U. Gosele, and J. Heydenreich. Ordered arrays of quantum dots: Formation, electronic spectra, relaxation phenomena, lasing. *Solid-State Electronics*, 40(1-8):785–798, 1996.

- [74] D. Bimberg, N. Kirstaedter, N. N. Ledentsov, Z. I. Alferov, P. S. Kopev, and V. M. Ustinov. Ingaas-gaas quantum-dot lasers. *Ieee Journal of Selected Topics in Quantum Electronics*, 3(2):196–205, 1997.
- [75] F. Heinrichsdorff, M. H. Mao, N. Kirstaedter, A. Krost, D. Bimberg, A. O. Kosogov, and P. Werner. Room-temperature continuous-wave lasing from stacked inas/gaas quantum dots grown by metalorganic chemical vapor deposition. *Applied Physics Letters*, 71(1):22–24, 1997.
- [76] D. L. Huffaker, G. Park, Z. Zou, O. B. Shchekin, and D. G. Deppe. 1.3 μm room-temperature gaas-based quantum-dot laser. *Applied Physics Letters*, 73(18):2564–2566, 1998.
- [77] Y. Nakamura, O. G. Schmidt, N. Y. Jin-Phillipp, S. Kiravittaya, C. Muller, K. Eberl, H. Gräbeldinger, and H. Schweizer. Vertical alignment of laterally ordered inas and ingaas quantum dot arrays on patterned (001) gaas substrates. *Journal of Crystal Growth*, 242(3-4):339–344, 2002.
- [78] T. Tran, A. Muller, C. K. Shih, P. S. Wong, G. Balakrishnan, N. Nuntawong, J. Tatebayashi, and D. L. Huffaker. Single dot spectroscopy of site-controlled inas quantum dots nucleated on gaas nanopylramids. *Applied Physics Letters*, 91(13), 2007.
- [79] C. Schneider, M. Strauss, T. Sunner, A. Huggenberger, D. Wiener, S. Reitzenstein, M. Kamp, S. Hofling, and A. Forchel. Lithographic alignment to site-controlled quantum dots for device integration. *Applied Physics Letters*, 92(18), 2008.
- [80] J. Tommila, C. Strelow, A. Schramm, T. V. Hakkarainen, M. Dumitrescu, T. Kipp, and M. Guina. The influence of temperature on the photoluminescence properties of single inas quantum dots grown on patterned gaas. *Nanoscale Research Letters*, 7, 2012.
- [81] D. Zhou, S. Anantathanasarn, P. J. van Veldhoven, F. W. M. van Otten, T. J. Eijkemans, T. de Vries, E. Smalbrugge, and R. Notzel. Submicron active-passive integration with position and number controlled inas/inp (100) quantum dots (1.55 μm wavelength region) by selective-area growth. *Applied Physics Letters*, 91(13), 2007.
- [82] T. P. Hsieh, J. I. Chyi, H. S. Chang, W. Y. Chen, T. M. Hsu, and W. H. Chang. Single photon emission from an ingaas quantum dot precisely positioned on a nanoplane. *Applied Physics Letters*, 90(7), 2007.
- [83] B. Fain, D. Elvira, L. Le Gratiet, L. Largeau, G. Beaudoin, D. Troadec, I. Abram, A. Beveratos, I. Robert-Philip, G. Patriarche, and I. Sagnes. Structural analysis of site-controlled inas/inp quantum dots. *Journal of Crystal Growth*, 334(1):37–39, 2011.
- [84] J. Y. Yuan, H. Wang, R. P. J. van Veldhoven, J. Wang, T. de Vries, B. Smalbrugge, C. Y. Jin, P. Nouwens, E. J. Geluk, A. Y. Silov, and R. Notzel. Controlling polarization anisotropy of site-controlled inas/inp (100) quantum dots. *Applied Physics Letters*, 98(20), 2011.

- [85] N. N. Ledentsov, V. A. Shchukin, M. Grundmann, N. Kirstaedter, J. Bohrer, O. Schmidt, D. Bimberg, V. M. Ustinov, A. Y. Egorov, A. E. Zhukov, P. S. Kopev, S. V. Zaitsev, N. Y. Gordeev, Z. I. Alferov, A. I. Borovkov, A. O. Kosogov, S. S. Ruvimov, P. Werner, U. Gosele, and J. Heydenreich. Direct formation of vertically coupled quantum dots in stranski-krastanow growth. *Physical Review B*, 54(12):8743–8750, 1996.
- [86] H. Ishikawa, H. Shoji, Y. Nakata, K. Mukai, M. Sugawara, M. Egawa, N. Otsuka, Y. Sugiyama, T. Futatsugi, and N. Yokoyama. Self-organized quantum dots and quantum dot lasers (invited). *Journal of Vacuum Science & Technology a-Vacuum Surfaces and Films*, 16(2):794–800, 1998.
- [87] J. He, R. Notzel, P. Offermans, P. M. Koenraad, Q. Gong, G. J. Hamhuis, T. J. Eijkemans, and J. H. Wolter. Formation of columnar (in,ga)as quantum dots on gaas(100). *Applied Physics Letters*, 85(14):2771–2773, 2004.
- [88] P. Ridha, L. Li, A. Fiore, G. Patriarche, M. Mexis, and P. M. Smowton. Polarization dependence study of electroluminescence and absorption from inas/gaas columnar quantum dots. *Applied Physics Letters*, 91(19), 2007.
- [89] A. Huggenberger, S. Heckelmann, C. Schneider, S. Hofling, S. Reitzenstein, L. Worschech, M. Kamp, and A. Forchel. Narrow spectral linewidth from single site-controlled in(ga)as quantum dots with high uniformity. *Applied Physics Letters*, 98(13), 2011.
- [90] B. D. Gerardot, S. Seidl, P. A. Dalgarno, R. J. Warburton, D. Granados, J. M. Garcia, K. Kowalik, O. Krebs, K. Karrai, A. Badolato, and P. M. Petroff. Manipulating exciton fine structure in quantum dots with a lateral electric field. *Applied Physics Letters*, 90(4), 2007.
- [91] S. Seidl, M. Kroner, A. Hoge, K. Karrai, R. J. Warburton, A. Badolato, and P. M. Petroff. Effect of uniaxial stress on excitons in a self-assembled quantum dot. *Applied Physics Letters*, 88(20), 2006.
- [92] A. Imamoglu, S. Falt, J. Dreiser, G. Fernandez, M. Atatüre, K. Hennessy, A. Badolato, and D. Gerace. Coupling quantum dot spins to a photonic crystal nanocavity. *Journal of Applied Physics*, 101(8), 2007.
- [93] M. Winger, T. Volz, G. Tarel, S. Portolan, A. Badolato, K. J. Hennessy, E. L. Hu, A. Beveratos, J. Finley, V. Savona, and A. Imamoglu. Explanation of photon correlations in the far-off-resonance optical emission from a quantum-dot-cavity system. *Physical Review Letters*, 103(20), 2009.
- [94] M. Kaniber, A. Laucht, A. Neumann, J. M. Villas-Boas, M. Bichler, M. C. Amann, and J. J. Finley. Investigation of the nonresonant dot-cavity coupling in two-dimensional photonic crystal nanocavities. *Physical Review B*, 77(16), 2008.

-
- [95] S. Ates, S. M. Ulrich, A. Ulhaq, S. Reitzenstein, A. Löffler, S. Hofling, A. Forchel, and P. Michler. Non-resonant dot-cavity coupling and its potential for resonant single-quantum-dot spectroscopy. *Nature Photonics*, 3(12):724–728, 2009.
- [96] A. Laucht, M. Kaniber, A. Mohtashami, N. Hauke, M. Bichler, and J. J. Finley. Temporal monitoring of nonresonant feeding of semiconductor nanocavity modes by quantum dot multiexciton transitions. *Physical Review B*, 81(24), 2010.
- [97] A. Majumdar, A. Faraon, E. D. Kim, D. Englund, H. Kim, P. Petroff, and J. Vuckovic. Linewidth broadening of a quantum dot coupled to an off-resonant cavity. *Physical Review B*, 82(4), 2010.
- [98] G. Biasiol and E. Kapon. Mechanisms of self-ordering of quantum nanostructures grown on nonplanar surfaces. *Physical Review Letters*, 81(14):2962–2965, 1998.
- [99] G. Biasiol, A. Gustafsson, K. Leifer, and E. Kapon. Mechanisms of self-ordering in nonplanar epitaxy of semiconductor nanostructures. *Physical Review B*, 65(20):15, 2002.
- [100] E. Kapon, D. M. Hwang, and R. Bhat. Stimulated-emission in semiconductor quantum wire heterostructures. *Physical Review Letters*, 63(4):430–433, 1989.
- [101] M. Walther, E. Kapon, J. Christen, D. M. Hwang, and R. Bhat. Carrier capture and quantum confinement in gaas/algaas quantum wire lasers grown on v-grooved substrates. *Applied Physics Letters*, 60(5):521–523, 1992.
- [102] C. Constantin, E. Martinet, A. Rudra, and E. Kapon. Observation of combined electron and photon confinement in planar microcavities incorporating quantum wires. *Physical Review B*, 59(12):R7809–R7812, 1999.
- [103] C. Constantin, E. Martinet, D. Y. Oberli, E. Kapon, B. Gayral, and J. M. Gerard. Quantum wires in multidimensional microcavities: Effects of photon dimensionality on emission properties. *Physical Review B*, 66(16), 2002.
- [104] D. Kaufman, Y. Berk, B. Dwir, A. Rudra, A. Palevski, and E. Kapon. Conductance quantization in v-groove quantum wires. *Physical Review B*, 59(16):10433–10436, 1999.
- [105] B. Dwir, D. Kaufman, E. Kapon, and A. Palevski. Quantized conductance and intersub-band scattering in serially connected quantum wires. *Europhysics Letters*, 55(1):80–85, 2001.
- [106] F. Vouilloz, D. Y. Oberli, S. Wiesendanger, B. Dwir, F. Reinhardt, and E. Kapon. Density dependence of localized excitonic recombination in quantum wires. *Physica Status Solidi a-Applied Research*, 164(1):259–263, 1997.
- [107] T. Guillet, R. Grousson, V. Voliotis, X.-L. Wang, and M. Ogura. Local disorder and optical properties in v-shaped quantum wires: Towards one-dimensional exciton systems. *Physical Review B*, 68:045319, 2003.

Bibliography

- [108] N. Moret, D. Y. Oberli, B. Dwir, A. Rudra, and E. Kapon. Diffusion of electron-hole pairs in disordered quantum wires. *Applied Physics Letters*, 93(19):–, 2008.
- [109] M. Felici, P. Gallo, A. Mohan, B. Dwir, A. Rudra, and E. Kapon. Site-controlled ingaas quantum dots with tunable emission energy. *Small*, 5(8):938–943, 2009.
- [110] A. Mohan, P. Gallo, M. Felici, B. Dwir, A. Rudra, J. Faist, and E. Kapon. Record-low inhomogeneous broadening of site-controlled quantum dots for nanophotonics. *Small*, 6(12):1268–1272, 2010.
- [111] K. A. Atlasov, K. F. Karlsson, E. Deichsel, A. Rudra, B. Dwir, and E. Kapon. Site-controlled single quantum wire integrated into a photonic-crystal membrane microcavity. *Applied Physics Letters*, 90(15), 2007.
- [112] P. Gallo, M. Felici, B. Dwir, K. A. Atlasov, K. F. Karlsson, A. Rudra, A. Mohan, G. Biasiol, L. Sorba, and E. Kapon. Integration of site-controlled pyramidal quantum dots and photonic crystal membrane cavities. *Applied Physics Letters*, 92(26):–, 2008.
- [113] M. Calic, P. Gallo, M. Felici, K. A. Atlasov, B. Dwir, A. Rudra, G. Biasiol, L. Sorba, G. Tarel, V. Savona, and E. Kapon. Phonon-mediated coupling of ingaas/gaas quantum-dot excitons to photonic crystal cavities. *Physical Review Letters*, 106(22), 2011.
- [114] R. Singh and G. Bester. Nanowire quantum dots as an ideal source of entangled photon pairs. *Physical Review Letters*, 103(6), 2009.
- [115] A. Schliwa, M. Winkelnkemper, A. Lochmann, E. Stock, and D. Bimberg. In(ga)as/gaas quantum dots grown on a (111) surface as ideal sources of entangled photon pairs. *Physical Review B*, 80(16), 2009.
- [116] V. Troncale, K. F. Karlsson, E. Pelucchi, A. Rudra, and E. Kapon. Control of valence band states in pyramidal quantum dot-in-dot semiconductor heterostructures. *Applied Physics Letters*, 91(24), 2007.
- [117] Q. Zhu, F. Karlsson, E. Pelucchi, and E. Kapon. Transition from 2d to 3d quantum confinement in semiconductor quantum wires/quantum dots. *Nano Letters*, 7(8):2227, 2007.
- [118] Q. Zhu, K. F. Karlsson, M. Byszewski, A. Rudra, E. Pelucchi, Z. B. He, and E. Kapon. Hybridization of electron and hole states in semiconductor quantum-dot molecules. *Small*, 5(3):329–335, 2009.
- [119] Q. Zhu, J. D. Ganiere, Z. B. He, K. F. Karlsson, M. Byszewski, E. Pelucchi, A. Rudra, and E. Kapon. Pyramidal gaas/al(z)ga(1-z)as quantum wire/dot systems with controlled heterostructure potential. *Physical Review B*, 82(16), 2010.
- [120] J. Szeszko, V. V. Belykh, P. Gallo, A. Rudra, K. F. Karlsson, N. N. Sibeldin, and E. Kapon. Exciton confinement and trapping dynamics in double-graded-bandgap quantum nanowires. *Applied Physics Letters*, 100(21), 2012.

-
- [121] M. H. Baier, C. Constantin, E. Pelucchi, and E. Kapon. Electroluminescence from a single pyramidal quantum dot in a light-emitting diode. *Applied Physics Letters*, 84(11):1967–1969, 2004.
- [122] A. Mohan, L. Nevou, P. Gallo, B. Dwir, A. Rudra, E. Kapon, and J. Faist. Photocurrent spectroscopy of site-controlled pyramidal quantum dots. *Applied Physics Letters*, 101(3), 2012.
- [123] F. Lelarge, C. Constantin, K. Leifer, A. Condo, V. Iakovlev, E. Martinet, A. Rudra, and E. Kapon. Effect of indium segregation on optical properties of v-groove ingaas/gaas strained quantum wires. *Applied Physics Letters*, 75(21):3300–3302, 1999.
- [124] A. Hartmann, Y. Ducommun, K. Leifer, and E. Kapon. Structure and optical properties of semiconductor quantum nanostructures self-formed in inverted tetrahedral pyramids. *J. Phys.: Condens. Matter*, 11:5901, 1999.
- [125] N. Kobayashi, T. Makimoto, and Y. Horikoshi. Flow-rate modulation epitaxy of gaas. *Japanese Journal of Applied Physics Part 2-Letters*, 24(12):L962–L964, 1985.
- [126] M. K. Lee and C. C. Hu. Flatness improvement of gaas observed by atomic force microscopy using flow rate modulation epitaxy. *Japanese Journal of Applied Physics Part 2-Letters*, 36(1AB):L15–L17, 1997.
- [127] M. Pristovsek, M. Zorn, and M. Weyers. In situ study of gaas growth mechanisms using tri-methyl gallium and tri-ethyl gallium precursors in metal-organic vapour phase epitaxy. *Journal of Crystal Growth*, 262(1-4):78–83, 2004.
- [128] T. Hakkarainen, J. Toivonen, H. Koskenvaara, M. Sopanen, and H. Lipsanen. Structural and optical properties of gainnas/gaas quantum structures. *Journal of Physics-Condensed Matter*, 16(31):S3009–S3026, 2004.
- [129] S. Kurtz, R. Reedy, B. Keyes, G. D. Barber, J. F. Geisz, D. J. Friedman, W. E. McMahon, and J. M. Olson. Evaluation of nf₃ versus dimethylhydrazine as n sources for gaasn. *Journal of Crystal Growth*, 234(2-3):323–326, 2002.
- [130] X. Wei, G. H. Wang, G. Z. Zhang, X. P. Zhu, X. Y. Ma, and L. H. Chen. Metalorganic chemical vapor deposition of ganas alloys using different ga precursors. *Journal of Crystal Growth*, 236(4):516–522, 2002.
- [131] A. Kaluza, A. Schwarz, D. Gauer, H. Hardtdegen, N. Nastase, H. Luth, T. Schapers, D. Meertens, A. Maciel, J. Ryan, and E. O’Sullivan. On the choice of precursors for the movpe-growth of high-quality al(0.30)gao(0.70)as/gaas v-groove quantum wires with large subband spacing. *Journal of Crystal Growth*, 221:91–97, 2000.
- [132] A. Surrente, P. Gallo, M. Felici, B. Dwir, A. Rudra, and E. Kapon. Dense arrays of ordered pyramidal quantum dots with narrow linewidth photoluminescence spectra. *Nanotechnology*, 20(41):–, 2009.

Bibliography

- [133] Irina Buyanova and Weimin Chen. *Physics and Applications of Dilute Nitrides*. Taylor & Francis Books, Inc., New York, 2004.
- [134] Mohamed Henini. *Dilute Nitride Semiconductors*. Elsevier, Amsterdam, 2005.
- [135] M. Kappelt, M. Grundmann, A. Krost, V. Turck, and D. Bimberg. Ingaas quantum wires grown by low pressure metalorganic chemical vapor deposition on inp v-grooves. *Applied Physics Letters*, 68(25):3596–3598, 1996.
- [136] M. Geiger, F. Adler, U. A. Griesinger, H. Schweizer, and F. Scholz. Gainas/inp quantum wires grown by metalorganic vapor phase epitaxy on v-grooved inp substrates. *Microelectronics Journal*, 28(8-10):903–908, 1997.
- [137] T. Schrimpf, P. Bonsch, D. Wullner, H. H. Wehmann, A. Schlachetzki, F. Bertram, T. Riemann, and J. Christen. Ingaas quantum wires and wells on v-grooved inp substrates. *Journal of Applied Physics*, 86(9):5207–5214, 1999.
- [138] D. Piester, P. Bonsch, T. Schrimpf, H. H. Wehmann, and A. Schlachetzki. Laser-action in v-groove-shaped ingaas-inp single quantum wires. *Ieee Journal of Selected Topics in Quantum Electronics*, 6(3):522–527, 2000.
- [139] J. Wang, B. J. Robinson, D. A. Thompson, and J. G. Simmons. Ingaas/inp quantum wires grown by gas-source molecular-beam epitaxy onto v-grooved inp substrates with (111)a facet sidewalls. *Applied Physics Letters*, 67(16):2358–2360, 1995.
- [140] I. Vurgaftman, J. R. Meyer, and L. R. Ram-Mohan. Band parameters for iii-v compound semiconductors and their alloys. *Journal of Applied Physics*, 89(11):5815–5875, 2001.
- [141] W. G. Bi and C. W. Tu. Bowing parameter of the band-gap energy of ganxas1-x. *Applied Physics Letters*, 70(12):1608–1610, 1997.
- [142] D. J. Friedman, A. G. Norman, J. F. Geisz, and S. R. Kurtz. Comparison of hydrazine, dimethylhydrazine, and t-butylamine nitrogen sources for movpe growth of gainnas for solar cells. *Journal of Crystal Growth*, 208(1-4):11–17, 2000.
- [143] S. Sakai, Y. Ueta, and Y. Terauchi. Band-gap energy and band lineup of iii-v-alloy semiconductors incorporating nitrogen and boron. *Japanese Journal of Applied Physics Part 1-Regular Papers Short Notes & Review Papers*, 32(10):4413–4417, 1993.
- [144] A. Rubio and M. L. Cohen. Quasi-particle excitations in gaas1-xnx and alas1-xnx ordered alloys. *Physical Review B*, 51(7):4343–4346, 1995.
- [145] J. Neugebauer and C. G. Vandewalle. Electronic-structure and phase-stability of gaas1-xnx alloys. *Physical Review B*, 51(16):10568–10571, 1995.
- [146] L. Bellaiche, S. H. Wei, and A. Zunger. Band gaps of gapn and gaasn alloys. *Applied Physics Letters*, 70(26):3558–3560, 1997.

-
- [147] D. G. Thomas, J. J. Hopfield, and C. J. Frosch. Isoelectronic traps due to nitrogen in gallium phosphide. *Physical Review Letters*, 15(22):857, 1965.
- [148] D. G. Thomas and J. J. Hopfield. Isoelectronic traps due to nitrogen in gallium phosphide. *Physical Review*, 150(2):680, 1966.
- [149] J. J. Hopfield, D. G. Thomas, and R. T. Lynch. Isoelectronic donors and acceptors. *Physical Review Letters*, 17(6):312, 1966.
- [150] Y. Zhang, B. Fluegel, A. Mascarenhas, H. P. Xin, and C. W. Tu. Optical transitions in the isoelectronically doped semiconductor gap : N: An evolution from isolated centers, pairs, and clusters to an impurity band. *Physical Review B*, 62(7):4493–4500, 2000.
- [151] B. Fluegel, Y. Zhang, J. F. Geisz, and A. Mascarenhas. Confirmation of the impurity-band model for gap1-xnx. *Physical Review B*, 72(7), 2005.
- [152] P. R. C. Kent and A. Zunger. Theory of electronic structure evolution in gaasn and gapn alloys. *Physical Review B*, 64(11), 2001.
- [153] W. Shan, W. Walukiewicz, J. W. Ager, E. E. Haller, J. F. Geisz, D. J. Friedman, J. M. Olson, and S. R. Kurtz. Band anticrossing in gainnas alloys. *Physical Review Letters*, 82(6):1221–1224, 1999.
- [154] A. Lindsay and E. P. O'reilly. Unification of the band anticrossing and cluster-state models of dilute nitride semiconductor alloys. *Physical Review Letters*, 93(19), 2004.
- [155] W. Shan, K. M. Yu, W. Walukiewicz, J. Wu, J. W. Ager, and E. E. Haller. Band anticrossing in dilute nitrides. *Journal of Physics-Condensed Matter*, 16(31):S3355–S3372, 2004.
- [156] J. Wu, W. Shan, and W. Walukiewicz. Band anticrossing in highly mismatched iii-v semiconductor alloys. *Semiconductor Science and Technology*, 17(8):860–869, 2002.
- [157] A. Lindsay and E. P. O'reilly. Theory of enhanced bandgap non-parabolicity in ganxas1-x and related alloys. *Solid State Communications*, 112(8):443–447, 1999.
- [158] I. Vurgaftman and J. R. Meyer. Band parameters for nitrogen-containing semiconductors. *Journal of Applied Physics*, 94(6):3675–3696, 2003.
- [159] W. Shan, W. Walukiewicz, J. W. Ager, E. E. Haller, J. F. Geisz, D. J. Friedman, J. M. Olson, and S. R. Kurtz. Effect of nitrogen on the band structure of gainnas alloys. *Journal of Applied Physics*, 86(4):2349–2351, 1999.
- [160] W. Shan, W. Walukiewicz, K. M. Yu, J. W. Ager, E. E. Haller, J. F. Geisz, D. J. Friedman, J. M. Olson, S. R. Kurtz, and C. Nauka. Effect of nitrogen on the electronic band structure of group iii-n-v alloys. *Physical Review B*, 62(7):4211–4214, 2000.

Bibliography

- [161] M. Galluppi, L. Geelhaar, H. Riechert, M. Hetterich, A. Grau, S. Birner, and W. Stolz. Bound-to-bound and bound-to-free transitions in surface photovoltage spectra: Determination of the band offsets for InxGa1-xAs and InxGa1-xAs1-yNy quantum wells. *Physical Review B*, 72(15), 2005.
- [162] N. Tansu and L. J. Mawst. The role of hole leakage in 1300-nm InGaAsN quantum-well lasers. *Applied Physics Letters*, 82(10):1500–1502, 2003.
- [163] J. Y. Yeh, N. Tansu, and L. J. Mawst. Temperature-sensitivity analysis of 1360-nm dilute-nitride quantum-well lasers. *Ieee Photonics Technology Letters*, 16(3):741–743, 2004.
- [164] A. Albo, G. Bahir, and D. Fekete. Improved hole confinement in InGaAsN-GaAsSbN thin double-layer quantum-well structure for telecom-wavelength lasers. *Journal of Applied Physics*, 108(9), 2010.
- [165] A. Polimeni, M. Bissiri, A. Augieri, G. B. H. von Hogersthal, M. Capizzi, D. Gollub, M. Fischer, M. Reinhardt, and A. Forchel. Reduced temperature dependence of the band gap in GaAs1-yNy investigated with photoluminescence. *Physical Review B*, 65(23), 2002.
- [166] I. Suemune, K. Uesugi, and W. Walukiewicz. Role of nitrogen in the reduced temperature dependence of band-gap energy in GaAsN . *Applied Physics Letters*, 77(19):3021–3023, 2000.
- [167] F. I. Lai, S. Y. Kuo, J. S. Wang, H. C. Kuo, S. C. Wang, H. S. Wang, C. T. Liang, and Y. F. Chen. Effect of nitrogen contents on the temperature dependence of photoluminescence in InGaAsN/GaAs single quantum wells. *Journal of Vacuum Science & Technology A*, 24(4):1223–1227, 2006.
- [168] R. J. Potter and N. Balkan. Optical properties of GaAsN and InGaAsN quantum wells. *Journal of Physics-Condensed Matter*, 16(31):S3387–S3412, 2004.
- [169] J. Endicott, A. Patane, J. Ibanez, L. Eaves, M. Bissiri, M. Hopkinson, R. Airey, and G. Hill. Magnetotunneling spectroscopy of dilute Ga(AsN) quantum wells. *Physical Review Letters*, 91(12), 2003.
- [170] P. N. Hai, W. M. Chen, I. A. Buyanova, H. P. Xin, and C. W. Tu. Direct determination of electron effective mass in GaAsN/GaAs quantum wells. *Applied Physics Letters*, 77(12):1843–1845, 2000.
- [171] S. Tomic, E. P. O'Reilly, P. J. Klar, H. Gruning, W. Heimbrodtt, W. M. M. Chen, and I. A. Buyanova. Influence of conduction-band nonparabolicity on electron confinement and effective mass in GaInAs1-x/GaAs quantum wells. *Physical Review B*, 69(24), 2004.
- [172] P. J. Klar, H. Gruning, W. Heimbrodtt, G. Weiser, J. Koch, K. Volz, W. Stolz, S. W. Koch, S. Tomic, S. A. Choulis, T. J. C. Hosea, E. P. O'Reilly, M. Hofmann, J. Hader, and J. V. Moloney. Interband transitions of quantum wells and device structures containing Ga(n, as) and (Ga, In)(n, as) . *Semiconductor Science and Technology*, 17(8):830–842, 2002.

-
- [173] T. Mattila, S. H. Wei, and A. Zunger. Localization and anticrossing of electron levels in $\text{GaAs}_{1-x}\text{N}_x$ alloys. *Physical Review B*, 60(16):11245–11248, 1999.
- [174] D. J. Friedman. Progress and challenges for next-generation high-efficiency multi-junction solar cells. *Current Opinion in Solid State & Materials Science*, 14(6):131–138, 2010.
- [175] E. P. O'Reilly, A. Lindsay, S. Tomic, and M. Kamal-Saadi. Tight-binding and k center dot p models for the electronic structure of $\text{Ga}(\text{In})\text{N}$ and related alloys. *Semiconductor Science and Technology*, 17(8):870–879, 2002.
- [176] A. Lindsay, S. Tomic, and E. P. O'Reilly. Derivation of a 10-band k center dot p model for dilute nitride semiconductors. *Solid-State Electronics*, 47(3):443–446, 2003.
- [177] A. Patane, J. Endicott, J. Ibanez, P. N. Brunkov, L. Eaves, S. B. Healy, A. Lindsay, E. P. O'Reilly, and M. Hopkinson. Breakup of the conduction band structure of dilute $\text{GaAs}_{1-y}\text{N}_y$ alloys. *Physical Review B*, 71(19), 2005.
- [178] G. Bentoumi, Z. Yaiche, R. Leonelli, J. N. Beaudry, P. Desjardins, and R. A. Masut. Low-temperature emission in dilute GaAsN alloys grown by metalorganic vapor phase epitaxy. *Journal of Applied Physics*, 103(6), 2008.
- [179] G. Bentoumi, V. Timoshevskii, N. Madini, M. Cote, R. Leonelli, J. N. Beaudry, P. Desjardins, and R. A. Masut. Evidence for large configuration-induced band-gap fluctuations in $\text{GaAs}_{1-x}\text{N}_x$ alloys. *Physical Review B*, 70(3), 2004.
- [180] G. B. von Hogersthal, A. Polimeni, F. Masia, M. Bissiri, M. Capizzi, D. Gollub, M. Fischer, and A. Forchel. Magnetophotoluminescence studies of $(\text{InGa})_{\text{AsN}}/\text{GaAs}$ heterostructures. *Physical Review B*, 67(23), 2003.
- [181] T. Taliercio, R. Intartaglia, B. Gil, P. Lefebvre, T. Bretagnon, U. Tisch, E. Finkman, J. Salzman, M. A. Pinault, M. Laugt, and E. Tournie. From $\text{GaAs} : \text{N}$ to oversaturated GaAsN : Analysis of the band-gap reduction. *Physical Review B*, 69(7), 2004.
- [182] F. Masia, G. Pettinari, A. Polimeni, M. Felici, A. Miriametro, M. Capizzi, A. Lindsay, S. B. Healy, E. P. O'Reilly, A. Cristofoli, G. Bais, M. Piccin, S. Rubini, F. Martelli, A. Franciosi, P. J. Klar, K. Volz, and W. Stolz. Interaction between conduction band edge and nitrogen states probed by carrier effective-mass measurements in $\text{GaAs}_{1-x}\text{N}_x$. *Physical Review B*, 73(7):–, 2006.
- [183] T. Dannecker, Y. Jin, H. Cheng, C. F. Gorman, J. Buckeridge, C. Uher, S. Fahy, C. Kurdak, and R. S. Goldman. Nitrogen composition dependence of electron effective mass in $\text{GaAs}_{1-x}\text{N}_x$. *Physical Review B*, 82(12), 2010.
- [184] G. Pettinari, F. Masia, A. Polimeni, M. Felici, A. Frova, M. Capizzi, A. Lindsay, E. P. O'Reilly, P. J. Klar, W. Stolz, G. Bais, M. Piccin, S. Rubini, F. Martelli, and A. Franciosi. Influence of nitrogen-cluster states on the gyromagnetic factor of electrons in $\text{GaAs}_{1-x}\text{N}_x$. *Physical Review B*, 74(24), 2006.

Bibliography

- [185] T. D. Veal, L. F. J. Piper, P. H. Jefferson, I. Mahboob, C. F. McConville, M. Merrick, T. J. C. Hosea, B. N. Murdin, and M. Hopkinson. Photoluminescence spectroscopy of bandgap reduction in dilute innas alloys. *Applied Physics Letters*, 87(18), 2005.
- [186] M. Merrick, S. A. Cripps, B. N. Murdin, T. J. C. Hosea, T. D. Veal, C. F. McConville, and M. Hopkinson. Photoluminescence of innas alloys: S-shaped temperature dependence and conduction-band nonparabolicity. *Physical Review B*, 76(7), 2007.
- [187] T. D. Das, S. C. Das, and S. Dhar. Bandgap reduction in dilute inpn grown by liquid phase epitaxy. *2nd National Workshop on Advanced Optoelectronic Materials and Devices (Aomd-2008)*, pages 275–282, 2008.
- [188] E. P. O'reilly, A. Lindsay, P. J. Klar, A. Polimeni, and M. Capizzi. Trends in the electronic structure of dilute nitride alloys. *Semiconductor Science and Technology*, 24(3), 2009.
- [189] I. H. Ho and G. B. Stringfellow. Solubility of nitrogen in binary iii-v systems. *Journal of Crystal Growth*, 178(1-2):1–7, 1997.
- [190] S. B. Zhang and A. Zunger. Surface-reconstruction-enhanced solubility of n, p, as, and sb in iii-v semiconductors. *Applied Physics Letters*, 71(5):677–679, 1997.
- [191] S. Kurtz, R. Reedy, G. D. Barber, J. F. Geisz, D. J. Friedman, W. E. McMahon, and J. M. Olson. Incorporation of nitrogen into gaasn grown by mocvd using different precursors. *Journal of Crystal Growth*, 234(2-3):318–322, 2002.
- [192] M. Fischer, M. Reinhardt, and A. Forchel. Gainasn/gaas laser diodes operating at 1.52 μm . *Electronics Letters*, 36(14):1208–1209, 2000.
- [193] M. Hugues, B. Damilano, J. Y. Duboz, and J. Massies. Optimum indium composition for (ga,in)(n,as)/gaas quantum wells emitting beyond 1.5 μm . *Applied Physics Letters*, 88(9), 2006.
- [194] R. Kudrawiec, M. Gladysiewicz, J. Misiewicz, F. Ishikawa, and K. H. Ploog. Ground and excited state transitions in as-grown $\text{ga}_{0.64}\text{in}_{0.36}\text{n}_{0.046}\text{as}_{0.954}$ quantum wells studied by contactless electroreflectance. *Applied Physics Letters*, 90(4), 2007.
- [195] V. V. Mamutin, A. Y. Egorov, and N. V. Kryzhanovskaya. Molecular beam epitaxy growth methods of wavelength control for inas/(in)gaasn/gaas heterostructures. *Nanotechnology*, 19(44), 2008.
- [196] J. Koch, F. Hohnsdorf, and W. Stolz. Optical characterization of (gain)(nas)/gaas mqw structures. *Journal of Electronic Materials*, 29(1):165–168, 2000.
- [197] T. Hakkarainen, J. Toivonen, M. Sopanen, and H. Lipsanen. Gainnas quantum well structures for 1.55 μm emission on gaas by atmospheric pressure metalorganic vapor phase epitaxy. *Journal of Crystal Growth*, 234(4):631–636, 2002.

- [198] M. Yokozeiki, J. Mitomo, Y. Sato, T. Hino, and H. Narui. 1.50 μm cw operation of $\text{InGaAsN}/\text{GaAs}$ laser diodes grown by MOCVD. *Electronics Letters*, 40(17):1060–1061, 2004.
- [199] A. J. Ptak, S. W. Johnston, S. Kurtz, D. J. Friedman, and W. K. Metzger. A comparison of MBE- and MOCVD-grown InGaAsN s. *Journal of Crystal Growth*, 251(1-4):392–398, 2003.
- [200] F. Hohnsdorf, J. Koch, C. Agert, and W. Stolz. Investigations of (gain)(InGaAsN) bulk layers and (gain)(InGaAsN)/ GaAs multiple quantum well structures grown using tertiarybutylarsine (TBA) and 1,1-dimethylhydrazine (DMH). *Journal of Crystal Growth*, 195(1-4):391–396, 1998.
- [201] E. Bourret-Courchesne, Q. Ye, D. W. Peters, J. Arnold, M. Ahmed, S. J. C. Irvine, R. Kanjolia, L. M. Smith, and S. A. Rushworth. Pyrolysis of dimethylhydrazine and its co-pyrolysis with triethylgallium. *Journal of Crystal Growth*, 217(1-2):47–54, 2000.
- [202] U. W. Pohl, C. Moller, K. Knorr, W. Richter, J. Gottfriedsen, H. Schumann, K. Rademann, and A. Fielicke. Tertiarybutylhydrazine: a new precursor for the MOVPE of group III-nitrides. *Materials Science and Engineering B-Solid State Materials for Advanced Technology*, 59(1-3):20–23, 1999.
- [203] K. Volz, J. Koch, F. Hohnsdorf, B. Kunert, and W. Stolz. MOVPE growth of dilute nitride III/V semiconductors using all liquid metalorganic precursors. *Journal of Crystal Growth*, 311(8):2418–2426, 2009.
- [204] A. J. Ptak, S. Kurtz, C. Curtis, R. Reedy, and J. M. Olson. Incorporation effects in MOCVD-grown (In)GaAsN using different nitrogen precursors. *Journal of Crystal Growth*, 243(2):231–237, 2002.
- [205] M. Weyers and M. Sato. Growth of GaAsN alloys by low-pressure metalorganic chemical vapor-deposition using plasma-cracked NH_3 . *Applied Physics Letters*, 62(12):1396–1398, 1993.
- [206] D. E. Mars, D. I. Babic, Y. Kaneko, Y. L. Chang, S. Subramanya, J. Kruger, P. Perlin, and E. R. Weber. Growth of 1.3 μm InGaAsN laser material on GaAs by molecular beam epitaxy. *Journal of Vacuum Science & Technology B*, 17(3):1272–1275, 1999.
- [207] A. Moto, S. Tanaka, N. Ikoma, T. Tanabe, S. Takagishi, M. Takahashi, and T. Katsuyama. Metalorganic vapor phase epitaxial growth of GaAsN using tertiarybutylarsine (TBA) and dimethylhydrazine (DMH). *Japanese Journal of Applied Physics Part 1-Regular Papers Short Notes & Review Papers*, 38(2B):1015–1018, 1999.
- [208] S. Kurtz, J. F. Geisz, B. M. Keyes, W. K. Metzger, D. J. Friedman, J. M. Olson, A. J. Ptak, R. R. King, and N. H. Karam. Effect of growth rate and gallium source on GaAsN. *Applied Physics Letters*, 82(16):2634–2636, 2003.
- [209] C. A. Larsen, S. H. Li, N. I. Buchan, and G. B. Stringfellow. Mechanisms of GaAs growth using tertiarybutylarsine and trimethylgallium. *Journal of Crystal Growth*, 94(3):673–682, 1989.

Bibliography

- [210] W. C. Chen, R. W. Chuang, Y. K. Su, and S. H. Hsu. Controlling the nitrogen composition of ingaasn quantum wells grown by movpe. *Journal of Physics and Chemistry of Solids*, 69(2-3):404–407, 2008.
- [211] J. N. Beaudry, R. A. Masut, and P. Desjardins. Gaas1-xnx on gaas(001): Nitrogen incorporation kinetics from trimethylgallium, tertiarybutylarsine, and 1,1-dimethylhydrazine organometallic vapor-phase epitaxy. *Journal of Crystal Growth*, 310(6):1040–1048, 2008.
- [212] D. J. Friedman, J. F. Geisz, S. R. Kurtz, J. M. Olson, and R. Reedy. Nonlinear dependence of n incorporation on in content in gainnas. *Journal of Crystal Growth*, 195(1-4):438–443, 1998.
- [213] M. Albrecht, H. Abu-Farsakh, T. Remmele, L. Geelhaar, H. Riechert, and J. Neugebauer. Compositional correlation and anticorrelation in quaternary alloys: Competition between bulk thermodynamics and surface kinetics. *Physical Review Letters*, 99(20):–, 2007.
- [214] J. M. Moison, C. Guille, F. Houzay, F. Barthe, and M. Vanrompay. Surface segregation of 3rd-column in group iii-v arsenide compounds - ternary alloys and heterostructures. *Physical Review B*, 40(9):6149–6162, 1989.
- [215] I. A. Buyanova, W. M. Chen, and C. W. Tu. Recombination processes in n-containing iii-v ternary alloys. *Solid-State Electronics*, 47(3):467–475, 2003.
- [216] K. Matsuda, T. Saiki, M. Takahashi, A. Moto, and S. Takagishi. Near-field photoluminescence study of ganas alloy epilayer at room and cryogenic temperature. *Applied Physics Letters*, 78(11):1508–1510, 2001.
- [217] M. A. Pinault and E. Tournie. On the origin of carrier localization in gal-xinxnyas1-y/gaas quantum wells. *Applied Physics Letters*, 78(11):1562–1564, 2001.
- [218] S. R. Bank, M. A. Wistey, H. B. Yuen, V. Lordi, V. F. Gambin, and J. S. Harris. Effects of antimony and ion damage on carrier localization in molecular-beam-epitaxy-grown gainnas. *Journal of Vacuum Science & Technology B*, 23(3):1320–1323, 2005.
- [219] M. Latkowska, R. Kudrawiec, G. Sek, J. Misiewicz, J. Ibanez, M. Henini, and M. Hopkinson. Thermal quenching of single localized excitons in gainnas layers. *Applied Physics Letters*, 98(13), 2011.
- [220] R. Kudrawiec, G. Sek, J. Misiewicz, F. Ishikawa, A. Trampert, and K. H. Ploog. Localized and delocalized states in ganas studied by microphotoluminescence and photoreflectance. *Applied Physics Letters*, 94(1), 2009.
- [221] N. Yamada, G. Roos, and J. S. Harris. Threshold reduction in strained ingaas single quantum-well lasers by rapid thermal annealing. *Applied Physics Letters*, 59(9):1040–1042, 1991.

- [222] H. Saito, T. Makimoto, and N. Kobayashi. Mowpe growth of strained ingaasn/gaas quantum wells. *Journal of Crystal Growth*, 195(1-4):416–420, 1998.
- [223] K. Volz, J. Koch, B. Kunert, I. Nemeth, and W. Stolz. Influence of annealing on the optical and structural properties of dilute n-containing iii/v semiconductor hetero structures. *Journal of Crystal Growth*, 298:126–130, 2007.
- [224] J. F. Geisz, D. J. Friedman, J. M. Olson, S. R. Kurtz, and B. M. Keyes. Photocurrent of 1 ev gainnas lattice-matched to gaas. *Journal of Crystal Growth*, 195(1-4):401–408, 1998.
- [225] O. Rubel, M. Galluppi, S. D. Baranovskii, K. Volz, L. Geelhaar, H. Riechert, P. Thomas, and W. Stolz. Quantitative description of disorder parameters in (gain)(nas) quantum wells from the temperature-dependent photoluminescence spectroscopy. *Journal of Applied Physics*, 98(6), 2005.
- [226] S. Francoeur, G. Sivaraman, Y. Qiu, S. Nikishin, and H. Temkin. Luminescence of as-grown and thermally annealed gaasn/gaas. *Applied Physics Letters*, 72(15):1857–1859, 1998.
- [227] K. Volz, T. Torunski, B. Kunert, O. Rubel, S. Nau, S. Reinhard, and W. Stolz. Specific structural and compositional properties of (gain)(nas) and their influence on optoelectronic device performance. *Journal of Crystal Growth*, 272(1-4):739–747, 2004.
- [228] O. Rubel, K. Volz, T. Torunski, S. D. Baranovskii, F. Grosse, and W. Stolz. Columnar [001]-oriented nitrogen order in ga(nas) and (gain)(nas) alloys. *Applied Physics Letters*, 85(24):5908–5910, 2004.
- [229] G. Bosker, N. A. Stolwijk, J. V. Thordson, U. Sodervall, and T. G. Andersson. Diffusion of nitrogen from a buried doping layer in gallium arsenide revealing the prominent role of as interstitials. *Physical Review Letters*, 81(16):3443–3446, 1998.
- [230] K. Volz, T. Torunski, O. Rubel, W. Stolz, P. Kruse, D. Gerthsen, M. Schowalter, and A. Rosenauer. Annealing effects on the nanoscale indium and nitrogen distribution in ga(nas) and (gain)(nas) quantum wells. *Journal of Applied Physics*, 102(8), 2007.
- [231] A. Janotti, S. H. Wei, S. B. Zhang, S. Kurtz, and C. G. Van de Walle. Interactions between nitrogen, hydrogen, and gallium vacancies in gaas_{1-x}nx alloys. *Physical Review B*, 67(16), 2003.
- [232] J. Toivonen, T. Hakkarainen, M. Sopanen, H. Lipsanen, J. Oila, and K. Saarinen. Observation of defect complexes containing ga vacancies in gaasn. *Applied Physics Letters*, 82(1):40–42, 2003.
- [233] R. Kudrawiec, M. Syperek, M. Latkowska, J. Misiewicz, V. M. Korpijarvi, P. Laukkanen, J. Pakarinen, M. Dumitrescu, M. Guina, and M. Pessa. Influence of non-radiative recombination on photoluminescence decay time in gainnas quantum wells with ga- and in-rich environments of nitrogen atoms. *Journal of Applied Physics*, 111(6), 2012.

Bibliography

- [234] M. Hugues, B. Damilano, J. M. Chauveau, J. Y. Duboz, and J. Massies. Blue-shift mechanisms in annealed (ga,in)(n,as)/gaas quantum wells. *Physical Review B*, 75(4), 2007.
- [235] J. M. Chauveau, A. Trampert, K. H. Ploog, and E. Tournie. Nanoscale analysis of the in and n spatial redistributions upon annealing of gainnas quantum wells. *Applied Physics Letters*, 84(14):2503–2505, 2004.
- [236] S. Kurtz, J. Webb, L. Gedvilas, D. Friedman, J. Geisz, J. Olson, R. King, D. Joslin, and N. Karam. Structural changes during annealing of gainasn. *Applied Physics Letters*, 78(6):748–750, 2001.
- [237] K. Volz, T. Torunski, and W. Stolz. Detection of nanometer-sized strain fields in (gain)(nas) alloys by specific dark field transmission electron microscopic imaging. *Journal of Applied Physics*, 97(1), 2005.
- [238] X. Kong, A. Trampert, E. Tournie, and K. H. Ploog. Decomposition in as-grown (ga,in)(n,as) quantum wells. *Applied Physics Letters*, 87(17), 2005.
- [239] V. Lordi, V. Gambin, S. Friedrich, T. Funk, T. Takizawa, K. Uno, and J. S. Harris. Nearest-neighbor configuration in (gain)(nas) probed by x-ray absorption spectroscopy. *Physical Review Letters*, 90(14), 2003.
- [240] P. J. Klar, H. Gruning, J. Koch, S. Schafer, K. Volz, W. Stolz, W. Heimbrod, A. M. K. Saadi, A. Lindsay, and E. P. O'Reilly. (ga, in)(n, as)-fine structure of the band gap due to nearest-neighbor configurations of the isovalent nitrogen. *Physical Review B*, 64(12), 2001.
- [241] K. Volz, D. Lackner, I. Nemeth, B. Kunert, W. Stolz, C. Baur, F. Dimroth, and A. W. Bett. Optimization of annealing conditions of (gain)(nas) for solar cell applications. *Journal of Crystal Growth*, 310(7-9):2222–2228, 2008.
- [242] K. Kim and A. Zunger. Spatial correlations in gainasn alloys and their effects on band-gap enhancement and electron localization. *Physical Review Letters*, 86(12):2609–2612, 2001.
- [243] S. G. Spruytte, C. W. Coldren, J. S. Harris, W. Wampler, P. Krispin, K. Ploog, and M. C. Larson. Incorporation of nitrogen in nitride-arsenides: Origin of improved luminescence efficiency after anneal. *Journal of Applied Physics*, 89(8):4401–4406, 2001.
- [244] C. S. Peng, J. Konttinen, H. F. Liu, and M. Pessa. Blue shift in ingaasn/gaas quantum wells with different width. *Iee Proceedings-Optoelectronics*, 151(5):317–319, 2004.
- [245] S. Fahy and E. P. O'Reilly. Intrinsic limits on electron mobility in dilute nitride semiconductors. *Applied Physics Letters*, 83(18):3731–3733, 2003.
- [246] F. Ishikawa, G. Mussler, K. J. Friedland, H. Kostial, K. Hagenstein, L. Daweritz, and K. H. Ploog. Impact of n-induced potential fluctuations on the electron transport in ga(as,n). *Applied Physics Letters*, 87(26), 2005.

-
- [247] H. E. Porteanu, O. Loginenko, and F. Koch. The dual role of nitrogen as alloying and confining element in gaas-based dilute nitride semiconductors. *Journal of Applied Physics*, 107(3), 2010.
- [248] A. J. Ptak, D. J. Friedman, and S. Kurtz. Effects of temperature, nitrogen ions, and antimony on wide depletion width gainnas. *Journal of Vacuum Science & Technology B*, 25(3):955–959, 2007.
- [249] D. B. Jackrel, S. R. Bank, H. B. Yuen, M. A. Wistey, and J. S. Harris. Dilute nitride gainnas and gainnassb solar cells by molecular beam epitaxy. *Journal of Applied Physics*, 101(11), 2007.
- [250] K. Nakahara, M. Kondow, T. Kitatani, M. C. Larson, and K. Uomi. 1.3- μm continuous-wave lasing operation in gainnas quantum-well lasers. *Ieee Photonics Technology Letters*, 10(4):487–488, 1998.
- [251] A. Y. Egorov, D. Bernklau, D. Livshits, V. Ustinov, Z. I. Alferov, and H. Riechert. High power cw operation of ingaasn lasers at 1.3 μm . *Electronics Letters*, 35(19):1643–1644, 1999.
- [252] S. Sato and S. Satoh. High-temperature characteristic in 1.3- μm -range highly strained gainnas ridge stripe lasers grown by metal-organic chemical vapor deposition. *Ieee Photonics Technology Letters*, 11(12):1560–1562, 1999.
- [253] M. A. Wistey, S. R. Bank, H. B. Yuen, H. Bae, and J. S. Harris. Nitrogen plasma optimization for high-quality dilute nitrides. *Journal of Crystal Growth*, 278(1-4):229–233, 2005.
- [254] H. B. Yuen, M. A. Wistey, S. R. Bank, H. Bae, and J. S. Harris. Investigation of nitrogen flow variation into a radio frequency plasma cell on plasma properties and gainnas grown by molecular beam epitaxy. *Journal of Vacuum Science & Technology B*, 23(3):1328–1332, 2005.
- [255] M. Hugues, B. Damilano, J. Barjon, J. Y. Duboz, J. Massies, J. M. Ulloa, M. Montes, and A. Hierro. Performance improvement of 1.52 μm (ga,in)(n,as)/gaas quantum well lasers on gaas substrates. *Electronics Letters*, 41(10):595–596, 2005.
- [256] G. Jaschke, R. Averbeck, L. Geelhaar, and H. Riechert. Low threshold ingaasn/gaas lasers beyond 1500 nm. *Journal of Crystal Growth*, 278(1-4):224–228, 2005.
- [257] X. Yang, M. J. Jurkovic, J. B. Heroux, and W. I. Wang. Molecular beam epitaxial growth of ingaasn : Sb/gaas quantum wells for long-wavelength semiconductor lasers. *Applied Physics Letters*, 75(2):178–180, 1999.
- [258] H. Shimizu, K. Kumada, S. Uchiyama, and A. Kasukawa. High performance cw 1.26 μm gainnassb-sqw and 1.20 μm gainnassb-sqw ridge lasers. *Electronics Letters*, 36(20):1701–1703, 2000.

- [259] J. Massies and N. Grandjean. Surfactant effect on the surface-diffusion length in epitaxial-growth. *Physical Review B*, 48(11):8502–8505, 1993.
- [260] E. Tournie, N. Grandjean, A. Trampert, J. Massies, and K. H. Ploog. Surfactant-mediated molecular-beam epitaxy of iii-v strained-layer heterostructures. *Journal of Crystal Growth*, 150(1-4):460–466, 1995.
- [261] S. R. Bank, H. Bae, L. L. Goddard, H. B. Yuen, M. A. Wistey, R. Kudrawiec, and J. S. Harris. Recent progress on 1.55- μ m dilute-nitride lasers. *IEEE Journal of Quantum Electronics*, 43(9-10):773–785, 2007.
- [262] J. S. Harris, R. Kudrawiec, H. B. Yuen, S. R. Bank, H. P. Bae, M. A. Wistey, D. Jackrel, E. R. Pickett, T. Sarmiento, L. L. Goddard, V. Lordi, and T. Gugen. Development of gainssb alloys: Growth, band structure, optical properties and applications. *Physica Status Solidi B-Basic Solid State Physics*, 244(8):2707–2729, 2007.
- [263] S. K. Mehta, T. Srinivasan, G. C. Dubey, and R. K. Jain. Influence of hydrogenation on photoluminescence of gaalas grown by molecular-beam epitaxy. *Journal of Applied Physics*, 77(11):6058–6060, 1995.
- [264] E. Grilli, M. Guzzi, R. Zamboni, A. Bosacchi, S. Franchi, L. Vanzetti, P. Allegri, and L. Pavesi. Effects of different processes with hydrogen on the photoluminescence of gaalas-si grown by molecular-beam epitaxy. *Applied Physics Letters*, 57(26):2797–2799, 1990.
- [265] K. Kondo, S. Muto, K. Nanbu, T. Ishikawa, S. Hiyamizu, and H. Hashimoto. Effect of h-2 on the quality of si-doped alxgal-xas grown by mbe. *Japanese Journal of Applied Physics Part 2-Letters*, 22(2):L121–L123, 1983.
- [266] A. Polimeni, G. Baldassarri, H. V. M. Bissiri, M. Capizzi, M. Fischer, M. Reinhardt, and A. Forchel. Effect of hydrogen on the electronic properties of inxgal-xas1-yny/gaas quantum wells. *Physical Review B*, 63(20):–, 2001.
- [267] M. Bissiri, G. B. H. von Hogersthal, A. Polimeni, V. Gaspari, F. Ranalli, M. Capizzi, A. A. Bonapasta, F. Jiang, M. Stavola, D. Gollub, M. Fischer, M. Reinhardt, and A. Forchel. Hydrogen-induced passivation of nitrogen in gaas1-yny. *Physical Review B*, 65(23), 2002.
- [268] P. J. Klar, H. Gruning, M. Gungerich, W. Heimbrod, J. Koch, T. Torunski, W. Stolz, A. Polimeni, and M. Capizzi. Global changes of the band structure and the crystal lattice of ga(n,as) due to hydrogenation. *Physical Review B*, 67(12), 2003.
- [269] G. Baldassarri, M. Bissiri, A. Polimeni, M. Capizzi, M. Fischer, M. Reinhardt, and A. Forchel. Hydrogen-induced band gap tuning of (inga)(asn)/gaas single quantum wells. *Applied Physics Letters*, 78(22):3472–3474, 2001.
- [270] A. Polimeni, M. Bissiri, M. Felici, M. Capizzi, I. A. Buyanova, W. M. Chen, H. P. Xin, and C. W. Tu. Nitrogen passivation induced by atomic hydrogen: The gap1-yny case. *Physical Review B*, 67(20), 2003.

-
- [271] A. Polimeni, G. B. H. von Hogerthal, F. Masia, A. Frova, M. Capizzi, S. Sanna, V. Fiorentini, P. J. Klar, and W. Stolz. Tunable variation of the electron effective mass and exciton radius in hydrogenated $\text{GaAs}_{1-x}\text{N}_x$. *Physical Review B*, 69(4), 2004.
- [272] G. Bisognin, D. De Salvador, A. V. Drigo, E. Napolitani, A. Sambo, M. Berti, A. Polimeni, M. Felici, M. Capizzi, M. Gungerich, and P. J. Klar. Hydrogen-nitrogen complexes in dilute nitride alloys: Origin of the compressive lattice strain. *Applied Physics Letters*, 89(6), 2006.
- [273] M. Berti, G. Bisognin, D. De Salvador, E. Napolitani, S. Vangelista, A. Polimeni, M. Capizzi, F. Boscherini, G. Ciatto, S. Rubini, F. Martelli, and A. Franciosi. Formation and dissolution of d-n complexes in dilute nitrides. *Physical Review B*, 76(20), 2007.
- [274] R. Trotta, A. Polimeni, and M. Capizzi. Hydrogen incorporation in iii-n-v semiconductors: From macroscopic to nanometer control of the materials' physical properties. *Advanced Functional Materials*, 22(9):1782–1801, 2012.
- [275] S. Sanna and V. Fiorentini. Lattice constant, effective mass, and gap recovery in hydrogenated $\text{GaAs}_{1-x}\text{N}_x$. *Physical Review B*, 69(12), 2004.
- [276] F. Jiang, M. Stavola, M. Capizzi, A. Polimeni, A. A. Bonapasta, and F. Filippone. Vibrational spectroscopy of hydrogenated $\text{GaAs}_{1-y}\text{N}_y$: A structure-sensitive test of an $\text{h-2}^{(*)}(\text{n})$ model. *Physical Review B*, 69(4), 2004.
- [277] G. Bisognin, D. De Salvador, E. Napolitani, M. Berti, A. Polimeni, M. Felici, M. Capizzi, G. Bais, F. Jabeen, M. Picein, S. Rubini, F. Martelli, and A. Franciosi. Thermal evolution of small n-d complexes in deuterated dilute nitrides revealed by in-situ high resolution x-ray diffraction. *Physica Status Solidi a-Applications and Materials Science*, 204(8):2766–2771, 2007.
- [278] L. Wen, F. Bekisli, M. Stavola, W. B. Fowler, R. Trotta, A. Polimeni, M. Capizzi, S. Rubini, and F. Martelli. Detailed structure of the h-n-h center in $\text{GaAs}_{1-y}\text{N}_y$ revealed by vibrational spectroscopy under uniaxial stress. *Physical Review B*, 81(23), 2010.
- [279] R. Trotta, D. Giubertoni, A. Polimeni, M. Bersani, M. Capizzi, F. Martelli, S. Rubini, G. Bisognin, and M. Berti. Hydrogen diffusion in $\text{GaAs}_{1-x}\text{N}_x$. *Physical Review B*, 80(19):–, 2009.
- [280] M. Felici, A. Polimeni, G. Salviati, L. Lazzarini, N. Armani, F. Masia, M. Capizzi, F. Martelli, M. Lazzarino, G. Bais, M. Piccin, S. Rubini, and A. Franciosi. In-plane bandgap engineering by modulated hydrogenation of dilute nitride semiconductors. *Advanced Materials*, 18(15):1993–+, 2006.
- [281] R. Trotta, L. Cavigli, L. Felisari, A. Polimeni, A. Vinattieri, M. Gurioli, M. Capizzi, F. Martelli, S. Rubini, L. Mariucci, M. Francardi, and A. Gerardino. Quantum confinement effects in hydrogen-intercalated $\text{Ga}_{1-x}\text{As}_x\text{N}_x\text{-GaAs}_{1-x}\text{N}_x$: H planar heterostructures investigated by photoluminescence spectroscopy. *Physical Review B*, 81(23), 2010.

Bibliography

- [282] A. Polimeni, R. Trotta, F. Martelli, G. Pettinari, M. Capizzi, L. Felisari, S. Rubini, M. Francardi, A. Gerardino, P. C. M. Christianen, and J. C. Maan. Fabrication of site-controlled quantum dots by spatially selective incorporation of hydrogen in $\text{Ga}(\text{AsN})/\text{GaAs}$ heterostructures. *Advanced Materials*, 23(24):2706–2710, 2011.
- [283] N. Balakrishnan, G. Pettinari, O. Makarovskiy, L. Turyanska, M. W. Fay, M. De Luca, A. Polimeni, M. Capizzi, F. Martelli, S. Rubini, and A. Patane. Band-gap profiling by laser writing of hydrogen-containing InN -vs. *Physical Review B*, 86(15), 2012.
- [284] D. Litvinov, D. Gerthsen, A. Rosenauer, M. Hetterich, A. Grau, P. Gilet, and L. Grenouillet. Determination of the nitrogen distribution in InGaN/GaAs quantum wells by transmission electron microscopy. *Applied Physics Letters*, 85(17):3743–3745, 2004.
- [285] A. Albo, C. Cytermann, G. Bahir, and D. Fekete. Utilizing the interface adsorption of nitrogen for the growth of high-quality InGaN/GaAs quantum wells by metal organic chemical vapor deposition for near infrared applications. *Applied Physics Letters*, 96(14), 2010.
- [286] T. Grehl, R. Mollers, E. Niehuis, and D. Rading. Application of tof-sims for high precision ion implant dosimetry: Possibilities and limitations. *Applied Surface Science*, 255(4):1404–1407, 2008.
- [287] J. S. Harris. InGaN long-wavelength lasers: progress and challenges. *Semiconductor Science and Technology*, 17(8):880–891, 2002.
- [288] P. Salet, F. Gaborit, P. Pagnod-Rossiaux, A. Plais, E. Derouin, J. Pasquier, and J. Jacquet. Room-temperature pulsed operation of 1.3 μm vertical-cavity lasers including bottom $\text{InGaAsP}/\text{InP}$ multilayer Bragg mirrors. *Electronics Letters*, 33(24):2048–2049, 1997.
- [289] E. Luna, M. Hopkinson, J. M. Ulloa, A. Guzman, and E. Munoz. Dilute nitride based double-barrier quantum-well infrared photodetector operating in the near infrared. *Applied Physics Letters*, 83(15):3111–3113, 2003.
- [290] M. Giehler, R. Hey, P. Kleinert, and H. T. Grahn. Intersubband transitions in dilute $(\text{In,Ga})(\text{As,N})/(\text{Al,Ga})\text{As}$ multiple quantum wells analyzed within a three-band k center dot p model. *Physical Review B*, 73(8), 2006.
- [291] Y. X. Dang and W. J. Fan. Dilute nitride based double-barrier quantum wells for intersubband absorption at 1.31 and 1.55 μm . *Physical Review B*, 77(12), 2008.
- [292] A. Albo, A. Vardi, D. Fekete, and G. Bahir. Polarization-independent intersubband based InGaN quantum-well photodetector with dominant detection at 1.42 μm . *Applied Physics Letters*, 94(9), 2009.
- [293] Z. Pan, T. Miyamoto, D. Schlenker, S. Sato, F. Koyama, and K. Iga. Low temperature growth of InGaN/GaAs quantum wells by metalorganic chemical vapor deposition using tertiarybutylarsine. *Journal of Applied Physics*, 84(11):6409–6411, 1998.

-
- [294] D. Fekete, R. Carron, P. Gallo, B. Dwir, A. Rudra, and E. Kapon. High-quality 1.3 μ m-wavelength gainas_n/gaas quantum wells grown by metalorganic vapor phase epitaxy on vicinal substrates. *Applied Physics Letters*, 99(7):072116, 2011.
- [295] N. Moret, D. Y. Oberli, E. Pelucchi, N. Gogneau, A. Rudra, and E. Kapon. Correlation between optical properties and interface morphology of gaas/algaas quantum wells. *Applied Physics Letters*, 88(14):-, 2006.
- [296] N. Moret, D. Y. Oberli, E. Pelucchi, N. Gogneau, A. Rudra, and E. Kapon. Optics, morphology, and growth kinetics of gaas/alxga_{1-x}as quantum wells grown on vicinal substrates by metalorganic vapor phase epitaxy. *Physical Review B*, 84(15), 2011.
- [297] G. Patriarche, L. Largeau, J. C. Harmand, and D. Gollub. Morphology and composition of highly strained ingaas and ingaas_n layers grown on gaas substrate. *Applied Physics Letters*, 84(2):203–205, 2004.
- [298] L. Largeau, C. Bondoux, G. Patriarche, C. Asplund, A. Fujioka, F. Salomonsson, and M. Hammar. Structural effects of the thermal treatment on a gainnas/gaas superlattice. *Applied Physics Letters*, 79(12):1795–1797, 2001.
- [299] G. Biasiol. *Formation mechanisms of low-dimensional semiconductor nanostructures grown by OMCVD on nonplanar substrates*. PhD thesis, 1998.
- [300] R. Carron, D. Fekete, P. Gallo, B. Dwir, A. Rudra, M. Felici, B. Bartova, M. Cantoni, and E. Kapon. Dilute nitride ingaas_n/gaas v-groove quantum wires emitting at 1.3 μ m wavelength at room temperature. *Applied Physics Letters*, 99(10):101107, 2011.
- [301] M. Felici, G. Pettinari, R. Carron, G. Lavenuta, E. Tartaglini, A. Polimeni, D. Fekete, P. Gallo, B. Dwir, A. Rudra, P. C. M. Christianen, J. C. Maan, M. Capizzi, and E. Kapon. Magneto-optical properties of single site-controlled ingaas_n quantum wires grown on prepatterned gaas substrates. *Physical Review B*, 85(15), 2012.
- [302] M. Felici, A. Polimeni, E. Tartaglini, A. Notargiacomo, M. De Luca, R. Carron, D. Fekete, B. Dwir, A. Rudra, M. Capizzi, and E. Kapon. Reduced temperature sensitivity of the polarization properties of hydrogenated ingaas_n v-groove quantum wires. *Applied Physics Letters*, 101(15), 2012.
- [303] C. Constantin, E. Martinet, A. Rudra, K. Leifer, F. Lelarge, G. Biasiol, and E. Kapon. Organometallic chemical vapor deposition of v-groove ingaas/gaas quantum wires incorporated in planar bragg microcavities. *Journal of Crystal Growth*, 207(3):161–173, 1999.
- [304] V. Grillo, M. Albrecht, T. Remmele, H. P. Strunk, A. Y. Egorov, and H. Riechert. Simultaneous experimental evaluation of in and n concentrations in ingaas_n quantum wells. *Journal of Applied Physics*, 90(8):3792–3798, 2001.

Bibliography

- [305] E. Luna, A. Trampert, E. M. Pavelescu, and M. Pessa. Nitrogen-enhanced indium segregation in (ga, in)(n, as)/gaas multiple quantum wells grown by molecular-beam epitaxy. *New Journal of Physics*, 9, 2007.
- [306] K. Leifer, P. A. Buffat, J. Cagnon, E. Kapon, A. Rudra, and P. A. Stadelmann. Quantitative imaging of ingaas/gaas layers using transmission electron microscopy methods: characterization of stresses and chemical composition. *Journal of Crystal Growth*, 237:1471–1475, 2002.
- [307] Joël Cagnon and Klaus Leifer. *Analyse quantitative des intensités diffractées en microscopie électronique à transmission*. PhD thesis, 2004.
- [308] X. Kong, A. Trampert, and K. H. Ploog. Composition fluctuations in dilute nitride (ga,in)(n,as)/gaas heterostructures measured by low-loss electron energy-loss spectroscopy. *Micron*, 37(5):465–472, 2006.
- [309] K. Leifer, P. A. Buffat, P. A. Stadelmann, and E. Kapon. Theoretical and experimental limits of the analysis of iii/v semiconductors using eels. *Micron*, 31(4):411–427, 2000.
- [310] T. Tanaka, Y. Arakawa, and G. W. E. Bauer. Magnetoexcitons in quantum wires with an anisotropic parabolic potential. *Physical Review B*, 50(11):7719–7723, 1994.
- [311] N. Moret, D. Y. Oberli, B. Dwir, A. Rudra, P. Gallo, and E. Kapon. Narrow inhomogeneous broadening of v-groove quantum wires grown on vicinal substrates. *Applied Physics Letters*, 93(17):–, 2008.
- [312] A. Dalla Volta, D. D. Vvedensky, N. Gogneau, E. Pelucchi, A. Rudra, B. Dwir, E. Kapon, and C. Ratsch. Step ordering induced by nonplanar patterning of gaas surfaces. *Applied Physics Letters*, 88:203104, 2006.
- [313] G. Bernatz, S. Nau, R. Rettig, and W. Stolz. Effect of movpe growth interruptions on the gallium arsenide interior interface morphology. *Journal of Electronic Materials*, 29(1):129–133, 2000.
- [314] A. Jasik, A. Wnuk, A. Wojcik-Jedlinska, R. Jakiela, J. Muszalski, W. Strupinski, and M. Bugajski. The influence of the growth temperature and interruption time on the crystal quality of ingaas/gaas qw structures grown by mbe and mocvd methods. *Journal of Crystal Growth*, 310(11):2785–2792, 2008.
- [315] G.B. Stringfellow. *Organometallic Vapor-phase Epitaxy: Theory and Practice*. Academic Press, 1999.
- [316] S. Mazzucato, R. J. Potter, A. Erol, N. Balkan, P. R. Chalker, T. B. Joyce, T. J. Bullough, X. Marie, H. Carrere, E. Bedel, G. Lacoste, A. Arnoult, and C. Fontaine. S-shaped behaviour of the temperature-dependent energy band gap in dilute nitrides. *Physica E-Low-Dimensional Systems & Nanostructures*, 17(1-4):242–244, 2003.

-
- [317] A. Hierro, J. M. Ulloa, J. M. Chauveau, A. Trampert, M. A. Pinault, E. Tournie, A. Guzman, J. L. Sanchez-Rojas, and E. Calleja. Annealing effects on the crystal structure of gainnas quantum wells with large in and n content grown by molecular beam epitaxy. *Journal of Applied Physics*, 94(4):2319–2324, 2003.
 - [318] A. Feltrin, R. Idrissi Kaitouni, A. Crottini, M. A. Dupertuis, J. L. Staehli, B. Deveaud, V. Savona, X. L. Wang, and M. Ogura. Exciton relaxation and level repulsion in gaas/alxgal-xas quantum wires. *Physical Review B*, 69(20), 2004.
 - [319] F. Vouilloz, D. Y. Oberli, M. A. Dupertuis, A. Gustafsson, F. Reinhardt, and E. Kapon. Polarization anisotropy and valence band mixing in semiconductor quantum wires. *Physical Review Letters*, 78(8):1580–1583, 1997.
 - [320] C. Constantin, E. Martinet, F. Lelarge, K. Leifer, A. Rudra, and E. Kapon. Influence of strain and quantum confinement on the optical properties of ingaas/gaas v-groove quantum wires. *Journal of Applied Physics*, 88(1):141–147, 2000.
 - [321] M. Asada, Y. Miyamoto, and Y. Suematsu. Gain and the threshold of 3-dimensional quantum-box lasers. *IEEE Journal of Quantum Electronics*, 22(9):1915–1921, 1986.
 - [322] N. N. Ledentsov, V. M. Ustinov, V. A. Shchukin, P. S. Kop'ev, Z. I. Alferov, and D. Bimberg. Quantum dot heterostructures: fabrication, properties, lasers (review). *Semiconductors*, 32(4):343–365, 1998.
 - [323] M. Grundmann. The present status of quantum dot lasers. *Physica E-Low-Dimensional Systems & Nanostructures*, 5(3):167–184, 1999.
 - [324] A. Imamoglu and Y. Yamamoto. Turnstile device for heralded single photons - coulomb-blockade of electron and hole tunneling in quantum-confined p-i-n heterojunctions. *Physical Review Letters*, 72(2):210–213, 1994.
 - [325] A. Surrente, M. Felici, P. Gallo, B. Dwir, A. Rudra, G. Biasiol, L. Sorba, and E. Kapon. Ordered systems of site-controlled pyramidal quantum dots incorporated in photonic crystal cavities. *Nanotechnology*, 22(46), 2011.
 - [326] C. Schneider, A. Huggenberger, T. Sunner, T. Heindel, M. Strauss, S. Gopfert, P. Weinmann, S. Reitzenstein, L. Worschech, M. Kamp, S. Hofling, and A. Forchel. Single site-controlled in(ga)as/gaas quantum dots: growth, properties and device integration. *Nanotechnology*, 20(43):–, 2009.
 - [327] A. Fiore, C. Zinoni, B. Alloing, C. Monat, L. Balet, L. H. Li, N. Le Thomas, R. Houdre, L. Lunghi, M. Francardi, A. Gerardino, and G. Patriarche. Telecom-wavelength single-photon sources for quantum communications. *Journal of Physics-Condensed Matter*, 19(22), 2007.
 - [328] M. Sopanen, H. P. Xin, and C. W. Tu. Self-assembled gainnas quantum dots for 1.3 and 1.55 μm emission on gaas. *Applied Physics Letters*, 76(8):994–996, 2000.

Bibliography

- [329] T. Hakkarainen, J. Toivonen, M. Sopanen, and H. Lipsanen. Self-assembled gain(n)as quantum dots: Enhanced luminescence at 1.3 μ m. *Applied Physics Letters*, 79(24):3932–3934, 2001.
- [330] O. Schumann, L. Geelhaar, H. Riechert, H. Cerva, and G. Abstreiter. Morphology and optical properties of inas(n) quantum dots. *Journal of Applied Physics*, 96(5):2832–2840, 2004.
- [331] V. Sallet, G. Patriarche, M. N. Merat-Combes, L. Largeau, O. Mauguin, and L. Travers. Structural and photoluminescence studies of inasn quantum dots grown on gaas by mbe. *Journal of Crystal Growth*, 290(1):80–86, 2006.
- [332] D. F. Reyes, D. Gonzalez, D. L. Sales, R. Gargallo-Caballero, A. Guzman, J. M. Ulloa, and A. Hierro. Inhibition of in desorption in diluted nitride inasn quantum dots. *Applied Physics Letters*, 98(7), 2011.
- [333] A. V. Osipov, S. A. Kukushkin, F. Schmitt, and P. Hess. Kinetic model of coherent island formation in the case of self-limiting growth. *Physical Review B*, 64(20), 2001.
- [334] A. Ueta, K. Akahane, S. Gozu, N. Yamamoto, and N. Ohtani. Study of inasn quantum dots on gaas substrates by molecular beam epitaxy. *Physica Status Solidi B-Basic Solid State Physics*, 243(7):1514–1518, 2006.
- [335] J. F. Falth, S. F. Yoon, K. H. Tan, and E. A. Fitzgerald. The effect of nitrogen pressure during molecular beam epitaxy growth of inasn quantum dots. *Nanotechnology*, 19(4):6, 2008.
- [336] J. F. Falth, S. F. Yoon, and E. A. Fitzgerald. The influence of substrate temperature on inasn quantum dots grown by molecular beam epitaxy. *Nanotechnology*, 19(45), 2008.
- [337] L. Ivanova, H. Eisele, A. Lenz, R. Timm, M. Dahne, O. Schumann, L. Geelhaar, and H. Riechert. Nitrogen-induced intermixing of inasn quantum dots with the gaas matrix. *Applied Physics Letters*, 92(20):–, 2008.
- [338] R. Gargallo-Caballero, A. Guzman, M. Hopkinson, J. M. Ulloa, A. Hierro, and E. Calleja. Dependence of n incorporation into (ga)inasn qds on ga content probed by rapid thermal annealing. *Physica Status Solidi C: Current Topics in Solid State Physics, Vol 6, No 6*, 6(6):1441–1444, 2009.
- [339] R. Gargallo-Caballero, A. Guzman, J. M. Ulloa, A. Hierro, M. Hopkinson, E. Luna, and A. Trampert. Impact of the ga/in ratio on the n incorporation into (in,ga)(as,n) quantum dots. *Journal of Applied Physics*, 111(8), 2012.
- [340] T. Hakkarainen, J. Toivonen, M. Sopanen, and H. Lipsanen. Wavelength extension of gainas/gain(n)as quantum dot structures grown on gaas. *Journal of Crystal Growth*, 248:339–342, 2003.

-
- [341] V. M. Ustinov, A. Y. Egorov, V. A. Odnoblyudov, N. V. Kryzhanovskaya, Y. G. Musikhin, A. E. Tsatsul'nikov, and Z. I. Alferov. Inas/ingaasn quantum dots emitting at 1.55 μm grown by molecular beam epitaxy. *Journal of Crystal Growth*, 251(1-4):388–391, 2003.
 - [342] Z. Z. Sun, S. F. Yoon, K. C. Yew, B. X. Bo, D. A. Yan, and T. Chih-Hang. Room-temperature continuous-wave operation of gainnas/gaas quantum dot laser with gaasn barrier grown by solid source molecular beam epitaxy. *Applied Physics Letters*, 85(9):1469–1471, 2004.
 - [343] S. Tomic. Electronic structure of inyga1-yas1-xnx/gaas(n) quantum dots by ten-band k center dot p theory. *Physical Review B*, 73(12):–, 2006.
 - [344] S. Tomic. Optical properties of dilute nitrogen gainnas quantum dots. *Applied Physics Letters*, 90(12), 2007.
 - [345] S. Tomic. Design issues of 1.55 μm emitting gainnas quantum dots. *Optical and Quantum Electronics*, 40(5-6):307–311, 2008.
 - [346] J. Chen, W. J. Fan, Q. Xu, X. W. Zhang, S. S. Li, and J. B. Xia. Electronic structure and optical gain of truncated inas1-xnx/gaas quantum dots. *Superlattices and Microstructures*, 46(3):498–506, 2009.
 - [347] V. Dimastrodonato, L. O. Mereni, G. Juska, and E. Pelucchi. Impact of nitrogen incorporation on pseudomorphic site-controlled quantum dots grown by metalorganic vapor phase epitaxy. *Applied Physics Letters*, 97(7):–, 2010.
 - [348] G. Juska, V. Dimastrodonato, L. O. Mereni, A. Gocalinska, and E. Pelucchi. A study of nitrogen incorporation in pyramidal site-controlled quantum dots. *Nanoscale Research Letters*, 6, 2011.
 - [349] L. O. Mereni, O. Marquardt, G. Juska, V. Dimastrodonato, E. P. O'Reilly, and E. Pelucchi. Fine-structure splitting in large-pitch pyramidal quantum dots. *Physical Review B*, 85(15), 2012.
 - [350] R. Carron, P. Gallo, B. Dwir, A. Rudra, and E. Kapon. Dilute-nitride gainasn/gaas site-controlled pyramidal quantum dots. *Applied Physics Letters*, 99(18):181113, 2011.
 - [351] A. Mohan, P. Gallo, M. Felici, B. Dwir, A. Rudra, J. Faist, and E. Kapon. Engineering conduction and valence band states in site-controlled pyramidal quantum dots. *Applied Physics Letters*, 98(25), 2011.
 - [352] C. Jarlov, P. Gallo, M. Calic, B. Dwir, A. Rudra, and E. Kapon. Bound and anti-bound biexciton in site-controlled pyramidal gainas/gaas quantum dots. *Applied Physics Letters*, 101(19), 2012.
 - [353] A. Hartmann, Y. Ducommun, E. Kapon, U. Hohenester, and E. Molinari. Few-particle effects in semiconductor quantum dots: Observation of multicharged excitons. *Physical Review Letters*, 84(24):5648–5651, 2000.

Bibliography

- [354] K. F. Karlsson, M. A. Dupertuis, D. Y. Oberli, E. Pelucchi, A. Rudra, P. O. Holtz, and E. Kapon. Fine structure of exciton complexes in high-symmetry quantum dots: Effects of symmetry breaking and symmetry elevation. *Physical Review B*, 81(16), 2010.
- [355] M. A. Dupertuis, K. F. Karlsson, D. Y. Oberli, E. Pelucchi, A. Rudra, P. O. Holtz, and E. Kapon. Symmetries and the polarized optical spectra of exciton complexes in quantum dots. *Physical Review Letters*, 107(12), 2011.
- [356] M. H. Baier, S. Watanabe, E. Pelucchi, and E. Kapon. High uniformity of site-controlled pyramidal quantum dots grown on prepatterned substrates. *Applied Physics Letters*, 84(11):1943–1945, 2004.
- [357] S. H. Lee, W. Moritz, and M. Scheffler. Gaas(001) surface under conditions of low as pressure: Evidence for a novel surface geometry. *Physical Review Letters*, 85(18):3890–3893, 2000.
- [358] N. Grandjean, J. Massies, and M. Leroux. Monte carlo simulation of in surface segregation during the growth of inxgal-xas on gaas(001). *Physical Review B*, 53(3):998–1001, 1996.
- [359] S. V. Khazanova and M. I. Vasilevskiy. Modelling of the composition segregation effect during epitaxial growth of ingaas quantum well heterostructures. *Semiconductor Science and Technology*, 25(8):–, 2010.
- [360] A. L. S. Chua, E. Pelucchi, A. Rudra, B. Dwir, E. Kapon, A. Zangwill, and D. D. Vvedensky. Theory and experiment of step bunching on misoriented gaas(001) during metalorganic vapor-phase epitaxy. *Applied Physics Letters*, 92(1):–, 2008.
- [361] E. Pelucchi, V. Dimastrodonato, A. Rudra, K. Leifer, E. Kapon, L. Bethke, P. A. Zestanakis, and D. D. Vvedensky. Decomposition, diffusion, and growth rate anisotropies in self-limited profiles during metalorganic vapor-phase epitaxy of seeded nanostructures. *Physical Review B*, 83(20):–, 2011.
- [362] V. Dimastrodonato, E. Pelucchi, and D. D. Vvedensky. Self-limiting evolution of seeded quantum wires and dots on patterned substrates. *Physical Review Letters*, 108(25), 2012.
- [363] R.L. Schwoebel. Step motion on crystal surfaces .2. *Journal of Applied Physics*, 40(2):614, 1969.
- [364] F. Lelarge, G. Biasiol, A. Rudra, A. Condo, and E. Kapon. Self-ordered nanostructures grown by organometallic chemical vapor deposition on v-grooved substrates: experiments and monte-carlo simulations. *Microelectronics Journal*, 30(4-5):461–466, 1999.

Acknowledgments

The redaction of the thesis manuscript is only the final and individual part of a long work, in which many people were involved at various degrees. Now it's time to try listing a few people who helped me during these years.

First of all i would like to thank my professor, Eli Kapon, who offered me the opportunity to join his group and get involved in a high-level experimental research activity, in very good conditions.

I would also like to thank the staff of the lab. Alok is dedicated to the maintenance of the MOVPE facility, and nevertheless always available for discussion. Benny performed the e-beam lithography and, among other qualities, masters the secret knowledge of setting up, and later repairing the most various electronic devices. All the sample preparation could not have been done as efficiently if not for Nicolas, Damien and Yoan who keep the clean room in excellent condition in spite of the many users. I am also indebted to Roger, who provided clever design suggestions and incredibly fast realizations of mechanical pieces for my evolving characterization setup. The secretaries deserve a special thank, as they allowed me to forget about the administrative work. Thank you Gabriella, Nadia, Anne-Valérie, Céline!

I would like to address a big thank to my officemates for standing me all these years. First of all to Nicolas, who taught me the work in clean room and gave me insights into the life of a PhD student. But also to Alessandro, a great guy who introduced remarkable cultural elements from Italy (amongst which a few unforgettable dishes). I really enjoyed your company, in Lausanne and abroad. For a time, I also had the pleasure to share the office with the hard-voiced mountaineer Lukas, with the nordic Guro and Helge, as well as with Zhanguo from the Chinese side of the world. In spite of his efforts, Kamil could not convince me to speak Polish during our lunch expeditions.

I'd like to express my gratitude to Pascal and Marco, the post-docs who shew me how to work as a scientist, taught me a great deal of what I know and were always available for help, discussion and encouragement. It was a real pleasure to work with you. Milan, please be quick with the writing so we can have beach-volley sessions before the winter! Justyna, I hope you managed to work efficiently in-between my calls for coffee breaks. Thank you radio animator Zlatko, for your hourly ideas about how to improve my English. Working with, meeting and

Acknowledgments

discussing with the other people of the lab was also a great pleasure. Thank you Elodie, Lydie, Clément, Nicolas, Alexey, Dalila, Chris! I definitely must thank a few former members of our group, especially you Arun, Kirill, Valentina and Qing, but also Sanna, Marcin, Lars, as well as the others I forgot to mention here.

Thank you Bénédicte, I cannot tell how your presence and your love were precious during the hardest moments of this long work. I would also thank my parents, my sister and brothers (look Julien, I finally made it!). Not forgetting Smash, a living proof that laziness can be an art of life. I'm also grateful to the coffee machine next to aquarium, without which nothing would have been possible (especially the redaction of the manuscript). And last, but not least, I would like to thank friends who reminded that life is best spend outside the darkness of the lab. Here a special thought to Jonathan, Ludovic, Niklaus, René, as well as the people of the champion volleyball team and of the CJL.

Publications and conferences

Journal Articles

High-quality 1.3 μ m-wavelength GaInAsN/GaAs quantum wells grown by metalorganic vapor phase epitaxy on vicinal substrates, D. Fekete, R. Carron, P. Gallo, B. Dwir, A. Rudra and E. Kapon,
Appl. Phys. Lett. **99** (7) (2011).

Dilute nitride InGaAsN/GaAs V-groove quantum wires emitting at 1.3 μ m wavelength at room temperature, R. Carron, D. Fekete, P. Gallo, B. Dwir, A. Rudra, M. Felici, B. Bartova, M. Cantoni and E. Kapon,
Appl. Phys. Lett. **99** (10) (2011).

Dilute-nitride GaInAsN/GaAs site-controlled pyramidal quantum dots, R. Carron, P. Gallo, B. Dwir, A. Rudra, and E. Kapon,
Appl. Phys. Lett. **99**, 181113 (2011).

Magneto-optical properties of single site-controlled InGaAsN quantum wires grown on prepatterned GaAs substrates, M. Felici, G. Pettinari, R. Carron, G. Lavenuta, E. Tartaglini, A. Polimeni, D. Fekete, P. Gallo, B. Dwir, A. Rudra, P. C. M. Christianen, J. C. Maan, M. Capizzi, and E. Kapon,
Physical Review B, **85** (15), (2012).

Reduced temperature sensitivity of the polarization properties of hydrogenated InGaAsN V-groove quantum wires, M. Felici, A. Polimeni, E. Tartaglini, A. Notargiacomo, M. De Luca, R. Carron, D. Fekete, B. Dwir, A. Rudra, M. Capizzi, and E. Kapon,
Applied Physics Letters, **101** (15), (2012).

Conferences and seminars

MOVPE grown InGaAsN/GaAs site-controlled quantum wires emitting at 1.3 μ m, R. Carron, D. Fekete, A. Rudra, B. Dwir, P. Gallo and Eli Kapon,
European Materials Research Society (EMRS) 2010, Strasbourg, France, June 9 - 11, 2009. Oral presentation.

MOVPE grown InGaAsN quantum wires and wells emitting at 1.3 μ m, Dan Fekete, Romain Carron, Alok Rudra, Benjamin Dwir, Pascal Gallo, Marco Felici and Eli Kapon,
15th International Conference on Metal Organic Vapor Phase Epitaxy (ICMOVPE), Lake Tahoe, NV, May 23-28, 2010. Oral presentation.

High density arrays of site-controlled GaInAsN/GaAs quantum dots, R. Carron, P. Gallo, A. Rudra, B. Dwir and E. Kapon,
XIV European Workshop on Metalorganic Vapor Phase Epitaxy, EW-MOVPE 2011, Wrocław, Poland, June 5-8 (2011). Poster presentation.

Nitrogen incorporation in MOVPE-grown GaInAs quantum dots, R. Carron, P. Gallo, A. Rudra, B. Dwir and E. Kapon,
12th International Conference on Optics of Excitons in Confined Systems, OECS12, Paris, France, September 12-16 (2011). Poster presentation.

Evolution of surface morphology during MOVPE on inverted tetrahedral recesses etched on (111)B GaAs substrate, A. Surrente, R. Carron, P. Gallo, A. Rudra, B. Dwir, and E. Kapon,
Site-controlled Epitaxy COST Workshop, COST action MP0805, Heraklion, Greece, April 29-May 1, 2012. Oral presentation.

Nitrogen incorporation in MOVPE-grown GaInAs site-controlled quantum dots, R. Carron, P. Gallo, A. Rudra, B. Dwir and E. Kapon,
Epitaxy & Structural analysis of III-V-N Semiconductor Nanostructures 2012, COST Action MP0805, Heraklion, Crete, Greece, April 29-May 02 (2012). Poster presentation.

Curriculum Vitae

Romain Carron

Rte de Berne 24, 1010 Lausanne

carron.romain@gmail.com

Born on December 26, 1983 in Sion (CH)

Swiss nationality

Education and research experience

2008 - 2013 PhD in Physics

Laboratory of Physics of Nanostructures (LPN), Prof. Eli Kapon,
Ecole Polytechnique Fédérale de Lausanne (EPFL).

*Dilute nitride low-dimensional nanostructures formed on non-planar
substrates.*

2003 - 2008 Ingénieur Physicien Diplômé EPFL (Master of Science MSc in Physics).

Master thesis at University of British Columbia (UBC), Vancouver, Canada.
*Face-centered-cubic Chromium investigated with the spin-polarized
scanning tunnelling microscopy.*

Semester project: *Propriétés magnétiques d'îlots de CoPd sur substrat Pt(111)*
(STM study).

Semester project: *RadialAverageTool* (Java software programming).

1997 - 2003 Maturité fédérale at Lycée-Collège des Creusets (Sion, oriented physics -
mathematics).

Expertise

Clean room facility: plasma enhanced chemical vapor deposition (PECVD), reactive ion
etching (RIE), inductively coupled plasma (ICP), optical and electron beam lithography, wet
etching, sputtering, etc.

Semiconductor epitaxy: metallorganic vapor phase epitaxy (MOVPE).

Characterization techniques: microphotoluminescence (μ PL - design and implementation of
a new setup), scanning electron microscopy (SEM), atomic force microscopy (AFM), scanning
tunneling microscopy (STM), transmission electron microscopy (TEM).

Experimental techniques: lasers, cryogenics, (ultra-)high vacuum.

Computer skills: Windows, Mac and Unix standard and office applications; Igor Pro, Matlab,
Labview, Latex, HTML and CSS; good notions in Photoshop, Illustrator, Comsol, C++, Java.

Teaching experience: assistant for General Physics (2009-2012).

Languages

French Mother tongue

English Fluent

German High school level

Extracurricular activities

Hiking, volleyball, singing.